

# Structural properties of Quantizer problem solutions

Strukturelle Eigenschaften von Quantizer-Problemlösungen

Der  
Naturwissenschaftlichen Fakultät  
Der  
Friedrich-Alexander-Universität Erlangen-Nürnberg



FRIEDRICH-ALEXANDER  
UNIVERSITÄT  
ERLANGEN-NÜRNBERG  
FACULTY OF SCIENCES

zur  
Erlangung des Doktorgrades Dr. rer. nat.  
vorgelegt von

**Jakov Lovrić**  
aus Zagreb, Kroatien



Als Dissertation genehmigt  
von der **Naturwissenschaftlichen Fakultät**  
der **Friedrich-Alexander-Universität Erlangen-Nürnberg**

Tag der mündlichen Prüfung:

8.7.2022.

Vorsitzender des Promotionsorgans:

Prof. Dr. Wolfgang Achtziger

Gutachter/in:

Prof. Dr. Ana-Sunčana Smith

Prof. Dr. Myfanwy Evans



*mojoj Diani i mojoj Teni*



## Acknowledgements

I would like to express my deepest gratitude to my supervisor, Ana-Sunčana Smith. Ana, thank you for giving me this project and guiding me through it with patience and belief in me. Thank you for all the knowledge you gave me throughout these years, which is of priceless value for me.

A special thanks go to Sara Kaliman. Sara, thank you for introducing me to this project and sharing all the insightful ideas during the past few years. It was a true joy working with you. I would like to express appreciation to Gerd Schröder-Turk for everything during my visit to Murdoch University at the beginning of this doctoral project, which brings me fond memories.

I am particularly grateful to Damir Vurnek, Maxime Hubert, Simone Gehrler, and Christiane Huck-Stiasny for selfless assistance in the final stages of my doctoral project.

I would like to take this opportunity and acknowledge Mislav Cvitković, Josip Vlajčević, Zlatko Brkljača, Nataša Vučemilović-Alagić, Marko Hanževački, Josip Augustin Janeš, Luka Bilić, Robert Stepić, Mario Špadina, Željka Medven Korman, Nikolina Bošnjak, Danijela Barić, Borislav Kovačević and David Smith for a pleasant time at Ruđer Bošković Institute. You have all been a constant source of motivation, support and a positive atmosphere during the previous years. I am looking forward to your future successes in your private lives and careers. I would also like to acknowledge all of the members of the PULS Group at FAU for hospitality during my visits and productive collaborations during my doctoral project.

I would like to acknowledge the institutional and financial support of my PhD study, namely Ruđer Bošković Institute in Zagreb, Cluster of Excellence: Engineering of Advanced Materials at FAU in Erlangen and the European Research Council, which provided this project financial support through the Starting Grant *MembranesAct 2013-337283*.

Last but not least, I would like to thank my family and friends for being always by my side and sharing both good and bad times with me. Special thanks to my parents for raising me into the person I am. Mama, hvala ti i volim te. Tata, sve znaš. Finally, the most enormous gratitude goes to my

wife Diana and daughter Tena. Thank you for your love and all the joy you bring into the world. You give the real meaning to the following pages.

Truly I tell you, if anyone says to this mountain, 'Go, throw yourself into the sea,' and does not doubt in their heart but believes that what they say will happen, it will be done for them.

---

Mark,11:23



# Summary

For a set of objects distributed in the space of a given volume, the Quantizer problem is finding a minimum of the sum of the squared distances between arbitrary spatial positions and the given set. Such optimal configuration tessellates the space in a way that the generating set is placed in the geometric centroids of the Voronoi cells. Obviously, the Quantizer problem has trivial solutions where the generating objects are equidistant. Finding non-trivial, disordered solutions, however, has been a difficult task. The work presented in this thesis addresses precisely this challenge.

Initially, solutions to the Quantizer problems are searched for point generators. The solution is sought using the iterative optimization procedure known as Lloyd's algorithm, the generalization of the famous k-means clustering primarily used to construct centroidal Voronoi diagrams. Lloyd's iteration is applied to a number of sets comprising points obtained from processes generating different types of disorder in 2D and 3D. Notably, a universal local Quantizer minimal state is obtained, irrespective of the starting configuration. Remarkably, while being fully amorphous in nature, this final state is also effectively hyperuniform, which means that long-range density fluctuations are suppressed.

Motivated by the previous findings, a generalization of the Quantizer problem to the systems built of extended convex objects rather than points is attempted. As a preliminary step, random assemblies of non-overlapping ellipses were generated using established algorithms. The obtained assemblies are fully characterized from the geometric and the topological points of view as a function of the shape and density of ellipses. This analysis provides detailed insights into the distributions of the scalar and vectorial morphological measures of the cells emerging from the set-based Voronoi tessellations. Furthermore, it analyses their cross-correlations, which is particularly important for comparison with experimental data.

The ensuing effort focused on solving the Quantizer problem for these "random" assemblies of ellipses. This required rephrasing of the Quantizer energy to account for the finite size of the generating objects. The optimal solution is now associated with finding the infimum of the sum of the squared distances between arbitrary spatial positions and the boundaries of a given set. By analogy with finding the solution to the Quantizer problem with point generators, local optimal distribution of ellipses is attempted using Lloyd's algorithm, which now has to be adapted to avoid overlap of ellipses. In the

limit of zero packing fraction, the solution of the point process optimisation is found. Beyond this limit, the structure of the spatially optimised assemblies is both shape and density-dependent. Nonetheless, the effectively hyperuniform assemblies are found in a broad range of the parameter space, which is extended to higher packing density as the ellipse becomes less elongated. At high packing fractions performing Lloyd iterations and avoiding overlap is not possible with the current algorithm, and no structure change is observed.

As the application of the above-developed concepts, the structure of a maturing epithelium tissue is analysed. The epithelium is typically comprised of a single layer of cells and can be regarded as tiling emerging from the set Voronoi tessellation built from the cell nuclei. It was found that morphologically, the tissue strongly resembles random packings at all stages of development. However, careful analysis of experimental data shows that during the process of tissue densification, nuclei are repositioned relative to the centre of the cell, which can be captured by initiating but not converging Lloyd's optimisation. As the tissue acquires its homeostatic steady state, density fluctuations are suppressed on well-defined length scales comprising neighbourhoods of 2 and 4 cells at low and high densities, respectively. However, at small wave vectors, the structure factor grows exponentially to a final value, contrary to predictions of the vertex model, which is the current state of the art approach to modelling tissue development. This analysis thus clearly demonstrates the need for quantitative statistical analysis of data. Finally, it points to a need for an improvement of tissue models.

# Zusammenfassung

Für eine Menge von Objekten, die in einem Raum mit festem Volumen verteilt sind, besteht das Quantisierer-Problem darin, ein Minimum der Summe der quadratischen Abstände zwischen beliebigen Positionen im Raum und der gegebenen Menge von Objekten zu finden. Eine solche optimale Konfiguration tesseliert den Raum so, dass die erzeugende Menge in den geometrischen Zentren der Voronoi-Zellen platziert wird. Offensichtlich hat das Quantisierer-Problem triviale Lösungen, bei denen die erzeugenden Objekte äquidistant sind. Nichttriviale, ungeordnete Lösungen zu finden ist jedoch eine schwierige Aufgabe. Die vorliegende Arbeit befasst sich genau mit dieser Herausforderung.

Zunächst wird in den Lösungen für das Quantisierer-Problem nach Punktgeneratoren gesucht. Die Lösung wird mit Hilfe eines iterativen Optimierungsverfahrens gefunden, das als Lloyd-Algorithmus bekannt ist, der Verallgemeinerung des berühmten k-means-Algorithmus, welcher in erster Linie zur Konstruktion von Schwerpunkt-Voronoi-Diagrammen verwendet wurde. Der Lloyd'sche Iterations-Algorithmus wird auf eine Reihe von Punktesätzen angewendet, die aus Prozessen stammen, die verschiedene Arten von Unordnung in 2D und 3D erzeugen. Dabei wird unabhängig von der Ausgangskonfiguration ein universeller lokaler Quantisierer-Minimalzustand erreicht. Bemerkenswerterweise ist dieser Endzustand, obwohl er völlig amorph ist, auch effektiv hyperuniform, was bedeutet, dass weitreichende Dichtefluktuationen unterdrückt werden.

Motiviert durch die vorangegangenen Erkenntnisse wird eine Verallgemeinerung des Quantisierer-Problems auf Systeme versucht, die nicht aus Punkten, sondern aus ausgedehnten konvexen Objekten bestehen. In einem ersten Schritt wurden mit Hilfe etablierter Algorithmen zufällige Anordnungen von sich nicht überlappenden Ellipsen erzeugt. Die erhaltenen Anordnungen können aus geometrischer und topologischer Sicht vollständig als Funktion von Form und Dichte der Ellipsen charakterisiert werden. Diese Analyse liefert detaillierte Einblicke in die Verteilungen der skalaren und vektoriellen morphologischen Maße der Zellen, die sich aus den mengenbasierten Voronoi-Tessellierungen ergeben. Außerdem werden ihre Kreuzkorrelationen analysiert, was für den Vergleich mit experimentellen Daten besonders wichtig ist.

Die anschließende Arbeit konzentrierte sich auf die Lösung des Quantisierer-Problems für diese "zufälligen" Anordnungen von Ellipsen. Dies erforderte

eine Umformulierung der Quantisierungsenergie, um der endlichen Größe der erzeugenden Objekte Rechnung zu tragen. Die optimale Lösung ist nun mit der Suche nach dem Infimum der Summe der quadratischen Abstände zwischen beliebigen räumlichen Positionen und den Grenzen einer gegebenen Menge verbunden. In Analogie zur Lösung des Quantisierer-Problems mit Punktgeneratoren wird eine lokal optimale Verteilung der Ellipsen mit Hilfe des Lloyd-Algorithmus versucht, der nun angepasst werden muss, um eine Überlappung der Ellipsen zu vermeiden. Im Grenzwert von verschwindenden Packungsdichten wird die Lösung der Punktprozessoptimierung gefunden. Jenseits dieser Grenze ist die Struktur der räumlich optimierten Anordnung sowohl form- als auch dichteabhängig. Nichtsdestotrotz werden in einem breiten Bereich des Parameterraums effektiv hyperuniforme Anordnungen gefunden. Der Parameterraum vergrößert sich zu höheren Packungsdichten wenn die Ellipsen weniger langgestreckt sind. Bei hohen Packungsanteilen ist die Durchführung von Iterationen des Lloyd-Algorithmus und die Vermeidung von Überlappungen der Ellipsen mit dem derzeitigen Algorithmus nicht möglich und es wird keine Strukturänderung beobachtet.

Als Anwendung der oben entwickelten Konzepte wird die Struktur eines sich entwickelnden Epithelgewebes analysiert. Das Epithel besteht typischerweise aus einer einzigen Schicht von Zellen und kann als ein aus dem Voronoi-Diagramm der Zellkerne gebildetes Mosaik betrachtet werden. Es wurde festgestellt, dass das Gewebe morphologisch in allen Entwicklungsstadien stark an zufällige Packungen erinnert. Eine sorgfältige Analyse der experimentellen Daten zeigt jedoch, dass bei steigender Zelldichte des Epithelgewebes die Zellkerne relativ zum Zentrum der Zelle neu positioniert werden, was durch eine initiierende, aber nicht konvergierende Lloyd-Optimierung erfasst werden kann. Wenn das Gewebe seinen homöostatischen Gleichgewichtszustand erreicht, werden Dichteschwankungen auf wohldefinierten Längenskalen unterdrückt, die Nachbarschaften von 2 bzw. 4 Zellen bei niedrigen bzw. hohen Dichten umfassen. Bei kleinen Wellenvektoren wächst der Strukturfaktor jedoch exponentiell bis zu einem endgültigen Wert an, was im Gegensatz zu den Vorhersagen des Vertex-Modells steht, das den derzeitigen Stand der Wissenschaft bei der Modellierung der Gewebeentwicklung darstellt. Diese Analyse verdeutlicht somit die Notwendigkeit einer quantitativen statistischen Analyse der Daten. Schließlich zeigt sie auf, dass die derzeitigen Gewebemodelle verbessert werden müssen.

# Contents

<b>Acknowledgements</b>	<b>v</b>
<b>Summary</b>	<b>vii</b>
<b>Zusammenfassung</b>	<b>ix</b>
<b>1 Introduction</b>	<b>1</b>
1.1 Optimizations in systems of particles . . . . .	1
1.2 Quantizer problem . . . . .	3
1.2.1 Definition of Quantizer problem . . . . .	3
1.2.2 Analysis of Quantizer error . . . . .	6
1.2.3 Lloyd's algorithm . . . . .	8
1.2.4 Solutions to Quantizer problem . . . . .	11
1.3 Hyperuniformity of systems . . . . .	13
1.3.1 Definition of hyperuniformity . . . . .	13
1.3.2 Structure factor of hyperuniform point patterns . . . . .	16
1.4 Outlook of this thesis . . . . .	18
<b>2 Universal hidden order in amorphous cellular geometries</b>	<b>21</b>
2.1 Introduction . . . . .	23
2.2 Methods . . . . .	24
2.2.1 Initial configurations . . . . .	24
Binomial point process (BPP) . . . . .	24
Determinantal point process (DPP) . . . . .	25
Permanental point process (PPP) . . . . .	26
Hyperplane (Hyperfluctuating) intersection process . . . . .	26
Maximally random jammed state (MRJ) . . . . .	27
Lubachevsky-Stillinger algorithm for sphere packings (LSPP) . . . . .	27
Stealthy hyperuniform point process (Stealthy PP) . . . . .	28
2.2.2 Implementation and convergence of Lloyd's algorithm	29
2.3 Properties of the Quantizer minimal states . . . . .	32

2.3.1	Density fluctuations of systems under Lloyd's algorithm	33
2.3.2	Amorphousness of structures . . . . .	36
2.3.3	Universality of the final structure . . . . .	37
2.3.4	Effect of Lloyd's algorithm to structures with crystalline patches . . . . .	38
2.4	Overview and discussion . . . . .	41
<b>3</b>	<b>Geometric effects in random assemblies of ellipses</b>	<b>43</b>
3.1	Introduction to random assemblies . . . . .	45
3.2	Methods . . . . .	47
3.2.1	Phase space of assemblies and calculation of morphological measures . . . . .	47
3.2.2	Packing algorithm and sampling procedure . . . . .	49
3.2.3	Statistical analysis . . . . .	51
3.3	Results . . . . .	53
3.3.1	Area and perimeter of Voronoi cells . . . . .	53
3.3.2	Local packing fraction . . . . .	58
3.3.3	Morphological measures of anisotropy . . . . .	59
3.3.4	Geometric effects in the vicinity of jamming transition	63
3.3.5	Centre of mass distance . . . . .	64
3.3.6	Neighbourhood statistics and the relation between geometry and topology in ellipse assemblies . . . . .	65
3.4	Conclusion . . . . .	67
<b>4</b>	<b>Quantization of the ellipse assemblies</b>	<b>69</b>
4.1	Introduction . . . . .	69
4.1.1	Modified Quantizer problem . . . . .	69
4.1.2	Calculation of the modified total energy . . . . .	72
4.1.3	Modified Lloyd's algorithm . . . . .	74
4.2	Simulations . . . . .	76
4.3	Convergence of the modified Lloyd's algorithm . . . . .	76
4.3.1	Modified total energy . . . . .	76
4.3.2	Relation to the modified Quantizer problem . . . . .	81
4.4	Structural properties of ellipse assemblies under modified Lloyd's algorithm . . . . .	83
4.5	Robustness of the results to the hyperparameters of the modified Lloyd's algorithm . . . . .	88
4.6	Conclusion of Chapter 4 . . . . .	92

<b>5</b>	<b>Theoretical model for epithelial tissues</b>	<b>95</b>
5.1	Introduction to epithelial tissue . . . . .	95
5.2	Structural properties of epithelial tissue . . . . .	99
5.2.1	Structure factor of tissue . . . . .	99
5.2.2	Set Voronoi tessellation based epithelial tissue model .	100
5.2.3	Morphology of cell nuclei . . . . .	103
5.2.4	Randomness in cell tissue . . . . .	104
5.3	Lloyd's iterations as a model for tissue . . . . .	106
5.3.1	Structure factors after applying the modified Lloyd's iterations . . . . .	107
5.3.2	Morphological measures after applying the modified Lloyd's iterations . . . . .	110
5.4	Discussion and outlook . . . . .	115
<b>6</b>	<b>General conclusion</b>	<b>117</b>
<b>A</b>	<b>Geometric effects in random assemblies of ellipses</b>	<b>121</b>
	<b>Bibliography</b>	<b>139</b>
	<b>List of publications</b>	<b>159</b>
	<b>Curriculum Vitae</b>	<b>161</b>
	<b>Statutory Declaration</b>	<b>163</b>





# Chapter 1

## Introduction

### 1.1 Optimizations in systems of particles

Systems containing particles or points are present all around us. Those systems can exist in reality, such as sand and snow, or be virtual, like points in a mesh representing a character in a computer game. Interactions and relations between concerned particles are of universal importance because they define the nature and behaviour of such systems. The equilibrium state of such systems can be associated with an optimization of an appropriate functional that depends on relations between constitutive particles.

Because of practical purposes, optimization problems of systems containing particles have been subjects of interest through the history [7]. The property of granular matter that drew people's attention the most in the past is the system's density. Density can be defined as a number of particles in some volume or a fraction of space occupied by concerning particles, later known as global packing fraction  $\phi_g$ . The motivation behind optimizing the density of particles in the system is very intuitive. The denser system is, the less space is occupied for the same amount of items which is important for practical purposes. For example, Johannes Kepler, motivated by the packing of cannonballs on ships, studied the highest possible packing fraction of equally sized spheres [7]. He conjectured in his book *De Nive Sexangula* (1611) that if the centers of spheres are placed as the atoms in the face centred cubic lattice (FCC, Figure 1.1a), the packing density is highest possible with value  $\frac{\pi}{3\sqrt{2}} \approx 0.74048$ . Kepler's conjecture, despite its simplicity, remained unproven for centuries. In 1998, Thomas Hales proved right the Kepler conjecture by representing the problem in the finite number of dimensions and further solving it using interval arithmetic and linear programming methods that require extensive use of computers [61].

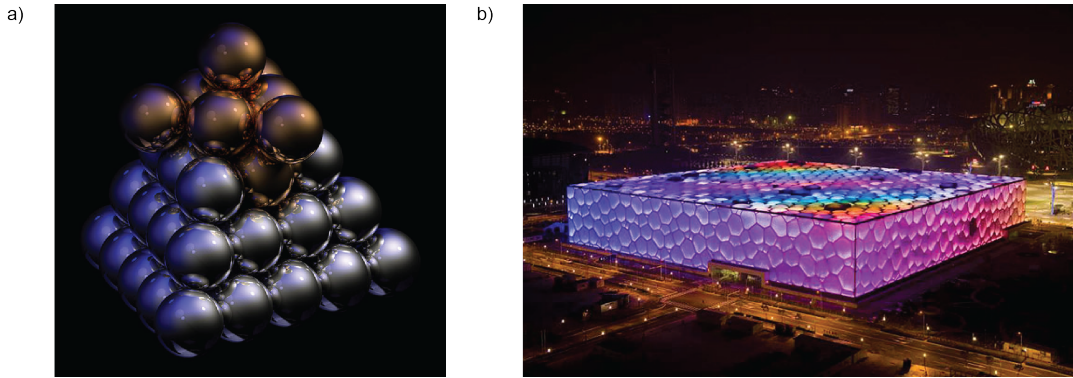


FIGURE 1.1: a) Packing of cannonballs with face centred cubic (FCC) unit cell. The image was taken from reference [22]. b) Weaire-Phelan structure inspired Tristram Carfrae when he designed Beijing National Aquatics Centre for the 2008 Olympic Games. The image was taken from reference [159].

Besides Kepler's conjecture that considers the maximum density of the system, optimizations of many other structural properties in the systems were subjects of interest. Thus, Sir William Thomson (Lord Kelvin), when investigating ideal structures of bubbles, set a problem of dividing space into cells with equal volume while minimizing their surface area [7]. Lord Kelvin suggested the tetrakaidecahedron shape of the cell, also known as a bitruncated cubic honeycomb cell, as a solution to this problem. It took over a century for people to disprove his conjecture when Denis Weaire and Robert Phelan found a structure with 0.3% smaller surface area than the Kelvin structure, later known as Weaire-Phelan structure [157] (Figure 1.1b).

Alongside these most famous structure optimization problems, we can think of many other similar questions both for scientific and industrial context [30, 4, 120, 94]. In this thesis, we will study the problem that concentrates on finding the nearest particle in the space from a given position, well known as the *Quantizer problem*. In the following sections of this chapter, we will define the Quantizer problem, provide a theoretical analysis of the quantization effects and present the method for solving the Quantizer problem. Moreover, we will define the properties of the systems that will be studied in the context of solutions to the Quantizer problem. Finally, we will give an overview of the research questions that will be addressed in this thesis.

## 1.2 Quantizer problem

### 1.2.1 Definition of Quantizer problem

Let us suppose that we have a collection of points contained in a volume. For any position in the volume, we can calculate the distance to the nearest of the concerning points. The Quantizer problem finds a point configuration that minimizes previously described distances for all positions in observed volume.

Because of its simplicity, the question of the Quantizer problem is very applicable [143]. For example, a bank has to solve the Quantizer problem to distribute ATMs optimally in some area. A telecommunication company addresses it when constructing the network of transmitters [111]. Other examples can be found in digital communications [30] as well as in computer sciences where quantization is vital for digital visualization of objects [30]. Moreover, the Quantizer problem is widely used in cryptography [18] and in the field of unsupervised machine learning where various clustering algorithms are based on quantization of the data set [23].

In order to define quantization more precisely and set it as an optimization problem, we have to introduce formal mathematical definitions of a few basic concepts such as point process, the density of a point process, and the closest neighbourhood of a point, the latter known as Voronoi cell.

Therefore, as it was defined in references [149, 164], let us consider  $d$ -dimensional Euclidean space  $\mathbb{R}^d$  and configuration  $\mathbf{R} = \{\mathbf{r}_i, i \in \mathbb{N}\}$  that are elements of  $\mathbb{R}^d$  ( $\mathbf{r}_i \in \mathbb{R}^d, \forall i$ ). The collection of points  $\mathbf{R}$  will be called a *point process* if two natural assumptions are met:

1.  $\mathbf{r}_i \neq \mathbf{r}_j, \forall i \neq j$ , meaning there are no overlapping points in the system and
2. each bounded subset  $S$  of  $\mathbb{R}^d$  contains only a finite number of points which will be labeled with  $N \in \mathbb{N}$ .

Following the previous assumptions, a point process can be statistically characterized by the specific probability density functions  $P_N(\mathbf{r}_1, \dots, \mathbf{r}_N)$  which provides probabilities of finding  $N$  points around the given positions  $(\mathbf{r}_1, \dots, \mathbf{r}_N)$ .

From here, we can define the  $n$ -particle generic probability density function labelled as  $\rho_n(\mathbf{r}_1, \dots, \mathbf{r}_n)$ ,  $n < N$  with

$$\rho_n(\mathbf{r}_1, \dots, \mathbf{r}_n) = \frac{N!}{(N-n)!} \int_V \dots \int_V P_N(\mathbf{r}_1, \dots, \mathbf{r}_N) d\mathbf{r}_{n+1} \dots d\mathbf{r}_N. \quad (1.1)$$

The generic  $n$ -particle probability density function  $\rho_n(\mathbf{r}_1, \dots, \mathbf{r}_n)$  is a non-negative function that is proportional to the probability of finding  $n \leq N$  particles around the positional configuration  $(\mathbf{r}_1, \dots, \mathbf{r}_n)$ .

The former definition becomes more clear if we set  $n = 1$  and calculate  $\rho_n(\mathbf{r}_1, \dots, \mathbf{r}_n)$  for statistically homogeneous point process. Then, the single-particle generic density function  $\rho_1(\mathbf{r}_1) = \rho \equiv \lim_{N, V \rightarrow \infty} \frac{N}{V}$ , is nothing more than the intensity of the point process. From the intensity of point process  $\rho$  we can simply calculate the expected number of points in some volume  $d\mathbf{r}$  around the position  $\mathbf{r}$ , which is given by  $\rho d\mathbf{r}$ . Furthermore, if a point process is translation invariant and uncorrelated, we have  $\rho_n(\mathbf{r}_1, \dots, \mathbf{r}_n) = \rho^n$ . An example of such point process is the Poisson point process where point positions  $\mathbf{r}_i$  are randomly and uniformly distributed in the volume  $V$ .

As we mentioned before, the Quantizer problem optimizes distances to the nearest point of a point process, and thus it is of major interest to define the closest neighbourhood of each point in a point process. Division of space into cells from a given set of points due to a simple rule of occupying the nearest neighbourhood is provided by *Voronoi tessellation*.

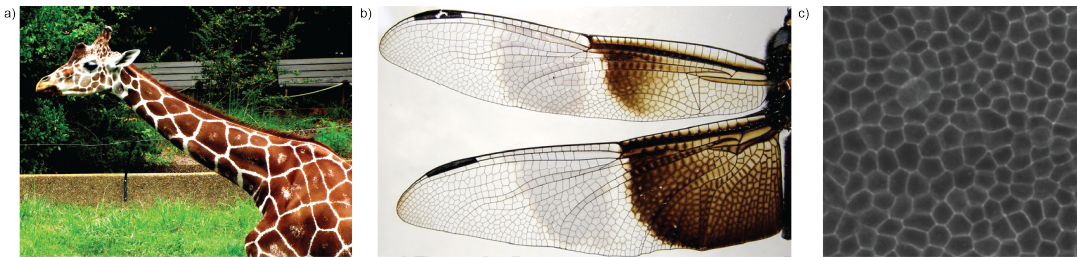


FIGURE 1.2: Examples of Voronoi diagrams that are found in nature. a) White stripes on giraffe skin form Voronoi diagram. This image was taken from reference [57]. b) Voronoi diagram at the wing of a dragonfly. This image was taken from reference [142]. c) Voronoi diagram is a good model for epithelial tissue membranes [75].

For a given set of points  $\mathbf{R} = \{\mathbf{r}_i, i \in \mathbb{N}\}$  in  $d$ -dimensional Euclidean space, a Voronoi cell  $\mathcal{V}_i$  of point  $\mathbf{r}_i$  consists of all points in space that are

closer to  $\mathbf{r}_i$  than to any other of the given points. Formally, the Voronoi cell  $\mathcal{V}_i$  of point  $\mathbf{r}_i$  is given by

$$\mathcal{V}_i = \{\mathbf{x} \in \mathbb{R}^k \mid \|\mathbf{x} - \mathbf{r}_i\| \leq \|\mathbf{x} - \mathbf{r}_j\| \forall j \neq i, j \in \mathbb{N}\} \quad (1.2)$$

where  $\|\cdot\|$  is the Euclidean norm in  $\mathbb{R}^k$ . A collection of Voronoi cells  $\mathcal{V} = \{\mathcal{V}_i, i \in \mathbb{N}\}$  is called Voronoi diagram and points  $\mathbf{r}_i$  are called generators of Voronoi diagram  $\mathcal{V}$ . Because of its generality and applicability to various problem, Voronoi diagrams have been widespread in nature [115] as well as a useful model used in various scientific studies [115, 19, 128, 113]. An example of Voronoi diagrams in a living systems are presented in Figure 1.2.

Now, after introducing precisely the basic concepts such as a point process and Voronoi cell, we can formalize the Quantizer problem and define it as an optimization problem. Like we had before, let  $\mathbf{R} = \{\mathbf{r}_i, i \in \mathbb{N}\}$  be a point process in  $d$ -dimensional Euclidean space  $\mathbb{R}^d$  with a single-particle generic density function  $\rho_1(\mathbf{r}_1)$  which will further be denoted just with  $\rho(\mathbf{r})$  and referred to as mass density function. Moreover, let  $\|\cdot\|$  be an Euclidean norm on  $\mathbb{R}^d$ . Then, solutions or minimal (optimal) states of Quantizer problem are identified with a choice of point positions  $\mathbf{r}_i, i \in \mathbb{N}$  that minimize the following *scaled dimensionless error* [143]:

$$E_Q = \frac{\lim_{n \rightarrow \infty} \frac{1}{n} \sum_{i=1}^n \int_{\mathcal{V}_i} \rho(\mathbf{x}) \|\mathbf{x} - \mathbf{r}_i\|^2 d\mathbf{x}}{d \langle V(\mathcal{V}) \rangle^{1 + \frac{2}{d}}} \quad (1.3)$$

where  $\langle V(\mathcal{V}) \rangle$  is the expected value of Voronoi cell volume,

$$\langle V(\mathcal{V}) \rangle = \lim_{n \rightarrow \infty} \frac{1}{n} \sum_{i=1}^n V(\mathcal{V}_i). \quad (1.4)$$

Moreover, for the reasons of simplicity, for an arbitrary region  $K \subset \mathbb{R}^d$  and point  $\mathbf{y} \in \mathbb{R}^d$  we will denote the integral in the Equation 1.3 with:

$$E(K, \mathbf{y}) = \int_K \rho(\mathbf{x}) \|\mathbf{x} - \mathbf{y}\|^2 d\mathbf{x}. \quad (1.5)$$

The scaled dimensionless error  $E_Q$  defined in the Equation 1.3 from now on

will be referred to as the *Quantizer error* or *Quantizer energy*. It is worth mentioning that in case of a finite number of points in set  $\mathbf{R}$ , both limits in Equations 1.3 and 1.4 have to be dropped. In that case, numerator in the Equation 1.3 becomes mean of the integral  $E(\mathcal{V}_i, \mathbf{r}_i)$  and  $\langle V(\mathcal{V}) \rangle$  is the mean Voronoi volume.

## 1.2.2 Analysis of Quantizer error

The Quantizer error is proportional to the ratio of the expected value of integral  $E(\mathcal{V}_i, \mathbf{r}_i)$  and the Voronoi cell volume expected value. Since the expected volume (i.e., the average when a system contains a finite number of points) of Voronoi cells in the system can be set to any value by rescaling the system, it becomes clear that the integral  $E(K, \mathbf{y})$  plays a pivotal role in the Quantizer error  $E_Q$ .

In definition of integral  $E(K, \mathbf{y})$  (Equation 1.5) we can see that the distance between points of region  $K$  and a fixed point  $\mathbf{y}$  are being integrated. Hence, the value of the integral  $E(K, \mathbf{y})$  will be minimized if the previously described distances are as small as possible. Thus, if we fix the area of a region  $K$  and make the region very elongated, the integral  $E(K, \mathbf{y})$  will have greater value, and if  $K$  is a sphere, the value of  $E(K, \mathbf{y})$  will be minimized. From there, we can conclude that by minimizing the Quantizer error  $E_Q$ , we are trying to find the tessellation of space where constitutive cells are as close to spheres as possible. Of course, concerned cells can not ever be spherical because they wouldn't be able to tessellate space.

In order to further investigate the Quantizer error, we have to define certain tools that will simplify our analysis. Thus, for a subset  $K$  of  $d$ -dimensional Euclidean space with mass density  $\rho(\mathbf{x})$ , we define Minkowski tensors of rank  $a$  [134] with:

$$W_0^{a,0}(K) = \int_K \mathbf{x}^a \rho(\mathbf{x}) d\mathbf{x} \quad (1.6)$$

where potential term  $\mathbf{x}^a = \underbrace{\mathbf{x} \otimes \mathbf{x} \dots \otimes \mathbf{x}}_{a \text{ times}}$ . Moreover, for  $\mathbf{x} = (x_1, \dots, x_d)$  and  $\mathbf{y} = (y_1, \dots, y_d)$ ,  $(\mathbf{x} \otimes \mathbf{y})_{i,j} = x_i y_j$  is a tensor product. Minkowski tensors can be defined more general and thus Equation 1.6 provides only a small subset of them [134]. By inserting different values of  $a$  into Equation 1.6 we can obtain Minkowski tensor  $W_0^{0,0}$  that is equal to the volume of body  $K$ ,

$W_0^{1,0}$  that is proportional to a mass centroid of  $K$  and  $W_0^{2,0}$  which produces a covariance matrix assuming  $W_0^{1,0} = \mathbf{0}$ .

Furthermore, let us define a translation for a vector  $\mathbf{v}$  as  $t_{\mathbf{v}} : \mathbb{R}^d \rightarrow \mathbb{R}^d$  with formula  $t_{\mathbf{v}}(\mathbf{x}) = \mathbf{x} + \mathbf{v}$ . We can generalize translation  $t_{\mathbf{v}}$  to the case when we want to translate any subset of  $\mathbb{R}^d$  for a vector  $\mathbf{v}$  by defining mapping  $T_{\mathbf{v}} : \mathcal{P}(\mathbb{R}^d) \rightarrow \mathcal{P}(\mathbb{R}^d)$  with formula:

$$T_{\mathbf{v}}(K) = \{t_{\mathbf{v}}(\mathbf{x}), \mathbf{x} \in K\} \quad (1.7)$$

where  $\mathcal{P}(\mathbb{R}^d)$  is the partitive set of  $\mathbb{R}^d$ .

Now, with the previous two definitions, we can derive the following calculations from the Equation 1.5:

$$E(K, \mathbf{y}) = \int_K \rho(\mathbf{x}) \|\mathbf{x} - \mathbf{y}\|^2 d\mathbf{x} \quad (1.8)$$

$$= \int_{T_{-\mathbf{y}}(K)} \rho(\mathbf{x}) \|\mathbf{x}\|^2 d\mathbf{x} \quad (1.9)$$

$$= \int_{T_{-\mathbf{y}}(K)} \rho(\mathbf{x}) (x_1^2 + x_2^2 + \dots + x_d^2) d\mathbf{x} \quad (1.10)$$

$$= \int_{T_{-\mathbf{y}}(K)} \rho(\mathbf{x}) x_1^2 d\mathbf{x} + \int_{T_{-\mathbf{y}}(K)} \rho(\mathbf{x}) x_2^2 d\mathbf{x} + \dots + \int_{T_{-\mathbf{y}}(K)} \rho(\mathbf{x}) x_d^2 d\mathbf{x} \quad (1.11)$$

$$= \left( W_0^{2,0}(T_{-\mathbf{y}}(K)) \right)_{1,1} + \left( W_0^{2,0}(T_{-\mathbf{y}}(K)) \right)_{2,2} + \dots + \left( W_0^{2,0}(T_{-\mathbf{y}}(K)) \right)_{d,d} \quad (1.12)$$

$$= \text{tr} \left( W_0^{2,0}(T_{-\mathbf{y}}(K)) \right). \quad (1.13)$$

In the previous set of equations, Equation 1.9 follows from the definition of translation (Equation 1.7), Equation 1.10 from the definition of Euclidean norm  $\|\cdot\|$  on  $\mathbb{R}^d$  and Equation 1.11 is a consequence of integral being a linear operator. Further, Equation 1.12 follows from the definition of a tensor product and Equation 1.13 from the definition of the trace of a matrix.

From the previous set of equations, we can see that the integral  $E(K, \mathbf{y})$  is nothing more than a trace of Minkowski tensor  $W_0^{2,0}$  calculated for a region  $K$  translated for a vector  $-\mathbf{y}$ . Since by solving the eigenvalue problem of Minkowski tensor  $W_0^{2,0}$  we can calculate the moments of inertia of a body, it

becomes even more clear that the Quantizer error defined in Equation 1.3 is closely related to the shape of Voronoi cells that tessellate the space.

Furthermore, by using the following property of Minkowski tensors [134];

$$W_0^{a,0}(T_{\mathbf{v}}(K)) = \sum_{c=0}^a \binom{a}{c} \mathbf{v}^c \otimes W_0^{a-c,0}(K) \quad (1.14)$$

we can eliminate the translation  $T_{-\mathbf{y}}(\cdot)$  from the Equation 12 by:

$$E(K, \mathbf{y}) = \text{tr} \left( W_0^{2,0}(T_{-\mathbf{y}}(K)) \right) \quad (1.15)$$

$$= \text{tr} \left( \sum_{c=0}^2 \binom{2}{c} (-\mathbf{y})^c \otimes W_0^{2-c,0}(K) \right) \quad (1.16)$$

$$= \text{tr} \left( W_0^{2,0}(K) - 2\mathbf{y} \otimes W_0^{1,0}(K) + W_0^{0,0}(K) \mathbf{y} \otimes \mathbf{y} \right) \quad (1.17)$$

$$= \text{tr} \left( W_0^{2,0}(K) \right) - 2\text{tr} \left( \mathbf{y} \otimes W_0^{1,0}(K) \right) + W_0^{0,0}(K) \text{tr} \left( \mathbf{y} \otimes \mathbf{y} \right) \quad (1.18)$$

$$= \text{tr} \left( W_0^{2,0}(K) \right) - 2\mathbf{y} \cdot W_0^{1,0}(K) + W_0^{0,0}(K) \mathbf{y} \cdot \mathbf{y} \quad (1.19)$$

where  $\cdot$  is a dot product of vectors. In the previous set of equations, Equation 1.16 follows from the Minkowski tensor property defined in Equation 1.14. Furthermore, Equation 1.17 is obtained by rewriting Equation 1.16 and calculating the binomial coefficients and Equation 1.18 follows from the linearity of matrix trace. Finally, Equation 1.19 is derived from the homogeneity of matrix trace and the fact that tensor product equals the dot product if concerned vectors are of the same dimension.

From the previous set of equations, we have learned that the integral  $E(K, \mathbf{y})$ , which is the key for the Quantizer error, depends directly on the Minkowski tensors of ranks 0,1 and 2 of the region  $K$ . Moreover, previous equations provide us an efficient way to calculate Quantizer energy since the tools for calculation of Minkowski tensors are already familiar [134].

### 1.2.3 Lloyd's algorithm

In previous subsections, we have defined the Quantizer problem and related it to the Quantizer error that has to be minimized to find solutions to the problem. Quantizer error  $E_Q$  can always be minimized via some frequently



used method such as gradient descent. However, even more efficient minimization can be achieved by Lloyd's algorithm.

Lloyd's algorithm is an iterative procedure that belongs to a class of clustering algorithms, and it is a generalization of the famous K-means algorithm. While the K-means algorithm deals with clustering with a discrete cardinal number, Lloyd's algorithm does the matching job in Euclidean space. Therefore, Lloyd's algorithm is well represented in many fields, particularly industry. In that manner, applications of Lloyd's algorithm can be found in artificial intelligence such as clustering problems, image analysis, and pattern recognition [23] as well as in biology as a model for explaining animal behaviour [42].

Lloyd's algorithm is one of the methods used for obtaining a centroidal Voronoi diagram (CVD) from a particular set of points [73]. Centroidal Voronoi diagrams are a class of more regular Voronoi diagrams where generators of Voronoi cells coincide with mass centroids of their Voronoi cells.

More formally, let  $\mathbf{z}_i$  be a mass centroid of Voronoi cell  $\mathcal{V}_i$ , for  $i \in \mathbb{N}$ , i.e.

$$\mathbf{z}_i = \frac{\int_{\mathcal{V}_i} \mathbf{x} \rho(\mathbf{x}) d\mathbf{x}}{\int_{\mathcal{V}_i} \rho(\mathbf{x}) d\mathbf{x}}. \quad (1.20)$$

A centroidal Voronoi diagram  $\mathcal{V}$  (notation from Equation 1.2) is a Voronoi diagram where  $\mathbf{r}_i = \mathbf{z}_i, \forall i$ .

Examples of CVD when  $\rho(\mathbf{x}) = 1$  are crystal lattices such as simple cubic (SC), body centred cubic (BCC), face centred cubic (FCC), hexagonal close packed (HCP) in 3D, and triangular, square and hexagonal lattices in 2D. Even though previous examples are crystal lattices are hence, well ordered, there exist structures that are CVD and amorphous at the same time [42]. Therefore, it is vital to understand how amorphous CVDs are formed and if such configurations share some common structural and geometrical properties.

As mentioned before, Lloyd's algorithm is an iterative procedure which means that the same step is repeated until some stopping criterion is met. As input for Lloyd's algorithm, we can use any desired point pattern, which is because of the practical purposes finite,  $\mathbf{R} = \mathbf{r}_i, i \in \{1, \dots, n\}$  contained in  $\Omega$ ,

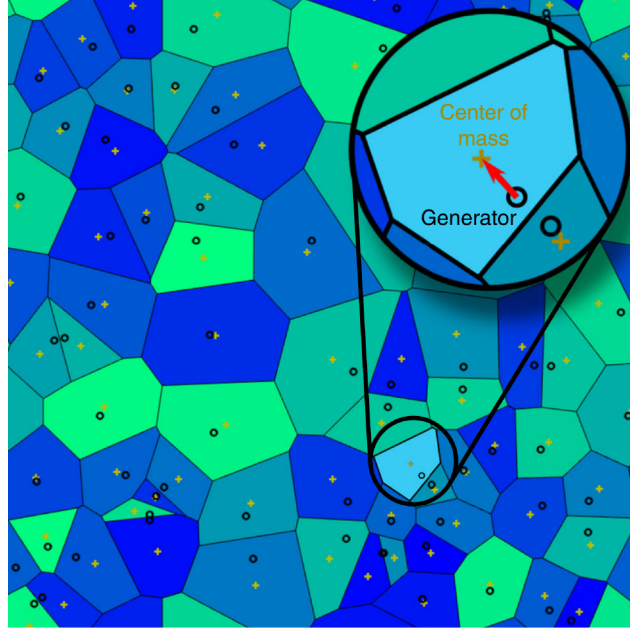


FIGURE 1.3: A visualization of Lloyd's iteration. Centres of mass of Voronoi diagrams are calculated, and then all of the generator points are replaced with the belonging centres of mass. This procedure is iteratively repeated. This picture was taken from the reference [85].

a subset of the  $d$ -dimensional Euclidean space with a mass density  $\rho : \mathbb{R}^d \rightarrow \mathbb{R}$ . An algorithm repeats the following three steps:

1. Calculate the Voronoi diagram  $\mathcal{V}$  of  $\Omega$  where  $\mathbf{r}_i, i \in \{1, \dots, n\}$  are generators.
2. Calculate the mass centroids  $\mathbf{z}_i$  of  $\mathcal{V}_i$  for each  $i \in \{1, \dots, n\}$  and replace current generators with mass centroids, i.e.  $\mathbf{r}_i = \mathbf{z}_i, \forall i$ .
3. Go to step 1. until some stopping criterion is met.

By closely studying previous steps of Lloyd's algorithm, we can see that Lloyd's algorithm pushes the Voronoi generators to centres of mass of Voronoi cells and, in that way, after a certain number of iterations, tries to force a point pattern to become a centroidal Voronoi diagram. However, we still need more rigorous proof that the algorithm's output will be a CVD and that such an algorithm converges. Moreover, it is not clear how does Lloyd's algorithm provide solutions to the Quantizer problem.

In order to address previous questions, we introduce an energy functional that depends on regions of  $\mathbb{R}^d$ ,  $K = \{K_i, i = 1, \dots, n\}$  and any points  $\mathbf{Y} = \{\mathbf{y}_i, i = 1, \dots, n\}$  contained in  $\Omega \subset \mathbb{R}^d$  with formula:

$$E_L(K, \mathbf{Y}) = \sum_{i=1}^n E(K_i, \mathbf{y}_i). \quad (1.21)$$

The energy functional  $E_L$  from now on will be referred to as the *Lloyd's energy* or *Lloyd's error*. We can note that Lloyd's error is proportional to the Quantizer error. Indeed, two errors differ only by a scaling factor in the definition of Quantizer error (Equation 1.3). Because of that, solutions to the Quantizer problem minimize Lloyd's error  $E_L$  as well. However, it remains unclear if Lloyd's iterations minimize Lloyd's energy.

The fundamental link between Lloyd's energy  $E_L$  and Lloyd's algorithm is provided in reference [43]. There, Du et al. present the theoretical proof that Lloyd's algorithm decreases the value of Lloyd's energy  $E_L$  in each iteration. That significant result proves the convergence of Lloyd's algorithm since the sequence of Lloyd's energies  $E_L$  generated by Lloyd's iterations is decreasing and bounded from below ( $E_L > 0$ ). Then, the concerned sequence converges due to the statement of the theorem that bounded and monotonic sequence is convergent. This result allows us to define the stopping criterion for Lloyd's iterations. Thus, we can terminate Lloyd's algorithm when the difference in energy  $E_L$  between two consecutive iterations falls below some threshold value.

Another essential theoretical result states that the local minima of Lloyd's energy  $E_L$  are achieved when set of regions  $K$  (Equation 1.21) is Voronoi tessellations  $\mathcal{V}$  and points  $\mathbf{Y}$  are generators and mass centroids of Voronoi diagram  $\mathcal{V}$ , namely when  $\mathcal{V}$  is CVD [20]. This result proves that Lloyd's algorithm produces a CVD implying that solutions of the Quantizer problem obtained with Lloyd's algorithm are also CVDs. Therefore, we will sometimes refer to the process of solving the Quantizer problem for a given set of points as a *centralization* procedure.

### 1.2.4 Solutions to Quantizer problem

Finding the globally optimal solution to the Quantizer problem has been a subject of study for many years. A pioneer work regarding the minima of the Quantizer problem in 3D was done by Allen Gersho in 1979 [56]. He conjectured that the body centred cubic (BCC) lattice is a structure that globally optimizes the Quantizer energy. The Gersho conjecture remains unproven

even though the supporting evidence was presented in [44] using computational means. However, it was shown that BCC is the optimal solution of the Quantizer problem among all of the crystal lattices [14]. In 2D, the globally optimal state of the Quantizer problem is proven to be a hexagonal lattice [31, 143].

Structure	Dimension	$E_t$
Hexagonal	2D	0.080187
Square	2D	0.08333
Body centered cubic (BCC)	3D	0.078543
Face centered cubic (FCC)	3D	0.078745
A15	3D	0.08098
Bravais lattice	3D	0.081236
Simple cubic (SC)	3D	0.08333
Integer (Z)	3D	0.08666

TABLE 1.1: Values of the total energy  $E_t$  for different lattices in two and three dimensional space [44, 85].

The fact that many crystal lattices were found to be locally optimal states of the Quantizer problem [56, 14] indicates that the landscape of Quantizer energy  $E_Q$  is complex with many valleys that correspond to local minima of  $E_Q$ . Because of that, it is crucial to understand the nature of Quantizer minima when starting from initial structures with different spatial properties. It is exciting to see if Lloyd's algorithm starting from an arbitrary structure will lead to a solution with crystalline order, or it will converge to an amorphous solution of the Quantizer problem. Moreover, many crystalline structures that solve the Quantizer problem, such as BCC and FCC lattices, correspond to packings of equally sized spheres. This fact motivates to generalize the Quantizer problem to the systems consisting of particles with non-trivial volume. In such a case, it would be interesting to address how solutions to the generalized Quantizer problem depend on the geometrical and structural properties of systems that are being optimized.

Last but not least, in order to effectively quantify solutions of the Quantizer problem, we introduce the *dimensionless rescaled total energy* of system of  $n$  points  $\mathbf{Y}$  contained in  $\Omega \subset \mathbb{R}^d$  with:

$$E_t = \frac{n^{\frac{2}{d}}}{dV(\Omega)^{1+\frac{2}{d}}} E_L(\mathcal{V}, \mathbf{Y}) \quad (1.22)$$

where  $V(\Omega)$  is volume of  $\Omega$  and  $\mathcal{V}$  is Voronoi diagram generated by points  $\mathbf{Y}$ . Moreover the total energy of a single cell is obtained by including  $n = 1$  and  $\Omega = \mathcal{V}_i$  in Equation 1.22, i.e.

$$E_t = \frac{1}{dV(\mathcal{V}_i)^{1+\frac{2}{d}}} E(\mathcal{V}_i, \mathbf{y}_i) \quad (1.23)$$

The total energy  $E_t$  is proportional both to Quantizer energy  $E_Q$  and Lloyd's energy  $E_L$ . However, we introduced the total energy  $E_t$  because it is most commonly used in the literature to quantify Quantizer minimal states (same as Lloyd's algorithm minimal states due to  $E_Q$  being proportional to  $E_L$ ) [43]. Total energy values for some notable lattices and structures are given in Table 1.1.

## 1.3 Hyperuniformity of systems

Properties related to density of the point patterns or systems of particles played a major role in many studies through the history [84, 129, 78, 16, 38, 7, 61]. An exciting feature of density is how it changes through different positions in the system. Therefore, fluctuations of the density in a system can provide essential information about the observed structures. Density fluctuations are essential for many fields of science such as physics, mathematics, chemistry, material science, biology, and engineering [147, 117, 155]. The study of density fluctuations in various systems was stimulated even more in the last 20 years by introducing a new concept well known as *hyperuniformity* [149].

### 1.3.1 Definition of hyperuniformity

Hyperuniformity is a geometrical property that classifies the behaviour of long-wavelength density fluctuations in particle materials so that a particular structure is considered hyperuniform only if it has suppressed long-wavelength density fluctuations. While it is obvious to see that well-ordered structures as crystals and quasi-crystals possess that property, a substantial collection of amorphous materials have been found hyperuniform [147]. Therefore, we can consider hyperuniformity as a system feature that characterizes order that may not be visible at first.

The easiest way to understand the concept of hyperuniformity more thoroughly is to examine the behaviour of the number variance  $\sigma_N^2(R)$  [147]. In order to define the number variance, let us consider a set of points  $\mathbf{Y}$  in a  $d$ -dimensional Euclidean space  $\mathbb{R}^d$  and an arbitrary sphere  $\Omega$  of radius  $R$  in  $\mathbb{R}^d$  (see Figure 1.4). When  $\Omega$  is placed randomly in space, it is always possible to count the number of points  $N(R)$  contained in  $\Omega$ . With the change of  $\Omega$  position, the number of points contained in it may also change (Figure 1.4). Therefore, it is convenient to define the number variance  $\sigma_N^2(R)$  as a variance of a random variable  $N(R)$ . The number variance  $\sigma_N^2(R)$  measures fluctuations of the number of points in a fixed volume and the fluctuations of density within a point pattern. Consequently, it is possible to characterize the concept of hyperuniformity as a long-range order with the behaviour of  $\sigma_N^2(R)$  when  $R$  is large enough.

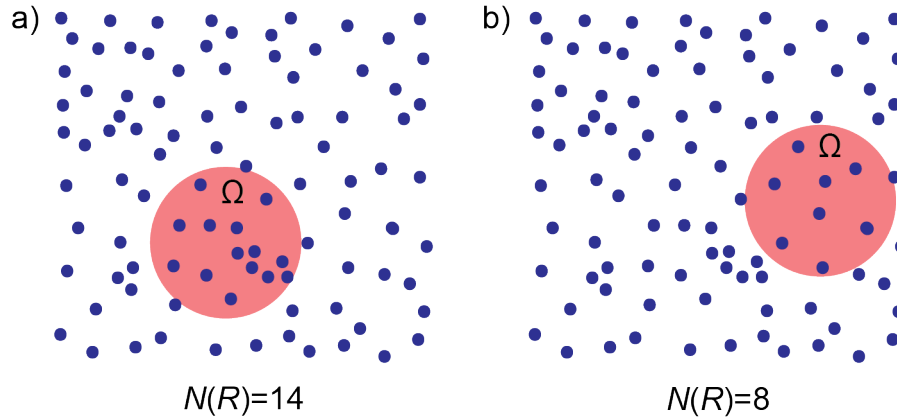


FIGURE 1.4: Visualization of the number variance in 2 - dimensional Euclidean space. The number of points  $N(R)$  contained in the observation window  $\Omega$  varies with the change of observation window position. a) The observation window  $\Omega$  contains 14 points. b) The observation window  $\Omega$  contains 8 points.

Following on from the previous discussion, a point pattern is considered hyperuniform when  $\sigma_N^2(R)$  grows more slowly than the volume of the observation window  $\Omega$ . More precisely,  $\frac{\sigma_N^2(R)}{R^k}$  has to be a decreasing function and

$$\lim_{R \rightarrow \infty} \frac{\sigma_N^2(R)}{R^k} = 0. \quad (1.24)$$

The visualization of a hyperuniform point pattern is presented in Figure 1.5.

A natural question that arises from the previous definition is how fast

does the limit in Equation 1.24 approach 0 if the observed point pattern is hyperuniform. It is well known that the number variance  $\sigma_N^2(R)$  can not grow slower than the surface area of the observation window for statistically homogeneous and isotropic point patterns [149]. Consequently, the growth rate of  $\sigma_N^2(R)$  has to be somewhere between  $R^{d-1}$  and  $R^d$  for a point process to be hyperuniform which raises the motivation to classify hyperuniform point patterns more precisely.

Therefore, based on the behaviour of  $\sigma_N^2(R)$ , this is convergence speed in the limit in Equation 1.24, we can observe three different classes of hyperuniform point processes [147]:

- CLASS I  $\sigma_N^2(R) \sim R^{d-1}$
- CLASS II  $\sigma_N^2(R) \sim R^{d-1} \ln R$
- CLASS III  $\sigma_N^2(R) \sim R^{d-\epsilon}, 0 < \epsilon < 1$

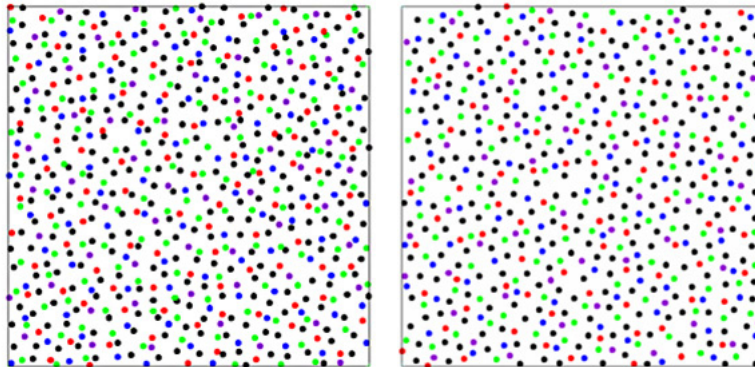


FIGURE 1.5: Visualization of the hyperuniform structure found in the chicken eyes. This image was taken from reference [25].

Class I structures, where number variance grows proportional to the surface area of observation window  $\Omega$  are most ordered among hyperuniform structures. Naturally, representatives of Class I are crystals [149], some quasicrystal structures [164, 114], perturbed lattices [53, 54, 55], Weyl-Heisenberg ensembles [3], one-component plasmas [67] and hard-sphere plasmas [95, 96]. Among the members of Class II structures are some quasi-crystals [114], and also a few exciting point patterns relevant in mathematics, such as zeros of Riemann zeta function [148, 59] and eigenvalues of random matrices [104]. Moreover, density fluctuations in early Universe [117], and maximally random jammed packings [40, 69, 87] also have the behaviour of number variance that classifies them into this class of hyperuniform structures. In the end, the most notable representatives of Class III hyperuniform structures

are some perturbed lattices [79] and random organization models [63].

As we can see from the previous lines, hyperuniformity was found in various systems that have different spatial characteristics. Among them, amorphous hyperuniform structures [100, 147] have raised a particular focus because, in such systems, the suppression of long-range density fluctuations is not intuitive as in systems with crystalline order. Moreover, it is fascinating to understand the origin of hyperuniformity in such amorphous systems, i.e., what procedure or property is vital for the observed system to be hyperuniform [146, 148, 117]. Furthermore, the property of hyperuniformity was not only identified in point patterns but also in systems consisting of non-trivial particles [40, 95, 87]. Therefore, it is crucial to understand why a particular particle system is hyperuniform and relate the geometric and structural properties of such systems to their hyperuniformity.

### 1.3.2 Structure factor of hyperuniform point patterns

In order to measure correlations between points in the system, building on the definition of  $n$ -particle probability density function (Equation 1.1) for a point process  $\mathbf{R} = \mathbf{r}_i, i \in \mathbb{N}$ , we can introduce the  $n$ -particle correlation functions with

$$g_n(\mathbf{r}_1, \dots, \mathbf{r}_n) = \frac{\rho_n(\mathbf{r}_1, \dots, \mathbf{r}_n)}{\rho^n}. \quad (1.25)$$

$N$ -particle probability density function  $g_n(\mathbf{r}_1, \dots, \mathbf{r}_n)$  measures the correlations in observed point process respective to the totally non-correlated point process such as Poisson point process. If the point process  $\mathbf{R}$  is non-correlated it is clear that the value of  $g_n(\mathbf{r}_1, \dots, \mathbf{r}_n)$  is equal to 1. The  $n$ -particle correlation function of particular importance for the translationally-invariant point processes is the *pair correlation function* ( $n = 2$ ), formalized with

$$g_2(\mathbf{r}) = \frac{\rho_2(\mathbf{r})}{\rho^2}, \text{ where } \mathbf{r} = \mathbf{r}_2 - \mathbf{r}_1. \quad (1.26)$$

Thus, the pair correlation function can be interpreted as a probability of finding two points at a distance  $\mathbf{r}$  respective to the Poisson point process.

Furthermore, from the pair correlation function we can calculate the *total correlation function* with

$$h(\mathbf{r}) = g_2(\mathbf{r}) - 1 \quad (1.27)$$



which is important for definition of *structure factor* of translational-invariant point process  $\mathbf{R}$ . Structure factor  $S(\mathbf{k})$  is defined with

$$S(\mathbf{k}) = 1 + \rho \hat{h}(\mathbf{k}) \quad (1.28)$$

where  $\hat{h}(\mathbf{k})$  is the Fourier transform of the total correlation function. Here, vector  $\mathbf{k}$  is known as a wave vector. The length of a wave vector  $\mathbf{k}$ , known as a wavenumber  $|\mathbf{k}|$ , corresponds to the wavelength  $\lambda$  in the system with formula

$$|\mathbf{k}| = \frac{1}{2\pi\lambda}. \quad (1.29)$$

Structure factor is a well-known mathematical tool used to clarify material scattering and scattering patterns in X-ray, electron or neutron diffraction experiments. In the scattering experiments, the values of structure factors are proportional to the scattered intensity of radiation from a system of points. Moreover, structure factor is a non-negative quantity, meaning  $S(\mathbf{k}) \geq 0$ , for all wave vectors  $\mathbf{k}$ .

Hyperuniformity of a given point process is defined by the behaviour of the structure factor for infinite wavelengths, that is, when the wavenumber  $|\mathbf{k}|$  approaches 0. More precisely, a point pattern is considered hyperuniform when  $S(\mathbf{k})$  vanishes as the wavenumber  $|\mathbf{k}|$  tends to zero, i.e.,

$$\lim_{|\mathbf{k}| \rightarrow 0} S(\mathbf{k}) = 0. \quad (1.30)$$

Similarly, as when hyperuniformity was defined via number variance  $\sigma_{N(R)}^2$ , the three classes of hyperuniformity can be characterized by examining the way structure factor approaches 0. In this sense, let us consider hyperuniform structure for which the structure factors obtains a power law in the vicinity of 0, i.e.,

$$S(\mathbf{k}) = |\mathbf{k}|^\alpha, \alpha > 0 \quad (1.31)$$

It is possible to show that the asymptotic behaviour of  $\sigma_{N(R)}^2$  depends on the coefficient  $\alpha$  in the Equation 1.31 [147]. Therefore, the classification of the hyperuniformity can be extended in the following way:

- CLASS I  $\sigma_{N(R)}^2 \sim R^{d-1}$  when  $\alpha > 1$
- CLASS II  $\sigma_{N(R)}^2 \sim R^{d-1} \ln R$  when  $\alpha = 1$

- CLASS III  $\sigma_N^2(R) \sim R^{d-\alpha}, 0 < \alpha < 1$ .

Besides the three classes of hyperuniformity, another two categories of hyperuniform point patterns are worth mentioning. First of them is *stealthy* hyperuniform point processes, which are characterized by the property that their structure factor is equal to 0 for all wave vectors  $\mathbf{k}$  that are shorter than some threshold value  $\epsilon$  [146]. Furthermore, since the condition from Equation 1.24 is quite strict and difficult to prove rigorously when numerical data is analysed, it is convenient to consider some point processes "nearly" hyperuniform or hyperuniform for numerical purposes. Such point processes are said to be *effectively* hyperuniform. For a strict description of effectively hyperuniform point patterns, we have to define a measure that characterizes how close a structure is to perfect hyperuniformity. Therefore, we define  $H$  measure [10, 100, 147] with

$$H = \frac{\hat{S}(0)}{S(\mathbf{k}_{peak})}. \quad (1.32)$$

where  $\hat{S}(0)$  is an estimated value of structure factor for  $\mathbf{k} = 0$  via linear regression and  $S(\mathbf{k}_{peak})$  is the value of structure factor at its largest peak. Then, the system is considered effectively hyperuniform if  $H \leq 10^{-3}$  [147].

## 1.4 Outlook of this thesis

In previous sections of the introduction to this thesis, we have described the Quantizer problem and long-range density fluctuations of the hyperuniform system. Hence, those two topics and their appearance in biological systems will be the central theme of this thesis.

Thus, in Chapter 2, we will study solutions of the Quantizer problem obtained by Lloyd's optimization of various amorphous and random point patterns in 3D. We will investigate long-range density fluctuations in the systems both before and after the application of Lloyd's algorithm. Further, we will study the morphology of concerned point patterns by studying volumes and total energies of Voronoi cells generated by the points. We will provide a mutual comparison of various Quantizer solutions properties and investigate the amorphousness of the observed structures. Finally, we will motivate the centralization of the Quantizer problem to systems consisting of particles with non-trivial volume.

In order to generalize the Quantizer problem for systems of non-trivial particles, in Chapter 3, we will define structures that will be later used as an input for generalized Quantizer optimization. Therefore, we will study random assemblies of ellipses with different elongations assembled at various packing fractions and an algorithm used to generate studied assemblies. By calculating the Voronoi diagram generated from ellipses, we will study the effects of ellipse shape and assembly packing fraction on various geometrical properties of systems such as area, perimeter, elongation, and more. Moreover, we will investigate the topology of ellipse assemblies and relate it to morphology by reproducing various previously known laws. Finally, we will study the effects of centralization and jamming in the ellipse systems governed by the system's density.

Chapter 4 of this thesis will expand the Quantizer problem to systems of non-trivial particles and try to find an extension of Lloyd's algorithm that solves it. We will study the link between two new definitions and optimize ellipse assemblies from Chapter 3 with modified Lloyd's algorithm. We will relate ellipse shape and assembly packing fraction to how the newly modified Lloyd's algorithm introduces changes to assemblies. Finally, we will investigate the concept of hyperuniformity in the ellipse assemblies before and after the application of modified Lloyd's algorithm.

Last but not least, in Chapter 5, we will apply previously studied theory to structures appearing in cellular geometries of the epithelial tissue. Will describe the theoretical model for epithelium that is based on ellipse assemblies and Voronoi tessellation. Furthermore, we will investigate optimization properties related to the Quantizer problem in the context of epithelial tissue. At last, we will calculate structure factors of epithelial tissue and try to reproduce actual experiments with our model where random assembly and Lloyd's algorithm have a pivotal role.



## Chapter 2

# Universal hidden order in amorphous cellular geometries

### Declaration for Chapter 1

The following chapter includes some text which is a paraphrase of the material published in the following article:

[JL1] Michael A. Klatt\*, **Jakov Lovrić\***, Duyu Chen, Sebastian C. Kapfer, Fabian M. Schaller, Philipp W. A. Schönhofer, Bruce S. Gardiner, Ana-Sunčana Smith, Gerd E. Schröder-Turk, Salvatore Torquato; "Universal hidden order in amorphous cellular geometries", *Nature Communications* 10 811 (2019), <https://www.nature.com/articles/s41467-019-08360-5>

In the aforementioned article, Jakov Lovrić developed a simulation program for the Lloyd algorithm of a 3D system and implemented structural analyses of those simulations (including those to classify Minkowski valuations, structure factors, and hyperuniformity), carried out simulations, and analysed simulation results. He contributed to the interpretation of the results, to the preparation of the figures, and to the writing of the paper.

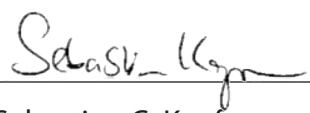
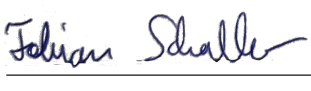

Michael A. Klatt, together with other authors, conceived of the research project and formulated the research question, carried out numerical calculations for 3D and 2D systems, prepared figures, and wrote the manuscript.


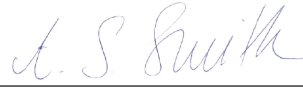

Other authors conceived of the research project, formulated the research question, carried out numerical calculations, contributed to morphometric analyses, generated initial structure data sets, prepared figures, wrote the manuscript, and commented on the manuscript.

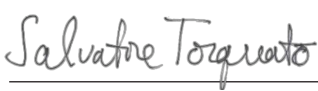
The authors declare no conflict of interest and confirm the correctness of the above statements.

Erlangen, 1 December 2021.

 _____	 _____	 _____
Michael A. Klatt	Jakov Lovrić	Duyu Chen

 _____	 _____	 _____
Sebastian C. Kapfer	Fabian M. Schaller	Phillip W. A. Schönhöfer

 _____	 _____	 _____
Bruce S. Gardiner	Ana-Sunčana Smith	Gerd E. Schröder-Turk

  
\_\_\_\_\_  
Salvatore Torquato

## 2.1 Introduction

This chapter will investigate solutions to the Quantizer problem in 3D more thoroughly. As we brought up in the introduction chapter of this thesis, the landscape of Quantizer energy  $E_Q$  is complex and has many local minima that correspond to crystal lattices [56, 14]. Therefore, it is interesting to investigate which solution of the Quantizer problem will Lloyd's algorithm provide when we start from an arbitrary initial configuration.

The case when we use crystalline structures as initial configurations for Lloyd's optimization is trivial because such patterns are fixed points of the algorithm. Indeed, crystalline structures are already CVDs, and Lloyd's iteration will not introduce any structural change to them [42, 43, 20]. A more interesting case is applying Lloyd's algorithm to point globally amorphous configurations. Then, Lloyd's algorithm will solve the Quantizer problem that possesses different spatial characteristics than the initial structure.

An exciting phenomenon to address is whether Lloyd's algorithm will converge to a globally optimal solution [56] when starting from an arbitrary disordered pattern or if Lloyd's algorithm will produce some of the local minima of the Quantizer problem. Moreover, it is very thought-provoking to study if obtained solutions will correspond to some of the already known Quantizer minima with crystalline order [56, 43] or amorphousness of the initial structure will be preserved throughout Lloyd's iterations.

We will study various properties of point patterns before and after the application of Lloyd's algorithm. We want to understand what changes are introduced to point processes when Lloyd's iterations are applied and what geometric characteristics are specific for minimal states of the Quantizer problem. Therefore, we will investigate probability distributions of volume and total energy  $E_t$  of Voronoi cells generated by concerned point processes. Moreover, we will study structure factors calculated from point patterns of our interest. This way, we will address previously recognised questions regarding the amorphousness of concerned systems and characterize how initial configurations and Quantizer solutions are arranged.

## 2.2 Methods

### 2.2.1 Initial configurations

We have applied Lloyd's algorithm to the following 3D structures with different structural properties:

- Binomial point process
- Permanental point process
- Hyperplane intersection process
- Determinantal point process
- Maximally random jammed state
- Lubachevsky-Stillinger algorithm for sphere packings
- Stealthy hyperuniform point process.

Some text from this subsection is paraphrased from reference [JL1].

#### Binomial point process (BPP)

The binomial point process is a point process that simulates the positions of ideal gas molecules in a container at some particular moment [27]. Hence, the binomial point process points are positioned uniformly and randomly inside the simulation box and mutually uncorrelated. A visualization of a binomial point process is presented in Figure 2.1a).

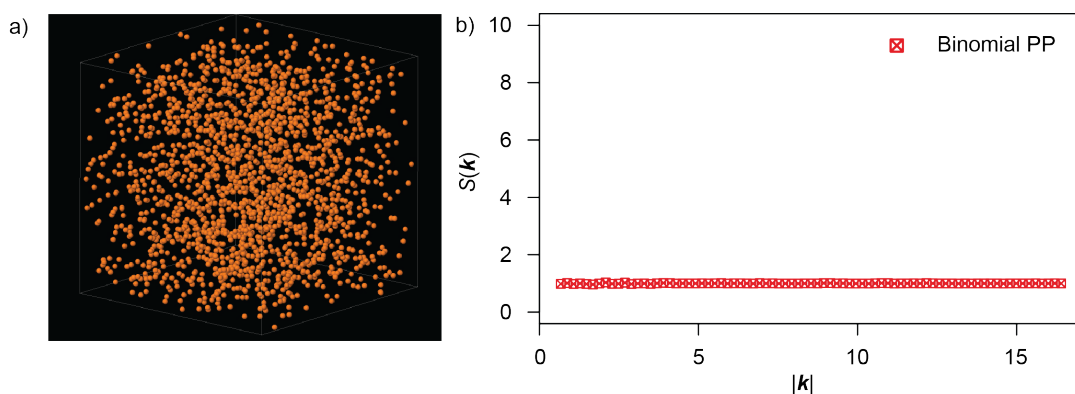


FIGURE 2.1: a) Binomial point processes in three dimensional space visualized by Jmol [71]. Point processes is contained in cuboidal simulation box with periodic boundary conditions. b) Structure factor of binomial point process.



Structure factor  $S(\mathbf{k})$  of the binomial point process is trivial and  $S(\mathbf{k}) = 1$ , for all wave vectors with wavenumbers  $|\mathbf{k}| > 0$  (Figure 2.1b). Thus, structure factor of binomial point process is often used as a reference when characterizing density fluctuations.

We have used three samples of 128000 points as an input of Lloyd's algorithm and run it for approximately 12400 iterations.

### Determinantal point process (DPP)

The determinantal point process is used to model random systems where particles exhibit repulsion. Examples of such systems are fermions in quantum mechanics as well as transmitters in wireless networks [86, 34]. Formally, given the kernel  $K : \mathbb{R}^k \times \mathbb{R}^k \rightarrow \mathbb{R}$ ,  $n$ -point correlation functions of DPP are defined with:

$$g_n(\mathbf{x}_1, \dots, \mathbf{x}_n) = \rho^{-n} \det(K(\mathbf{x}_i, \mathbf{x}_j))_{1 \leq i, j \leq n}$$

where  $\det$  is a determinant of a kernel.

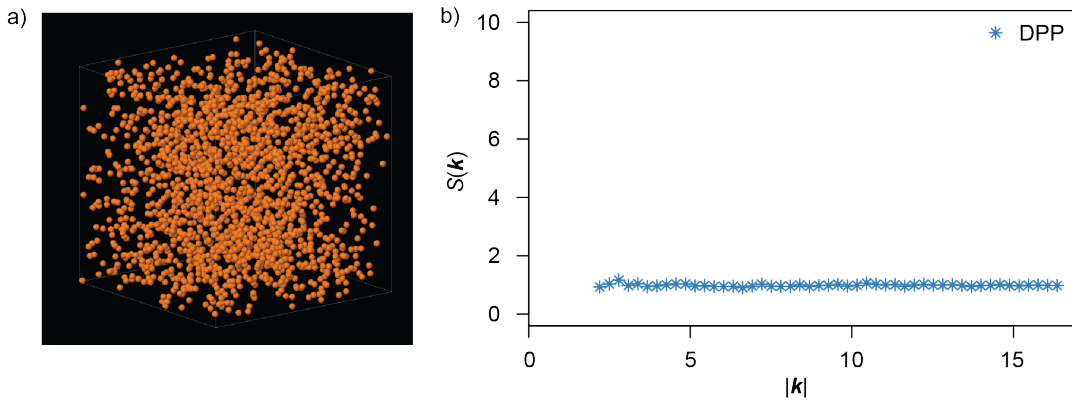


FIGURE 2.2: a) Determinantal point processes in three dimensional space visualized by Jmol [71]. b) Structure factor of determinantal point process.

We simulated 2 samples consisting of around 2750 points generated by the power exponential spectral model, a member of a broad class of DPP models [90]. The points were generated using a package Spatstat [12, 13, 11] with parameters  $\nu = 10$ ,  $\alpha = 0.12$  in notation as in paper [90]. The example of such point pattern can be seen in Figure 2.2a). Generated point patterns, later used as an input of Lloyd's algorithm, are not hyperuniform even though point patterns generated by the power exponential spectral model can be hyperuniform [85] (Figure 2.2b).

### Permanental point process (PPP)

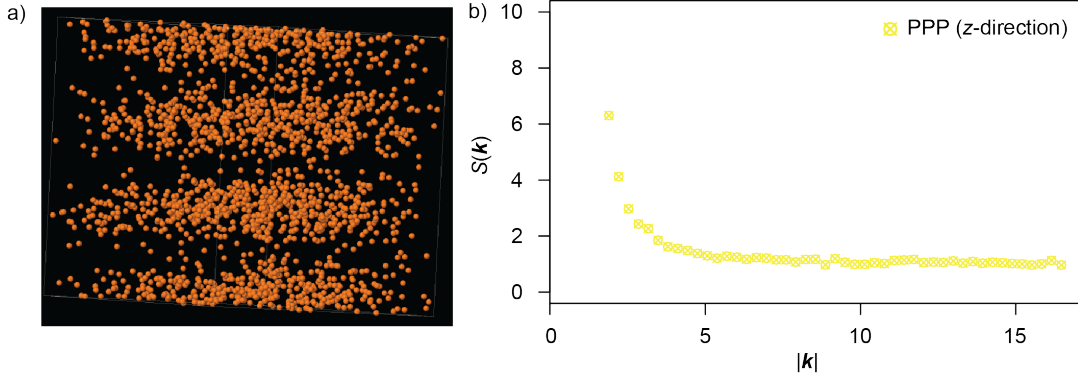


FIGURE 2.3: a) Permanental point processes in three dimensional space visualized by Jmol [71]. b) Structure factor of permanental point process. Density fluctuations in  $z$ -direction are present due to grouping of the points in separate clusters.

The permanental point process is an attractive counterpart of the repulsive determinantal point process and it is used to model bosons in quantum mechanics [86]. It can be defined, similarly to the Determinantal point process, using a kernel  $K : \mathbb{R}^k \times \mathbb{R}^k \rightarrow \mathbb{R}$ , with

$$g_n(\mathbf{x}_1, \dots, \mathbf{x}_n) = \rho^{-n} \text{per}(K(\mathbf{x}_i, \mathbf{x}_j))_{1 \leq i, j \leq n}$$

where  $\text{per}$  is a permanent of a kernel (sum of products of sets of matrix elements that lie in distinct rows and columns).

We simulated two samples of the Gaussian random waves model, a subclass of the PPP, using parameters  $L = 25$ ,  $|k_i| = \frac{10}{L}$ ,  $a_w = \frac{1}{2}$ ,  $\omega = 0.1$  as explained in reference [86]. Such system have a strong density fluctuations in a  $z$ -direction in Cartesian coordinate system as it can be observed from Figure 2.3).

### Hyperplane (Hyperfluctuating) intersection process

The hyperplane intersection process is a point process generated by intersections of randomly placed hyperplanes in space, known as Poisson hyperplane tessellations [62]. The Poisson hyperplane tessellation is constructed so that a certain number (drawn from Poisson distribution) of hyperplanes is randomly placed inside a ball in Euclidean space. Then, the point process is obtained by the intersections of three hyperplanes in space. The visualization of the characteristic clusters of points from two different angles of the hyperplane intersection process is presented in Figure 2.4a.

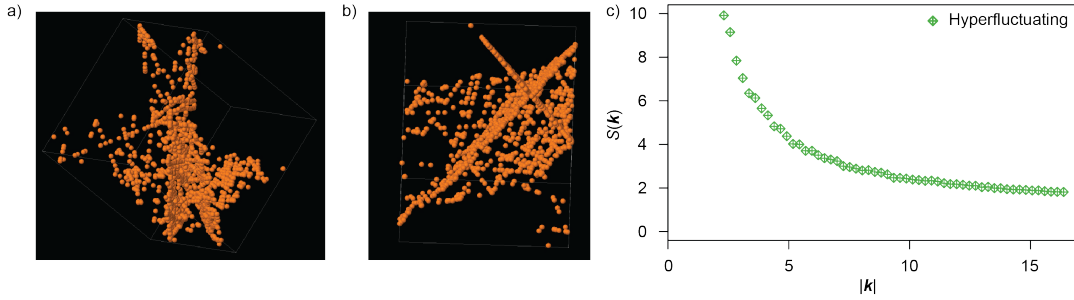


FIGURE 2.4: a) Hyperplane intersection process in cuboidal container visualized by Jmol [71]. Significant clustering of the points is present which indicates strong density fluctuations in the systems. Different view angle reveals shapes of hyperplanes embedded in space. b) Structure factor of hyperplane intersection point process.

We simulated two samples of the hyperplane intersection process, containing around 10500 and 99700 points. Spatial density fluctuations in the hyperplane intersection process have an arbitrary long range, which is referred to in the literature as a hyperfluctuating [147]. It was calculated that the number variance  $\sigma_N^2(R)$  grows like  $R^{2k-1}$  in  $k$ -dimensional space, i.e., faster than the volume of the observation window. Hence the structure factor  $S(\mathbf{k})$  diverges when  $|\mathbf{k}| \rightarrow 0$  (Figure 2.4b).

### Maximally random jammed state (MRJ)

The maximally random jammed state is a state that minimizes any order parameter among all of the isotropic and statistically homogeneous jammed states of an identical sphere system. Intuitively, it is the most random among all of the systems where any of the particles cannot be moved without moving all of the other particles [145].

We applied Lloyd's algorithm to 1015 such packings consisting of 2000 monodisperse spheres generated with procedures described in [144, 9]. The point process is obtained by taking centres of mass of jammed spheres. Such point process was found hyperuniform [40] and it is visualized in Figure 2.5).

### Lubachevsky-Stillinger algorithm for sphere packings (LSPP)

This point process consists of centres of jammed packings of monodisperse, frictionless hard spheres obtained by the Lubachevsky-Stillinger algorithm [98, 78]. Lubachevsky-Stillinger algorithm is one of the most famous numerical procedures that simulate a packing of hard particles by compressing their assembly to the given simulation box.

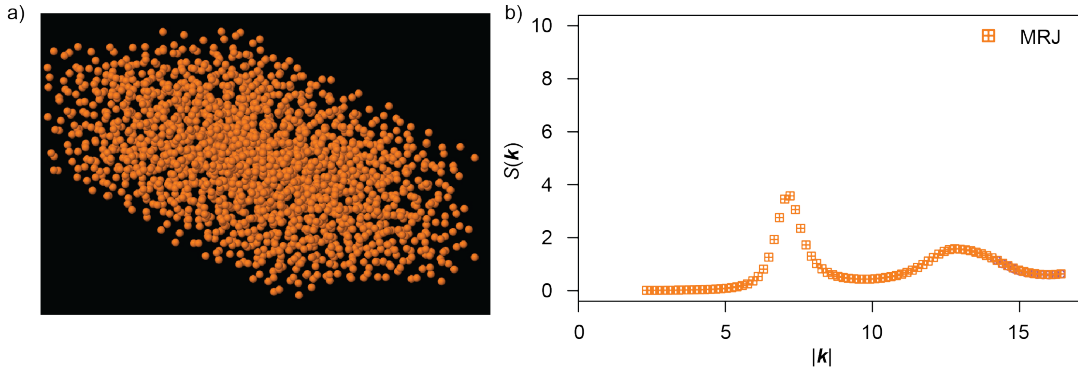


FIGURE 2.5: a) Maximally random jammed point processes in three dimensional space visualized by Jmol [71]. b) Structure factor of MRJ point process.

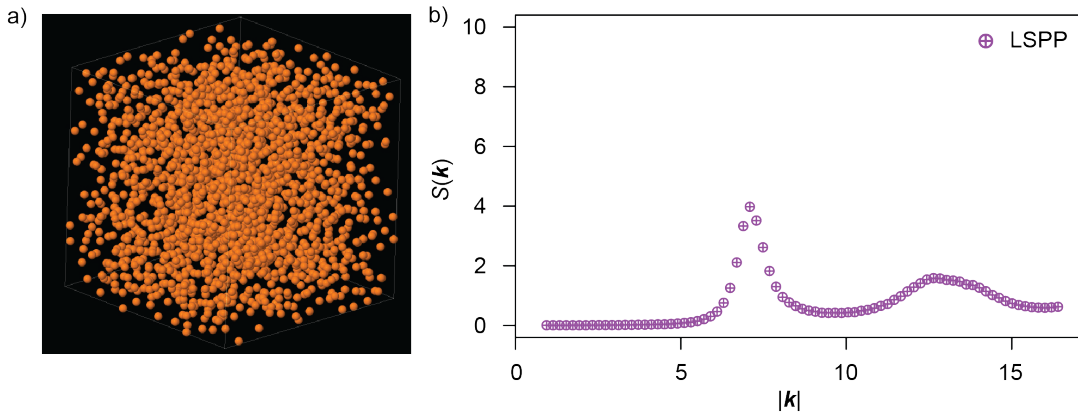


FIGURE 2.6: a) Point process generated by Lubachevsky-Stillinger algorithm for sphere packings in three dimensional space visualized by Jmol [71]. b) Structure factor of LSPP.

Our two samples consisted of 40000 spheres packed at global packing fraction  $\phi_g = 0.640639$  and  $\phi_g = 0.661073$  (see Figure 2.6a)). The difference in the packing fraction of two samples is key for one of the vital properties of the system. Sphere packing at packing fraction  $\phi_g = 0.640639$  is fully amorphous, meaning there are no crystalline patches in the system while packing fraction  $\phi_g = 0.661073$  exceeds random close packing limit [78] when crystalline domains start to form. The systems were generated using parameters taken from reference [78], and implementation of the Lubachevsky-Stillinger algorithm from [139].

### Stealthy hyperuniform point process (Stealthy PP)

Stealthy hyperuniform point processes are a class of point structures characterized by a structure factor  $S(\mathbf{k})$  that equals 0 for wavenumbers below

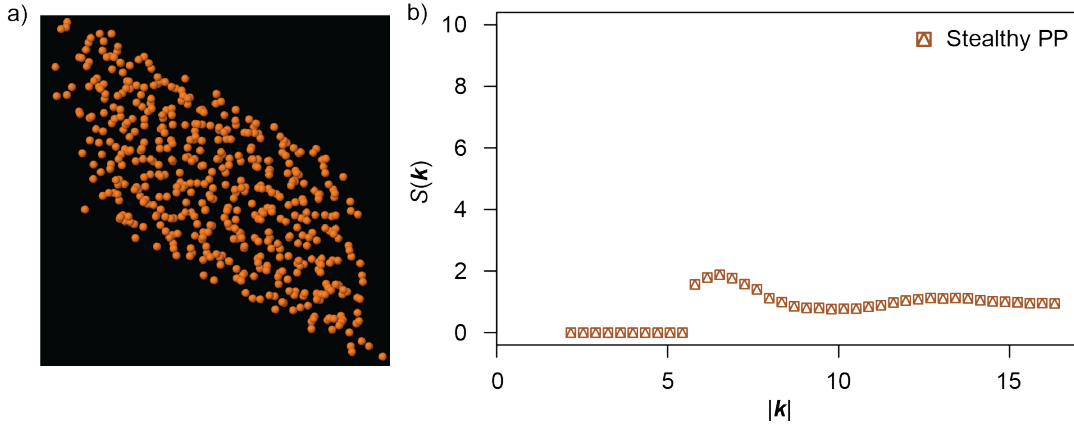


FIGURE 2.7: a) Stealthy hyperuniform point process in three dimensional space visualized by Jmol [71]. b) Structure factor of stealthy hyperuniform point process.

some threshold value  $\epsilon$  (Figure 2.7b). Trivial examples of stealthy hyperuniform point processes are crystal structures whose structure factors only have Bragg peaks [146]. However, statistically isotropic stealthy hyperuniform point processes can be surprisingly disordered, but still, hyperuniform [146].

For  $m \in \mathbb{N}$  points in the exclusion sphere, we can define parameter  $\chi = \frac{m}{d(n-1)}$  that measures the degeneracy and disorder in stealth hyperuniform point processes. With value  $\chi < 0.5$ , a stealthy hyperuniform point process is disordered and degenerate while for value  $\chi = 0.5$  the system transitions to crystalline state.

We generated twelve samples with disordered or so-called entropy favoured ground states ( $\chi = 0.494$ ), each containing 500 points using procedure described in reference [167] in order to apply Lloyd's algorithm to them. An example of the stealthy hyperuniform point process is presented in Figure 2.7a.

## 2.2.2 Implementation and convergence of Lloyd's algorithm

We implemented Lloyd's algorithm using two open-source software packages. We constructed Voronoi diagrams with Pomelo, a software package developed initially for calculation 3D set Voronoi diagrams for generic particles [131]. For calculation of mass centroids and total energies, we used Karambola [132, 134, 105], a software that calculates arbitrary Minkowski tensors of bodies and surfaces in 3D. In our simulations, all of the simulation boxes have periodic boundary conditions. Moreover, we self-developed

all other necessary scripts for calculations and data analysis in R [122], and Python [151]. For visualization of structures, we used Jmol: an open-source Java viewer for chemical structures in 3D [71].

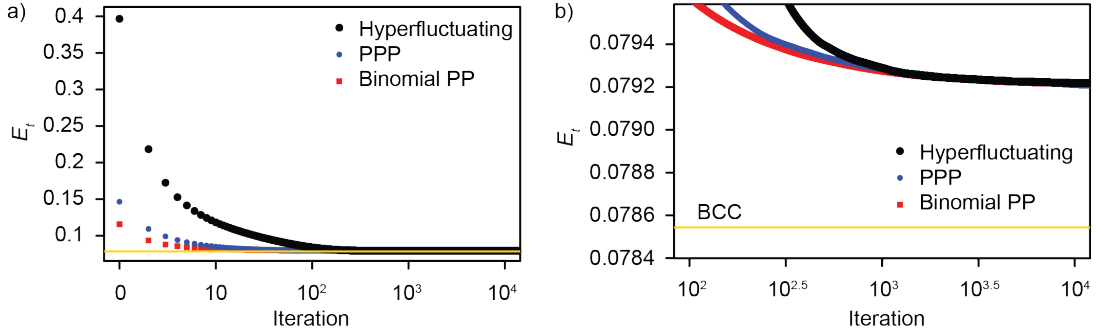


FIGURE 2.8: Total energy  $E_t$  (Introduction, Equation 22) calculated for Lloyd iterations. Different colours denote different initial configurations. Yellow solid line stands for total energy of BCC lattice,  $E_t \approx 0.078543$ . a) In first 10 iterations total energy decreases rapidly, while later the curve representing total energy saturates. b) After approximately  $10^3$  iterations, total energy is invariant on different initial structures. Moreover, the curve decreases slower over time indicating the convergence of Lloyd's algorithm.

We applied  $\mathcal{O}(10^4)$  iteration of Lloyd's algorithm to all of the structures described in Subsection 2.2.1 of this chapter. In order to justify convergence of Lloyd's algorithm after  $\mathcal{O}(10^4)$  iterations, we can observe the behaviour of the total energy  $E_t$  (Introduction, Equation 22) throughout the application of the algorithm (Figure 2.8). In the figure, different colours refer to different initial configurations, and the solid yellow line represents the total energy value of BCC,  $E_t \approx 0.078543$ . Concerned initial configurations were chosen because they have the greatest values of the total energy among the 7 initial configurations and are most instructive to present.

Hence, Figure 2.8a illustrates that values of the total energy  $E_t$  decrease quickly under Lloyd's algorithm, especially in the first 10 iterations. After that, the decrease in the total energy values is slighter, and the difference between values that correspond to different iterations gets smaller and smaller. Moreover, in Table 2.1 we present values of the total energy after a various number of Lloyd's iterations for all three different initial configurations. From there, we can observe that values of the total energy between iterations 1000 and 10000 differ only at the order of magnitude  $10^{-5}$ . Thus, based on the previous analysis, we can conclude the performed number of iterations is sufficient to consider Lloyd's algorithm fully converged. Therefore, obtained

Iteration	Binomial PP	PPP	Hyperfluctuating
0	0.1157	0.14656	0.39667
10	0.08172	0.08453	0.116045
100	0.07961	0.0798	0.08393
1000	0.07927	0.07928	0.07929
10000	0.07921	0.07921	0.07922

TABLE 2.1: Total energy of system given different initial structures and different number of Lloyd's iterations.

structures are suitable for further analysis.

Furthermore, from Figure 2.8b, we observe that after iteration 1000, the total energy values are nearly independent of the initial structure even though at the beginning, there is a significant difference between values of the total energy. Those differences between values of the total energy regarding different initial configurations diminish through time. In the beginning, before the application of Lloyd's algorithm, different systems have different values of the total energy  $E_t$  (Table 2.1). Interestingly, as the initial structure is more disordered and density fluctuations in the system are higher, the total energy value is greater and further from the total energy of BCC, which is considered a global optimum. This greater gap to the optimal value can be explained by Voronoi cells of many different shapes in such systems, especially more elongated ones that adopt higher values of the total energy. As we mentioned, while the number of iterations increases, the difference between the total energy values of different initial configurations vanishes. In particular, after 10000 iterations, differences between the total energies of different systems are the order of magnitude  $10^{-5}$  or even lower.

Another important aspect regarding the convergence of Lloyd's algorithm is the effect of the sample size of the configurations optimized by Lloyd's algorithm. We applied Lloyd's algorithm to two samples of the binomial point process, one consisting of 500 points and the other one consisting of 50000 points. We can observe from Figure 2.9a) that even though before the application of Lloyd's iterations exists a difference in total energy between two systems, the total energy value is nearly equal between samples for all except the first few iterations. Indeed, the difference is of order of magnitude  $10^{-4}$  or even lower even after 100 iterations (Figure 2.9b)).

Accordingly, considering the previous discussion, we can conclude that

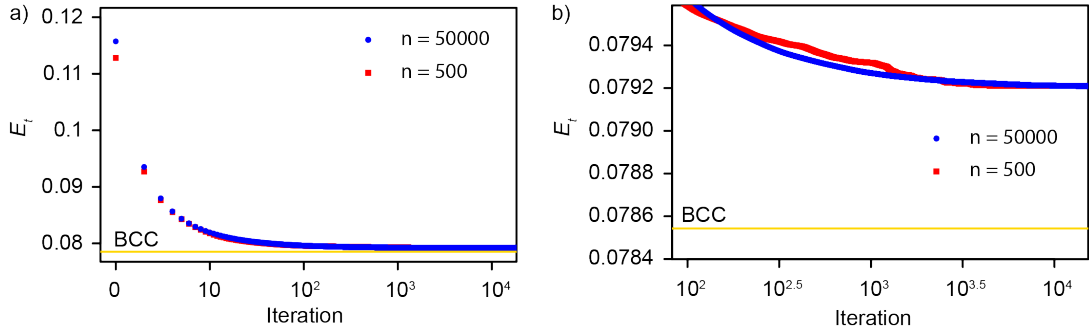


FIGURE 2.9: Total energy  $E_t$  (Introduction, Equation 22) calculated for Lloyd iterations. Different colours denote the binomial point process samples with a different number of points. Yellow solid line stands for total energy of BCC lattice,  $E_t \approx 0.078543$ . a) In the first few iterations, a small difference between total energies exists due to different realizations of the binomial point process. As the number of iterations rises, the difference between total energies vanishes. b) After approximately  $10^3$  iterations, the difference between energies is insignificant, meaning that Lloyd's algorithm converges with the same speed independently of the sample size.

the convergence of Lloyd's algorithm does not depend on the size of the systems used and that the number of points in each sample mentioned in subsection 2.2.1 is sufficient to draw valid conclusions about the properties of Lloyd's algorithm. Moreover, we observed that even after 1000 iterations, there is no significant difference in the total energy, and therefore,  $\mathcal{O}(10^4)$  Lloyd's iterations are plentiful to obtain fully equilibrated systems. Further proof of the respective claims arises from the fact that the mean distance between centres of mass and generators of Voronoi cells after  $\mathcal{O}(10^4)$  iterations is an order of magnitude  $\mathcal{O}(10^{-8})$  when meaning volume in systems is set to unity. Therefore, obtained configurations are CVD with the error being of an order of magnitude  $\mathcal{O}(10^{-8})$ .

## 2.3 Properties of the Quantizer minimal states

Here, we will present results regarding the application of Lloyd's algorithm to structures introduced in Subsection 2.2.1. We will characterize long-range density fluctuations of Quantizer optimal configurations after applying Lloyd's iterations by studying the properties of their structure factors. Furthermore, we will investigate the amorphousness of the obtained systems by marking out properties of Voronoi cell energy and volume probability distributions.



Finally, we will compare the outputs of Lloyd's algorithm to each other and examine the level of universality of Quantizer solutions.

### 2.3.1 Density fluctuations of systems under Lloyd's algorithm

In order to identify the effect of Lloyd's iterations to point different processes, we studied behaviour of structure factor of point patterns. Figure 2.10 presents structure factors of fully amorphous point processes described in subsection 2.2.1 before (Figure 2.10a) and after (Figure 2.10b) application of Lloyd's algorithm.

We can note that before applying Lloyd's algorithm, structure factors of different point configurations adopted different behaviours. Structure factors of more disordered point processes such as hyperfluctuating and permanent point processes obtain no peaks at any wavenumbers but diverge when wavenumber approaches zero. As mentioned before, such structures possess large density fluctuations at long wavelengths. On the other hand, systems with suppressed long-wavelength density fluctuations possess structure factors with expressed peaks at some wavenumbers and property that it approaches zero for small wavenumbers. Significantly, the structure factor of the stealthy hyperuniform point process is equal to zero when wavenumber  $k$  is lower than  $k_0 \approx 5.5$ . At last, some structure factors are constant with a value of 1 for all wavenumbers (binomial point process) or slightly fluctuate around 1 (determinantal point process).

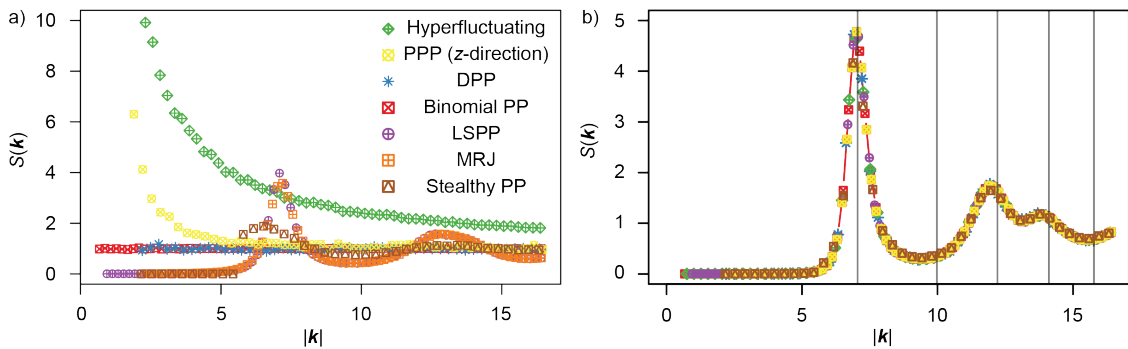


FIGURE 2.10: Structure factors of various amorphous point processes before (a) and after (b) application of Lloyd's algorithm. Differently coloured symbols denote different point patterns. Horizontal lines in b) part of the figure denote Bragg peaks of BCC lattice structure factor. This figure was adapted from reference [JL1].

After applying Lloyd's algorithm, we observe that all structure factors overlap into a universal curve. The obtained curve has expressed peaks distinct from Bragg peaks of the structure factor of the BCC lattice, a structure that is conjectured to be optimal in minimizing total energy  $E_t$ . Moreover, the final structure factor decays quickly from its most pronounced peak and approaches 0 as wavenumber  $k \rightarrow 0$ .

The previously mentioned phenomenon indicates a high suppression of long-wavelength density fluctuations in the systems after applying Lloyd's algorithm. It drives us to the conclusion that Lloyd's algorithm introduces a great order into systems regardless of the initial configuration, and therefore it justifies why it is frequently used when structures with desired "good" properties are needed [42].

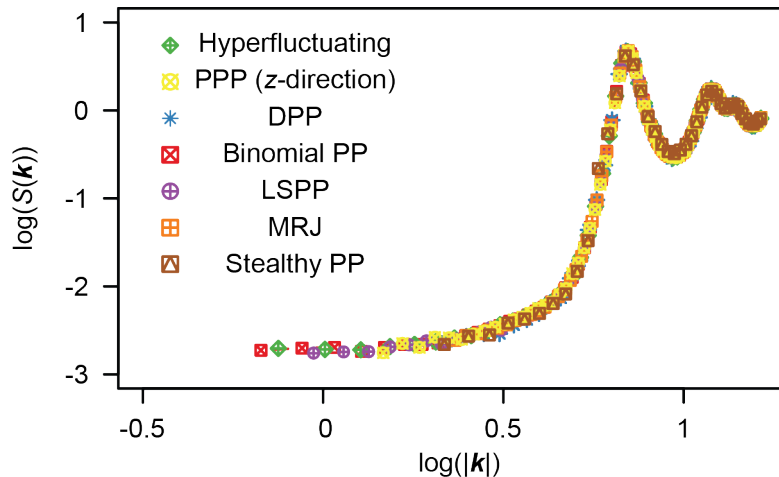


FIGURE 2.11: Structure factors of the different point processes after application of Lloyd's algorithm. Structure factors are plotted on log-log scale. Different coloured symbols denote different initial point processes.

In order to further examine the structure factor of the final configurations, we can picture structure factors on a logarithmic scale (Figure 2.11). Figure 2.11 reveals the order of magnitude to which structure factors dropped at short wave vectors  $\mathbf{k}$ . We can see that the structure factor has dropped close to  $10^{-3}$  for the smallest considered wavenumbers. That fact confirms the existence of long-range order and suppression of density fluctuations in final systems. Moreover, the obtained structure factors are of a similar order as ones obtained for maximally random jammed sphere packings, which are considered to be hyperuniform [40].

However, we can not conclude if obtained CVDs are strictly hyperuniform based on our study due to a few technical limitations. As it was discussed in reference [JL1], "we consider only a finite number of Lloyd's iterations. As seen from our study, Lloyd's iterations cancel out long-wavelength density fluctuations in concerned systems (such as in the case of hyperfluctuating point patterns). More precisely, in each step, a local optimization event (replacement Voronoi cell generator with its centre of mass) induces an optimization (suppression) of density fluctuations on a long-range. Therefore, a finite number of Lloyd's iterations can not modify density fluctuations on infinite wavelengths meaning valid conclusions about  $S(0)$  can not be made. Moreover, it was shown that Lloyd's algorithm modifies structure factor quickly in the first 1000 iterations and after that decays structure factor towards 0 slower after each iteration [85].

Further limitations of our study are the effects of the finite system size. The first of them is due to the boundary conditions of our simulation box. Even though the periodic boundary conditions minimize the boundary effect, since Lloyd's iterations influence long-wavelength density fluctuations, the boundary effect is undoubtedly present. Moreover, the finite size of the system influences the small wavenumbers that we can consider. The density fluctuations at the length of the simulation box are hard to calculate, and therefore, we only consider the wavenumbers greater than  $4.5 \times \frac{1}{a}$  where  $a$  is a simulation box length. The exceptions are the Determinantal PP and Stealthy hyperuniform PP, where we consider the wavenumbers greater than  $1.5 \times \frac{1}{a}$  due to small system sizes.

Last but not most negligible effect on our study is a limitation that wavenumbers taken into consideration obtain only discrete values meaning only a few wave vectors are taken in count. Therefore, an effect of low statistics can cause more significant variations in the estimation of the structure factor."

However, even though we can not address if obtained CVDs are strictly hyperuniform, we find that they are effectively hyperuniform with  $H$  measure  $H \leq 10^{-4}$ . The obtained value of the hyperuniformity measure  $H$  is one of the smallest known among the effective hyperuniform systems [148]. Therefore, we can conclude that obtained CVDs are surely hyperuniform for all practical purposes while studying strict hyperuniformity is beyond the reach of this thesis.

### 2.3.2 Amorphousness of structures

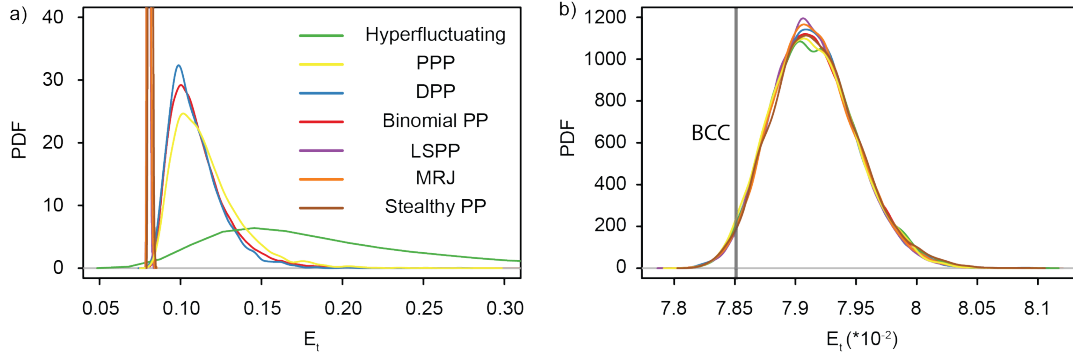


FIGURE 2.12: Distributions of the total cell energy  $E_t$  (Introduction Equation 23). Different colours denote different point patterns. a) Initial configurations. The distributions of the total cell energy  $E_t$  differ both in width and in position on the  $E_t$  axes depending on different point patterns. b) Final configurations. Distributions of the total cell energy overlap for all initial configurations. A significant fraction of cells ( $\approx 3\%$ ) obtain total energies that are lower than total energy of the BCC cell ( $E_t \approx 0.078543$ ).

As mentioned earlier, we applied Lloyd's algorithm to point processes that form very different spatial structures but have a common property - amorphousness. The latter claim can be justified by examining energies (Figure 2.12) and volumes (Figure 2.13) of Voronoi cells generated by the observed point processes. Indeed, neither do the total cell energy (Figure 2.12a)) or volume (Figure 2.13a)) distributions of the initial structures possess peaks in the distributions, which would indicate if ordered domains or crystalline patches are over-expressed in the systems. Observed distributions are smooth, and some of them are very narrow compared to the others, but they all have a long tail, as appropriate for amorphous structures. Furthermore, although structure factors of initial configuration differ a lot, no Bragg peaks that would be characteristic for systems with expressed crystalline domains are observed (Figure 2.10a).

Surprisingly, even though Lloyd's algorithm introduces a great amount of order in the systems and nearly fully suppresses long-range density fluctuations, characteristic of the crystals, the obtained final structures also remain fully amorphous. Truly, energy (Figure 2.12b)) and volume (Figure 2.13) distributions associated with the final structures have no overexpressed peaks

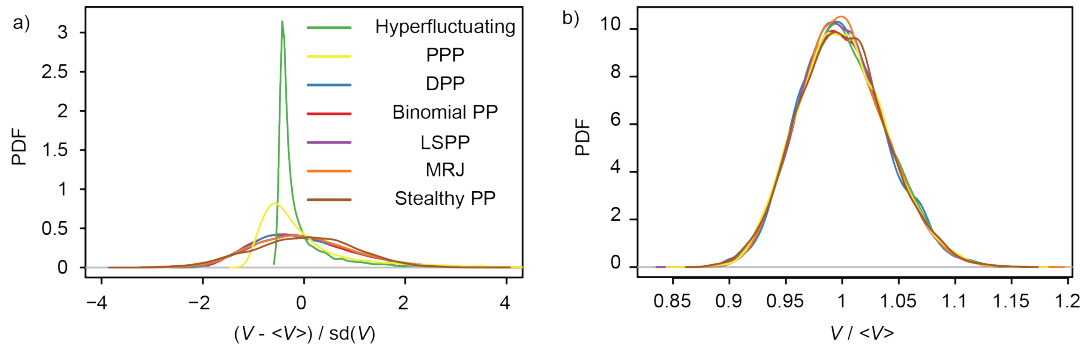


FIGURE 2.13: Distributions of the Voronoi cell volumes. Different colours denote different point patterns. a) Volumes are scaled such that all of the distributions have zero mean and standard deviation equal to 1. b) Volumes are scaled such that all of the distributions have a mean equal to unity.

and adopt a fully smooth shape which shows that the obtained systems are amorphous.

Further evidence of the amorphousness of the final systems can be found by investigating their structure factors (Figure 2.10b)). Similarly, as in the case of initial structures, the structure factors of final structures are smooth and possess no Bragg peaks. Moreover, the structure factors of the final configurations gain peaks at different wavenumbers from the Bragg peaks of the BCC lattice, a conjectured global optimal structure. Therefore, the obtained local minima have different spatial properties than the BCC lattice, which suggests further evidence of the amorphousness of the systems.

Ultimately, proof of the final, as well as amorphousness of the initial structure, can also be found by analysing Minkowski structure metrics [78]. In the reference [85], the distributions of Minkowski structure metrics are also smooth with the absence of sharp peaks, which would indicate overexpression of specific structures such as ordered domains and crystalline patches in the systems.

### 2.3.3 Universality of the final structure

Another remarkable property of a system gained under Lloyd's iterations is the universality of the final point configurations. As mentioned before, initial configurations differ significantly regarding their structural properties, such as long-range order and visual appearance. Opposite of that, the obtained structures after application of Lloyd's algorithm possess an astonishing level

Point process	Final $E_t$
Binomial PP	0.07921215
PPP	0.07920569
Hyperfluctuating PP	0.07921685
DPP	0.07920274
LSPP	0.07920299
MRJ	0.07920828
Stealthy PP	0.07922498

TABLE 2.2: Mean of final total energies for each concerned point process. Total energies are clearly greater than the total energy of the BCC lattice ( $E_t \approx 0.078543$ ).

of universality.

We find an overlap of the final configuration structure factors (Figures 2.10b and 2.11) as well as an overlap of their total energy (Figure 2.12b) and volume (Figure 2.13) distributions if starting from a fully amorphous state of any type. That phenomenon suggests that the obtained optimal structures correspond to one of the infinitely many valleys of the total energy landscape with the same universal spatial properties such as long-range order and the same distributions of single-cell energy and cell volume.

Further evidence of the later claims can be found by observing the total energies  $E_t$  of the final point configurations (Table 2.2). We find that the final energies start to differ only at the fifth decimal position between the samples, which confirms the claim regarding the properties of the total energy landscape.

### 2.3.4 Effect of Lloyd's algorithm to structures with crystalline patches

If we apply Lloyd's algorithm to Lubachevsky-Stillinger sphere packing at packing fraction  $\phi_g = 0.661073$  with crystalline patches in it, we observe significantly different properties of the obtained configurations.

We observe that the final structure carries some commons and different properties to the universal system described earlier. We find that the main result, suppression of long-wavelength density fluctuations, is attained when the initial structures have crystalline domains. The obtained structure has measure  $H = \mathcal{O}(10^{-5})$  meaning it is also effectively hyperuniform. However, the final configuration's structure differs significantly from those produced from the completely amorphous systems.

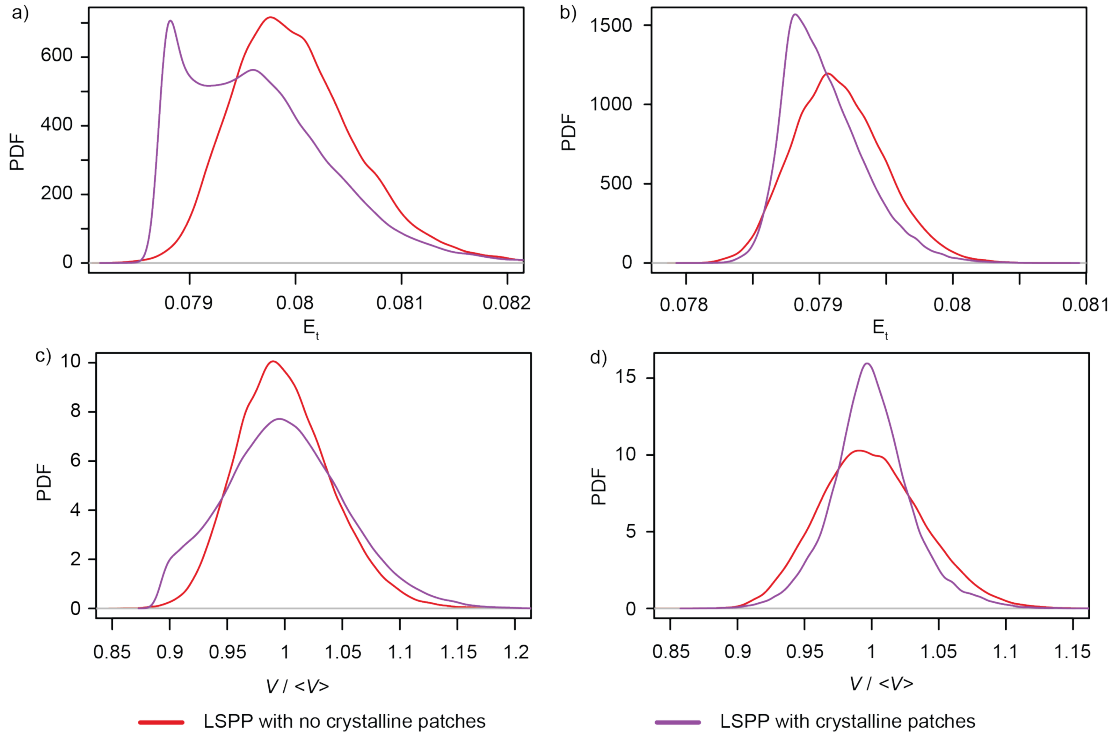


FIGURE 2.14: Distributions of total cell energy (Introduction, Equation 23)

and cell volume of LSPP systems with and without crystallines. Different colours denote different LSPP systems. a) Total cell energy distributions before the application of Lloyd's algorithm. b) Total cell energy distributions after the application of Lloyd's algorithm. c) Volume distributions before the application of Lloyd's algorithm. d) Volume distributions after the application of Lloyd's algorithm.

First of all, there exists a substantial gap between the final total energies of systems with and without initial crystalline patches. The total energy of the final configuration of amorphous LSPP equals 0.07920299 while the total energy of the final configuration of LSPP with crystalline patches achieves a value of 0.07907405. This difference is of an order of magnitude. Therefore the total energy obtained from the system with crystalline domains is closer to the total energy of BCC, a conjectured global minimum. Therefore, systems with crystalline domains are more ordered than systems without crystallites in their structure after applying Lloyd's algorithm.

Indeed, the former claim can be further confirmed by studying the properties of volumes and cell total energies of the systems. Figure 2.14 shows total cell energy and volume distributions of the LSPP with and without crystalline domains before and after the application of Lloyd's algorithm.

By observing Figures 2.14 a) and c), we can detect the presence of crystalline patches in the initial LSPP sample. The distribution of a single cell

total energy (Figure 2.14a)) for the LSPP structure with crystalline patches obtains two expressed peaks. In contrast, the LSPP without crystalline domains possesses only one expressed peak. The peak of the LSPP with crystalline patches around value  $E_t \approx 0.07881$  is more expressed than the other peak meaning the concerned total energy value is most probable in the system. Furthermore, the probability density curve on the left side of that peak is very steep, indicating only a few cells in the system with a lower total cell energy value than  $E_t \approx 0.07881$ . Moreover, the whole total cell energy distribution regarding LSPP with crystalline is shifted to the left, meaning total energies in the system are lower. Therefore, the system is more ordered because of the total energy properties discussed earlier. Similarly, the LSPP with crystalline volume distribution (Figure 2.14c)) obtains a more expressed value around  $V \approx 0.9$ , which also indicates the existence of crystalline patches in the system.

After applying Lloyd's algorithm to LSPP with and without crystallines, total cells energy and volume distributions share a common property. First of all, the final distributions (Figure 2.14 b) and d)) related to LSPP with crystallines differ from the distributions related to LSPP without ordered domains. Thus, the configuration obtained from the LSPP with crystallines has a significant structural difference to the universal structure obtained by applying Lloyd's algorithm to various completely amorphous structures. Hence, the amorphousness of the system plays a crucial role in determining which local minimum will be achieved by the convergence of Lloyd's algorithm. Moreover, the final distributions related to LSPP with crystalline patches have more expressed peaks, and they are also much narrower. Even though the obtained structure is still disordered, the structural features such as total cell energy and volume are more pronounced than in the universal structure discussed earlier. Further evidence that the locally ordered domains induce final structures that are more ordered can be found by analysing distributions of the total cell energy. Even though the distribution of the final configuration related to the structure with crystalline patches does not have two peaks like the initial one, it is shifted to the left, indicating lower energies and, therefore, more order in the system.



## 2.4 Overview and discussion

We have seen that Lloyd's algorithm introduces a connection between the famous Quantizer problem and effective hyperuniformity in the systems. Thus, it was shown that a local optimization process such as replacing generators of Voronoi cells with its mass centroids could introduce a global order to the system in terms of suppressing the long-wavelength density fluctuations. The particular results may be of interest for any systems where similar local optimization events occur.

An important finding is that most of our results mentioned earlier are also valid for planar tessellations [85]. Here Lloyd's algorithm transforms various amorphous planar point processes to an effectively hyperuniform structure with a great degree of universality. However, in 2D, the obtained systems contain small ordered domains where cells tend to be nearly regular hexagons [85]. Interestingly, similar dependence on dimension can be found in other optimization problems. For example, in Kelvin problem 2D the optimal foam is predisposed to forming optimal hexagonal structures while in 3D ordering is not found [48]. Similar to that, random packing of spheres in 3D can reach random close packing limit [15], while in 2D monodisperse systems do not achieve maximally random packing density.

The presented results are essential for understanding existing scientific problems, but they also open many questions and possibly exciting research topics. Accordingly, it would be of great importance for our results if an analytical relation between the centroidal Voronoi diagram and long-wavelength density fluctuations would be provided. Another intriguing question is whether different optimization protocols such as gradient descent produce the same or similar structures to solve the Quantizer problem. Such studies would broaden our knowledge about the landscape of the Quantizer total energy and therefore provide properties that would be important for practical purposes. Moreover, the study of the Quantizer problem solutions can be generalised to systems with random and inhomogeneous density or to the systems in higher dimensions. Addressing such questions would be fundamental for data science and machine learning since most data is high dimensional and follows a non-uniform distribution. Further exciting generalization of the Quantizer problem is when the studied structure isn't a point process but rather an assembly of an object with non-trivial volume. In such a case, a

minimal distance between an arbitrary point in the system and the closest object to that point is observed. Such questions are fundamental for new technologies such as self-driving cars and robotics and many living systems, including cell tissues. Therefore, in the following chapters of this thesis, we focus on the concerned generalization of the Quantizer problem.

## Chapter 3

# Geometric effects in random assemblies of ellipses

### Declaration for Chapter 3

The following chapter includes the text, clearly noted by the quotation marks ("..."), and the figures, which are literal of a partially paraphrased copy of the material published in the following article:

[JL2] **Jakov Lovrić**, Sara Kaliman, Wolfram Barfuss, Gerd E. Schröder-Turk, Ana-Sunčana Smith; "Geometric effects in random assemblies of ellipses", *Soft Matter* 15 8566-8577 (2019), <https://doi.org/10.1039/C9SM01067J>

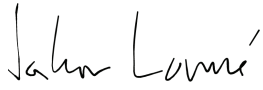
All contents are reproduced from reference [JL2] with permission from the Royal Society of Chemistry.

In the aforementioned article, Jakov Lovrić programmed the simulator, ran the simulations, and obtained the data. Moreover, he analysed the collected data, interpreted most of the results, generated all of the figures, wrote the first draft, and prepared the manuscript for publication.

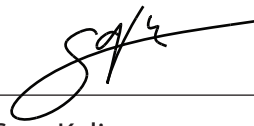
Other authors of the paper conceived and supervised the research project, obtained preliminary results on the topic of the paper, took part in the interpretation of obtained results, commented on the results, and contributed to the writing of the final draft.

The authors declare no conflict of interest and confirm the correctness of the above statements.

Erlangen, 1 December 2021.



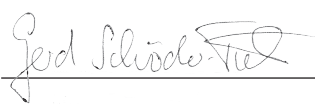
Jakov Lovrić




Sara Kaliman



Wolfram Barfuss



Gerd E. Schröder-Turk



Ana-Sunčana Smith

## 3.1 Introduction to random assemblies

The general objective of this thesis is to find non-trivial solutions to the Quantizer problem. In a previous chapter, this was achieved using Lloyd's algorithm in structures generated by points. We realised that the amorphousness of the initial state is essential to obtain a universal hyperuniform structure. We would like to solve the Quantizer problem for assemblies of hard particles in the future. However, before attempting to do so, we first engage in thoroughly characterising the geometric and topological properties of 2D assemblies. We focus on ellipse assemblies because of their significant variability in the shape of constitutive particles.

The most suitable assemblies for investigating the effects of density and particle shape on assembly structural properties are ones that are considered random. By random, we mean that in such systems, the optimisation process does not exist and that they are generated using a stochastic process [145]. Such assemblies exist in many systems such as living matter, liquids, glasses, amorphous solids, and granular media [41, 7].

Random assemblies of various particles were studied extensively in the past through experiments [135, 126, 49, 72] as well as with help of theoretical models and algorithms that were developed to generate them [98, 33, 36, 68, 161]. Thus, since assemblies of particles occur in many materials both liquid or solid, scientists have spent a lot of time to characterize important states of particle assemblies such as maximally random jammed state [145, 169, 39, 38, 133], random close packing [50, 165] and random loose packing [138, 165]. Moreover, properties of random assemblies such as correlations between neighbouring particles [37, 129] and many others were studied extensively in the context of system's dimension, assembly packing fraction and particle shape or dispersivity [39, 50, 70, 106, 112, 163].

Random assemblies are often studied by calculating the Voronoi diagram from the particles in assemblies and then investigating the nature of obtained tessellations. We can perform such an analysis of systems by calculating Minkowski tensors of Voronoi cells. Therefore, as we explained in the reference [JL2], "in the absence of long-range interactions between particles, it was demonstrated that the so-called Minkowski functionals provide a useful set of structure metrics to characterise the morphology, which are endowed with some completeness with respect to additive properties [5]. Interestingly, for a broad range of systems, a subset of measures consisting of selected

Minkowski scalars (area, perimeter, mean curvature) and tensors (moments of inertia) capture the bulk of the information about the assembly [134, 132]. This approach leads to the understanding that in assemblies of circles at high packing fractions (where crystalline order is expected at zero temperature), quenching yields glassy states with a number particles having five and seven neighbours [89]. Latter, in hard-sphere systems, the number of contacts was calculated as a function of packing fraction [129], and the maximally random jammed packings were fully characterised [84]. Minkowski functionals were furthermore applied for quantifying structural similarity of crystalline patterns, and used in an accurate identification of the ordering transition and the random close packing limit [78] the latter found to be higher than previously determined [16, 38]."

Since Minkowski functionals provide effective formulas to calculate various morphological measures such as area, perimeter, and elongation of Voronoi cells [134], probability distributions of such measures were subjects of many studies. Interestingly, Gamma distribution appears to be the most common probability model for various morphological measures. This phenomenon can be explained by the fact that Gamma distribution adopts a broad range of shapes when tuning its parameters and its positive domain, which perfectly describes the non-negativity of morphological measures. Thus, the so-called k-gamma distributions appear as a model for the distribution of Voronoi cell volume in sphere packings when entropy in the system is maximised [6]. Moreover, cell volume, area, perimeter, and number of neighbours follow gamma distributions when Voronoi cells are generated by various point processes such as Poisson point process both in 2D and 3D [168, 65, 88].

Although the study of morphological measures provides insight into the geometry of Voronoi cells generated by the assembly, it is not possible to draw valid conclusions about the organisation and topology of systems [83, 81]. Thus, in the reference [JL2], we summarise: "Understanding the relationship between the geometry and topology of the assembly actually requires the analysis of correlations between various measures and the number of neighbours [46, 45]. While second order correlations between the mean of several morphological Voronoi cell measures and the number of neighbours were discovered in tessellations generated from Poisson points [168], most works so far focused on first order correlations. Perhaps the most famous examples of the latter are the Lewis' [92, 93, 26, 82] and the Desch's [35, 123]

laws, predicting a linear increase of the average area and the perimeter of cells with a particular number of neighbours, respectively. Both of these relationships suggest that large cells have a tendency to have more neighbours, compared to small cells. Furthermore, the fact that cells with fewer neighbours tend to have neighbours with more sides is captured by the so-called Aboav-Weaire's law [2, 1, 156]. This law was found to change for the diffusion limited colloidal aggregation to an inverse square-root dependence [64, 47]. However, the validity of the Lewis, Desch's and Aboav-Weaire's law was confirmed in a number of systems including biological tissues [92, 108, 107, 118, 125, 82, 74], foam structures [158, 58, 152], grain distribution of 2D polycrystalline films [52, 28], and even in the analysis of the polygonal networks on Mars surface [127]."

This chapter will study monodisperse random assemblies of ellipses concerning a broad range of packing fractions and different ellipse shapes. In that manner, we will cover structures that are very similar to point processes and jammed states. We will focus on geometrical measures that illustrate the size of the Voronoi cells and the ones that characterise cell shape. Furthermore, we will investigate centralisation in random assemblies governed by the packing fraction and ellipse shape, which will help us separate optimisation effects to system properties that are just consequences of the particle being assembled. Finally, we will investigate topological aspects of ellipse assemblies and relate them to the geometry of the system.

## 3.2 Methods

In this section, we will describe the phase space of ellipse shapes and packing fractions that will be in focus in this chapter. Moreover, we will present the algorithm that we used for the generation of ellipse assemblies and define statistical methods that will be used to characterise various assembly morphological and topological properties.

### 3.2.1 Phase space of assemblies and calculation of morphological measures

The shape of the ellipses that will be the subject of our study can be characterised by its *aspect ratio* (or elongation)  $e$ , that is, the ratio between the major and minor ellipse semi-axis. From its definition, we can see that the aspect

ratio  $e > 1$  adopts greater values if a concerned particle is more elongated. Here, we study assemblies of monodisperse ellipses with  $e=3.33, 2, 1.25, 1$  which covers ellipses from highly elongated ones ( $e = 3.33$ ) to circles ( $e = 1$ ). The considered ellipses will be assembled at global packing fraction  $\phi_g = 0.2, 0.35, 0.5, 0.65, 0.8$ , which covers a range of densities characteristic for liquid states and states that are similar to a point processes to nearly jammed states ( $\phi_g = 0.8$ ) [16]. Examples of studied assemblies can be found in Figure 3.1a,b and Appendix A, Figures A.1-A.5.

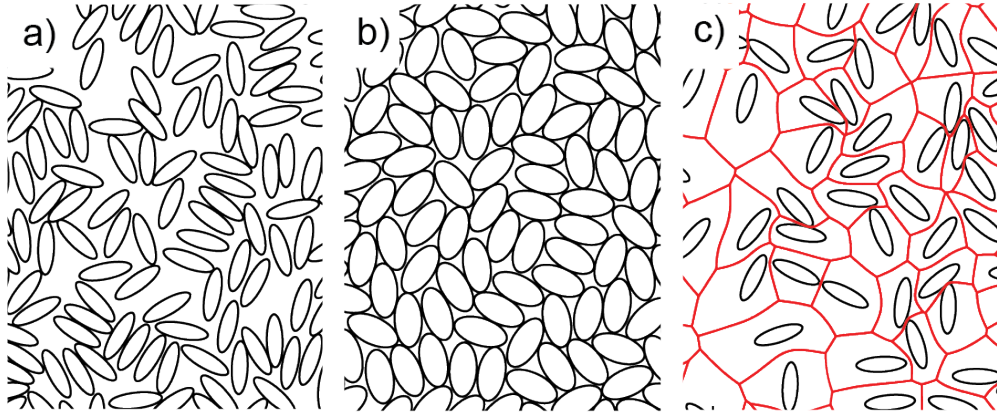


FIGURE 3.1: Random assemblies of ellipses. a) Ellipses with the elongation  $e = 3.33$  at a packing fraction of  $\phi_g = 0.5$  b) Ellipses with  $e = 2$  at  $\phi_g = 0.8$  c) Set Voronoi diagram built from the shapes of the generating ellipses with aspect ratio  $e = 3.33$  at packing fraction  $\phi_g = 0.2$ , clearly demonstrating the non-polygonal nature of the tessellation. Image was taken from reference[JL2].

In order to evaluate morphological measures that will identify properties of particles in assembly, we calculate the so-called Set Voronoi tessellation (SVT) from ellipses in the assembly [131, 160]. The calculation of SVT is analogous to the calculation of the standard Voronoi diagram, with the condition that the generating particles are objects with non-zero areas rather than points. More formally, if  $E_i, i = 1, \dots, N, N \in \mathbb{N}$  are ellipses, then Voronoi cell  $\mathcal{V}_i$  of particle  $E_i$  is defined with:

$$\mathcal{V}_i = \{\mathbf{x} \in \mathbb{R}^2 | d_E(\mathbf{x}, E_i) \leq d_E(\mathbf{x}, E_j), \forall j \neq i, j \in \{1, \dots, N\}\} \quad (3.1)$$

where  $d_E$  is the Euclidean metric.

We can see from the previous definition that SVD takes in count shape of the particles and therefore obtained Voronoi cells are not convex like ones



of standard Voronoi diagram. Moreover, edges of CVD can have arbitrary curvatures that depend on the positions of two neighbouring particles (see Fig. 3.1c).

After calculation of SVD, we calculate Minkowski tensors for each Voronoi cell using the procedure described in reference [134]. From calculated Minkowski tensors, we derive desired morphological measures such as area, perimeter, elongation (ratio of principal moments of inertia), the distance between the centre of ellipse and centre of mass of its Voronoi cell (CM distance) and standard deviation of each Voronoi cell edge lengths (standard deviation of contact length).

### 3.2.2 Packing algorithm and sampling procedure

We generate random assemblies of ellipses with a modified version of the algorithm from reference [33]. In the reference [JL2], we provide details of the algorithm (Flowchart in Figure 3.2): "Initially, a chosen number of ellipses (200) are reduced to 20% of their final area of a constitutive ellipse (area of an ellipse assembled on the desired packing fraction) and are randomly placed into the simulation box. If there is overlap between ellipses, one ellipse is randomly chosen (equal probability for each member of the set), and a random translation and rotation is performed. The translation is defined by a vector whose length is drawn from the uniform distribution on the interval  $[-\frac{b}{2}, \frac{b}{2}]$  where  $b$  is a semi-minor axis of the ellipses at full size. Translations in  $x$  and  $y$  directions are executed independently. The value of the rotation angle is a random variable, drawn from the uniform distribution on the interval  $[0, \pi]$ . The movement (2 translations + rotation) is accepted if the total overlap decreases or stays the same. The procedure is repeated until the total overlap is 0 (minimal significant value in double floating precision arithmetic), when all ellipses are simultaneously dilated by 0.5% of their final area of a constitutive ellipse. If the total overlap caused by the growth is greater than 0, then translations and rotations of ellipses are repeated until the overlap vanishes again. The procedure is terminated when the desired packing fraction is reached and the total ellipse overlap area is zero in double precision.

All simulations were performed with periodic boundary conditions and with the simulation box of the predefined resolution. This ensures that the mean area of Voronoi cells is constant for all data and, hence, that morphological measures are all calculated with the same accuracy, irrespective of the

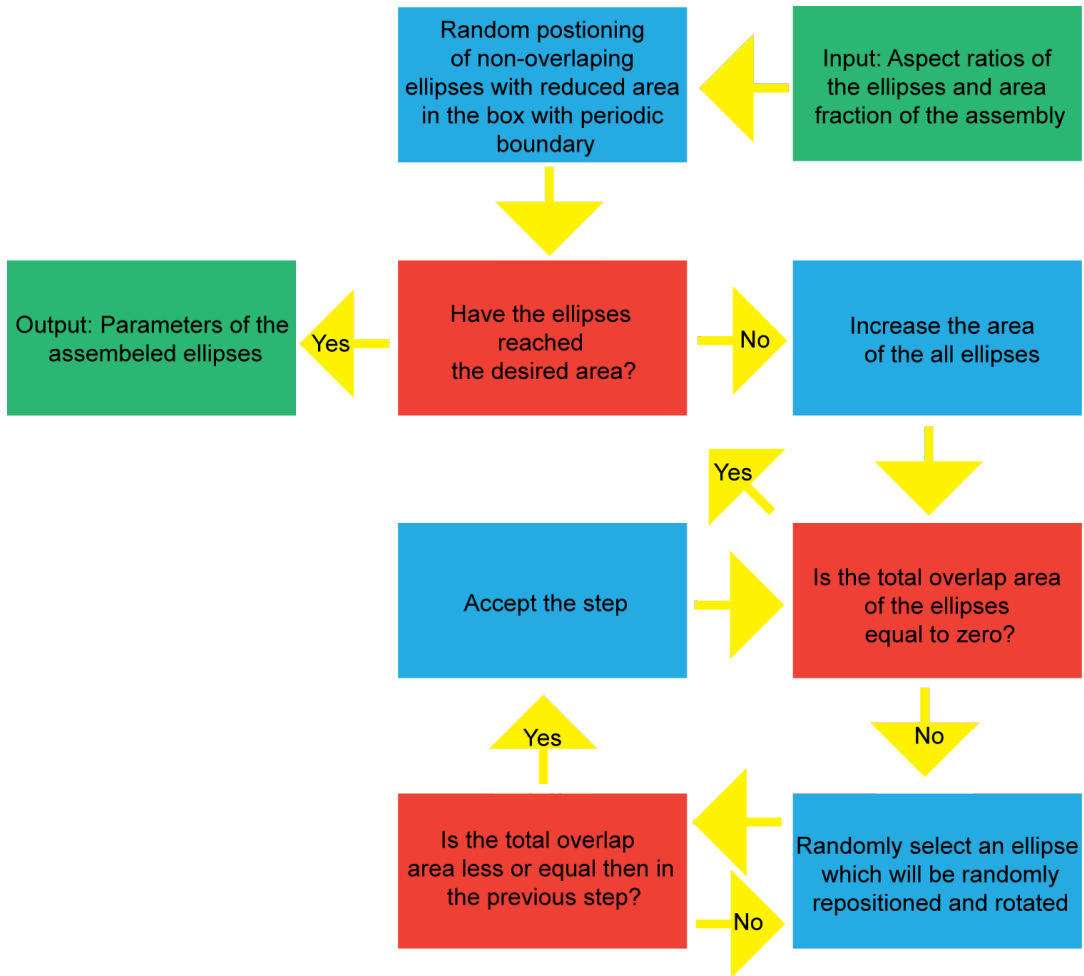


FIGURE 3.2: Flowchart of the algorithm used to generate ellipse assemblies. Green rectangles stand for input and output of the algorithm, red rectangles for decisions and blue rectangles for steps of the algorithm. Image was taken from reference [JL2].

choice of parameters  $e$  and  $\phi_g$ ."

For each ellipse assembly in the phase space of aspect ratios and packing fractions, we have generated 25 assemblies of 200 ellipses, meaning the total sample size is 5000. We investigated the appearance of cell area distributions for different sample sizes. We found that there is no significant difference in the distribution appearances even for sample sizes larger than 1000 (Figure 3.3a). Therefore, we conclude that our sample of 5000 is sufficiently large to obtain convergence of any statistics calculated.

Moreover, one can question whether our sampling procedure is valid since it is different from a random sampling procedure. If a sample is considered random, all of the observations have to be independent and drawn from the same distribution. Clearly, in our samples, all distributions are not

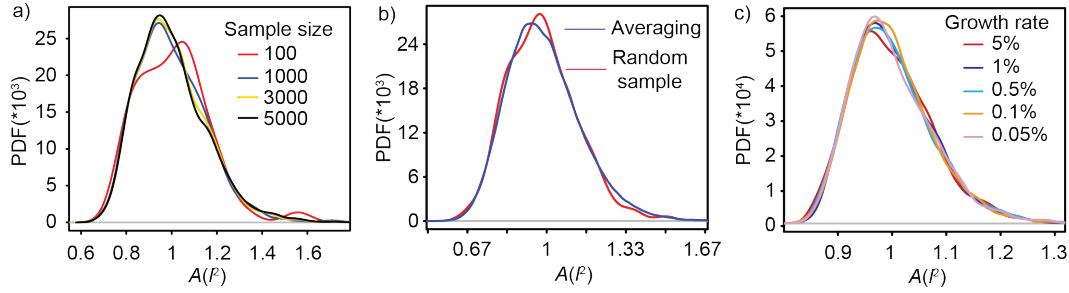


FIGURE 3.3: Validation of the sampling procedure. a) Convergence of the cell area distributions shape is achieved for sample size  $N > 1000$ . b) Distributions of cell area for packings generated with different ellipse growth rates do not statistically differ (characteristic p-value between 0.39 and 0.96). c) Distributions of data collected cumulatively (blue curve) using all cells from 25 samples of assemblies with 200 ellipses (total of 5000 cells) data) and by sampling one random cell in from each of 5000 samples of assemblies of 200 ellipses (red curve). The comparison of the two approaches shows no statistically significant difference (Kolmogorov-Smirnov test p-value = 0.7). This image was taken from reference [JL2].

independent because of the correlations between particles in each of the 25 assemblies. However, we find that there is no statistically significant difference between our sampling method (averaging) and random sampling (Figure 3.3b). Therefore, our samples are valid for calculating any statistics that require a random sample.

Last but not least, we find that our assembly properties do not depend on the parameters in the packing algorithm that could be potentially tuned, such as the growth rate of the ellipses and parameters of the uniform distributions that are used to sample ellipse translations and rotations (Figure 3.3c).

### 3.2.3 Statistical analysis

From any of the studied systems, and any measure  $X$  (area, elongation and others), let  $\mathbf{x} = \{x_i, i \in \{1, \dots, N\}, x_i \in \mathbb{R}\}$ , be a random sample. We can model distribution of  $X$  with the generalized gamma distribution that is defined by its density function  $f(x|\theta)$ ,

$$f(x|\theta) = \frac{\tau}{\lambda \Gamma(\alpha)} \left( \frac{x - x_0}{\lambda} \right)^{\alpha\tau - 1} e^{-\left(\frac{x - x_0}{\lambda}\right)^\tau} \mathbb{1}_{[x_0, +\infty)}(x), \quad (3.2)$$

which is parametrized by  $\theta = (\alpha, \tau, \lambda) \in \mathbb{R}_+^3$ , and  $x_0 \in \mathbb{R}$ . Here,  $\Gamma(\cdot)$  denotes a Gamma function. From the Equation 3.2, by setting  $\tau = 1$  we can recover the Gamma distribution,  $\alpha = 1$  provides the Weibull distribution

density function,  $\alpha = df/2, \tau = 1, \lambda = 2$  deliver  $\chi^2$  distribution with  $df$  degrees of freedom and  $\alpha = \tau = 1$  define and exponential distribution with parameter  $\lambda$ . Moreover, the number of neighbours  $n$ , which is a discrete random variable, can be estimated with continuous distribution using identity  $\mathbb{P}(n = m) = \mathbb{P}(Y \in \langle m - 0.5, m + 0.5 \rangle], m \in \mathbb{N}$ , where random variable  $Y$  has continuous density function.

We estimate parameters of the generalized gamma distribution (Equation 3.2) with the *maximum likelihood estimator* (MLE), defined with,

$$\hat{\theta} = \max_{\theta \in \mathbb{R}_+^3} L(\theta), \text{ where } L(\theta) = \prod_{i=1}^n f(x_i | \theta). \quad (3.3)$$

MLE is one of the most famous estimators in the field of statistics. It predicts desired parameters by maximising the probability of obtaining sample  $\mathbf{x}$  over the concerned parametric space.

After estimating the parameters of distributions with MLE, we test the goodness of the fit with the Pearson's  $\chi^2$ -test. Pearson's  $\chi^2$ -test, uses the test statistics

$$H = \sum_{j=1}^k \frac{(N_j - n_j)^2}{n_j} \quad (3.4)$$

which is nothing more than a least square error between estimated frequencies  $n_j$  and observed frequencies  $N_j$  binned in  $k \in \mathbb{N}$  bins. Further, we calculate the p-value of the test using the  $\chi^2$ -test statistics  $H$  property that it follows the  $\chi^2(df)$  distribution with degrees of freedom given with formula  $df = k - d - 1$  where  $d$  is the number of estimated parameters.

We tested equality of two distributions with the Kolmogorov-Smirnov (KS) test. KS test questions if distribution functions  $F_X$  and  $F_Y$  of two random variables  $X$  and  $Y$ . From the two samples  $\mathbf{x}$  and  $\mathbf{y}$  with sample sizes  $nm$  and  $n$ , we can calculate their empirical distribution functions  $F_m$  and  $F_n$ . From there, we can obtain the test statistics

$$D_{mn} = \sqrt{\frac{mn}{m+n}} \sup_{x \in \mathbb{R}} |F_m(x) - F_n(x)|. \quad (3.5)$$

We calculate the p-value of the test from the fact that test statistic  $D_{mn}$  follows the Kolmogorov-Smirnov distribution.

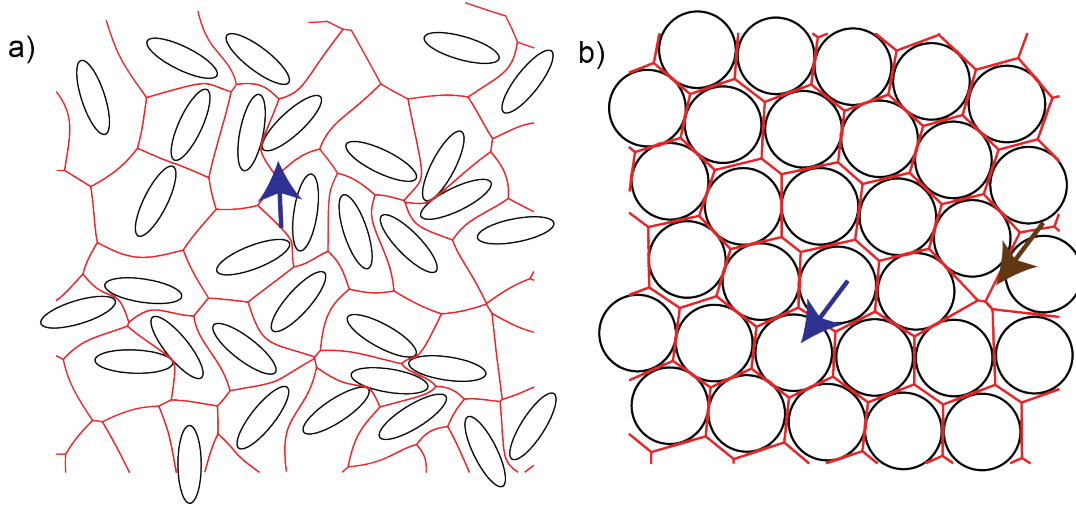


FIGURE 3.4: a) Voronoi tessellation calculated from randomly assembled ellipses. a) Ellipses with aspect ratio  $e = 0.3$  assembled at packing fraction  $\phi_g = 0.2$  b) Ellipses with aspect ratio  $e = 1$  assembled at packing fraction  $\phi_g = 0.8$  This figure was taken from reference [JL2].

Finally, we estimate correlation between two random variables  $X$  and  $Y$  represented by random samples  $\mathbf{x}$  and  $\mathbf{y}$ , by the Pearson correlation coefficient  $\rho$ ,

$$\rho = \frac{\sum_{i=1}^m (x_i - \bar{x})(y_i - \bar{y})}{\sqrt{\sum_{i=1}^m (x_i - \bar{x})^2} \sqrt{\sum_{i=1}^m (y_i - \bar{y})^2}} \quad (3.6)$$

where  $\bar{x}$  represents the mean of random sample  $\mathbf{x}$ .

## 3.3 Results

### 3.3.1 Area and perimeter of Voronoi cells

First of all, we analyse distributions of Voronoi cell area for all studied ellipse assemblies (Figure 3.5a). As we mentioned before, our simulations were set so that all of the area distributions have mean at unity. However, we can observe that with the increase of packing fraction  $\phi_g$ , area distributions are narrower. They do not depend on the aspect ratio of the assembled ellipses except at the highest concerned packing fraction  $\phi_g = 0.8$ . The previously mentioned phenomenon can also be noted by investigating standard deviations of cell area distributions (Figure 3.5b). Standard deviations, which decrease with  $\phi_g$ , have approximately the same values regarding different

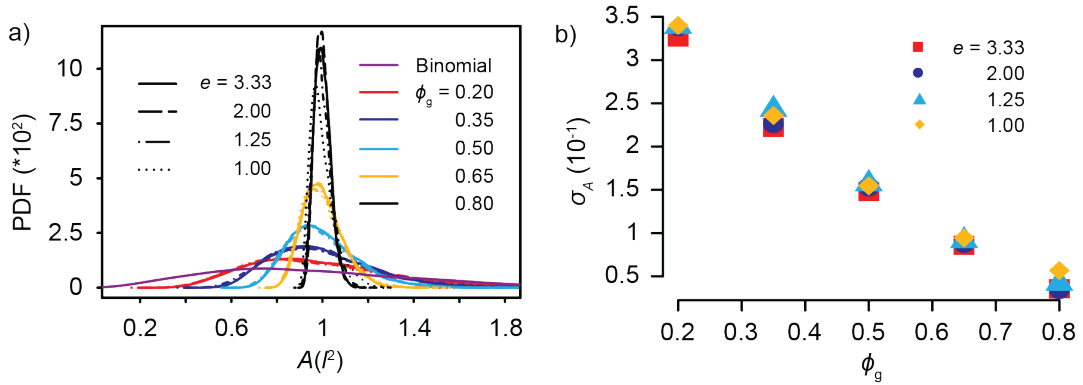


FIGURE 3.5: a) Distributions of Voronoi cell area calculated from ellipse assemblies and binomial (Poisson) point process. The average area is set to one in all systems. Packing fractions and ellipses shapes are denoted by the curve's colour and type, respectively. b) Standard deviations ( $\sigma_A$ ) of cell area distributions as a function of global packing fraction. Different symbols denote different shapes. This figure was taken from reference [JL2].

aspect ratios of ellipses at all packing fractions  $\phi_g < 0.8$ .

After observing the basic properties such as mean value and standard deviations of area distributions, we attempted to find the best probability model for the area distributions. Hence, as we stated in the reference [JL2]: "We find that generalised gamma distribution (Equation 3.2) fits Voronoi cell area nicely with parameter  $\tau \approx 1$  for most packings at packing fractions below 0.8. Therefore, we set parameter  $\tau = 1$  in our fits and in agreement with previous work on cell area distributions emerging from a Poisson process [65, 88, 91, 6], and ellipsoidal assemblies in 3D [130, 128], find gamma distributions in the bulk of the phase space ( $\phi_g < 0.8$  and all  $e$ ). In this regime, the  $\chi^2$  test typically gives  $p$ -values significantly larger than 0.1 and deviations between the fit and the sampled distributions have no structure (see Appendix A, Figures A.6-A.10 for details). Importantly, this level of significance is obtained only if all parameters of the gamma distribution fit ( $\alpha, \lambda, x_0$ ) are left free, allowing  $\alpha$  not to adopt integer values suggested previously [6]."

As we noticed in the previous paragraph, gamma distribution fits cell area distributions nicely in all systems except for disc ( $e = 1$ ) assemblies at packing fractions  $\phi_g = 0.8$ . This can be explained by the fact that the packing fraction of the system in question falls within the packing fractions where the jamming transition occurs ( $\phi_g = 0.82 \pm 0.02$  [16]). Thus, in those systems,

locally ordered patches appear (blue arrow in Figure 3.4b), which potentially cause irregularities in distributions that prevent us from finding an adequate probability model that fits area distributions.

Opposite of the cell area distributions, we find that cell perimeter distributions (Figure 3.6a) depend significantly on the aspect ratio of assembled ellipses even at packing fraction  $\phi_g > 0.2$ . Thus, we find that more elongated ellipses have on average greater cell perimeter (Figure 3.6c). This phenomenon becomes more evident as the packing fraction increases, meaning that as the packing fraction is greater, the Voronoi cells start to adopt the shape of the generating ellipse. Moreover, we find that with an increase of packing fraction, the perimeter distributions get narrower, meaning the Voronoi cells in systems have mutually more similar perimeter (Figure 3.6a,d,e). However, we find that widths of distributions do not depend significantly on the shape of assembled ellipses (Figure 3.6d,e). Furthermore, we also find that gamma distribution fits the cell perimeter distributions with good precision (see Appendix A, Figures A.11-A.15 for details). This property of the cell perimeter distribution follows the result that gamma distribution was found a good fit for the distribution of Voronoi cell perimeters for the Poisson point process [65, 88].

Besides the cell regular perimeter distributions, we studied the standardised perimeter distributions. The latter was obtained by subtracting the mean of the perimeter from each data point and dividing the result by the standard deviation of the same distribution. We found that such distributions do not differ much for most of the assemblies (Figure 3.6b). However, as we summarised in the reference [JL2]: "The exception is the significantly more positively skewed distribution for assemblies at high packing fraction (e.g.  $\phi_g = 0.8$ ). This suggests that a large number of cells associated with ellipse assemblies at high packing fraction have perimeters smaller than the average one, an effect that is most likely a result of counterbalancing the appearance of a small number of structural defects (holes), in a vicinity of which a small number of cells have areas larger than the average (brown arrow in Figure 3.4b)."

After studying Voronoi cell area and perimeter distributions, we investigated correlations between those two measures. Hence, the dependence of cell perimeter on cell area for individual cells is presented in Figure 3.7. We can see that presented data in both sub-plots of the Figure 3.7 follow dashed curves that denote dependence of hexagon perimeter on its area. Therefore,

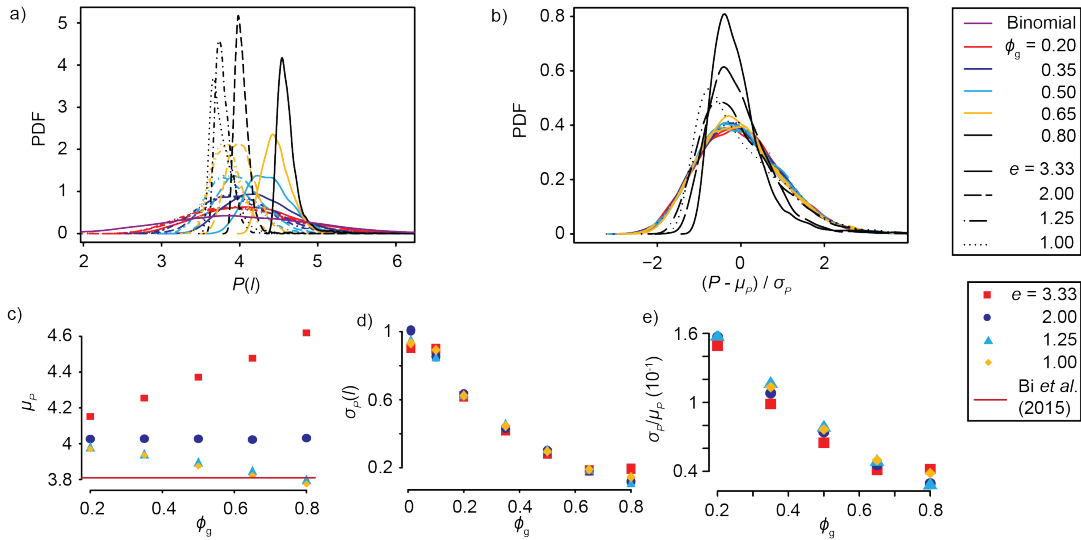


FIGURE 3.6: Characteristics of Voronoi cell perimeter distributions calculated from ellipse assemblies and binomial (Poisson) point process. In the top row packing fractions and shapes are denoted by the curve's colour and type, respectively. In the bottom row, different ellipse shapes are denoted by symbols. a) Distributions of cell perimeters. Given that the average area of Voronoi cells is set to one, the cell perimeter is equal to the isoperimetric ratio of the cell. b) Standardised distributions of the cell perimeter. c) Means ( $\mu_p$ ) of the Voronoi cell perimeter (isoperimetric ratio) distributions as a function of the global packing fraction. d) Standard deviations ( $\sigma_p$ ) of the cell perimeter (isoperimetric ratio) distributions as a function of the global packing fraction. e) Coefficients of variation of cell perimeter (isoperimetric ratio) distributions as a function of the global packing fraction. This image was taken from reference [JL2].

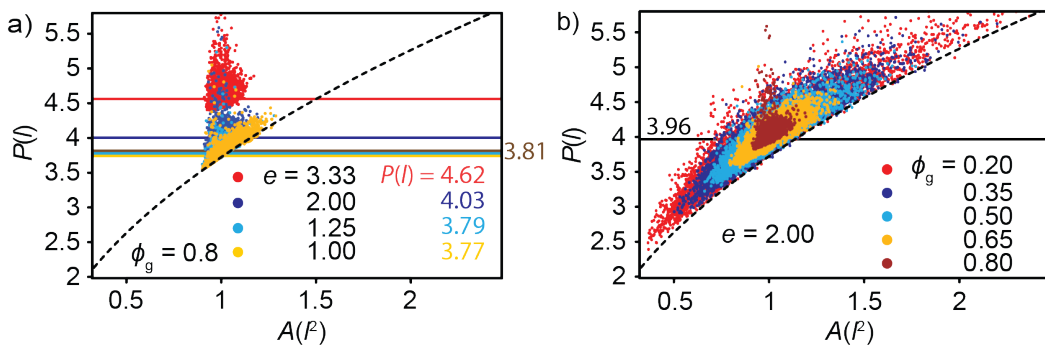


FIGURE 3.7: Correlations between cell area and cell perimeter. Each point represents one cell and displays cell perimeter as a function of cell area. a) Packing fraction is fixed,  $\phi_g = 0.8$  b) Ellipse aspect ratio is fixed,  $e = 2$ . The dashed curves represent the dependence of the hexagon perimeter on the hexagon area,  $P_{hex} = (8\sqrt{3}A_{hex})^{1/2}$ . The coloured solid lines represent the isoperimetric ratios of respective ellipses building the assembly.

This image was taken from reference [JL2].



the perimeters of cells in our assemblies also have square root dependence on cell area, which is expectable. Moreover, we can note that both aspect ratio and packing fraction influence the nature of the studied correlation. If we keep packing fraction fixed and plot data for different aspect ratios (Figure 3.7a), we can see that with the increase of ellipse aspect ratio, the clouds are representing data move away from the hexagonal curve. This distancing from the hexagonal curve suggests what we perceived by studying perimeter distributions, that more elongated ellipses have cells with a greater perimeter. Moreover, as the aspect ratio of assembled ellipses increases, the data clouds are wider but not longer. This phenomenon indicates that more elongated particles have a wider range of possible cell perimeters for a fixed area. Furthermore, if we fix the shape of the cells and study correlations between area and perimeter for different packing fractions (Figure 3.7b), we find that data clusters are less dispersed with an increase of packing fraction but still have the same centres. Because of that, at higher packing fractions, Voronoi cells have less accessible shapes than at lower packing fractions.

In addition to the previous discussion, we find that area and perimeter are strongly correlated for all studied assemblies simply because larger cells tend to have greater cell perimeter. Nonetheless, as we outlined in the reference [JL2]: "the correlations between  $A$  and  $P$  decrease with increasing the global packing fraction and the elongation of the particles. These results are contrasted by the correlations between the cell area and the so-called rescaled perimeters (square root of the isoperimetric ratio for each cell) (Fig. 3.9c). The latter are dimensionless numbers calculated by dividing the original perimeter of the cell with the square root of its area. In such a representation, the lower bound of the rescaled perimeter is 3.54, which is the rescaled perimeter of a circular object, while a hexagonal object would have a rescaled perimeter of 3.72. Interestingly, in most of the parameter space, we find weak negative correlations between the rescaled perimeter and the cell area, suggesting that larger cells are more hexagonal than smaller cells. This trend is clearly violated for disks packed at high global packing fractions (top right corner of the correlation matrix), where ordered domains, in which cells with high local packing fractions (cells smaller than average) adopt locally hexagonal structures (blue arrow in Figure 3.4b), occur."

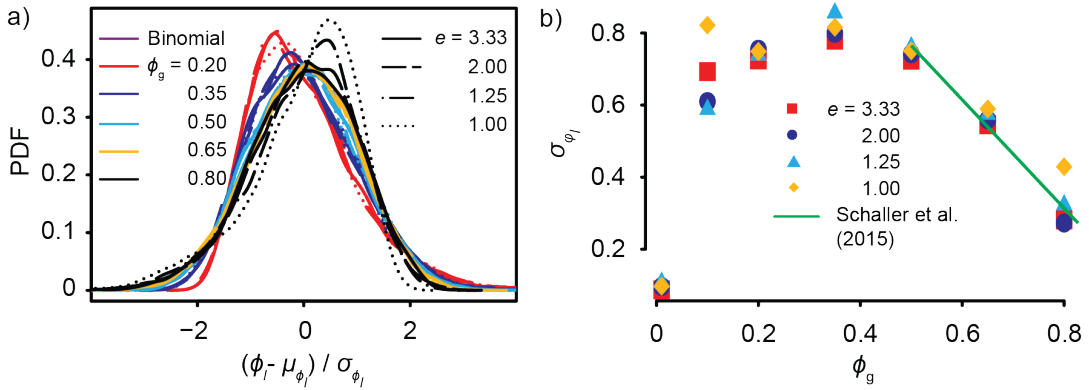


FIGURE 3.8: a) Standardized distributions of local packing fractions. Distributions overlap at global packing fractions  $\phi_g = 0.5, 0.65$  with p-values in range  $[0.02, 0.97]$ . Packing fractions and shapes of ellipses are denoted by colour and type of the curve, respectively. b) Standard deviations of local packing fraction distributions as a function of global packing fraction.

This figure was taken from reference [JL2].

### 3.3.2 Local packing fraction

Another interesting attribute of the system that we study is how particles occupy space locally. Measure that carries bulk of information about local arrangement is local packing fraction  $\phi_l$ , the latter defined as ratio of ellipse area  $A_E$  and corresponding Voronoi cell area  $A_V$  [130], i.e.:

$$\phi_l = \frac{A_E}{A_V}. \quad (3.7)$$

The local packing fraction can be considered as a local density of particles in the assembly.

In the reference [129], Schaller et al. report normality of the standardised local packing fractions distributions for jammed but disordered ellipsoids at global packing fractions  $\phi_g \in [0.55, 0.72]$  in 3D. Moreover, those distributions were found invariant to the shape of the packed particle and global packing fraction. In our systems, we find such overlap of standardized local packing fraction distributions only at intermediate packing fraction  $\phi_g = 0.5, 0.65$  (Figure 3.8a). Moreover, we find that concerning distributions become negatively skewed for assemblies of discs and oblate ellipses ( $e = 1.25$ ) at high packing fraction  $\phi_g = 0.8$ . Unlike in low-density assemblies (Appendix A, Figure A.1 and A.2), in dense systems, there are more cells with a value of local packing fraction that is greater than the average. Those cells are a repercussion of the local order in systems that yields higher local packing fraction values (blue arrow in Figure 3.4b). Furthermore, at low packing fraction

( $\phi_g = 0.2$ ), we find that standardised local packing fraction distributions are positively skewed (Figure 3.8a), meaning more cells have lower local packing fraction than average. Mentioned positive skewness can be explained by the fact that when two particles are close to each other at low packing fractions, their Voronoi cell area is greater than the average. Therefore, their local packing fraction is lower than the average (blue arrow in Figure 3.4a). Because of the previous findings regarding skewness of standardised local packing fraction distributions, we can conclude that concerned distributions deviate from normality.

Additionally, we studied fluctuations of the local packing fractions in our assemblies. Hence, as hypothesized in reference [JL2]: "The standard deviation of the distribution of local packing fractions  $\sigma(\phi_l)$ , due to homogeneity of standard deviation ( $\sigma(cK) = |c|\sigma(K), \forall c \in \mathbb{R}$ ) and the fact that our system is monodisperse becomes

$$\sigma(\phi_l) = \sigma\left(\frac{A_E}{A_V}\right) = A_E \sigma\left(\frac{1}{A_V}\right). \quad (3.8)$$

At small  $\phi_g$ , the assembly adopts a structure similar to that generated by a Poisson point process for which  $A_E = 0$ . Hence, as  $\phi_g \rightarrow 0$ ,  $\sigma(\phi_l) \rightarrow 0$ . On the other hand, at high  $\phi_g$ , as the maximum packing fraction is approached where  $\sigma\left(\frac{1}{A_V}\right) \rightarrow 0$ ,  $\sigma(\phi_l)$  decays nearly linearly (Fig. 3.8b). A maximum in the standard deviation of local packing fraction appears at  $\phi_g \simeq 0.35$ , at the crossover between trends associated with these two limits. This non-monotonous behaviour is contrasted by previously reported continuous linear decay of  $\sigma(\phi_l)$  as a function of  $\phi_g$  for assemblies of 3D oblate ellipsoids [129], although that study considered only mechanically jammed ellipsoid configurations, with a much smaller range of packing fractions."

### 3.3.3 Morphological measures of anisotropy

Morphological measures that we addressed earlier in this chapter, such as area and perimeter, are closely related to the size of the Voronoi cell. Therefore, if we want to investigate anisotropy, i.e. shape of the cells, we have to introduce additional measures. Therefore, as we pointed out in the reference [JL2]: "the most natural measure of anisotropy is the cell elongation, which is a ratio of the two principal moments of inertia calculated under the assumption of the uniform distribution of mass over the area. Furthermore, the analysis of the tessellations in epithelial tissues identified the standard deviation

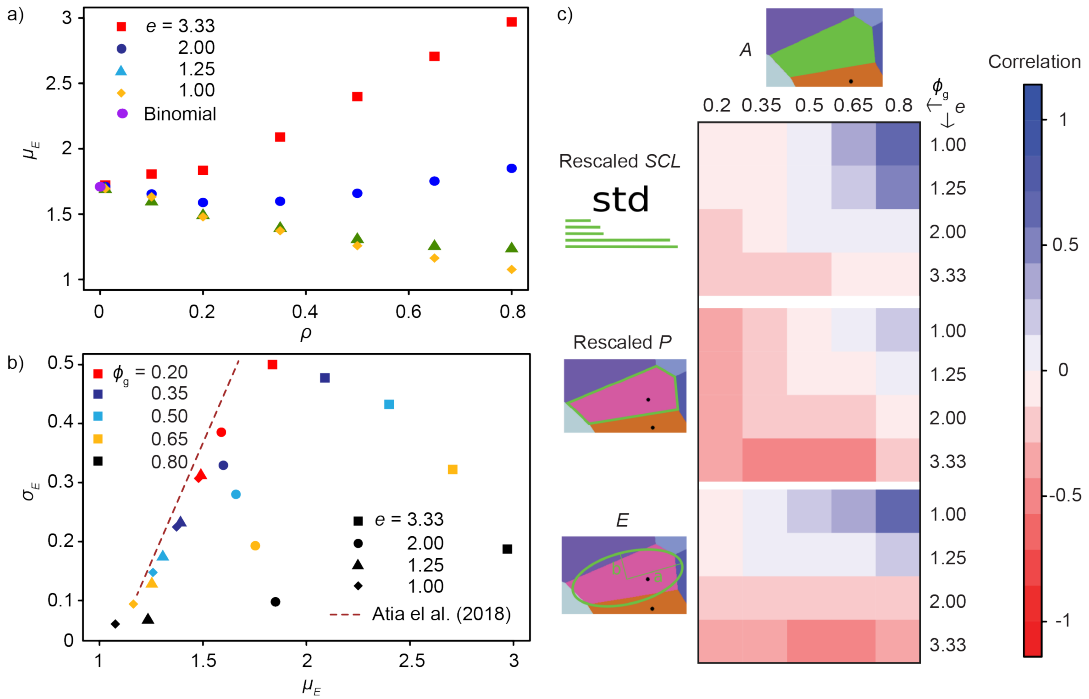


FIGURE 3.9: Elongation statistics and its correlations with other morphological measures of shape. a) Mean elongations for all of the considered ellipse assemblies. b) Relation between mean and standard deviation of elongation for all of the considered ellipse assemblies. Packing fractions are associated with a particular colour, while different symbols denote the shapes of ellipses. c) Correlations between the area and rescaled versions of morphological measures of shape. This image was taken from reference [JL2].

of contact lengths (SCL) as a measure that reflects the anisotropy of the tessellation [74]. Namely, because the contact length is a section of the perimeter shared by two neighbouring cells, and because the mean number of neighbours is approximately constant across the whole range of packing fractions, more elongated Voronoi cells have both short and long edges, which yields the greater standard deviation of contact lengths."

We can observe further evidence that concerned measures are referencing the shape of the cells from the fact that they are mutually positively correlated and by analysing their correlations with cell area. Hence, Figure 3.9c presents correlations of cell area to rescaled standard deviation of contact length, rescaled perimeter and elongation. We find that all three measures have similar correlations with cell area. Moreover, the nature of these correlations changes in the same manner across phase space of ellipse elongations and packing fractions. Thus, we find positive correlations for round particles

at high packing fraction ( $\phi_g = 0.8$ ). In contrast, we find negative correlations in the opposite side of phase space for highly elongated ellipses at low packing fractions.

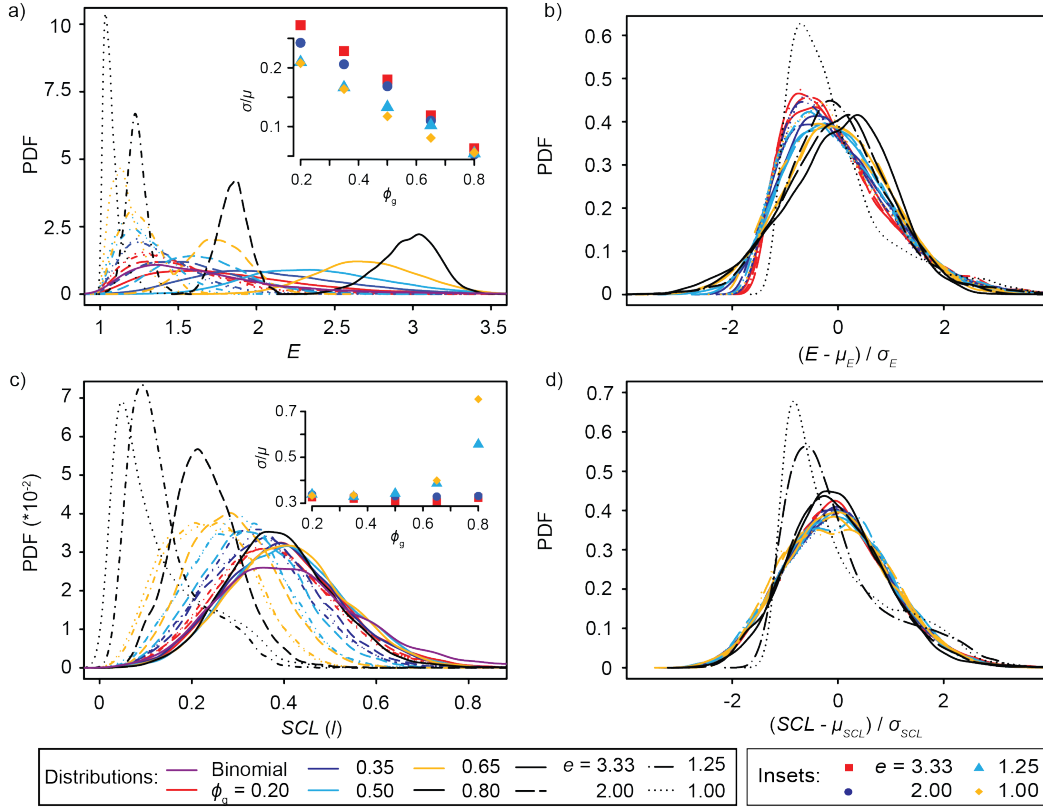


FIGURE 3.10: Regular and standardised distributions of cell anisotropy morphological measures. Colours indicate different packing fractions, while curve types denote different elongations of ellipses. a) Distributions of cell elongation. Insert shows coefficients of variation of cell elongation distributions. b) Standardised cell elongation distributions. c) Distributions of the standard deviation of contact length. Insert shows coefficients of variation of the standard deviation of contact length distributions. d) Standardised distributions of the standard deviation of contact length. This image was taken from reference [JL2].

Dependence of the mean shape of Voronoi cells on the global packing fraction was found in a study of 3D ellipsoid packings [130]. As we have formulated in reference [JL2]: "Our results in 2D show similar trends (Fig.3.9a). As the maximum packing fractions is approached for disks, the Voronoi cells adopt more isotropic hexagonal shapes resulting in a continuous decrease of mean elongation. The opposite trend is found for highly elliptical objects, suggesting that at higher densities, the shape of the cell and the generating

body become more alike. Actually, as  $\phi_g \rightarrow 0$ , mean cell elongations approach value for Poisson point process ( $\approx 1.71$  in 2D), and as  $\phi_g \rightarrow 1$ , mean cell elongation of Voronoi cells approaches the aspect ratio  $e$  of packed particles (Fig.3.9a)."

Furthermore, we investigated the relation between the mean and standard deviation of elongations because their linear relationship was reported in epithelial tissues [8]. However, just as we report in reference [JL2]: "it was not clear if this dependence is a result of an active regulation or merely a consequence of assembly of cell nuclei in a plane. In our random assemblies, we find that the standard deviation of elongation systematically decreases with the global packing fraction (at the constant shape of the packed objects, Figure 3.9b). As the shapes approach  $e \simeq 1.71$  from above, the standard deviation decreases with the mean elongation. However, once more circular shapes are used to generate assemblies ( $e < 1.71$ ), the standard deviation increases as a function of mean elongation (assemblies are more Poisson like), and a linear dependence is recovered, as a property of the average shape of the packed objects."

Atia et al.(2018) also suggest gamma density function as a probability model for cell elongation distributions [8]. We find that gamma distribution fits the elongation data well only at a low packing fraction  $\phi_g = 0.2$  irrespective of the particle shape. At packing fractions  $\phi_g > 0.35$ , we find that gamma distribution does not provide good fits to elongation data. However, suppose we fit a generalised gamma distribution with one additional parameter. In that case, we can recover negative skewness of elongation distributions for systems containing highly elongated ellipses at high packing fractions (for details, see Appendix A, Figure A.16).

Moreover, we studied the appearance of true and standardised distributions of morphological measures of anisotropy (Fig 3.10). We find that the true distributions (Figure 3.10a,c) become narrower as the packing fraction increases, which can also be concluded by inspecting a decreasing trend of their coefficients of variation (inserts in Figure 3.10a,c). Moreover, we observe that as the packing fraction increases, the effects of the ellipse aspect ratio become more and more pronounced. Hence, as the assembled particles are more elongated, their distributions of anisotropy are shifted more to the right, indicating that belonging Voronoi cells are also more elongated. Finally, we find that the standardised distributions of anisotropy measures

(Figure 3.10b,d) have the same behaviour as the standardised perimeter distributions (Figure 3.6b), which further points out the relation between these measures.

### 3.3.4 Geometric effects in the vicinity of jamming transition

Jamming of the hard elliptical particles in 2D has been characterised extensively in the past. It was found that systems with packing fraction  $\phi_g > 0.82$  are jammed independent of the shape of the particles. However, critical density was found to be higher for ellipses than circles [33, 39]. Recently, it was found that order parameters for the jamming are related to the shape of the Voronoi cells generated from the packings. This finding allows the study of jamming in particle systems by investigating measures that characterise the anisotropy of the Voronoi cells.

In that manner, the interplay between the geometry of the system and jamming was explored in the context of the vertex model, which minimises deviations of cell area and cell isoperimetric ratio in the systems from a target shape [17]. It was found that the isoperimetric ratio is an order parameter for jamming. Moreover, jammed structures have values below 3.81 which is the approximately isoperimetric ratio of a regular pentagon.

We have to point out that all of our data is strictly below the jamming transition limit, but as we reported in the reference [JL2]: "by focusing on assemblies with  $\phi_g = 0.8$  which are approaching jamming one can explore the geometric effects in the vicinity of the jamming transition. Notably, we find that Voronoi tessellations emerging from assemblies of discs and nearly-isotropic ellipses at this packing fraction have an average isoperimetric ratio below 3.81 (Figure 3.6c), and indeed, the hexagons are the most common shapes. This points to an interesting geometric correspondence between jamming in isotropic particulate systems and the standard vertex model, also noted before [17]. A more detailed analysis of particulate assemblies built from anisotropic particles shows, on the other hand, that the characteristic Voronoi cell of that assembly adopts shapes with the mean isoperimetric ratio approaching the isoperimetric ratio of the constitutive bodies, as the assembly comes close to the jamming transition. This is an indication that for packings of hard objects, there is no universal isoperimetric ratio of Voronoi cells that marks the jamming transition. On the other hand, if the underlying anisotropy of the packing is known, the mean isoperimetric ratio (Fig. 3.6c) as well as the mean elongation (Fig. 3.9a) of cells in the Voronoi tessellation,

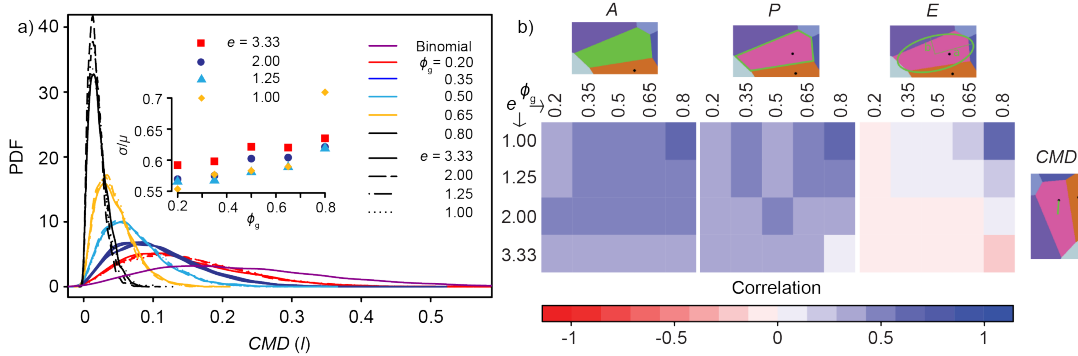


FIGURE 3.11: Distance between the centre of the ellipse and the centre of mass of its Voronoi cell ( $CMD$ ) calculated for all assemblies and binomial (Poisson) point process a) Distributions of  $CMD$  as a function of the packing fraction (denoted by colours), and elongation of ellipses (denoted by the curve type). Insert shows  $CMD$  coefficients of variation as a function of the global packing fraction (different symbols denote ellipse aspect ratios). b) Correlations between  $CMD$  and cell area, perimeter and elongation. This image was taken from reference [JL2].

become good candidates for simple geometric parameters of jamming. Like the parameters suggested earlier [109], both capture the anisotropy of the constitutive particle, and their standard deviation drops significantly (Figures 3.6d and 3.9b), pointing to a broader class of measures that should have a tendency to saturate at jamming."

### 3.3.5 Centre of mass distance

Another important morphological measure that we examine is the distance between the centre of the ellipse and the centre of mass of its Voronoi cell ( $CMD$ ). As we have commented in previous chapters of this thesis,  $CMD$  carries essential information about the order in the system. Thus, if points of a point process are distributed randomly, this will result in wide distributions of  $CMD$  (purple curve in Figure 3.11a). On the other side, if concerned systems are orders, such as crystal structures, the centres of particles and Voronoi cells coincide, resulting in distribution with only one delta peak.

In our systems of random assemblies, we find that  $CMD$  distributions depend primarily on the global packing fraction (Figure 3.11a). Thus, as the global packing fraction increased, the distributions became narrower and shifted closer towards zero. On the other hand, we find that  $CMD$  is positively correlated with the area and perimeter, meaning that larger cells have, on average greater  $CMD$  value (Fig. 3.11b). Moreover, we notice that  $CMD$



and elongation are not correlated significantly except for disk assemblies at high packing fraction ( $\phi_g = 0.8$ ), which the defects in regular hexagonal assembly can explain (brown arrow in Figure 3.4b).

### 3.3.6 Neighbourhood statistics and the relation between geometry and topology in ellipse assemblies

The last morphological measure that we examine is the number of neighbours of the Voronoi cell. Unlike the previously studied ones, the number of neighbours is a topological measure that captures only the geometrical properties of systems. By observing distributions of the number of neighbours (Figure 3.12a), we find that distributions become narrower, just like the distributions of other morphological measures. Moreover, we systematically find more cells with 5 neighbours than with 7 neighbours in our assemblies. This property that implies positive skewness of distributions allows us to fit discrete version of gamma distribution with great statistical accuracy for all assemblies except at packing fraction  $\phi_g = 0.8$  where cells with 6 neighbours dominate in the appearance of distributions.

Furthermore, we explore relation between geometry and topology in random assemblies of ellipses by reproducing two famous laws. The first of them is the Lewis' law [92, 93, 26, 80] which predicts a linear dependence of the mean area of cells with  $n$  neighbours  $\mu_{A(n)}$  on the number of neighbours  $n$  following the formula:

$$\mu_{A(n)} = \mu_A [1 + a(n - 6)]. \quad (3.9)$$

where  $a$  is a free parameter.

Similarly, Desch's law [35, 123] suggests linear relationship between the mean perimeter of cells with  $n$  neighbours  $\mu_{P(n)}$  and number of neighbours  $n$  in manner:

$$\mu_{P(n)} = \mu_P [1 + b(n - 6)], \quad (3.10)$$

where  $b$  is a free parameter. These laws suggest a positive correlation between area and perimeter to the number of neighbours meaning that the cells with more neighbours are larger on average.

Moreover, as we mention in reference [JL2]:" In assemblies of ellipses, we observe that Lewis' and Desch's laws (Fig. 3.12b,c) have the same range of

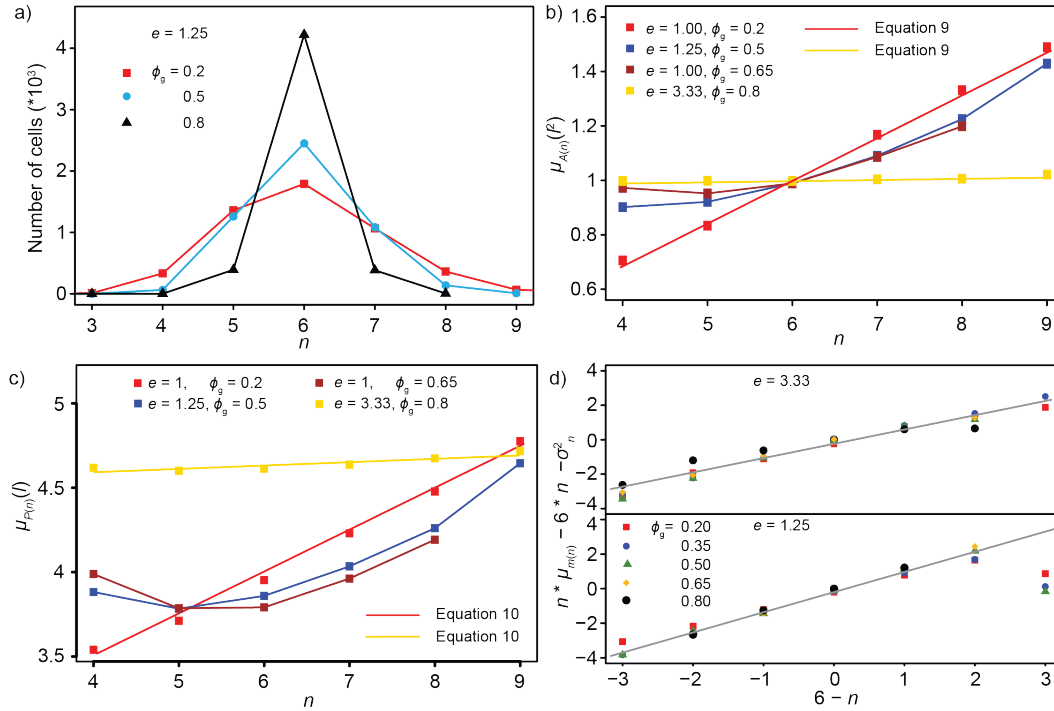


FIGURE 3.12: Number of neighbours as a morphological measure and its correlations. a) Histograms of number of neighbours for ellipses of aspect ratio  $e = 1.25$ . Different colours and symbols represent different global packing fractions. b) Representation of Lewis' law in different parts of the studied space of ellipse aspect ratios and packing fractions. Symbols denote data points while red and yellow lines are linear fits to data using Equation 3.9. Brown and blue curves are guidance for the eye. c) Representation of Desch's law in different parts of the studied ellipse aspect ratios and packing fractions. Symbols denote data points while red and yellow lines are linear fits to data using Equation 3.10. Brown and blue curves are guidance for the eye. d) Aboav-Weaire's law for ellipses with  $e = 3.33$  (top graph) and  $e = 1.25$  (bottom graph). Different symbols denote different packing fractions, while the grey line represents a fit using Equation 3.11.

validity. This is, of course, promoted by the strong positive correlations between the cell area and cell perimeter. Specifically, at low packing fractions and independent of particle shape, strong linear dependence (e.g.  $e = 1$  and  $\phi_g = 0.2$  in Fig. 3.12b) can be confirmed in agreement with previous reports [92, 93]. Indeed, it is possible to observe in those assemblies that cells with more neighbours have, on average greater cell area and perimeter (Appendix A, Figure A.1b,c). However, deviations from the Lewis' and Desch's laws is confirmed at intermediate packing fractions ( $\phi_g = 0.5, 0.65$ ), where the data are more consistent with a quadratic, rather than a linear relation (Fig. 3.12b,c). This second order dependence was also predicted by calculating the

probabilities of establishing a certain size and the certain number of neighbours [80]. Interestingly, however, the average area and the perimeter of the cell become, by and large, independent of the neighbourhood for highly elongated particles at high packing fractions (e.g.  $e = 3.33$  and  $\phi_g = 0.8$  in Fig. 3.12b,c). Consequently, Lewis' and Desch's laws are recovered but with no statistically significant slope. This effect is exemplified in Appendix A, Figure A.5a showing an assembly containing a cell with 8 and 4 neighbours, both having nearly equal areas and perimeters. It is important to notice that this result is a consequence of the set Voronoi tessellation. Actually, linear dependence with a strong slope is recovered for the centre-of-mass based tessellation performed on the same data set (Appendix A, Figure A.17), as suggested previously [92, 80]."

Last but not least, we study the Aboav-Weaire's law [2, 1, 156] which implies that cells with a fewer number of neighbours have neighbours with more neighbouring cells than the average, and vice-versa. Aboav-Weaire's law is given by the formula:

$$\mu_{m(n)} = 6 - \gamma + (6\gamma + \sigma_n^2)/n. \quad (3.11)$$

where  $\mu_{m(n)}$  is the average number of neighbors of cells adjacent to ones that have  $n$  neighbors,  $\sigma_n^2$  is the variance of number of neighbours distribution and  $\gamma$  is a constant that can decrease as  $\sigma_n^2$  increases [21, 153] or be independent of  $\mu_{m(n)}$  [127].

As we point out in reference [JL2]: "Current analysis shows a relatively large range of validity of the Aboav-Weaire's law, with  $\gamma$  being independent of  $\sigma_n^2$  (which decreases with  $\phi_g$ ), but sensitive to the elongation of the packed ellipses (Figure 3.12d). Deviations from Aboav-Weaire's law become more important for strongly elongated packed objects at high packing fractions (circular symbols in the top panel of Figure 3.12d). Furthermore, for discoid shapes, strong departures from linearity are observed for  $n > 8$  (bottom panel of Figure 3.12d)."

### 3.4 Conclusion

This chapter provides a systematic overview of geometrical and topological properties of random ellipse assemblies by investigating selected morphological measures such as area, perimeter, elongation, the standard deviation

of contact lengths, CM distance and number of neighbours. We studied their distributions and found that the packing fraction highly influences ellipse assemblies in the way that at higher densities, variability of possible Voronoi cell geometries decreases. Moreover, we studied correlations between morphological measures and found that some measures can be classified so that they provide the same information about the anisotropy of structures. By observing those measures in the context of previous work [17], we conjectured that measures of shape are good candidates for order parameters of jamming transition in hard particle systems.

We believe that our study motivates further possible research questions. Thus, it would be of great interest to investigate the effects of ellipse aspect ratios on assemblies' geometry more closely. Such a study can be done by studying polydisperse ellipse assemblies where shapes of the assembled particles follow a more complex distribution. Furthermore, we believe that study presented in this chapter could be a valuable guideline for the investigation of systems composed of particles with even more complex shapes than ellipses. Moreover, as we discussed in the reference [JL2]: "We hope, furthermore, that our work will provide a framework for the analysis of assemblies with more complex interactions, which are now starting to be investigated. Notably, by comparison with data generated with a variety of methods and in experimental systems of different origin [8, 33, 92, 6, 130], several key observations are recovered in the matching parameter space, which suggests that the average quantities associated with the tiling are not extremely sensitive to the means of production. As such, the results presented herein could be relevant not only to assemblies of soft objects but also active particles [136, 162, 102, 103, 32]. In the latter case, it is very important to delineate the geometric effects of density and shape, which have been meticulously studied herein, from the effects of the activity."

Following the previous paragraph, the results presented in this chapter helped us understand the nature of the random ellipse assemblies that will be used as an initial configuration for studying solutions of the Quantizer problem via Lloyd's algorithm. Thus, the effects of the Quantizer minimisation will be easier to distinguish in the following pages of this thesis.

## Chapter 4

# Quantization of the ellipse assemblies

### 4.1 Introduction

As we presented in Chapter 1 of this thesis, one of the most exciting assets of the Quantizer problem is the hyperuniformity of its optimal states. This hyperuniformity of Quantizer minima is governed by the centralization procedure of Lloyd's algorithm. In the past, hyperuniformity was found in systems of non-trivial particles that are in some sense optimal[40, 95, 87]. Therefore, it is essential to understand what processes are responsible for the hyperuniformity of such non-trivial systems. Because of that, we aim to modify the Quantizer problem so that it generalizes to systems of non-trivial particles (volume greater than 0) and study long-range density fluctuations in the context of solutions of the newly modified Quantizer problem. Since Lloyd's algorithm solves the Quantizer problem for point processes, we will focus on modifying it in a way that applies to systems of non-trivial particles. We have decided to study ellipse assemblies among two-dimensional particle systems that could be interesting to investigate in the mentioned context, motivated by Chapter 3 of this thesis. Ellipses possess a desirable property of covering a broad range of shapes only by tuning one parameter (aspect ratio) that makes the effects of the particle shape on the process of quantization simple to address.

#### 4.1.1 Modified Quantizer problem

As we pointed out in the Introduction chapter, solving the Quantizer problem in the case of point generators is equivalent to minimizing the Quantizer energy  $E_Q$  or the total energy of the system,  $E_t$ . Therefore, to generalize the

problem of quantization to ellipse assemblies, we will modify the total energy  $E_t$  accordingly.

In the introduction of this thesis, we defined the total energy  $E_t$  as a normalized sum of the integrals over Voronoi cells, where the sub-integral function is the squared distance between an arbitrary point and Voronoi cell generator. Therefore, a central role in minimizing total energy  $E_t$  is taken by the distance between arbitrary points inside the Voronoi cell and the generator object. In case of point generators in 2-dimensional space, that distance function used is the standard Euclidean distance, i.e.  $\|\mathbf{x} - \mathbf{y}\| = \sqrt{(x_1 - y_1)^2 + (x_2 - y_2)^2}$ . Therefore, to modify the total energy  $E_t$  to the case of non-trivial area generators (in our case, ellipses), we have to specify a function that provides a distance between a point in space and an arbitrary object with a non-zero area. Intuitively, a natural candidate for distance to an arbitrary object in space is the shortest distance to any part of that object. Precisely, if  $O$  is subset of a space, then the distance between a point  $\mathbf{x}$  and  $O$  is given by  $\|\mathbf{x} - O\| = \inf_{\mathbf{y} \in O} \|\mathbf{x} - \mathbf{y}\|$  where  $\inf$  is infimum of a set. In the literature, distance function  $\|\mathbf{x} - O\|$  is also referred to as the Euclidean distance function because it is equal to standard Euclidean distance when  $O$  is a point. It is worth mentioning that in the definition of Euclidean distance  $\|\mathbf{x} - O\|$  infimum of standard Euclidean distances is preferred to the minimum of standard Euclidean distances in order to allow set  $O$  to be both opened and closed. If the maximum function was used instead of infimum, then  $\|\mathbf{x} - O\|$  would not be well defined if  $O$  is an open set. The previously mentioned claim is true because the maximum of a continuous function on an arbitrary set  $O$  is guaranteed to exist only if  $O$  is compact and, following that, a closed set.

Now, when we understand the concept of a distance between point and set, we can modify the total energy of a system  $E_t$  in a way that it addresses assemblies of arbitrary particles  $P = \{P_i, i = 1, \dots, n\}$  contained in  $\Omega \subset \mathbb{R}^d$ , with volume  $V(\Omega)$  and mass density  $\rho(\mathbf{x}) = 1, \forall \mathbf{x} \in \mathbb{R}^d$ . Thus, the modified dimensionless rescaled total energy of such system is given with:

$$E_T(\mathcal{V}, P) = \frac{n^{\frac{2}{d}}}{dV(\Omega)^{1+\frac{2}{d}}} \sum_{i=1}^n \int_{\mathcal{V}_i} \|\mathbf{x} - P_i\|^2 d\mathbf{x} \quad (4.1)$$

where  $\mathcal{V} = \{\mathcal{V}_i, i = 1, \dots, n\}$  are Voronoi cells generated by  $P$ .

Motivated by the previous definition, we can define the modified Quantizer problem as an optimization of the modified total energy  $E_T$ . This way, we aim to minimize the total distance between points inside Voronoi cells and non-trivial generator particles, which expands the idea of solving the classical Quantizer problem. Although the intuition behind the definition of the modified Quantizer problem is evident, due to the complexity of sub-integral function  $\|\mathbf{x} - P\|$  when  $P$  has an arbitrary shape, it is vague how theoretical result as in case of classical Quantizer problem can be derived [56, 43].

Nonetheless, the special case when we consider  $P$  to be a sphere of radius  $r$  positioned at  $\mathbf{x}_0$  can help us to understand the modified total energy  $E_T$  more in detail. Then, for an arbitrary position  $\mathbf{x} \in \mathbb{R}^d$  we can simply derive that

$$\|\mathbf{x} - P\| = \|\mathbf{x} - \mathbf{x}_0\| - r. \quad (4.2)$$

Because of that, a sub-integral function in Equation 4.1 (function from Equation 4.2 squared) becomes

$$\|\mathbf{x} - P\|^2 = \|\mathbf{x} - \mathbf{x}_0\|^2 - 2r\|\mathbf{x} - \mathbf{x}_0\| + r^2. \quad (4.3)$$

Further, we can evaluate the modified total energy  $E_T$  in the following way:

$$E_T(\mathcal{V}_P, P) = \frac{1}{dV(\mathcal{V}_P)^{1+\frac{2}{d}}} \int_{\mathcal{V}_P} \|\mathbf{x} - P\|^2 d\mathbf{x} \quad (4.4)$$

$$= \frac{1}{dV(\mathcal{V}_P)^{1+\frac{2}{d}}} \int_{\mathcal{V}_P} \left( \|\mathbf{x} - \mathbf{x}_0\|^2 - 2r\|\mathbf{x} - \mathbf{x}_0\| + r^2 \right) d\mathbf{x} \quad (4.5)$$

$$= \frac{1}{dV(\mathcal{V}_P)^{1+\frac{2}{d}}} \int_{\mathcal{V}_P} \|\mathbf{x} - \mathbf{x}_0\|^2 d\mathbf{x} - \frac{2r}{dV(\mathcal{V}_P)^{1+\frac{2}{d}}} \int_{\mathcal{V}_P} \|\mathbf{x} - \mathbf{x}_0\| d\mathbf{x} \quad (4.6)$$

$$+ \frac{r^2}{dV(\mathcal{V}_P)^{1+\frac{2}{d}}} \int_{\mathcal{V}_P} d\mathbf{x} \\ = E_t(\mathcal{V}_P, \mathbf{x}_0) - \frac{2r}{dV(\mathcal{V}_P)^{1+\frac{2}{d}}} \int_{\mathcal{V}_P} \|\mathbf{x} - \mathbf{x}_0\| d\mathbf{x} + \frac{r^2}{dV(\mathcal{V}_P)^{\frac{2}{d}}} \quad (4.7)$$

In the previous set of equations, Equation 4.4 follows from Equation 4.1 and Equation 4.5 is consequence of Equation 4.3. Moreover, Equation 4.6 is valid because integral is a linear operator and Equation 4.7 follows from the definition of total energy  $E_t$  and the fact that  $V(\mathcal{V}_P) = \int_{\mathcal{V}_P} d\mathbf{x}$ .

Equation 4.7 shows a relation between the modified total energy  $E_T$  and classical total energy  $E_t$ . If we set  $r = 0$  i.e. if  $P$  is a point with coordinates  $\mathbf{x}_0$ , then  $E_T = E_t$  which means that  $E_T$  can be considered as a generalization  $E_t$ . We can also see that the modified total energy  $E_T$  depends on sphere radius  $r$ , implying that  $E_T$  depends on the size of the circle and consequently on the packing fraction of the assembly. Moreover, it is difficult to derive more complex analysis of  $E_T$  from the previous equations because of the unclear interplay between terms  $E_t(\mathcal{V}_P, \mathbf{x}_0)$  and  $\int_{\mathcal{V}_P} \|\mathbf{x} - \mathbf{x}_0\| d\mathbf{x}$ . It is important to emphasize that previous analysis is done only for the case when the system consists of only one circle  $P$ . Thus, further study of  $E_T$  for more complex systems has to be done numerically.

### 4.1.2 Calculation of the modified total energy

Calculation of total energy for point systems is an exact and straightforward task due to the nice representation of the integral in the total energy formula with Minkowski tensors[134] (Introduction, Equation 1.19). However, such or similar representation of the integral from the Equation 4.1 is challenging to obtain because of the more complicated form of a sub-integral distance function. Hence, in the following lines, we will describe how we calculated numerically integral from the Equation 4.1 in 2-dimensional space when ellipses are considered particles.

In that sense, to calculate concerned integral, we have to calculate squared distance between ellipse  $P = \{\mathbf{y} = (y_1, y_2) \in \mathbb{R}^2 : \frac{y_1^2}{a^2} + \frac{y_2^2}{b^2} \leq 1\}$  and arbitrary point  $\mathbf{x} = (x_1, x_2)$  that is not part of the ellipse  $E$  (otherwise trivially  $\|\mathbf{x} - P\|^2 = 0$ ). Without loss of generality, we can assume that the ellipse is positioned at the origin of the coordinate system with major and minor axis collinear with the coordinate axis. Indeed, such configuration can always be achieved by rotating and translating point and ellipse while preserving all of



the distances in the system. Taking into count previous assumption we have:

$$\|\mathbf{x} - P\|^2 = \left( \inf_{\mathbf{y} \in P} \|\mathbf{x} - \mathbf{y}\| \right)^2 \quad (4.8)$$

$$= \inf_{\mathbf{y} \in P} (\|\mathbf{x} - \mathbf{y}\|)^2 \quad (4.9)$$

$$= \inf_{(y_1, y_2) \in P} (x_1 - y_1)^2 + (x_2 - y_2)^2 \quad (4.10)$$

$$= \min_{(y_1, y_2) \in P} (x_1 - y_1)^2 + (x_2 - y_2)^2 \quad (4.11)$$

$$= \min_{t \in [0, 2\pi]} (x_1 - a \cos t)^2 + (x_2 - b \sin t)^2 \quad (4.12)$$

Here, equality 4.9 stands because  $f(x) = x^2, x \in \mathbb{R}$  is a monotonic function for positive  $x$ , and equality 4.11 is valid because ellipse is a compact set. Therefore a continuous function achieves minimum on it. Equality 4.12 is a consequence of the fact that from an arbitrary point, the closest point of the ellipse has to be on the edge of an ellipse, which is parametrized with  $\{(a \cos t, b \sin t), t \in [0, 2\pi]\}$ .

Further, Fermat's Theorem provides necessary condition for minimum of a function:

$$\frac{d((x_1 - a \cos t)^2 + (x_2 - b \sin t)^2)}{dt} = 0. \quad (4.13)$$

After applying derivative to the previous equation, we obtain a trigonometric equation:

$$ax_1 \sin t - bx_2 \cos t + (b^2 - a^2) \sin t \cos t = 0. \quad (4.14)$$

The obtained trigonometric equation can be solved using trigonometric identity  $\cos t = \sqrt{1 - \sin^2 t}$  which gives:

$$ax_1 \sin t - bx_2 \sqrt{1 - \sin^2 t} + (b^2 - a^2) \sin t \sqrt{1 - \sin^2 t} = 0. \quad (4.15)$$

After squaring and transforming the previous equation, we obtain the following trigonometric polynomial equation:

$$(b^2 - a^2)^2 \sin^4 t - 2(b^2 - a^2)bx_2 \sin^3 t + (a^2 x_1^2 + b^2 x_2^2 - (b^2 - a^2)^2) \sin^2 t + 2(b^2 - a^2)bx_2 \sin t - b^2 x_2^2 = 0. \quad (4.16)$$

Real solutions of the former equation give us candidates for a minimum

of a distance function. After that, we calculate values of the distance function for each of that real solution, and the lowest of those values is our desired minimum of a distance function.

Previous procedures give us an efficient way to evaluate sub-integral function in the Equation 4.1 at any desired point. In order to evaluate integral in the total energy equation, we construct a mesh over the Voronoi cell and calculate the value of the distance function at every point of the mesh. Values of the distance function of the mesh points inside the ellipse are set to 0. After that, we calculate the integral in the total energy equation using the trapezoidal integral formula.

### 4.1.3 Modified Lloyd's algorithm

In order to study solutions of the modified Quantizer problem on elliptical particles, it is crucial to find an acceptable method that will generate structures with desired properties. Since effective quantization of point processes, as it was described earlier, can be achieved by Lloyd's algorithm, it would be ideal for applying the same method to ellipse assemblies. Since ellipses are bodies with the non-trivial area while translating ellipses to centres of mass of its Voronoi cells, Lloyd's algorithm would yield overlap between particles. For that reason, we propose a modification to Lloyd's algorithm that solves the issue with the overlap of the ellipses.

After the step of Lloyd's algorithm, when we move ellipses to centres of mass of their Voronoi cells, in order to remove overlaps between ellipses in the system, we "shake" the whole system. We shake the system by moving and rotating ellipses in the assembly. Due to computational simplicity, we randomly sample the translations and rotations of ellipses and accept them only if the total overlapping condition is being optimized, i.e. if the total overlap area of ellipses does not increase. We perform the shaking step as specified in the packing algorithm introduced in Chapter 3 of this thesis.

Therefore, the obtained algorithm can be formalized through the following steps:

1. Input of the algorithm is an assembly of ellipses  $\{P_i, i = 1, \dots, n\}$  contained in a square simulation box  $B$  with periodic boundary conditions.
2. The set Voronoi diagram  $\mathcal{V}$  (definition in Chapter 3) is calculated with assembled ellipses  $P_i$  as the generators of Voronoi cells.

3. For each Voronoi cell  $\mathcal{V}_i$  a centre of mass  $\mathbf{z}_i$  is calculated.
4. Each centre of ellipse  $P_i$  is replaced by the centre of mass  $\mathbf{z}_i$  of its Voronoi cell  $\mathcal{V}_i$ .
5. If any two ellipses overlap, an ellipse is randomly selected from a system. The selection is performed so that all ellipses have the same probability of being chosen, no matter if they overlap. After that, the chosen ellipse is moved and rotated randomly. The movement is sampled independently in  $x$  and  $y$  direction, both from the uniform distribution on the interval  $[-\frac{b}{2}, \frac{b}{2}]$  where  $b$  is semi-minor axis of the ellipse. The rotation angle is sampled from the uniform distribution on the interval  $[0, \pi]$ . The movement and rotation for selected ellipses are accepted if the total overlap is not increased. The procedure of selecting, moving and rotating an ellipse is repeated until there are no intersecting ellipses in the assembly (total overlap equals 0 in double precision).
6. If the desired number of iterations is not reached, then steps beginning with step 2 are iteratively repeated. Else, the algorithm is terminated, and the current assembly is given as an output.

Given that the proposed algorithm differs from classical Lloyd's algorithm, it will be referred to as the modified Lloyd's algorithm due to its motivation and considerable similarities to the original algorithm.

The proposed algorithm should be effective in annulling overlaps. After a certain number of ellipse translations and rotations, all the overlaps will be removed from the system due to constant optimization of the total overlap area. However, the modified Lloyd's algorithm for ellipses has a few limitations to address. The first and most fundamental question is whether modified Lloyd's algorithm solves the modified Quantizer problem for ellipses. It is not clear if it introduces any novelties when applied to ellipse assembly because there is a possibility that "shaking" from step 5 of modified Lloyd's algorithm cancels out centralizing step of the algorithm and therefore introduces no change to the initial structure.

A further question is the robustness of the obtained results to the values of hyperparameters (parameters whose values we set before execution of the algorithm). An especially interesting hyperparameter is the length of ellipse movement towards Voronoi centres of mass. It is worth exploring if the movement for a certain fraction of a distance rather than for total distance

in modified Lloyd's iteration would yield the same structural properties of obtained systems.

## 4.2 Simulations

We apply modified Lloyd's algorithm to random assemblies of ellipses presented in Chapter 3 of this thesis. Those systems cover a broad range of differently shaped ellipses assembled at various packing fractions. The number of assembled ellipses varies between assemblies due to the speed limitations of our simulator. Thus, our simulator takes more time to produce output if the ellipses are more elongated and the packing fraction is higher. Therefore, at low packing fractions ( $\phi_g = 0.2, \dots, 0.5$ ) our assemblies contain 1000 ellipses, when packing fraction  $\phi_g = 0.65$  assemblies have 400 or 500 ellipses and at highest packing fraction  $\phi_g = 0.8$  we assemble 200 ellipses. We choose a number of runs so that for every assembly in the phase space, we have 10000 data points (10000 ellipses together).

We execute modified Lloyd's algorithm until it reaches a convergence which typically takes place in less than 1000 iterations.

## 4.3 Convergence of the modified Lloyd's algorithm

### 4.3.1 Modified total energy

In order to address the convergence of modified Lloyd's algorithm, we can visualize ellipse assemblies before and after application of 1000 modified Lloyd's iterations (Figure 4.1). Figures 4.1a and 4.1b present the appearance of ellipse assemblies under modified Lloyd's iterations at low packing fraction. Before application of any iterations (Figure 4.1a), the ellipses are randomly assembled without regularity. On the other side, after the application of 1000 iterations, the assembly is highly ordered, with ellipses being well organized in terms of their positions in the system. Such ordered structure already appears after around 100 Lloyd's iterations and does not change for the remainder of the simulation. On the other side, Figures 4.1c and 4.1d present system at higher packing fraction where ellipse assemblies do not change their appearances significantly under modified Lloyd's iterations. Same as within random assembly of ellipses (Figure 4.1c), after 1000 modified Lloyd's iterations (Figure 4.1d), ellipses in the system are randomly positioned with

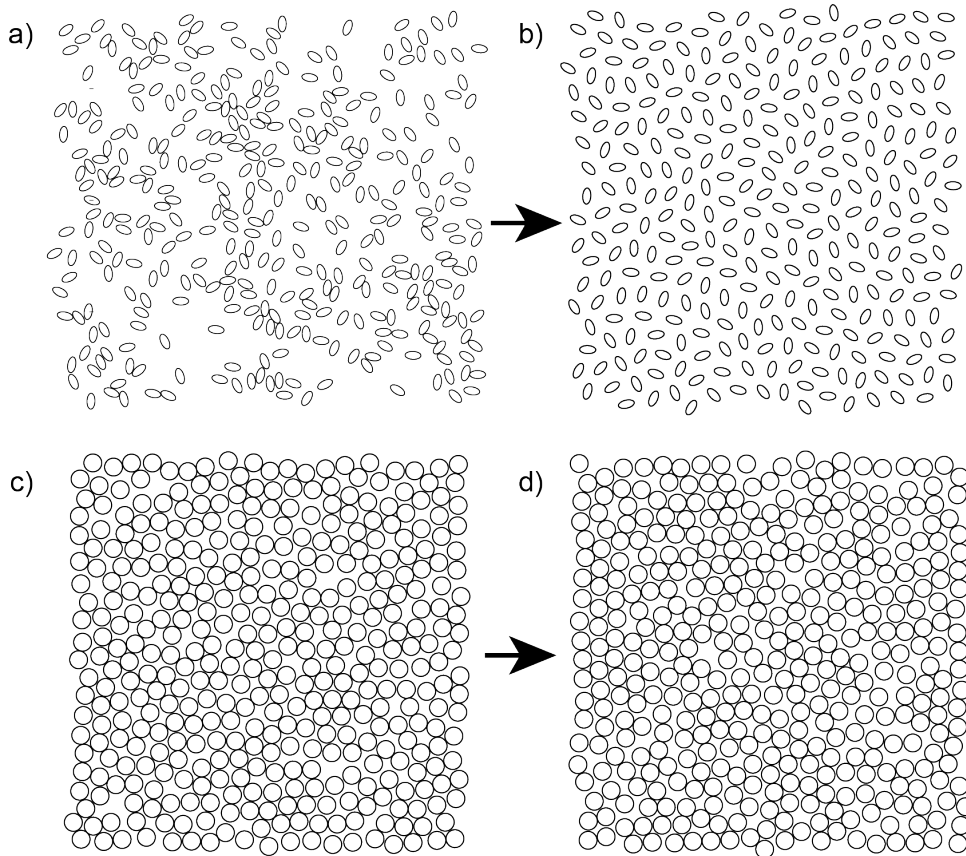


FIGURE 4.1: Assemblies of ellipses before and after application of 1000 modified Lloyd's iterations. Ellipses with aspect ratio  $e = 2$  assembled at packing fraction  $\phi_g = 0.2$  before (a) and after (b) application of modified Lloyd's algorithm. Ellipses with aspect ratio  $e = 1$  assembled at packing fraction  $\phi_g = 0.65$  before (c) and after (d) application of modified Lloyd's algorithm.

no signs of the organization such as it was presented in Figure 4.1b.

In pursuance of further investigation of convergence of modified Lloyd's algorithm for ellipses and, more fundamentally, determining if the proposed algorithm introduces any structural change into the system, we studied behaviours of the modified total energy  $E_T$  during modified Lloyd's iteration. The first notable phenomenon that we observe are two distinct regimes that total energy exhibits during iterations of modified Lloyd's algorithm (Figure 4.2).

In the first of those two regimes, the modified total energy follows a curve that decreases rapidly in roughly the first 100 iterations. It then oscillates around reached value in remaining modified Lloyd's iterations (Figure 4.2a). Those oscillations are small with a high correlation between values of the

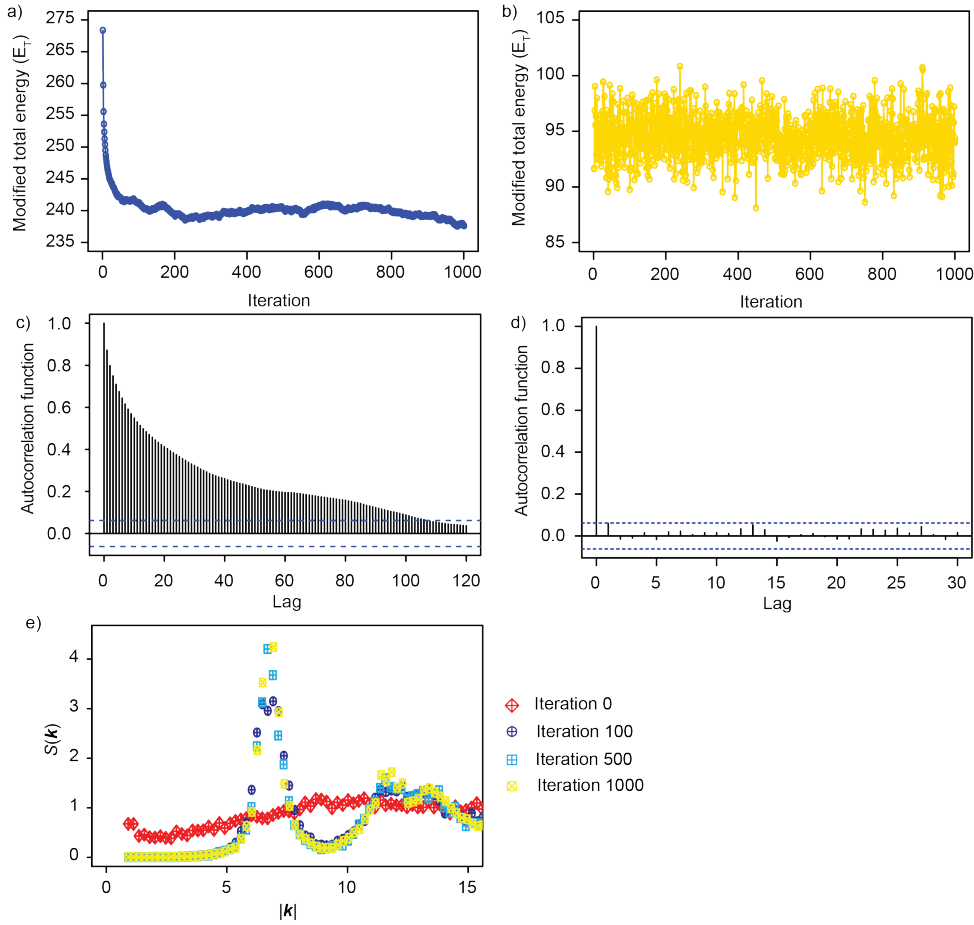


FIGURE 4.2: Visualization of the two regimes of the modified total energy. a) Regime one: Modified total energy quickly decreases and then fluctuates around reached value. Assembly of ellipses with  $e = 2$  at packing fraction  $\phi_g = 0.2$ . (Figure 4.1a,b) b) Regime two: Modified total energy fluctuates throughout all iterations and stays approximately the same. Assembly of ellipses with  $e = 1$  at packing fraction  $\phi_g = 0.65$ . (Figure 4.1c,d). c) Autocorrelation function of time series presented in a) part of this Figure. Blue dashed lines present significance threshold value for autocorrelation function. d) Autocorrelation function of time series presented in b) part of this Figure. e) Evolution of the structure factor under modified Lloyd's algorithm. Assembly of ellipses with  $e = 2$  at packing fraction  $\phi_g = 0.2$ .

modified total energy-related to different modified Lloyd's iterations (Figure 4.2c). Therefore, this regime's modified total energy time series adopts a relatively smooth shape. Furthermore, we can see that the structure factor of the ellipse assembly changes significantly only in the first 100 iterations of the modified Lloyd's algorithm (Figure 4.2e). Even though structure factors of assemblies at iterations 100 and 500 are very similar, we can see a slight

difference between them around their peak values. Finally, there is no visible difference between structure factors of the iterations 500 and 1000 (Figure 4.2e).

Opposite of the previous regime, in the second one, values of the modified total energy oscillate around a single value with the absence of any trend (Figure 4.2b). Those oscillations are much more expressed than in the first regime and completely uncorrelated (Figure 4.2d), giving the noise-like appearance to the modified total energy time series.

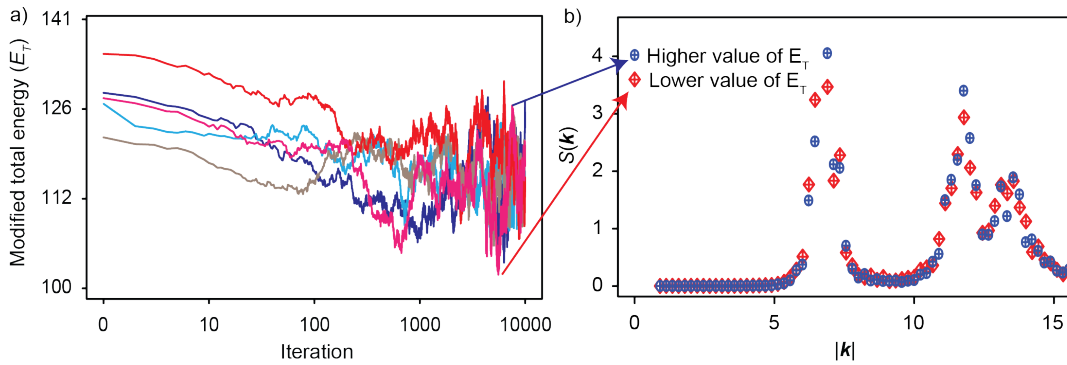


FIGURE 4.3: a) Visualization of modified total energy  $E_T$  for first 10000 iterations of modified Lloyd's algorithm. Colours represent different runs of modified Lloyd's algorithm from distinct initial configurations of disc ( $e = 1$ ) assemblies at packing fraction  $\phi_g = 0.35$ . Both coordinate axis are logarithmic. b) Structure factors of ellipse assemblies that represent different iterations of the modified Lloyd's algorithm. Red colour represents iteration where the modified total energy  $E_T$  adopts lower value in its oscillations and blue colour represents iteration where the modified total energy  $E_T$  adopts higher value in its oscillations.

Even though both regimes of the modified total energy are different, they carry the same information about the convergence of modified Lloyd's algorithm. As we pointed out earlier, in the first regime, after the initial decrease, the modified total energy starts to oscillate around a particular value. As we can see from Figure 4.3a, those oscillations start around the hundredth iteration, meaning that performed 1000 iterations are enough to converge modified Lloyd's algorithm fully. Figure 4.3b visualizes structure factors of the ellipse assemblies with higher and lower values of the modified total energy during the previously mentioned oscillations. It is vital to specify that the assembly structure remains the same under those oscillations meaning that the reached state can have a relatively wide range of values of the modified total energy  $E_T$ . Moreover, Figure 4.2e provides us with a conclusion that the

structure of the ellipse assembly also converges after 1000 modified Lloyd's iterations.

Similarly, in the second regime, the modified total energy oscillates around a particular value from the first iteration meaning that, on average, it does not change. Therefore, 1000 iterations are certainly enough to converge modified Lloyd's algorithm in this case too.

$e \searrow \phi_g \rightarrow$	0.2	0.35	0.5	0.65	0.8
3.33	REG 1	REG 2	REG 2	REG 2	REG 2
2	REG 1	REG 1	REG 2	REG 2	REG 2
1.25	REG 1	REG 1	REG 2	REG 2	REG 2
1	REG 1	REG 1	REG 2	REG 2	REG 2

FIGURE 4.4: Visualization of total energy regimes throughout phase space of different ellipse aspect ratios and packing fractions. **REG 1** denotes first total energy regime and **REG 2** stands for second total energy regime.

Another even more important phenomenon regarding modified Lloyd's algorithm arises from the properties of the modified total energy. Hence, we can relate the two observed regimes of the modified total energy to whether any significant structural changes happened under the application of modified Lloyd's algorithm. Thereby, the first regime where modified total energy decreases indicates a difference in ellipse organization after applying modified Lloyd's iterations. Such reorganization can be detected even by observing visualizations of ellipse assemblies (Figure 4.1a, b). Such structural difference is not evident in the second regime where the value of modified total energy stays roughly the same (Figure 4.1c, d).

Due to the previously described phenomenon, it is natural to investigate the modified total energy regimes across the studied phase space of ellipse aspect ratios and packing fractions. Thereby, a visualization of the modified total energy regimes is presented in Figure 4.4). We can detect a relatively clear border between areas of the phase space where modified total energy follows different regimes. Hence, for all ellipse assemblies at lower packing fractions ( $\phi_g = 0.2, 0.35$ ) except for highly elongated ellipses ( $e = 3.33$ ) assembled at packing fraction  $\phi_g = 0.35$ , we witness that the modified total energy embraces behaviour of first, decreasing and smooth regime. Therefore,



in that part of phase space dominated by the low packing fraction, modified Lloyd's algorithm introduces effects to the ellipse assemblies similar to ones presented in the Figure 4.1b. On the other hand, for the part of phase space where intermediate and high packing fractions dominate, the modified total energy values follow a noisy regime which implies that modified Lloyd's iterations do not introduce any significant visual changes to concerned ellipse assemblies.

### 4.3.2 Relation to the modified Quantizer problem

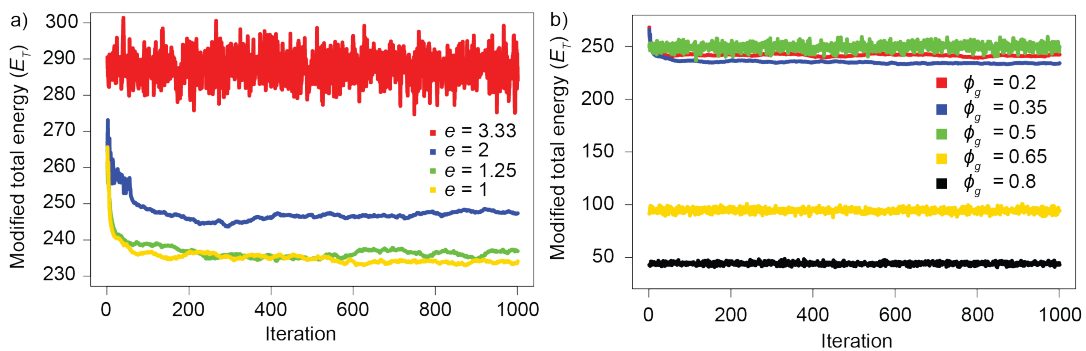


FIGURE 4.5: a) Modified total energy values for 1000 Lloyd's iterations of assemblies at packing fraction  $\phi_g = 0.35$ . Different colours denote different aspect ratios of assembled ellipses. b) Modified total energy values for 1000 Lloyd's iterations of circle assemblies ( $e = 1$ ). Different colours denote different assembly packing fractions.

In the introduction of this chapter, we motivated the definition of modified Lloyd's algorithm with solving the modified Quantizer problem. It remains unclear how modified Lloyd's algorithm and modified Quantizer problem are connected. We concluded in the previous subsection that modified Lloyd's algorithm has a significant effect on ellipse assemblies only in one part of the phase space (Figure 4.4). In that case, Lloyd's algorithm decreases the value of the modified total energy (Figure 4.2a) and therefore produces a more optimal state of the system in the context of the modified Quantizer problem. Additionally, we saw that the modified total energy fluctuates around a specific value if we perform more modified Lloyd's iterations. Nonetheless, those fluctuations are tiny compared to the initial decrease. This phenomenon provides us with evidence that modified Lloyd's

algorithm produces modified Quantizer optimal states even though the rigorous proof of this claim remains beyond the reach of this thesis.

As we know from the Introduction of this Thesis, the Quantizer problem and Lloyd's algorithm are related to minimizing elongation of the Voronoi cells in the system. By observing values of the modified total energy related to different aspect ratios of the assembled ellipses, we can draw a similar conclusion to the modified Lloyd's algorithm and modified Quantizer problem.

Figure 4.5a displays modified total energies related to ellipse assemblies with different aspect ratios at packing fraction  $\phi_g = 0.35$ . We can observe that assemblies of more elongated ellipses have greater values of the modified total energy throughout the modified Lloyd's algorithm applications. Since assemblies of more elongated ellipses have, on average, a greater mean of Voronoi cell elongation (Chapter 3), we can conclude that greater values of the modified total energy are also related to the greater mean elongation of the Voronoi cells in studied assemblies. The latter positive correlation is present throughout the phase space of our simulations, i.e. the same trend is observable for all packing fractions. Accordingly, since lower values of the modified total energy indicate less elongated Voronoi cells, the modified Quantizer problem prefers tessellations with less elongated Voronoi cells, as was the case with point generators.

In addition to the aspect ratios of assembled ellipses, packing fractions also reveal an interesting aspect of the modified total energy of the system. Figure 4.5b presents modified total energies of the circle assemblies ( $e = 1$ ) along the whole scale of studied packing fractions. Before applying modified Lloyd's algorithm (Iteration 0), assemblies at higher packing fractions have, on average greater value of the modified total energy. However, during the algorithm itself, that relation changes due to different regimes of the modified total energy discussed earlier. The trend in the modified total energies values related to random assemblies of ellipses (Iteration 0) is explainable by the definition of the modified total energy. In the Equation 4.1, the sub-integral function trivially adopts value 0 for the points contained in the ellipse that generates the concerned Voronoi cell. At a higher packing fraction, ellipses occupy a greater fraction of its Voronoi cells meaning that the value of the sub-integral function is 0 on the greater proportion of the Voronoi cell resulting in lower values of the integrals in the modified total energy definition and, accordingly, a lower value of the modified total energy of the

system.

## 4.4 Structural properties of ellipse assemblies under modified Lloyd's algorithm

After we got convinced that modified Lloyd's algorithm fully converges and produces meaningful results, we would like to investigate the organization of the ellipses under the application of the algorithm more thoroughly. To address this question, as in Chapter 2 of this thesis, we calculate and analyse the structure factor of ellipse assemblies before and after applying modified Lloyd's algorithm. Hence, Figures 4.6 and 4.7 present the critical result of this chapter, as well as another link between modified and classical Lloyd's algorithm.

In the left column of Figures 4.6 and 4.7 structure factors of the random assemblies of ellipses are plotted. Each graph presents ellipse assemblies at one specific packing fraction starting from top with lowest in Figure 4.6 ( $\phi_g = 0.2$ ) and ending at the bottom of Figure 4.7 with the highest ( $\phi_g = 0.8$ ). The first notable phenomenon related to densities of ellipse assemblies is dependence of the structure factors on elongation of the assembled ellipses. Accordingly, at the lowest packing fraction ( $\phi_g = 0.2$ , Figure 4.6a), the observed structure factors do not depend much on the shape of assembled ellipses and, therefore, nearly coincide with a curve with no notable sharp peaks. They adopt values close to 1 for large wavenumbers while they halve when wavenumber vanishes. Most of the mentioned properties are also common for a structure factor of binomial point process that has constant structure factor ( $S(\mathbf{k}) = 1, \forall \mathbf{k}$ ). Therefore, ellipse assemblies at the lowest studied packing fraction ( $\phi_g = 0.2$ ) share common structural properties with binomial point processes, namely disorder and relatively uniform spatial distribution of particles.

The dependence of the structure factors on the shape of the assembled particles becomes more evident as the packing fraction increases. While structure factors of assemblies consisting of highly elongated ellipses remain flat, peaks become more pronounced as the assembled ellipses are more circle-like. Moreover, structure factors obtain lower values for small wavenumbers as the packing fraction increases. At the highest packing fraction ( $\phi_g = 0.8$ ,

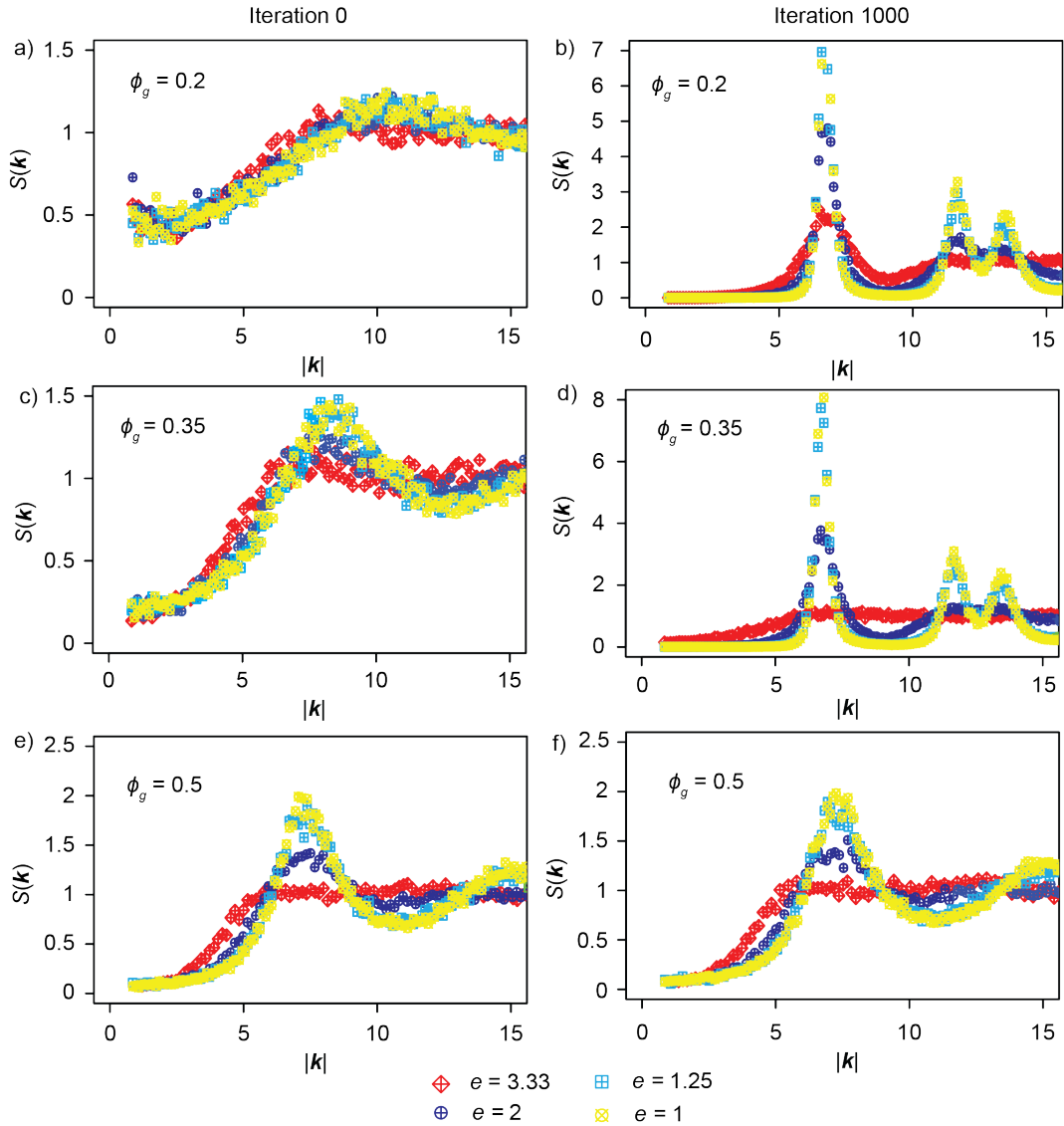


FIGURE 4.6: We calculated structure factors of assemblies by taking in count centres of assembled particles. Left column contains structure factors of random assemblies before application of modified Lloyd's algorithm and right column contains structure factors of ellipse assemblies after application of 1000 modified Lloyd's iterations. Every row in the figure represents particular packing fraction. Differently coloured symbols represent distinct aspect ratios of assembled ellipses. Structure factors were observed only for wavenumbers  $|\mathbf{k}| \geq 4 \times |\mathbf{k}_{min}|$  for assemblies at packing fraction  $\phi_g \leq 0.5$  where  $|\mathbf{k}_{min}|$  is the shortest possible wavenumber. a) Iteration 0,  $\phi_g = 0.2$  b) Iteration 1000,  $\phi_g = 0.2$  c) Iteration 0,  $\phi_g = 0.35$  d) Iteration 1000,  $\phi_g = 0.35$  e) Iteration 0,  $\phi_g = 0.5$  f) Iteration 1000,  $\phi_g = 0.5$

Figure 4.7c), the dependence of the systems spatial characteristics on the ellipse elongation in terms of previously described properties of structure factors is most obvious. While the structure factors of circle-like particle assemblies have pronounced peaks, structure factors of highly elongated ellipse

assemblies remain flat.

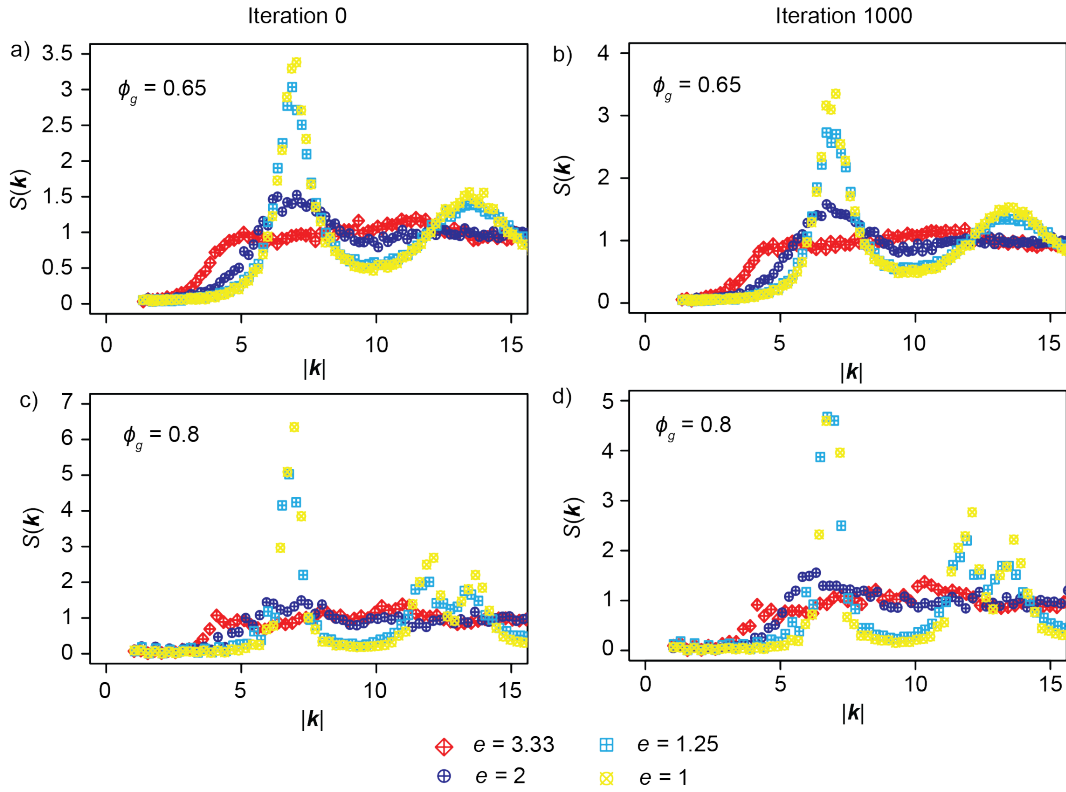


FIGURE 4.7: Structure factors of ellipse assemblies. Left column contains structure factors of random assemblies before application of modified Lloyd's algorithm and right column contains structure factors of ellipse assemblies after application of 1000 modified Lloyd's iterations. Every row in the figure represents particular packing fraction. Differently coloured symbols represent distinct aspect ratios of assembled ellipses. Structure factors were observed only for wavenumbers  $|\mathbf{k}| \geq 2 \times |\mathbf{k}_{min}|$  for assemblies at packing fraction  $\phi_g \geq 0.65$  where  $|\mathbf{k}_{min}|$  is the shortest possible wavenumber. a) Iteration 0,  $\phi_g = 0.65$  b) Iteration 1000,  $\phi_g = 0.65$  c) Iteration 0,  $\phi_g = 0.8$  d) Iteration 1000,  $\phi_g = 0.8$

The previous discussion concludes that elongation of the ellipses introduces variability and disorder in the ellipse assemblies. At the same time, its absence generates systems that are structured more regularly. Similarly, packing fraction plays the same role, with systems at higher packing fraction being more ordered. Interestingly, the earlier analysis extends the results in Chapter 3 of this thesis and provides the same conclusions about the role of particle shape and packing fraction in geometrical properties of the ellipse assemblies.

Right column of the figures 4.6 and 4.7 present structure factors after application of modified Lloyd's algorithm. The first evident information from the considered figures is that at intermediate and high packing fractions (Figures 4.6f and 4.7b,d) impact of Lloyd's algorithm is little significant and barely observable from the figures. In those systems, Lloyd's algorithm does not introduce any structural change but rather reorganize positions of particles in the way that their structural properties stay roughly the same (Figure 4.1d).

Opposite of that, a significant reorganization of particles occurs under modified Lloyd's algorithm in the systems at low packing fractions (Figure 4.6b and d), which have more similar geometric properties to point processes. In such systems, structure factor changes significantly under modified Lloyd's iterations. Before modified Lloyd's iterations, as mentioned earlier, the shape of the structure factor was flat with the absence of expressed peaks which would indicate regularities in the ellipse organization. However, the final configuration structure factors at low densities adopt shapes that imply higher order in the systems. They possess clear and expressed peaks for certain wavenumbers as well as obtain very small values for short wave vectors ( $S(\mathbf{k}) < 10^{-2}$ ). Nonetheless, despite having clear peaks, the structure factors do not obtain Bragg peaks, which indicates that the final configurations remain amorphous although they are highly ordered and structured. Mentioned characteristics of structure factors that demonstrate a higher degree of order in systems are more pronounced if particles in the assemblies are rounder, i.e. more circle-like. The fact that supports the previous claim is that the only system at lower densities that does not have such properties of the structure factor is the assembly of highly elongated ellipses ( $e = 3.33$ ) at packing fraction  $\rho = 0.35$ .

Mentioned strong decay of structure factor for small wavenumbers indicates suppression of long-wavelength density fluctuations in the systems. To investigate long-range density properties of the systems even further, we have calculated  $H$  measure (Introduction) for structure factors of observed systems that are presented in Figure 4.8. We find that hyperuniformity measure  $H$  in the systems at low packing fractions where modified Lloyd's algorithm introduces structural change falls strictly below  $10^{-3}$  and therefore, by definition, those systems can be considered effectively hyperuniform or hyperuniform for all practical purposes. Moreover, an assembly of circles at packing fraction  $\rho = 0.8$  is also effectively hyperuniform with  $H = \mathcal{O}(10^{-3})$ .

$e \searrow \phi_g \triangleright$	0.2	0.25	0.3	0.35	0.4	0.45	0.5
3.33	EH	EH	X	X	X	X	X
2.86	EH	EH	EH	X	X	X	X
2.5	EH	EH	EH	X	X	X	X
2.22	EH	EH	EH	EH	X	X	X
2	EH	EH	EH	EH	X	X	X
1.25	EH	EH	EH	EH	EH	X	X
1	EH	EH	EH	EH	EH	EH	X

FIGURE 4.8: Visualisation of an effective hyperuniformity in studied phase space of ellipse aspect ratios and packing fractions after application of modified Lloyd's algorithm. Each row represents one aspect ratio of assembled ellipses and each column represents one packing fraction of assembly. **EH** denotes if system is effective hyperuniform and **X** denotes if system is not effective hyperuniform. Effective hyperuniformity of the systems was inspected by the criteria that hyperuniformity measure  $H \leq 10^{-3}$ .

However, there is a difference between the origin of effective hyperuniformity in systems at low packing fraction and in the assembly of discs at packing fraction  $\phi_g = 0.8$ . The effective hyperuniformity in systems at low packing fractions is driven by the out-turn of modified Lloyd's iterations and not by the density and particle characteristics. The fact that supports the previous claim is that random assemblies of ellipses before application of algorithm are not even close to being effectively hyperuniform with their structure factors in the vicinity of 0 being for at least 2 orders of magnitude greater than structure factors of final configurations.

On the other hand, effective hyperuniformity of disc assemblies at packing fraction  $\rho = 0.8$  after applying modified Lloyd's algorithm is the outcome of systems geometrical properties guided by packing fraction and shape of the particles. This second source of effective hyperuniformity can be justified by the phenomenon that structure factors of the system before and after modified Lloyd's iterations roughly obtain the same values with their  $H$  measure being of the same order of magnitude.

Figure 4.8 presents another interesting result regarding effective hyperuniformity of the modified Lloyd's algorithm final configurations. We can

observe that question of whether modified Lloyd's algorithm introduces hyperuniformity to the system depends on the shape of assembled ellipses at all studied packing fractions. As the packing fraction gets higher, the aspect ratio of the assembled ellipses has to be lower for the algorithm to introduce effective hyperuniformity to the system. That law introduces an oblique line in observed phase space that separates two different regimes of Lloyd's algorithm. The first one introduces effective hyperuniformity into systems, and the other that does not significantly affect ellipse assemblies.

## 4.5 Robustness of the results to the hyperparameters of the modified Lloyd's algorithm

Earlier in this chapter, when defining modified Lloyd's algorithm, we pointed out that to fully understand the newly proposed algorithm, we have to investigate the effects of hyperparameters that can be tuned. First of those parameters, denoted by  $\eta$ , controls ellipse freedom of movement when they are rearranging in order to annul the overlaps caused by the centralization step in the modified Lloyd's algorithm. More precisely,  $\eta$  is a value that determines the interval from which the movement of the ellipse will be randomly sampled. As mentioned before, movements are performed independently in both coordinate axis directions for a distance sampled uniformly from interval  $[-\eta, \eta]$ . As a default value, the parameter  $\eta = \frac{b}{2}$  where  $b$  is length of minor semi-axis of ellipse.

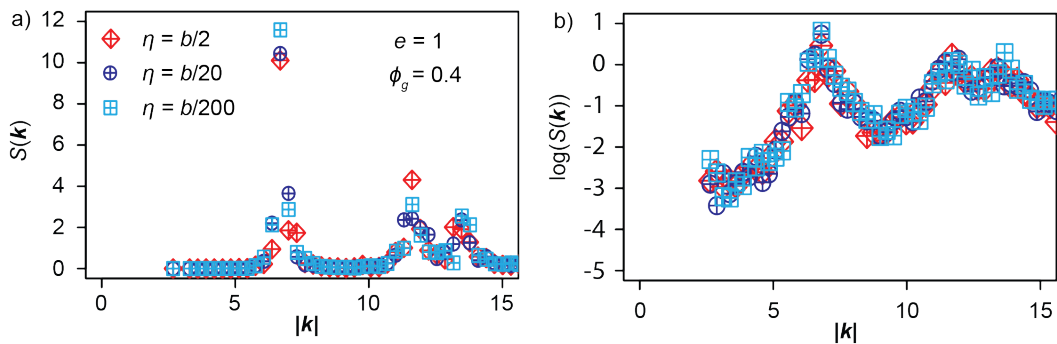


FIGURE 4.9: Structure factors of disc assemblies at packing fraction  $\phi_g = 0.4$  in respect to different values of parameter  $\eta$  in the modified Lloyd's algorithm. Different coloured symbols denote different values of parameter  $\eta$ . a) Structure factors on standard scale. b) Structure factors on log scale.



We are interested in what will happen to the final structures of the modified Lloyd's algorithm if we decrease the value of  $\eta$  and constrain the freedom of movement for ellipses even further. Hence, we will disable ellipses to reorganize more than necessary when they are removing overlaps from the system. In such a way, we will disallow them to cancel out the effects of centralization.

Figure 4.9 presents optimisation of the circle assemblies at packing fraction  $\phi_g = 0.4$  with different values of the parameter  $\eta$ . The parameter alpha was chosen over three orders of magnitude. We can see that structure factors of the final assemblies are invariant on the choice of  $\eta$  and that the structure factor overlap is almost perfect. Therefore, the structures produced by the modified Lloyd's algorithm are robust to different values of parameter  $\eta$ . Same as here, we can recall that parameter  $\eta$  did not influence the geometry of random assemblies of ellipses either (Chapter 3). All of this means that the original choice of parameter  $\eta = \frac{b}{2}$  is small enough not to cancel out optimization effects in our procedures.

Another parameter of our interest,  $\kappa$ , is a fraction of the distance between the Voronoi centre of mass and the ellipse centre for which ellipses will be moved in the modified Lloyd's algorithm. Thus, this parameter can be regarded as a controlling parameter for the centralization speed in the algorithm.

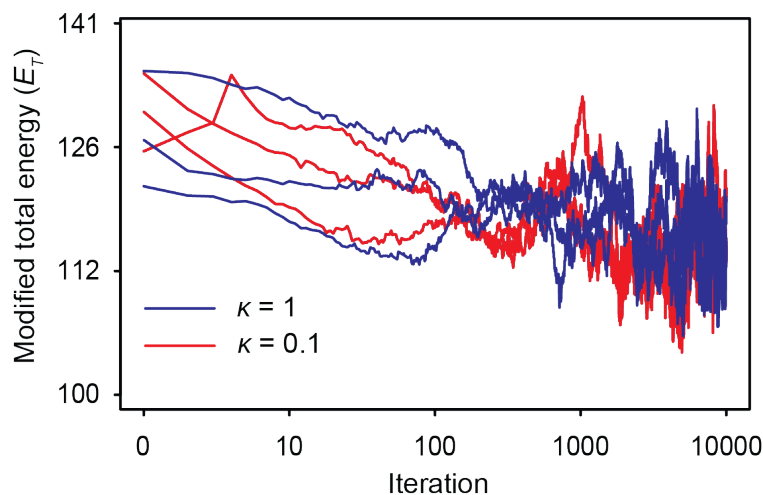


FIGURE 4.10: Modified total energy  $E_T$  for first 10000 iterations of modified Lloyd's algorithm. Colours represent different parameter  $\kappa$  values in modified Lloyd's algorithm runs. Observed systems are disc ( $e = 1$ ) assemblies at packing fraction  $\phi_g = 0.35$ . Both coordinate axis are logarithmic.

The first important question that we addressed regarding parameter  $\kappa$  is how it affects the convergence of modified Lloyd's algorithm in terms of the modified total energy  $E_T$ . Therefore, Figure 4.10 presents the behaviour of the modified total energy when it follows the first of previously mentioned regimes in the case when we decrease  $\kappa$  for an order of magnitude. We find from Figure 4.10 that a decrease of  $\kappa$  does not introduce any significant changes in convergence speed in terms of the modified total energy. Indeed, we can observe that after approximately 100 iterations, the total energy starts to vary around the reached values independent on the choice of parameter  $\kappa$  in Lloyd's algorithm.

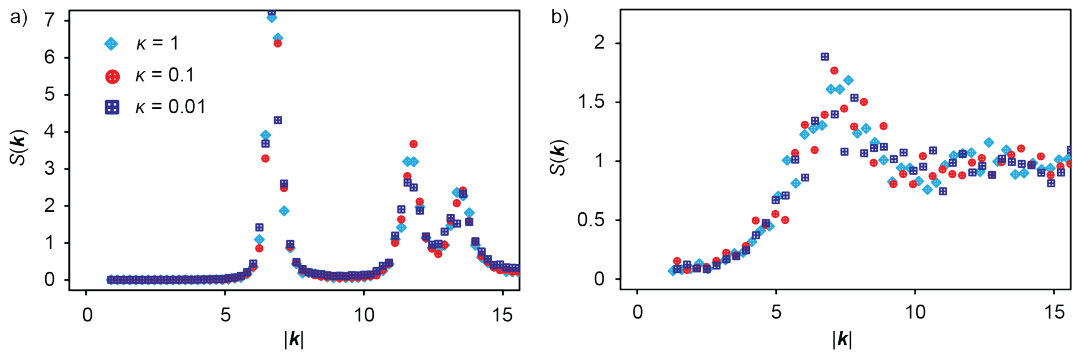


FIGURE 4.11: Structure factors of ellipse assemblies after application of modified Lloyd's algorithm in respect to different values of parameter  $\kappa$ . Different coloured symbols denote different values of parameter  $\kappa$ . a) Assembly of discs ( $e = 1$ ) at packing fraction  $\phi_g = 0.2$  b) Assembly of ellipses with aspect ratio  $e = 2$  at packing fraction  $\phi_g = 0.5$ .

Furthermore, we have investigated how Lloyd's algorithm with different parameter  $\kappa$  values affect the structural properties of ellipse assemblies. First of all, we observed systems that are some part away from the line that separates two different regimes of the modified Lloyd's algorithm, as we presenter earlier in Figure 4.8. Thus, Figure 4.11 presents structure factors after application of modified Lloyd's algorithm due to different choice of parameter  $\kappa$  for systems that follow both first (Figure 4.11a) and second (Figure 4.11b) regime of the modified Lloyd's algorithm. We find that structure factors concerning different values of  $\kappa$  coincide with great precision in both regimes of the modified Lloyd's algorithm. Because of the previous fact, decreasing parameter  $\kappa$  for two orders of magnitude does not introduce any significant structural changes to the obtained ellipse assemblies. However, it remains unclear if reduction of both parameters  $\eta$  and  $\kappa$  even further in case of the ellipse assemblies that follow the second regime of the modified

Lloyd's algorithm would introduce a significant change to the system. This way, we would centralize systems slowly and move the particles as little as possible to remove ellipse overlaps from the systems.

More exciting results appear for the ellipse systems in the vicinity of the border between two different Lloyd's algorithm regimes (Figure 4.12). Hence, we obtain different spatial properties of final configurations by reducing the value of parameter  $\kappa$  for an order of magnitude ( $\kappa = 0.1$ ) when applying modified Lloyd's algorithm. As we can see from Figure 4.12, structure factor after application of modified Lloyd's algorithm with  $\kappa = 0.1$  adopts lower values for small wavenumbers. Accordingly, the concerned system is effectively hyperuniform while the system obtained by applying modified Lloyd's algorithm with  $\kappa = 1$  is not effectively hyperuniform. By further investigation of reducing parameter  $\kappa$  for an order of magnitude, we find that the border in the phase space that separates different regimes of modified Lloyd's algorithm (Figure 4.8) shifts for approximately 0.1 towards higher packing fractions. Therefore, by reducing parameter  $\kappa$  for an order of magnitude, effective hyperuniformity will be achieved at a slightly higher packing fraction than in the case of the default value of parameter  $\kappa = 1$ . This result points out that parameter  $\kappa$  controls the speed of centralization and that by decreasing it, the need for random shaking of the systems to annul overlaps is reduced. Then, the randomness introduced to the systems by shaking does not cancel out the optimization done by the movement of ellipses towards centres of mass.

Another interesting phenomenon regarding parameter  $\kappa$  occurs when it is reduced for another order of magnitude (Figure 4.12). From Figure 4.12 we can see that reducing parameter  $\kappa$  even further does not have any new effect but even cancels out the first reduction of parameter  $\kappa$ . As we can see, when we set parameter  $\kappa = 0.1$ , the structure factor will obtain lower values for small wavenumbers as well as more expressed peaks meaning that systems with  $\kappa = 0.1$  have lower hyperuniformity  $H$  measure values than systems with  $\kappa = 1$  or  $\kappa = 0.01$ . This result points out that if the speed of centralization is too low, the randomness of the algorithm will also have a greater influence which will yield less ordered systems. So to maximize the effect of centralization, for the ellipse assemblies in the vicinity of the border between two different regimes of modified Lloyd's algorithm, the parameter  $\kappa$  has to be selected carefully with values around 0.1.

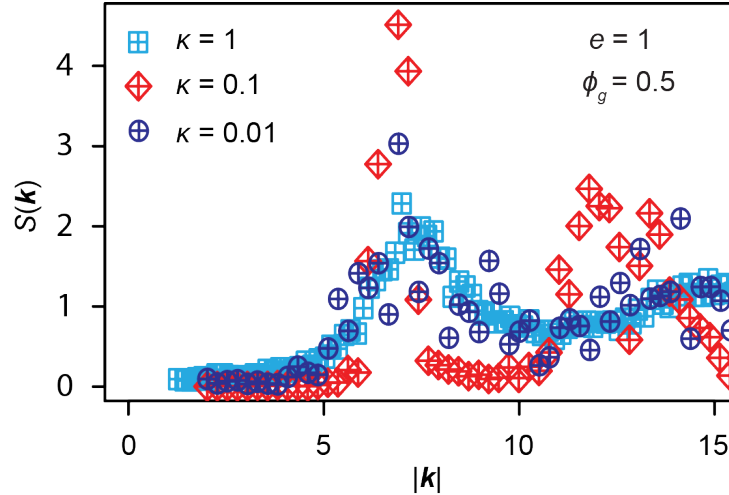


FIGURE 4.12: Structure factors of disc assemblies at packing fraction  $\phi_g = 0.5$  after application of 5000 modified Lloyd's iterations in respect to different values of parameter  $\kappa$ . Different coloured symbols denote different values of parameter  $\kappa$ .

## 4.6 Conclusion of Chapter 4

In this chapter, we generalized the Quantizer problem to systems of particles with non-zero areas by modifying the total energy defined in the introduction of this thesis. The newly modified total energy differs from the standard total energy in the sub-integral function that provides the distance between an arbitrary position in the space and the considered particle. We showed that the modified total energy  $E_T$  is equal to the standard total energy  $E_t$  when it is calculated for point patterns. Additionally, we modified Lloyd's algorithm so that it becomes applicable to systems of particles by introducing an additional step to the procedure that annuls appearing overlaps between ellipses. We proved that the proposed algorithm converges by investigating the evolution of the modified total energy and the structure factors of ellipse assemblies throughout different iterations. Moreover, we presented numerical evidence that newly modified Lloyd's algorithm can be used to solve the modified Quantizer problem.

By studying modified total energies, we anticipated two different regimes of modified Lloyd's algorithm that depend on the aspect ratios and packing fractions of concerned ellipse assemblies. In the first regime that is dominant at lower packing fractions, modified Quantizer solutions obtained by the modified Lloyd's algorithm are effectively hyperuniform with hyperuniformity measure  $H \leq 10^{-4}$ . On the other hand, at higher packing fraction

modified Lloyd's algorithm does not introduce significant systems changes. Moreover, we show that effective hyperuniformity of final configurations of the modified Lloyd's algorithm also occurs at intermediate packing fractions for systems composed of particles that are either circles or very similar to circles. These phenomena show that effective hyperuniformity can occur in assemblies of ellipses under the procedure that actively positions particles towards centres of mass of their Voronoi region. Therefore, the results presented in this chapter contribute to a deeper understanding of the origins of hyperuniformity in particle systems.

Presented property that modified Lloyd's algorithm introduces effective hyperuniformity to ellipse assemblies is interesting because it extends results from Chapter 2 of this thesis. In the case of non-trivial particles, effective hyperuniformity under modified Lloyd's algorithm occurs only at low packing fractions. Therefore, it would be interesting to adapt Lloyd's algorithm to significantly reorganize systems of particles at higher packing fractions as well. Previously mentioned reorganization can be done by additional control of particle orientations in the iterations of the algorithm. This way, we would try to introduce a nematic order to systems and possibly produce effective hyperuniformity at higher packing fractions. Furthermore, it would be interesting to address the modified Quantizer problem for other types of particles besides ellipses both in 2D and in higher dimensions.



## Chapter 5

# Theoretical model for epithelial tissues

### 5.1 Introduction to epithelial tissue

In previous chapters, we have investigated geometric optimization of spatial structures consisting of trivial particles (points) or more complex particles with both area and arbitrary shape (ellipses). We found that Lloyd's algorithm, in those systems, affects local properties such as centrality and long-range density fluctuations. Such complexity of Lloyd's optimization implies its great applicability to a broad range of problems both in science in industry. This chapter will study how Lloyd's algorithm comes into play when modelling epithelial tissue.

Epithelial tissue is beside muscle, connective and nervous, one of four tissue types. It is considered the first tissue that emerged during phylogenetic, 600 million years ago. Nowadays, over 150 types of epithelial cells have many functionalities in our bodies. Thus, epithelial tissue separates our body from its surroundings or lies between different tissue types and has essential roles in digestive, respiratory, reproductive, sensory, vascular, neural and hormonal systems. In those systems, epithelium takes over functions of secretion, selective absorption, protection, sensing and transcellular transport[124]. Epithelium also has a pivotal role in processes such as tumour progression and wound healing[74, 154, 101, 170].

In order to perform all its functions in the organism, epithelial tissue has to adopt structures with various distinct appearances[154, 29, 101, 60]. Hence, epithelial cells have all kinds of different shapes and forms, both individually and collectively. We differentiate cuboidal, squamous and columnar epithelial cells that can be arranged in one (simple) or more layers (stratified). Visualizations of such epithelial tissue appearances are presented in Figure

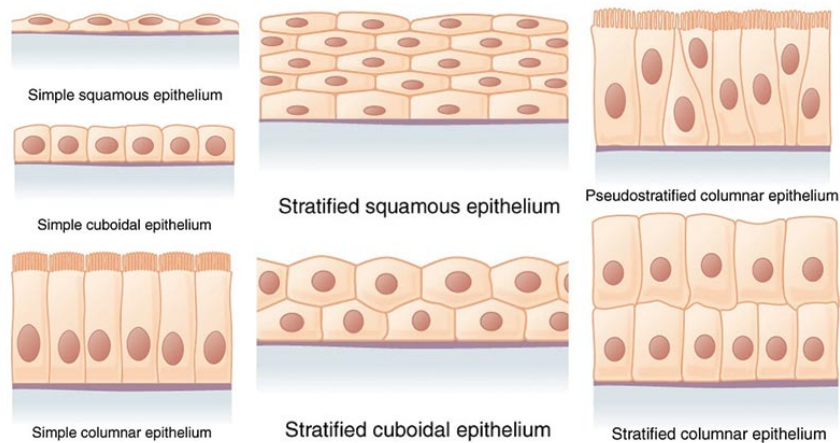


FIGURE 5.1: Appearances of epithelial cell tissue. Image was taken from <https://microbenotes.com/epithelial-tissue>.

### 5.1.

Epithelial tissue has been a subject of studies *in-vivo* as well as *in-vitro*. Those models have some important advantages that make them favourable for specific studies. Thus, *in-vivo* studies provide a more realistic approach. In contrast, *in-vitro* studies are performed in a familiar environment where parameters of the model are easy to control [75].

One of the most popular *in-vitro* models for studying epithelial tissues is Madin-Darby Canine Kidney (MDCK) cell culture. MDCK cells, originally derived by S.H. Madina and N.B. Darby in 1958, originate from an adult Cocker Spaniel[66]. Because of the variability of the original MDCK cell culture, many different cell lines were derived from it. Nowadays, those cell lines are used to study various phenomena related to epithelial tissues. Hence, MDCK cells are suitable models to study development of tumours[140, 116] and also used as substrates for research of influenza virus[66, 99] and production of vaccines. Moreover, MDCK cell lines were used to investigate regimes of epithelial tissue growth[77], collective cell motion[119, 150], morphological properties[74, 166] as well as cell proliferation[141].

A fascinating study of MDCK tissue's structuring is presented in reference [76]. In this paper, the authors investigate epithelial tissues grown on substrates of different stiffness. They find that epithelial tissues, depending on the stiffness of the substrate, possess different morphological properties and different cell densities but the same topology in the homeostatic state of the tissue (Figure5.2). These results provide a deeper understanding of the



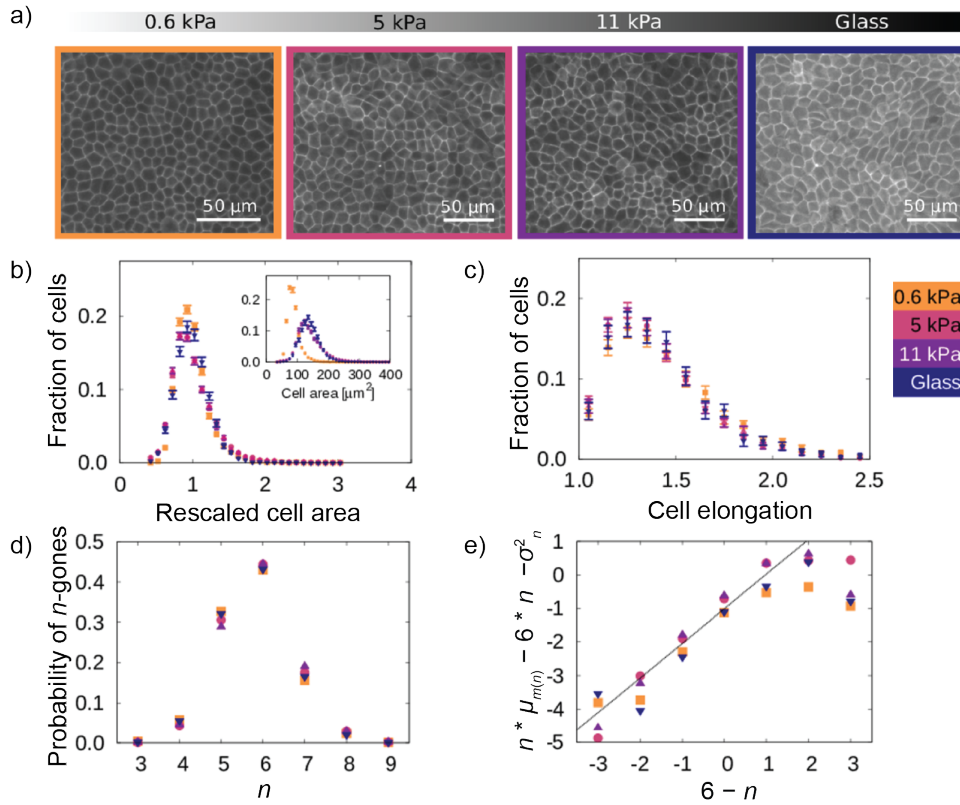


FIGURE 5.2: Geometric and topological properties of epithelium in the homeostatic state grown on substrates with different stiffness. a) Appearance of the cell membranes in a steady state. b) Distributions of the rescaled cell area (cell area divided by its mean). Inset shows distributions of the non-rescaled cell areas c) Distributions of the cell elongation. d) Distribution of the number of neighbours. e) Aboav-Weaire's law (Chapter 3).

This figure was taken from the reference [76].

mechanosensitive properties of cells to the macroscopic structuring of the tissue.

On the other hand, the organization of the epithelial tissue during maturation remains unfamiliar. During the growth and maturation, while densifying, epithelial tissue must actively maintain its structure and optimize to perform its functions. Structural characterization of the epithelium was a topic of studies in the past [24], and interestingly, hyperuniform density fluctuations were found in the context of the vertex model for the epithelial tissue [137].

In order to address the question of epithelial structuring under the process of maturation, we will study experimental data taken from Sara Kaliman PhD thesis[75]. Considered experimental data comes from the MDCK II strain, the most used strain developed from the parental MDCK cell line.

Studied tissues were grown on 2D glass and hard gels. In such environments, MDCK cells can form circular monolayers that grow with time up to a few millimetres in diameter. Moreover, it is possible to distinguish the bulk of such epithelial clusters from their edge. The bulk of the cluster is positioned in the centre of the cluster where cells reach steady-state density while towards the outer parts of cluster density decreases and reaches its minimum at very edge[77, 75, 76]. An example of such a cluster is shown in Figure 5.3.

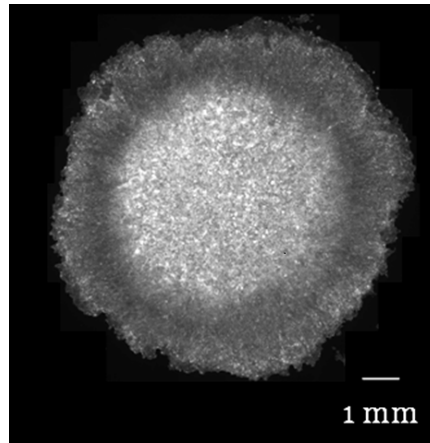


FIGURE 5.3: MDCK II cell cluster grown on glass substrate. This image was taken from reference [75].

This chapter will aim to model the epithelium and show how specific features of the epithelial tissue can be described efficiently by simple mathematical concepts such as an ellipse or Voronoi tessellation. We will characterize the structure of epithelial tissue by calculating structure factors of experimentally obtained tissue data. Moreover, we will study the effects of centrality in the epithelial tissues by observing simple and intuitive morphological measures defined in Chapter 3 of this thesis. The behaviour of those morphological measures will be a great motivation to investigate the modified Lloyd's optimization in the context of epithelial tissues.

As we mentioned before, parts of this chapter were done by Sara Kaliman (PhD thesis[75]) or in collaboration with her [97]. The rest of this chapter will clearly state which results are paraphrased from either of the previous references.

## 5.2 Structural properties of epithelial tissue

### 5.2.1 Structure factor of tissue

In order to further understand the structuring of epithelial tissues, we have investigated the structure factors of the tissue clusters. Figure 5.4a presents point process that is generated by the centres of mass of cell nuclei in the tissue cluster. We calculated structure factors of such point processes to investigate the structuring of the tissue. We examined tissue clusters at two different timestamps after their seeding, which yielded two different mean cell densities of tissue. Each dataset consists of around 50000 epithelial cells.

Figure 5.4c reveals very interesting facts about epithelial structuring. We find that structure factors at both timestamps possess clear peaks. However, concerned peaks are much more pronounced, as expected, in the case of tissue clusters at day 4 due to the higher cell density. Besides the appearance of peaks, we can see that both structure factors decrease rapidly towards smaller wavenumbers and adopt relatively flat shapes around their minimal value. The flat regions of the structure factors correspond to the neighbourhood of 2 and 4 cells at low and high density, respectively. We find the minimal values of the structure factor  $S(\mathbf{k}) = 0.12$  for  $\mathbf{k}$  corresponding to wave-lengths of  $42\mu\text{m}$  for clusters at the day 2 and  $S(\mathbf{k}) = 0.04$  for  $\mathbf{k}$  corresponding to wave-lengths of  $27\mu\text{m}$  at the day 4. After reaching their minimal values, both structure factors increase towards 0. The increase follows a line on a logarithmic graph with linear coefficients approximately  $-1$  for low-density and  $-1.2$  for high-density tissues (Figure 5.4d). This suggests that structure factor achieves a finite value for  $|\mathbf{k}| = 0$ .

Previously mentioned decrease and levelling of structure factors in the case of both timestamps indicate the existence of locally ordered domains in tissue with the absence of strong variability in density. Such domains can be seen as darker and lighter patches on Figure 5.4a. Point configurations in such ordered domains are plotted in Figure 5.4b. An increase in structure factor values when  $|\mathbf{k}|$  approach 0 points out more significant fluctuations in cell density on greater length scales which is also appearing on the Figure 5.4a. These fluctuations imply more irregular patterning on greater length scales.

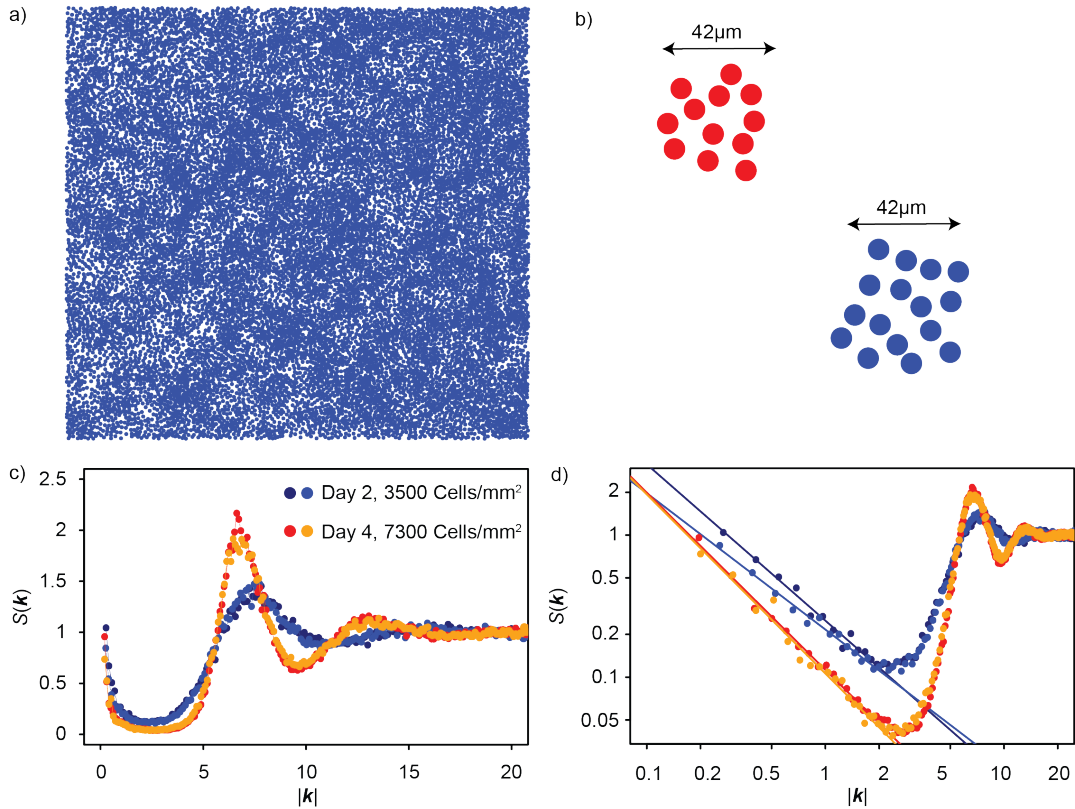


FIGURE 5.4: Structuring of the epithelial tissue a) Image of a point process generated by the tissue cluster 2 days after its seeding. Each point represents a centre of mass of cell nuclei in a tissue cluster. b) Examples of points from a) part of the figure at length-scale of  $42\mu\text{m}$  that corresponds to the ordered domains in tissue. c) Structure factors of the epithelial tissue. Cold colours represent two tissue samples 2 days after seeding, while warm colours represent two tissue samples 4 days after seeding. Data is scaled so that the mean cell area is equal to unity. Coordinate axes are linear. d) Structure factors where the coordinate axes are logarithmic. Lines represent fits to the tail towards 0 of the structure factors.

### 5.2.2 Set Voronoi tessellation based epithelial tissue model

The studied epithelial tissue forms monolayer sheets. Each cell occupies a fraction of the substrate on which tissue grows. Hence, when looking from above, cells tile the substrate plane where each cell corresponds to one tile. Edges of tiles represent cell membranes, and vertices of tiles represent junctions where at least three cells meet. Cells adopt various shapes due to curvature of the membranes and different topological properties of cells in tissue (Figure 5.5). However, the curvature of the edges is not too expressed, which motivated many studies to approximate cells with simple polygons [170, 51, 17, 110].

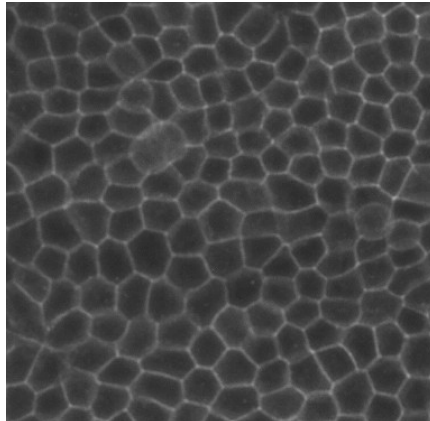


FIGURE 5.5: MDCK II epithelial cells form monolayer meaning that the cell membranes define a tessellation of plane. This image was taken from reference [75].

Voronoi tessellation has a pivotal role in our model of epithelial tissue. Modelling epithelial cells with Voronoi tessellation has been a well-known approach for years, and many studies of cell morphology were performed with Voronoi cells representing epithelial cells [170, 166, 141, 121]. These studies have in common that the Voronoi tessellation was constructed from a single point, namely, being the centre of mass of cell nuclei. With this perspective, cells are polygons which makes *in-silico* studies easy to perform both algorithmically and computationally. Despite this approach being simple and very effective, it has its limitations. Hence, Kaliman et al. [74] performed an extensive study of Voronoi tessellation built from the centre of mass of cell nuclei (CMVT) by comparing various morphological measures of CMVT and actual tissue. Experimental data is extracted from tissue images via image analysis tools. They find that many morphological measures of tissue are approximated well by the CMVT with error varying between 10% and 15% (Figure 5.6 a). However, they observe significant errors when CMVT reproduces some morphological measures such as perimeter, elongation and number of neighbours due to the polygonal nature of CMVT. Therefore, despite CMVT being widely used and a relatively good approximation for morphological properties of cells, an upgrade to the CMVT model is needed to capture some properties of epithelial cells, such as shape and topology.

A natural extension to the CMVT model is a set Voronoi tessellation model (SVT) that would generate Voronoi tessellation from the shape of the cell nuclei. Thus Kaliman, in her PhD thesis[75] continues the study of Voronoi tessellations as an approximation for cell membrane by calculating SVT from

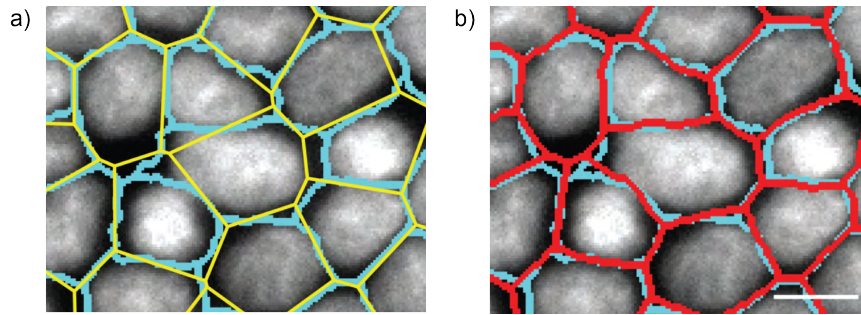


FIGURE 5.6: Visualization of Voronoi tessellations compared to the cell membrane (blue). The cell membrane was segmented from the images of tissue with advanced image analysis tools described in reference [75]. a) CMVT (yellow) approximates the membranes relatively well with some significant mistakes where it splits across cell nuclei (white objects). b) SVT (red) follows the membrane curves with great precision, placing each nucleus inside its cell. These images were taken from reference [75].

the cell nuclei and comparing obtained morphological measure data to actual experimental data. She finds that SVT coincides with cell membrane even better and that it outperforms CMVT with the error being below 10% (Figure 5.6 b). Moreover, all of the morphological measures were calculated more precisely, especially ones where CMVT made the most significant errors, such as cell elongation.

The result that SVT calculated from the cell nuclei represents cell membranes with excellent accuracy provides us with a new insight into tissue organization. It motivates a novel approach to tissue modelling. Positions of the cell membranes are strongly correlated to the positions and orientations of the cell nuclei. This correlation means that tissue can be considered an assembly of its nuclei, implicating that the structure of nuclei assembly dictates the morphological properties of studied epithelial tissue. Therefore if we want to reproduce morphological properties of epithelial tissue, we have to generate an assembly of cell nuclei that provides the best approximation of the cell tissue.

Since our goal is to assemble cell nuclei, we have to track their shape. Tracking of the cell nuclei can be very challenging computationally since cell nuclei adopt various shapes (Figure 5.6), and we would have to remember somehow the exact shapes of the edge of the cell nuclei. Because of the round shape of the cell nuclei (Figure 5.6), Kaliman, in her PhD thesis[75] approximates cell nuclei with ellipses. Fitting an ellipse to the cell nucleus is done

with the principal component analysis (PCA). When applied to the cell nucleus, PCA provides an optimal fit of the ellipse to the cell nucleus. After fitting an ellipse, the cell nucleus is characterized by only five parameters (ellipse axis, position in coordinate system and orientation). By approximating cell nuclei with ellipses, we can simplify the nuclei data very effectively, which makes our model computationally much more feasible.

### 5.2.3 Morphology of cell nuclei

Since cell nuclei are the objects used to calculate the positions of membranes, it is clear that they have a central role in our tissue model. Because of that, it is vital to have an insight into cell nuclei morphology to understand what our model predicts.

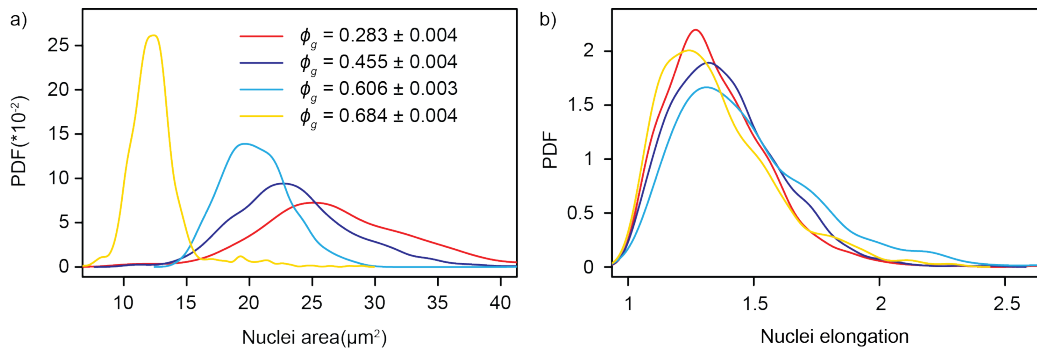


FIGURE 5.7: Distributions of area and elongation of the cell nuclei. Different coloured lines denote different cell densities. a) Area distributions. b) Elongation distributions.

To achieve that goal, we investigate distributions of nuclei area and elongation at various cell densities in tissue. Calculation of the nuclei statistics is done by calculating the area and elongation of ellipses that were fitted to cell nuclei (data is taken from Kaliman PhD thesis [75]). Figure 5.7a presents distributions of cell nuclei area at different cell densities. The first notable fact is that distributions of nuclei area are shifted towards the left as cell density increases meaning that as the cell density is higher, cell nuclei are smaller on average. Moreover, cell density influences variability of the distributions because nuclei area distributions are narrower as cell density is higher, meaning also fewer fluctuations in the size of the nuclei.

On the other side, distributions of cell nuclei elongation reveal different nature of the nuclei shape regarding different cell densities (Figure 5.7 b). We

find that cell density does not dictate the shape of the nuclei as much as it influences the nuclei area. Even though there is a statistically significant difference between nuclei elongation distributions, all distributions have similar positively skewed shapes and a mean of around 1.4. Moreover, the width of all nuclei elongation distributions is approximately equal, which indicates that cell density does not affect the shapes of the nuclei as much as it affects the size of the nuclei.

#### 5.2.4 Randomness in cell tissue

Now that we described the appearance of cell nuclei, we can continue building the epithelial tissue model. Since SVT reconstructs membranes from cell nuclei, our goal is to assemble somehow ellipses fitted to cell nuclei to reproduce the tissue's morphology.

In order to do so, firstly, we decided to compare tissue to the random assembly of concerned ellipses. A random assembly of ellipses as a model for epithelial tissue structure has both advantages and disadvantages. Thus, it is the most simple model and very easy to implement. Furthermore, by understanding the effects of randomness in the assembly of ellipses, we can easily distinguish which other active process governs the properties of epithelial tissue. Hence, since we are already familiar with the properties of random assemblies of ellipses (Chapter 3), we can easily recognize the nature of these different processes that form the morphology of epithelium which will help us implement them into our model efficiently. On the other side, random assembly is an improbable model for epithelial structure since the morphology of tissue, as a living system, is highly influenced by many biological, chemical and physical processes that are certainly not random. Thus, by comparing tissue to a random model, many of these processes could be misinterpreted by randomness in the assembly. Another disadvantage is that at the beginning, we know that our model will probably misjudge some properties of epithelial morphology. For example, in the random assembly of ellipses, two ellipses can be arbitrary close to each other. Opposite of that, this is certainly not the case in epithelial tissue because we always need to have some space for cell membranes between two cell nuclei.

As part of our previous work, we compared random assemblies of ellipses fitted to cell nuclei with experimental cell tissue morphological measures. We found that random assembly of ellipses recovers distributions of



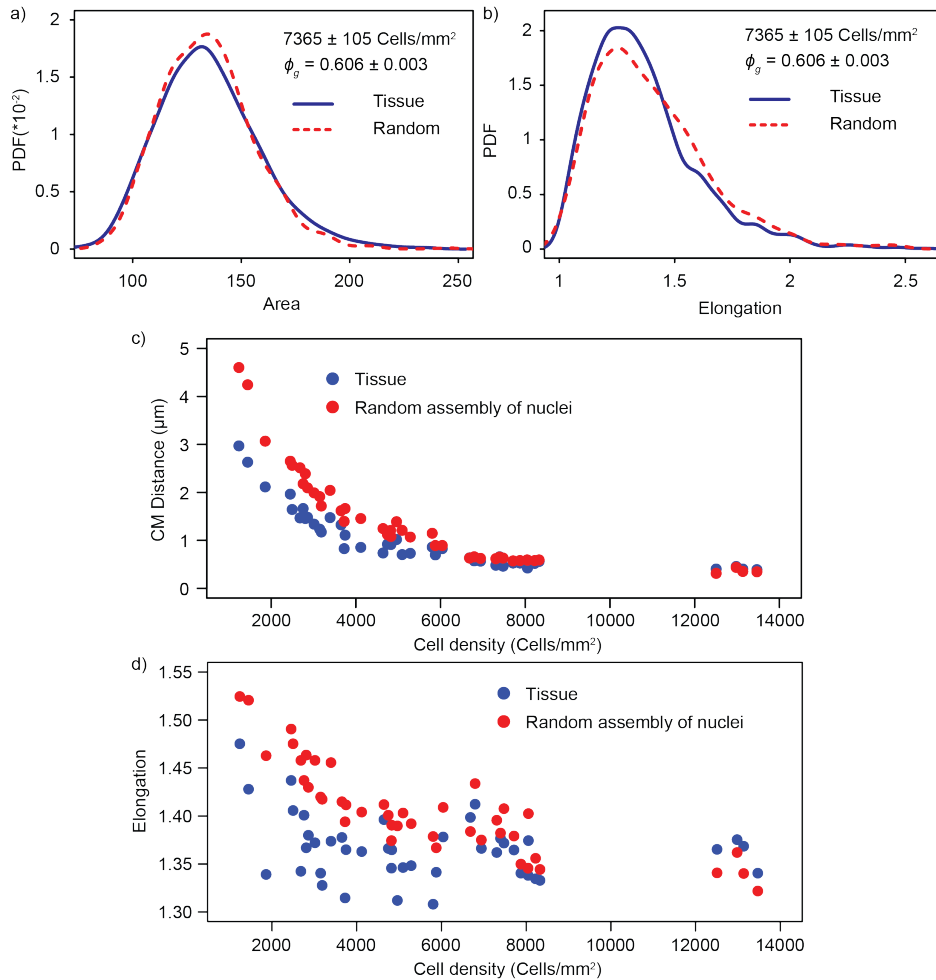


FIGURE 5.8: Comparison of the cell tissue to the random assembly of ellipses fitted to cell nuclei. Blue colour denotes experimental data, and red colour denotes random assemblies. a) Distributions of the cell area at cell density of approximately  $7365 \text{ Cells/mm}^2$ . b) Distributions of the cell elongation at cell density of approximately  $7365 \text{ Cells/mm}^2$ . c) Means of the CM distance plotted versus various cell densities. d) Means of the cell elongation plotted versus various cell densities.

morphological measures of tissue well at all cell densities. However, the difference between compared distributions is statistically significant (example in Figure 5.8a,b). The details of this work were published in references [75, 97].

The actual deviations of tissue from the random assembly of ellipses are apparent when observing the cell nuclei positions inside the cells and the shape of the cells. Thus, Figure 5.8c presents the distance between the centre

of the mass of the Voronoi cell to the centre of mass of cell nuclei (CM distance) plotted for experimental data and a random assembly of ellipses. We find that in tissue, cell nuclei tend to be closer to the centre of mass of the cell than in a random model. This difference in the CM distance is systematic for all cell densities but more pronounced at low cell densities. The cell nucleus has more spatial freedom to actively position itself at the low density than on high cell densities. Another phenomenon regarding CM distance is that both in cell tissues and random assemblies, the CM distance points follow a decreasing line when plotted versus cell density. This phenomenon can be explained by the fact that ellipses or nuclei have less space to adopt arbitrary positions at high cell density because they occupy more space inside cells.

As we mentioned before, another morphological measure that points out the difference between random model and actual tissue is cell elongation, a measure that describes the cell shape. Figure 5.8d presents the mean elongation of cells for random assembly and actual cell tissue at given cell densities. Similar to the case of CM distance, we find that at the same cell density, tissue cells are generally less elongated, and therefore rounder, than Voronoi cells of randomly assembled ellipses. The difference in elongation between the two systems is also more pronounced at low cell densities than at high cell densities. However, opposite the case with CM distance, the mean elongation both in cell tissue and random model has a different trend when studying its dependence on cell density. Firstly, mean elongations drop when cell density increases to around 3000 and remain approximately constant for the following densities. We believe this is since as cell density increases, the Voronoi cells tend to adopt the shape of its generating ellipses, as was shown in Chapter 3. Further evidence of this claim can be found in the fact that the mean elongations adopt similar values to the elongation values of cell nuclei presented in Figure 5.7b.

### 5.3 Lloyd's iterations as a model for tissue

Results presented earlier in this chapter suggest an active mechanism that keeps tissue in a steady state. One of the main properties of this mechanism is pushing cell nuclei towards the centres of mass of its cells. While doing that, tissue tends to keep cell elongation approximately constant for different densities (Figure 5.8d) with values that are lower than in the random model.

Moreover, as discussed in the previous section, patterns in tissue with a relatively uniform density point out other properties of such an active mechanism. Previously mentioned facts that tissue actively regulates its structure are basic properties related to Lloyd's algorithm in previous chapters of this thesis. Therefore, these results motivate us to introduce modified Lloyd's iterations as an upgrade to a model based on the random assembly of cell nuclei.

Because random assemblies of ellipses are a good approximation for epithelial tissue morphology, it is natural to use them as a starting point for modified Lloyd's optimization. We hope that after modified Lloyd's algorithm converges, the obtained structures will be a better approximation for epithelial tissue than the random assembly of ellipses. We performed modified Lloyd's optimization of random assemblies of ellipses fitted to nuclei with the same algorithm that we defined in Chapter 4 of this thesis. In the simulations, we set parameter  $\eta$ , which is responsible for controlling the movement freedom of the ellipses when annulling overlaps caused by the centralization, to the mean value of minor semi-axis of ellipses fitted to cell nuclei. It is important to recall that the final structures of Lloyd's algorithm do not depend on values of parameter  $\eta$ , as was shown in Chapter 4. We applied 1000 iterations of Lloyd's algorithm to ellipse assemblies since it is enough to converge the structure fully (Chapter 4).

Since we found locally ordered domains with an absence of significant density fluctuations in tissue clusters, we decided to use such tissue patches as targets for our model. Thus, because of Lloyd's algorithm suppression of density fluctuations, such tissue parts seem like datasets that might be reproducible by our simulations. Those tissue patches consist of a few hundred cells. For each studied cell density in the following lines, we have simulated a few such datasets and then combined them to achieve larger samples.

### 5.3.1 Structure factors after applying the modified Lloyd's iterations

Figure 5.9 presents structure factors of experimental tissue data, random assemblies of ellipses fitted to cell nuclei and systems after application of 1 and 1000 Lloyd's iterations. Depending on the system, structure factors were also calculated for point patterns defined by centres of mass of nuclei or ellipses.

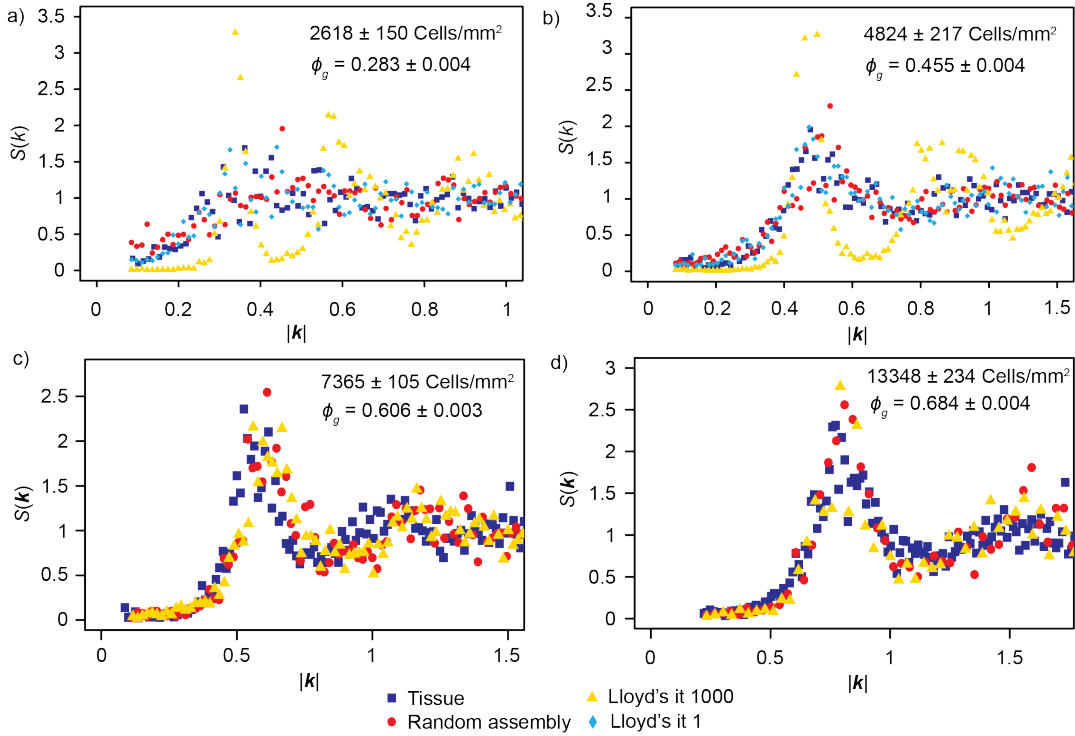


FIGURE 5.9: Structure factors of experimental tissue (dark blue), random assemblies of ellipses fitted to cell nuclei (red) and modified Lloyd's iterations of those assemblies (light blue for iteration 1 and yellow for iteration 1000). Insets in the figures denote cell densities and packing fractions of the systems. All wavelengths  $\lambda$  are in micrometers ( $|\mathbf{k}| = \frac{1}{2\pi\lambda}$ ). a) Cell density 2618 Cells/mm<sup>2</sup> b) Cell density 4824 Cells/mm<sup>2</sup> c) Cell density 7365 Cells/mm<sup>2</sup> d) Cell density 13348 Cells/mm<sup>2</sup>

We considered wavenumbers  $|\mathbf{k}|$  that are greater than  $4 \times |\mathbf{k}_{min}|$  where  $|\mathbf{k}_{min}|$  is the shortest possible wavenumber that corresponds to the size of the system.

The first notable phenomenon from Figure 5.9 is that, similar as it was the case with morphological measures, structure factors of the experimental epithelial tissue data and random assemblies coincide very well. The overlap of structure factors between tissue data and random assemblies is most pronounced at higher cell densities (Figure 5.9c and 5.9d). At lower cell densities (Figure 5.9a and 5.9b), structure factors also agree very well, but with some deviations for small wavenumbers. On the other side, structure factors of assemblies after application of 1000 modified Lloyd's iterations reveal entirely different behaviours and trends. At low cell densities (Figure 5.9a and 5.9b), structure factors possess clear and expressed peaks, unlike the structure factors of random ellipse assemblies and tissue. Moreover, structure factors adopt very small values for small wavenumbers with  $H$  measure below

$10^{-2}$  meaning the obtained systems are effectively hyperuniform. On the other hand, at higher cell densities (Figure 5.9c and 5.9d), structure factors of assemblies after application of Lloyd's iterations overlap with structure factors of the other two systems with great precision. Furthermore, we find that structure factors of ellipse assemblies after just 1 iteration of modified Lloyd's algorithm have approximately the same appearance as structure factors of random assemblies of tissue (Figure 5.9a and 5.9b). Such appearance can be explained by the fact that significant reorganization does not occur only after 1 iteration of modified Lloyd's algorithm.

After applying modified Lloyd's algorithm, previously presented results concerning the system's structural properties are not surprising considering the results discussed in Chapter 4 of this thesis. Let us remember that modified Lloyd's optimization introduced effective hyperuniformity at small packing fractions into monodisperse assemblies. At higher packing fractions, it did not change the ellipse organization significantly. Hence, previous results are mostly the consequence of the effects of modified Lloyd's iterations on systems due to different densities. Our findings become even more obvious if we observe packing fractions  $\phi_g$  that correspond to considered cell densities and place the systems according to the packing fraction and the mean nuclei elongation into the phase space presented in Chapter 4. We find that the tissue with the lowest studied cell density (2618 Cells/mm<sup>2</sup>) where final configurations are effectively hyperuniform falls to the part of the phase space where such effects are expected. Similarly, tissues with cell densities 7365 Cells/mm<sup>2</sup> and 13348 Cells/mm<sup>2</sup> belong to the part of phase space where the modified Lloyd's algorithm is expected not to have any significant effect on structural characteristics of the assembly. The only exception is a tissue with cell density of 4824 Cells/mm<sup>2</sup>. According to the mentioned phase space diagram (Chapter 4), Lloyd's algorithm should not introduce effective hyperuniformity to this system (since packing fraction  $\phi_g = 0.455$  and mean nuclei elongation  $e \approx 1.4$ ), which is opposite of our previous finding. This deviation can be explained by the fact that considered visualization of the phase space examines monodisperse assemblies, and our system is polydisperse, meaning all cell nuclei have a different shape (Figure 5.7). Since the mentioned system is very close to the border that separates two different regimes of the modified Lloyd's algorithm, the fact that our system is polydisperse could explain different behaviour of the system under modified Lloyd's iterations than predicted by the phase space diagram.

### 5.3.2 Morphological measures after applying the modified Lloyd's iterations

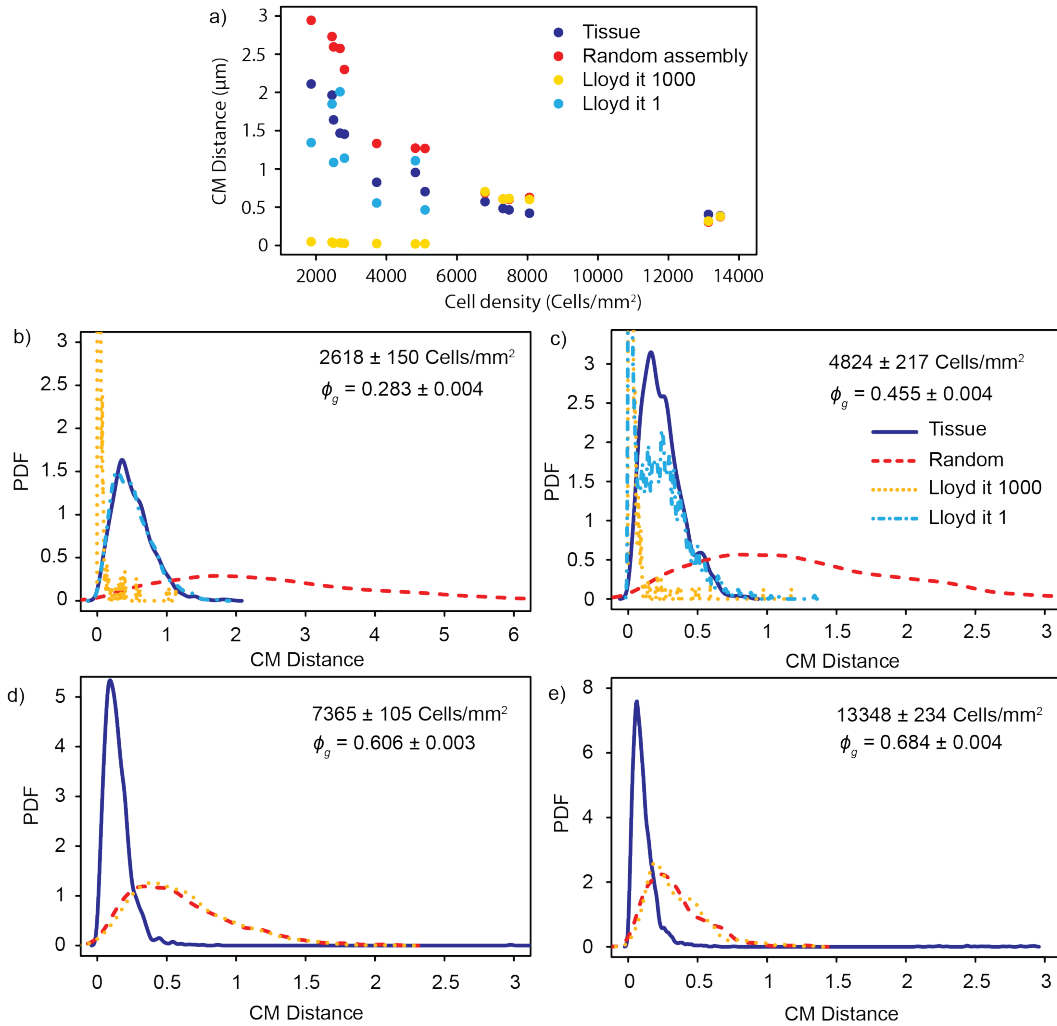


FIGURE 5.10: Properties of CM distance morphological measure distributions. Dark blue colour represents real experimental tissue data, red colour denotes random assembly of ellipses fitted to cell nuclei, light blue colour represents ellipse assembly after only 1 iteration of modified Lloyd's algorithm and yellow colour denotes ellipse assembly after 1000 modified Lloyd's iterations. a) Means of the CM distance plotted versus various cell densities. b) CM distance distributions at cell density of  $2618 \pm 150 \text{ Cells}/\text{mm}^2$  c) CM distance distributions at cell density of  $4824 \pm 217 \text{ Cells}/\text{mm}^2$  d) CM distance distributions at cell density of  $7365 \pm 105 \text{ Cells}/\text{mm}^2$  e) CM distance distributions at cell density of  $13348 \pm 234 \text{ Cells}/\text{mm}^2$

In order to further investigate the outcome of modified Lloyd's iterations in tissue modelling, we studied properties of distributions of various morphological measures defined in Chapter 3 calculated for systems that are an outcome of Lloyd's algorithm. First of all, we investigated distributions of CM distance morphological measure and presented the most exciting results in Figure 5.10. We find that at low cell densities, the mean CM distance falls close to 0 after application of Lloyd's algorithm, proving that those systems are nearly fully centralized (Figure 5.10a). Thus, Lloyd's algorithm decreases the mean CM distance much more than cell tissue from the random assemblies point of view, meaning random assembly approximates CM distance of tissue much better than fully converged modified Lloyd's optimization. However, we find that the first iteration of modified Lloyd's algorithm reproduces the mean CM distance better than the fully converged modified Lloyd's algorithm. At higher cell densities, the mean CM distance after applying modified Lloyd's algorithm is almost equal to the mean CM distance of the random assemblies.

We can draw similar conclusions based on the appearance of CM Distance empirical probability density functions (Figures 5.10b-e). We find that independent of cell density, CM distance distributions in tissue are much narrower than random nuclei assembly distributions with a shift to the left at lower cell densities. Moreover, after fully applying modified Lloyd's algorithm, the CM distance distributions become even narrower with an additional shift to the left at low densities. In contrast, they remain similar to the CM distance distributions of random assemblies at higher densities. This phenomenon is a sign of centralization that occurs under Lloyd's algorithm at lower densities of the system. Similar to the case of the mean CM distance (Figure 5.10a), distributions after only 1 iteration of modified Lloyd's algorithm approximate tissue data much better than the fully converged modified Lloyd's algorithm.

Similar conclusions can be derived by observing distributions of cell elongation after application of modified Lloyd's algorithm (Figure 5.11). We find that at lower cell densities, modified Lloyd's algorithm decreases mean elongation in the systems significantly, resulting in that the random assemblies approximate morphology of tissue much better than 1000th iteration of modified Lloyd's optimization (Figure 5.11a). However, similarly to the CM distance measure, iteration 1 of modified Lloyd's algorithm approximates tissue data better than the fully converged algorithm. At higher cell densities, the

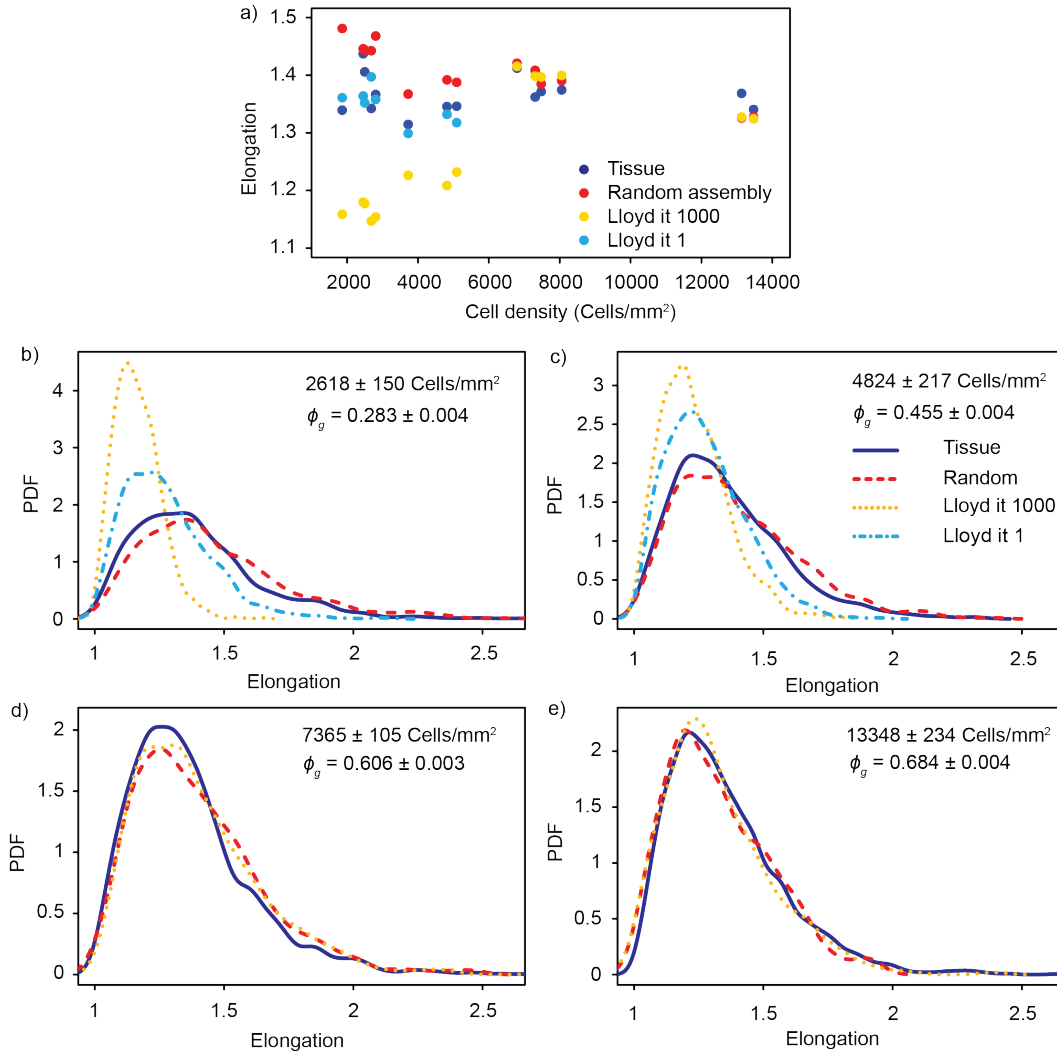


FIGURE 5.11: Properties of cell elongation morphological measure distributions. Dark blue colour represents real experimental tissue data, red colour denotes random assembly of ellipses fitted to cell nuclei, light blue colour represents ellipse assembly after only 1 iteration of modified Lloyd's algorithm and yellow colour denotes ellipse assembly after 1000 modified Lloyd's iterations. a) Means of the cell elongation plotted versus various cell densities. b) Cell elongation distributions at cell density of  $2618 \pm 150$  Cells/mm<sup>2</sup> c) Cell elongation distributions at cell density of  $4824 \pm 217$  Cells/mm<sup>2</sup> d) Cell elongation distributions at cell density of  $7365 \pm 105$  Cells/mm<sup>2</sup> e) Cell elongation distributions at cell density of  $13348 \pm 234$  Cells/mm<sup>2</sup>

mean cell elongation of random assemblies and assemblies after application of modified Lloyd's iterations is nearly equal, further proving that modified Lloyd's algorithm does not introduce any novelty to systems at high cell densities.



Moreover, by investigating true distributions of cell elongation after application of modified Lloyd's iterations (Figure 5.11b-e), we find, as in the case of CM distance, narrowing of distributions at low cell densities. This result points out a decrease in cell elongation variability in systems after applying modified Lloyd's iterations, which indicates that we obtain more ordered configurations. Similar to the case of CM distance distributions, at higher cell densities, elongation distributions remain unchanged after application of modified Lloyd's algorithm.

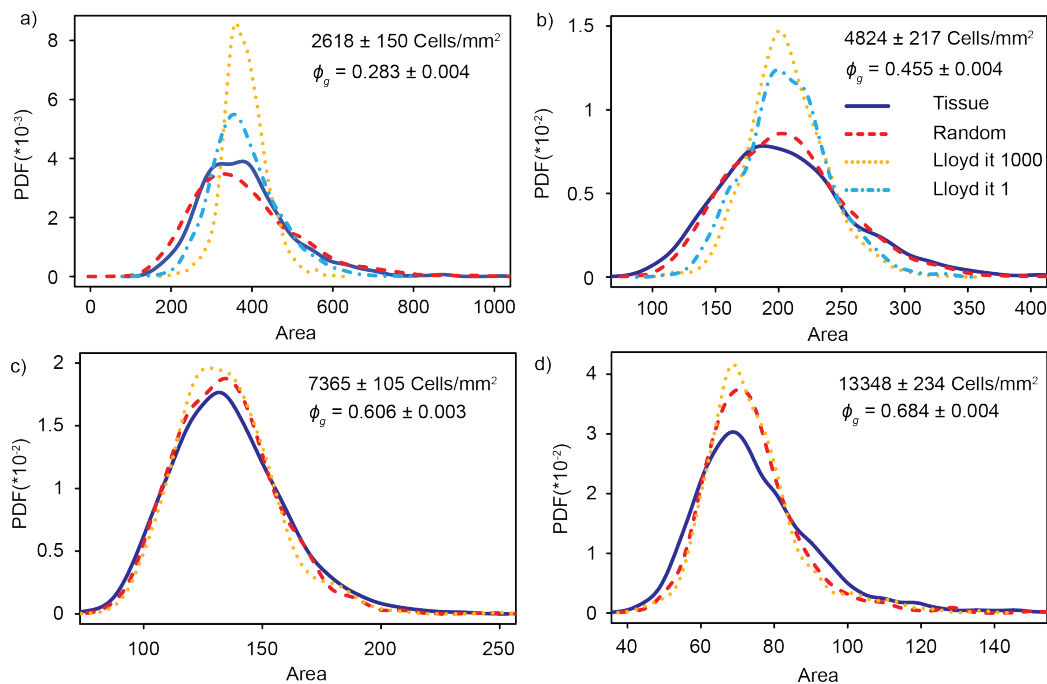


FIGURE 5.12: Cell area distributions. Dark blue colour represents real experimental tissue data, red colour denotes random assembly of ellipses fitted to cell nuclei, light blue colour represents ellipse assembly after only 1 iteration of modified Lloyd's algorithm and yellow colour denotes ellipse assembly after 1000 modified Lloyd's iterations. a) Cell density of  $2618 \pm 150$  Cells/mm<sup>2</sup> b) Cell density of  $4824 \pm 217$  Cells/mm<sup>2</sup> c) Cell density of  $7365 \pm 105$  Cells/mm<sup>2</sup> d) Cell density of  $13348 \pm 234$  Cells/mm<sup>2</sup>

Another morphological measure that we have investigated is cell area. As we pointed out earlier and as it can be concluded based on the Figure 5.12, random assembly of ellipses reproduces cell area distributions very well at all concerned cell densities. We find, in agreement with previously observed morphological measures, that modified Lloyd's algorithm narrows down cell area distributions at low packing fractions. In contrast, cell area distributions

remain practically unchanged at high packing fractions. Furthermore, the first iteration of modified Lloyd's algorithm, despite not being as good as the random model, is more similar to cell tissue than the 1000th iteration of modified Lloyd's algorithm.

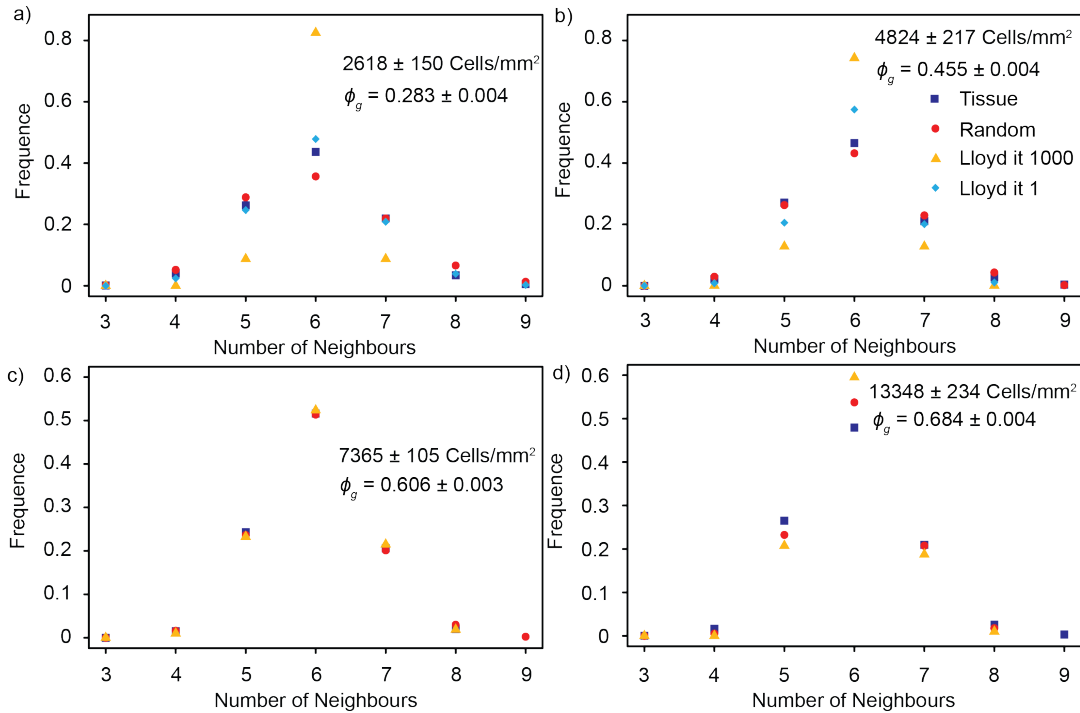


FIGURE 5.13: Number of neighbours distributions. Dark blue colour represents real experimental tissue data, red colour denotes random assembly of ellipses fitted to cell nuclei, light blue colour represents ellipse assembly after only 1 iteration of modified Lloyd's algorithm and yellow colour denotes ellipse assembly after 1000 modified Lloyd's iterations. a) Cell density of  $2618 \pm 150 \text{ Cells/mm}^2$  b) Cell density of  $4824 \pm 217 \text{ Cells/mm}^2$  c) Cell density of  $7365 \pm 105 \text{ Cells/mm}^2$  d) Cell density of  $13348 \pm 234 \text{ Cells/mm}^2$

Finally, we have investigated the number of neighbours of cells, a morphological measure that reveals information about the topological organization of cells in observed systems (Figure 5.13). Similarly to the case of previously studied morphological measures, we find that at lower cell densities modified Lloyd's algorithm narrows significantly the number of neighbours distributions resulting in a notable change in systems topology. As we can see from Figures 5.13a and 5.13b, around 80% of cells are hexagonal after application of Lloyd's algorithm, which is near twice as much as in actual tissue or random model. This phenomenon indicates a significant reorganization of cell neighbourhood under Lloyd's iterations. On the other hand, at

higher cell densities (Figure 5.13c and 5.13d), distributions of the number of neighbours remain practically unchanged. In agreement with the other morphological measures, we find that the first iteration approximates cell tissue much better than the 1000th iteration. However, it does not introduce any improvement to the random model.

## 5.4 Discussion and outlook

In the previous sections of this chapter, we have built our model for epithelial tissue structure from cell nuclei and described how an assembly of cell nuclei determines morphological properties of tissue. It was found earlier[75, 97] that random assembly of ellipses that represent cell nuclei can approximate tissue structure with great precision. Furthermore, we found interesting differences between random assembly as a model and actual tissue that point out an optimization mechanism in tissue that is similar to Lloyd's optimization.

However, when applying modified Lloyd's algorithm to random assemblies of ellipses fitted to cell nuclei, we saw that such optimization does not introduce any upgrade to our model. Hence, we found that random assembly is a much better model for tissue morphology at lower cell densities because modified Lloyd's optimization introduces a high degree of order to systems. On the other hand, modified Lloyd's optimization does not introduce any significant structural change to random assemblies of ellipses fitted to cell nuclei at higher cell densities. Both of these findings are in agreement with results presented and discussed earlier in Chapter 4.

However, it is interesting to notice that at lower cell densities, iteration 1 of modified Lloyd's algorithm approximates morphology of tissue with greater precision than fully converged modified Lloyd's algorithm. Even though the first iteration does not introduce any upgrade to the random model, it can motivate further study of the structuring of the epithelial tissue. Since data related to cell tissue, at low densities, lay somewhere between the random assembly of ellipses and converged modified Lloyd's algorithm, we can ask a question if only a partial movement of cell nuclei towards centres of mass of its cells would explain the morphology and structuring of the epithelium. As we see in Chapter 4, this partial movement can be achieved by tuning the parameter  $\kappa$  in modified Lloyd's algorithm. Since  $\kappa$  controls

the speed of centralization in modified Lloyd's algorithm by moving particles towards the centre of mass only by a fraction, a careful choice of  $\kappa$  could provide a better approximation of cell tissue at low cell densities.

## Chapter 6

# General conclusion

This thesis provided an extensive study of the Quantizer problem, an optimization question that is important for both scientific and practical purposes. The quantization problem can be solved by minimizing the total energy that calculates the total distance from arbitrary positions in space to the concerning points. The most effective and elegant way to solve the Quantizer problem is with Lloyd's algorithm, an iterative method that pushes generator point towards centres of mass of its Voronoi cells.

In the first chapter of this thesis, we studied the Quantizer problem's solutions in three-dimensional space obtained by Lloyd's minimization. As initial configurations for Lloyd's algorithm, we have used several amorphous point configurations with different spatial properties. Even though all initial configurations were random, they included both very disordered and highly ordered structures. After applying Lloyd's algorithm to those point processes, we found that the obtained solutions of the Quantizer problem have a universal structure. This structure is just like initial configurations amorphous, but it possesses a remarkable property of suppressed long-range density fluctuations, better known as effective hyperuniformity. This result provides new insight into the emergence of hyperuniformity in systems and links it to widely used concepts such as quantization and Lloyd's algorithm.

Moreover, we applied Lloyd's algorithm to point patterns that possess local crystalline patches and found that the corresponding Quantizer solutions have lower values of the total energy than the previously mentioned universal structure. Moreover, we found that those systems, despite the initial crystalline patches, are globally amorphous and effectively hyperuniform. This result contributes to the understanding of the complex total energy landscape, which has many local minima that correspond to locally optimal Quantizer solutions.

Motivated by the finding of effective hyperuniformity in the context of Quantizer solutions, we were curious how such long-range property appears in the systems composed of particles. Therefore, we decided to expand the Quantizer problem to assemblies of ellipses. First of all, in Chapter 3, we presented an in-depth study of assemblies of monodispersed ellipses that cover a broad range of shapes at different packing fractions. By studying distributions and correlations of various morphological measures, we were able to characterize how geometrical and topological properties of the assemblies are governed by the shape of the ellipses and different packing fractions. Besides that, we could reproduce and generalise many previously known results relevant to the study of particle assemblies and packings.

After understanding the fundamental properties of ellipse assemblies, we modified the Quantizer problem to generalize to the systems of non-trivial particles. Moreover, we modified Lloyd's algorithm by introducing an additional step that annuls particle overlaps into the procedure. By studying the modified total energy throughout modified Lloyd's iterations, we could relate the algorithm and newly modified Quantizer problem and provide numerical proof that the algorithm can be used to solve the problem. Similar to the case of the point generators, we have shown that modified Lloyd's algorithm can introduce effective hyperuniformity to systems of particles. Effective hyperuniformity was found for systems at lower packing fractions and assemblies at intermediate packing fractions that are consisted of circle-like particles. This exciting phenomenon shows that effective hyperuniformity can occur in assemblies of ellipses under the procedure that actively positions particles towards centres of mass of their Voronoi region. Therefore, the results presented in this chapter contribute to a deeper understanding of the origins of hyperuniformity in systems consisting of non-trivial particles.

Finally, as an example of a system that actively maintains its structure, we studied epithelial tissue. Because set Voronoi tessellation calculated from the tissue nuclei approximates cell membranes with very good accuracy, we studied the assemblies of cell nuclei to learn about the structure of the epithelium. We found that random assembly of ellipses fitted to cell nuclei is a good approximation for the epithelial geometry. However, by carefully studying chosen morphological measures, we found the fundamental difference between tissue and random assembly that motivated us to implement modified Lloyd's algorithm as a method to approximate the epithelium structure.

We find that fully converged modified Lloyd's algorithm, as concluded from the results presented in Chapter 4 of this thesis, produces structures that are much more ordered than the epithelium. However, we find that the first iteration of the modified Lloyd's algorithm explains some geometrical aspects of the epithelium well.

This thesis provided a link between two fundamental concepts, the Quantizer problem, and hyperuniformity of the system. Moreover, we generalized the Quantizer problem to systems of particles and showed that solving it introduces effective hyperuniformity to systems of particles. Therefore, we believe that our work provides a solid foundation for investigating properties such as hyperuniformity in systems consisting of particles.





## **Appendix A**

# **Geometric effects in random assemblies of ellipses**

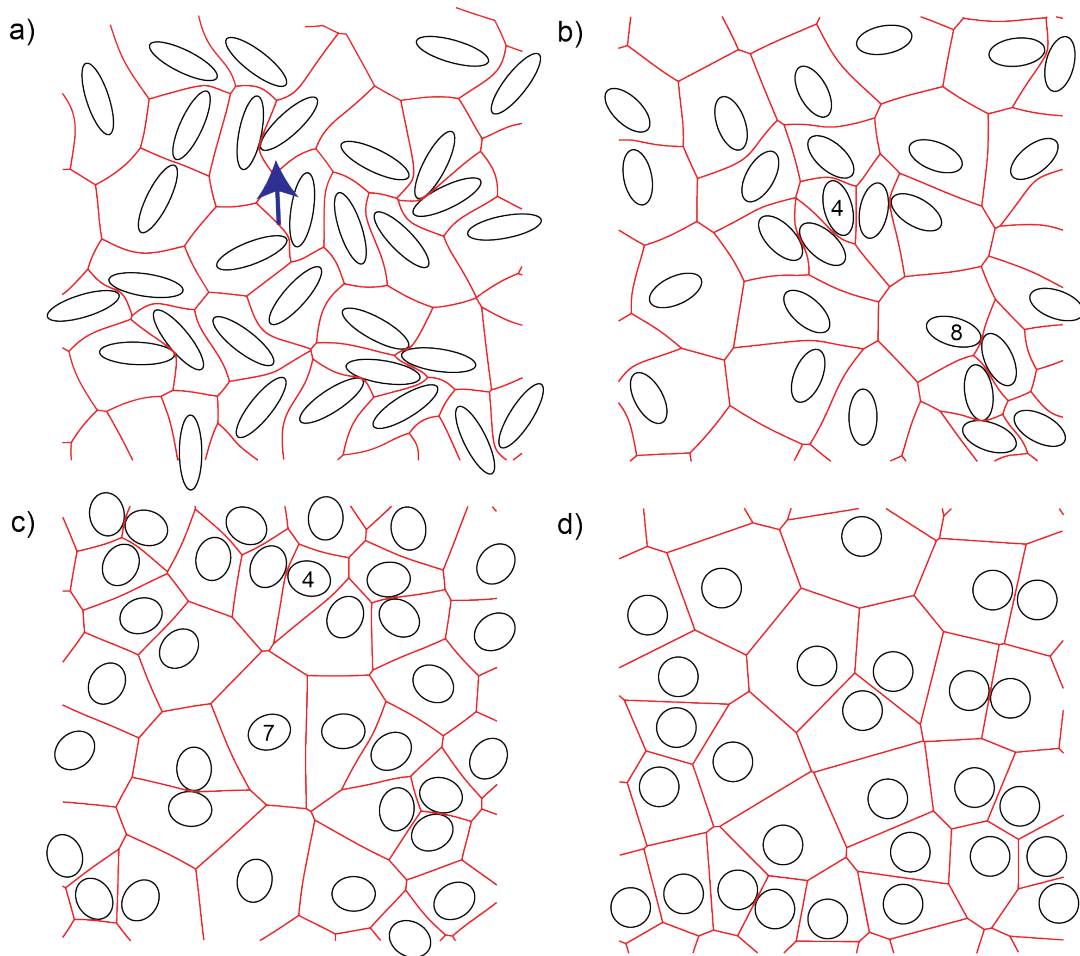


FIGURE A.1: Voronoi tessellation of randomly assembled ellipses at packing fraction  $\phi_g = 0.2$ . a)  $e = 3.33$  b)  $e = 2$ , c)  $e = 1.25$ , d)  $e = 1$ . This image was taken from reference [JL2].

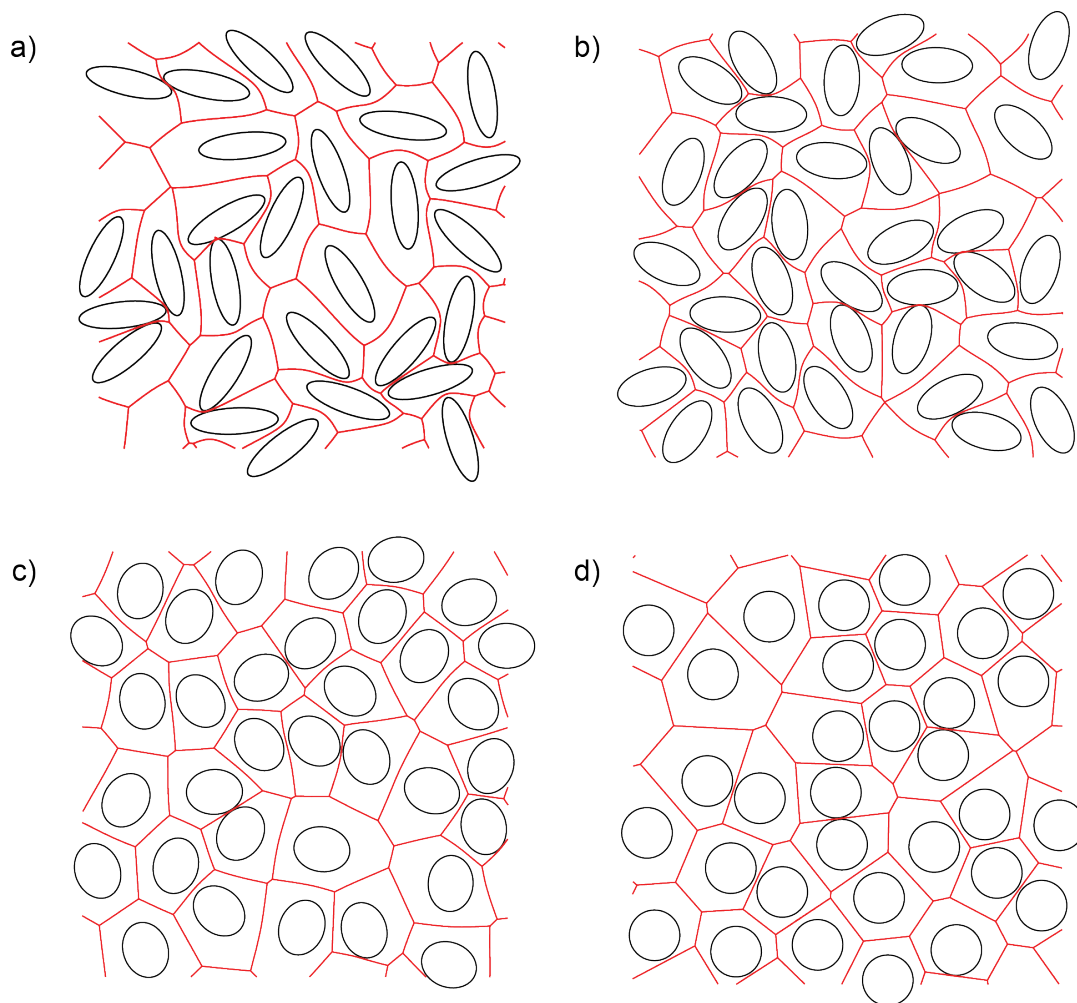


FIGURE A.2: Voronoi tessellation of randomly assembled ellipses at packing fraction  $\phi_g = 0.35$ . a)  $e = 3.33$  b)  $e = 2$ , c)  $e = 1.25$ , d)  $e = 1$ . This image was taken from reference [JL2].

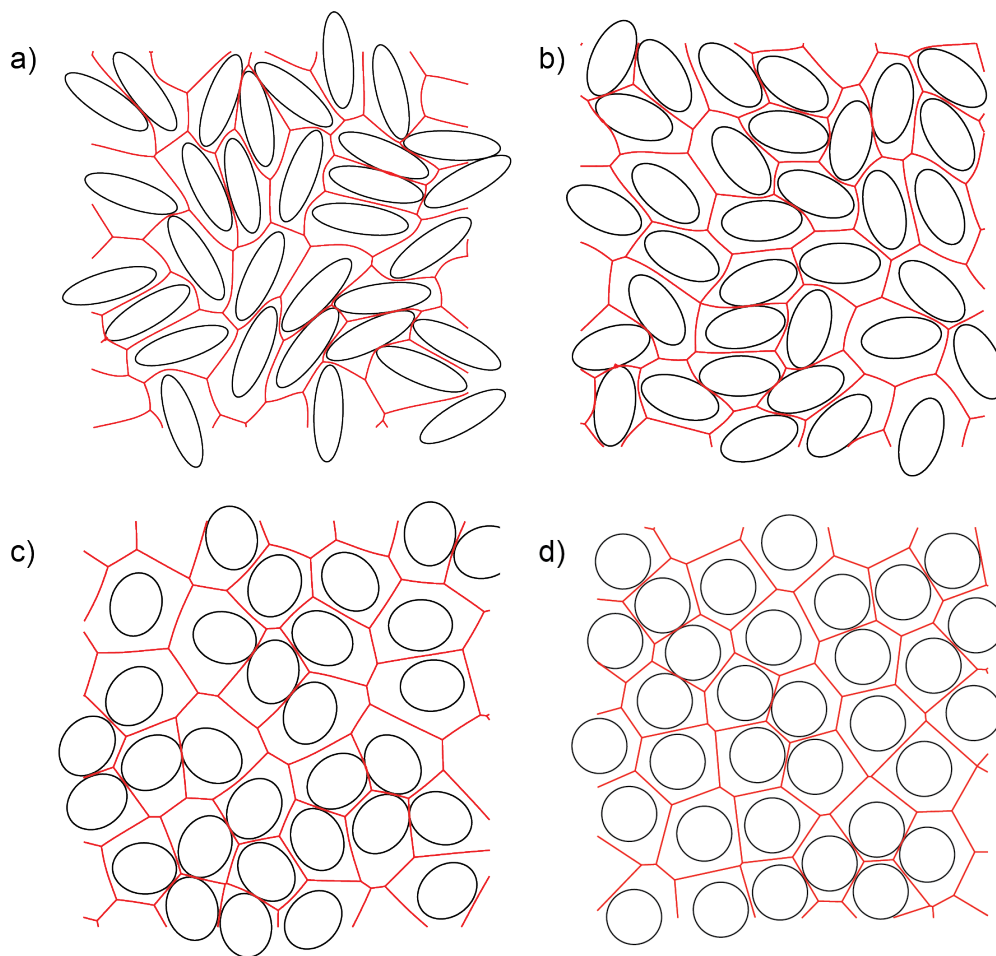


FIGURE A.3: Voronoi tessellation of randomly assembled ellipses at packing fraction  $\phi_g = 0.5$ . a)  $e = 3.33$  b)  $e = 2$ , c)  $e = 1.25$ , d)  $e = 1$ . This image was taken from reference [JL2].

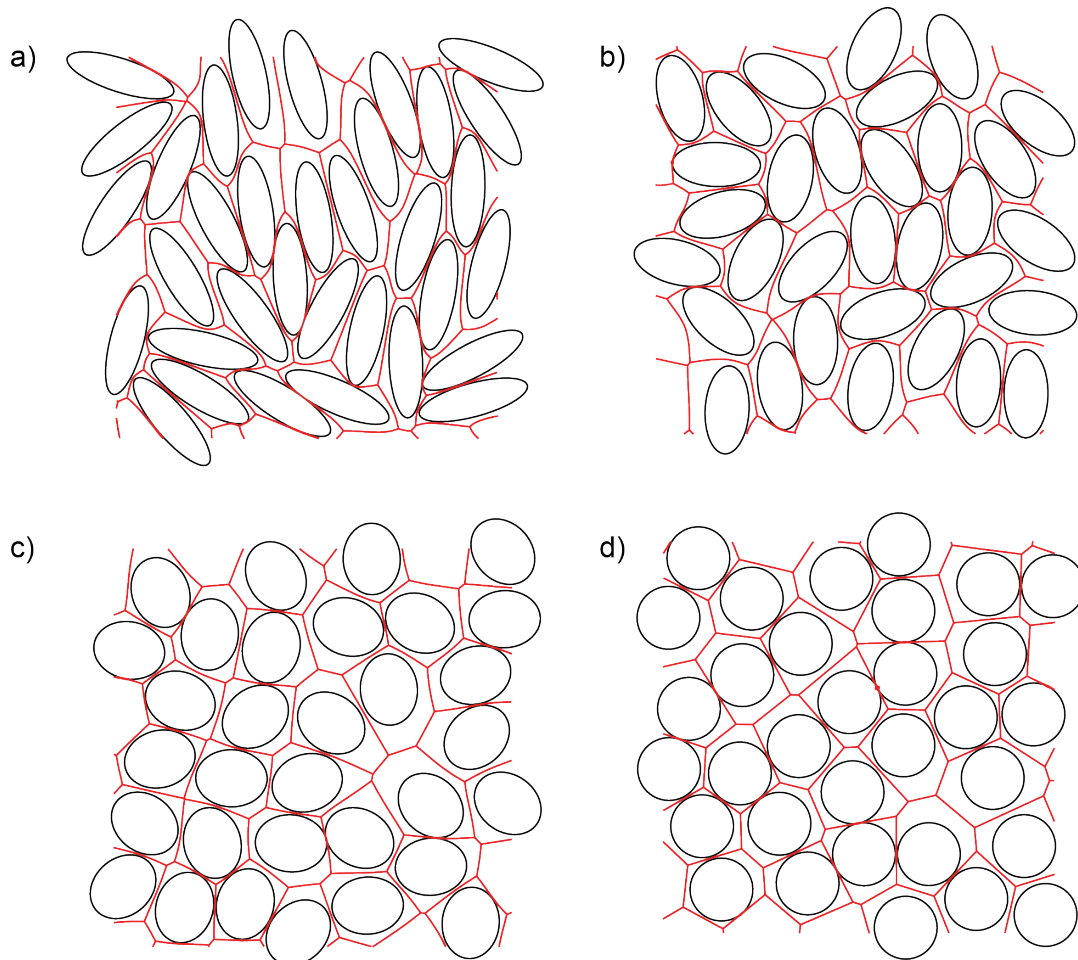


FIGURE A.4: Voronoi tessellation of randomly assembled ellipses at packing fraction  $\phi_g = 0.65$ . a)  $e = 3.33$  b)  $e = 2$ , c)  $e = 1.25$ , d)  $e = 1$ . This image was taken from reference [JL2].

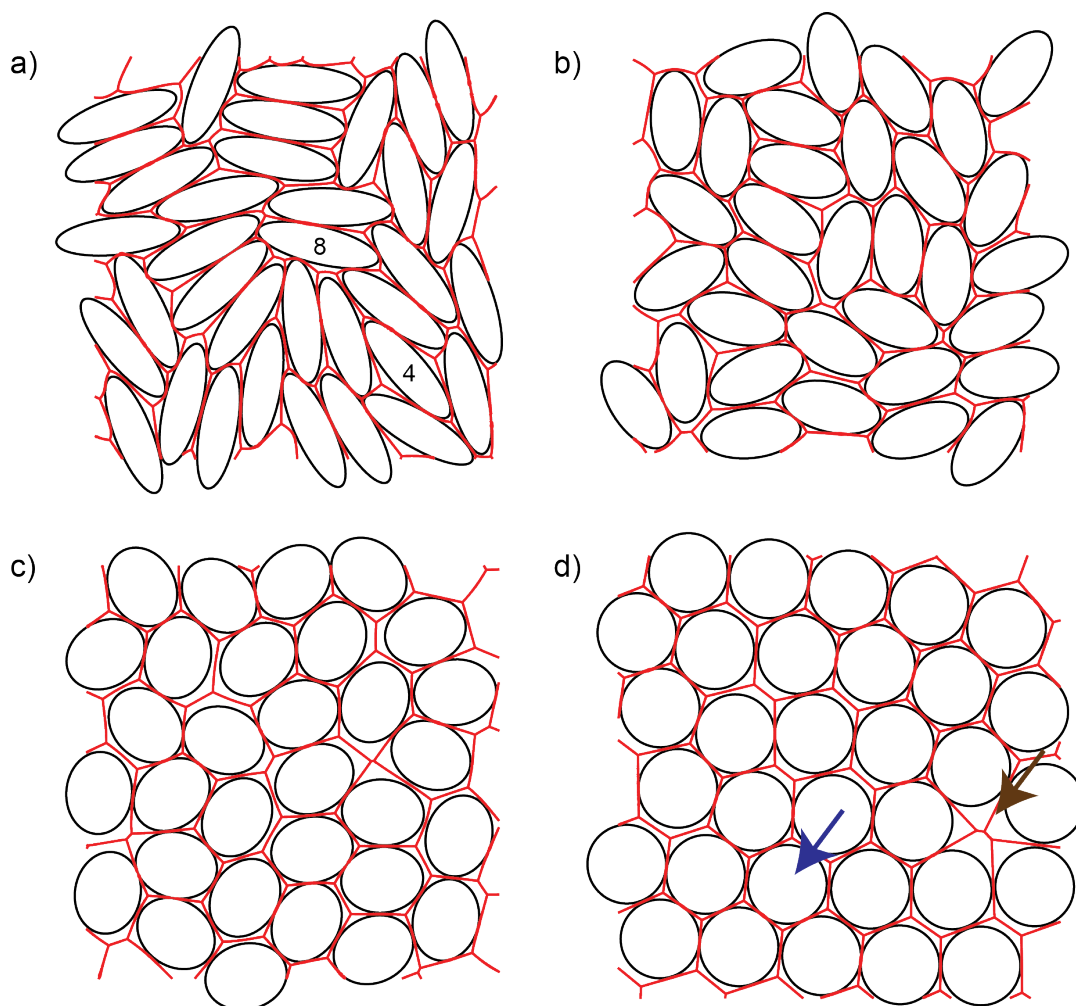


FIGURE A.5: Voronoi tessellation of randomly assembled ellipses at packing fraction  $\phi_g = 0.8$ . a)  $e = 3.33$  b)  $e = 2$ , c)  $e = 1.25$ , d)  $e = 1$ . This image was taken from reference [JL2].

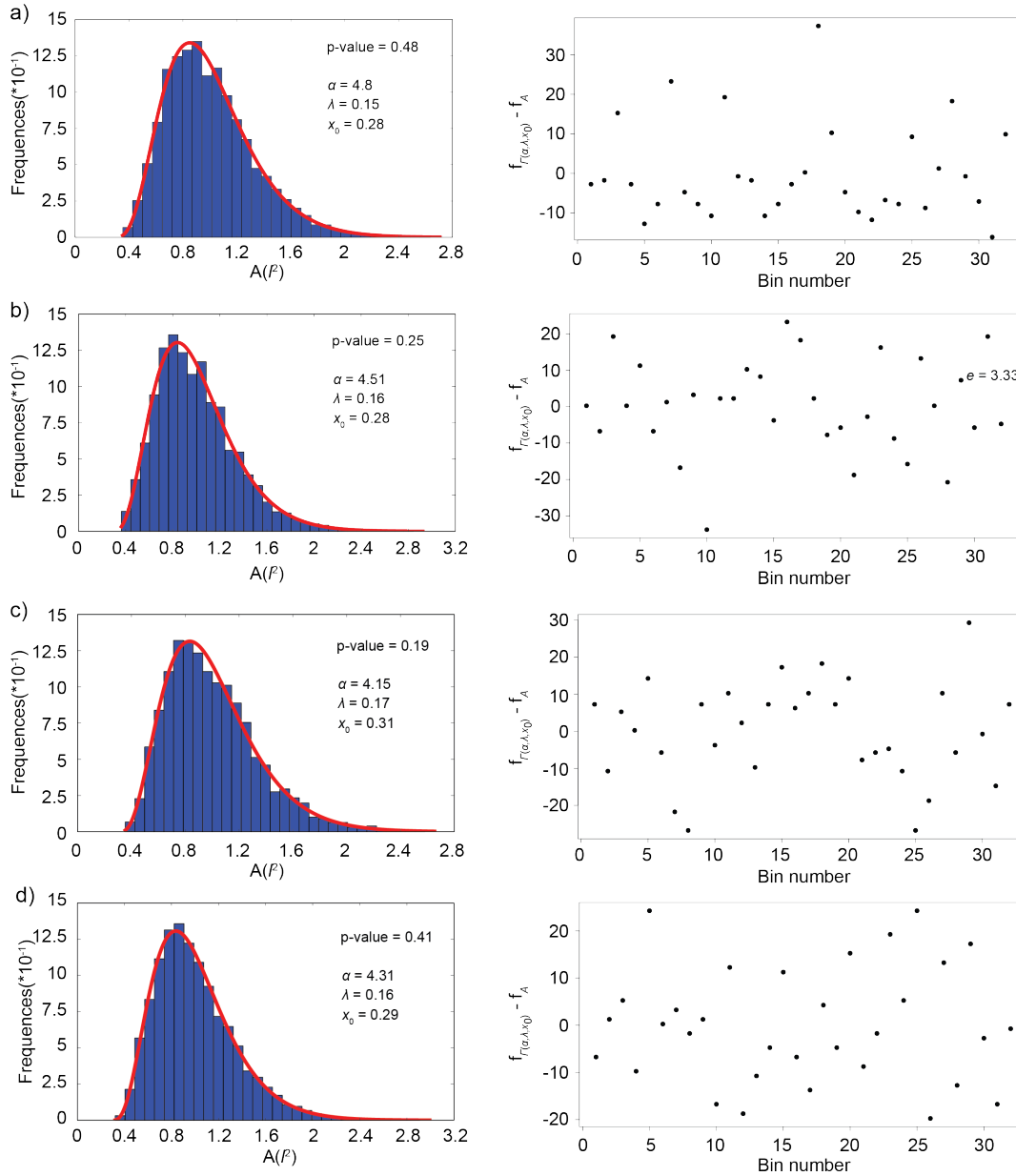


FIGURE A.6: Fits of gamma distribution to the cell area measure at packing fraction  $\phi_g = 0.2$ . Left figure shows fit together with  $p$ -value of  $\chi^2$  test and parameters of fitted distribution. Right figure shows difference between estimated(fitted) frequencies and observed frequencies for each bin in  $\chi^2$  test. a)  $e = 3.33$  b)  $e = 2$ , c)  $e = 1.25$ , d)  $e = 1$

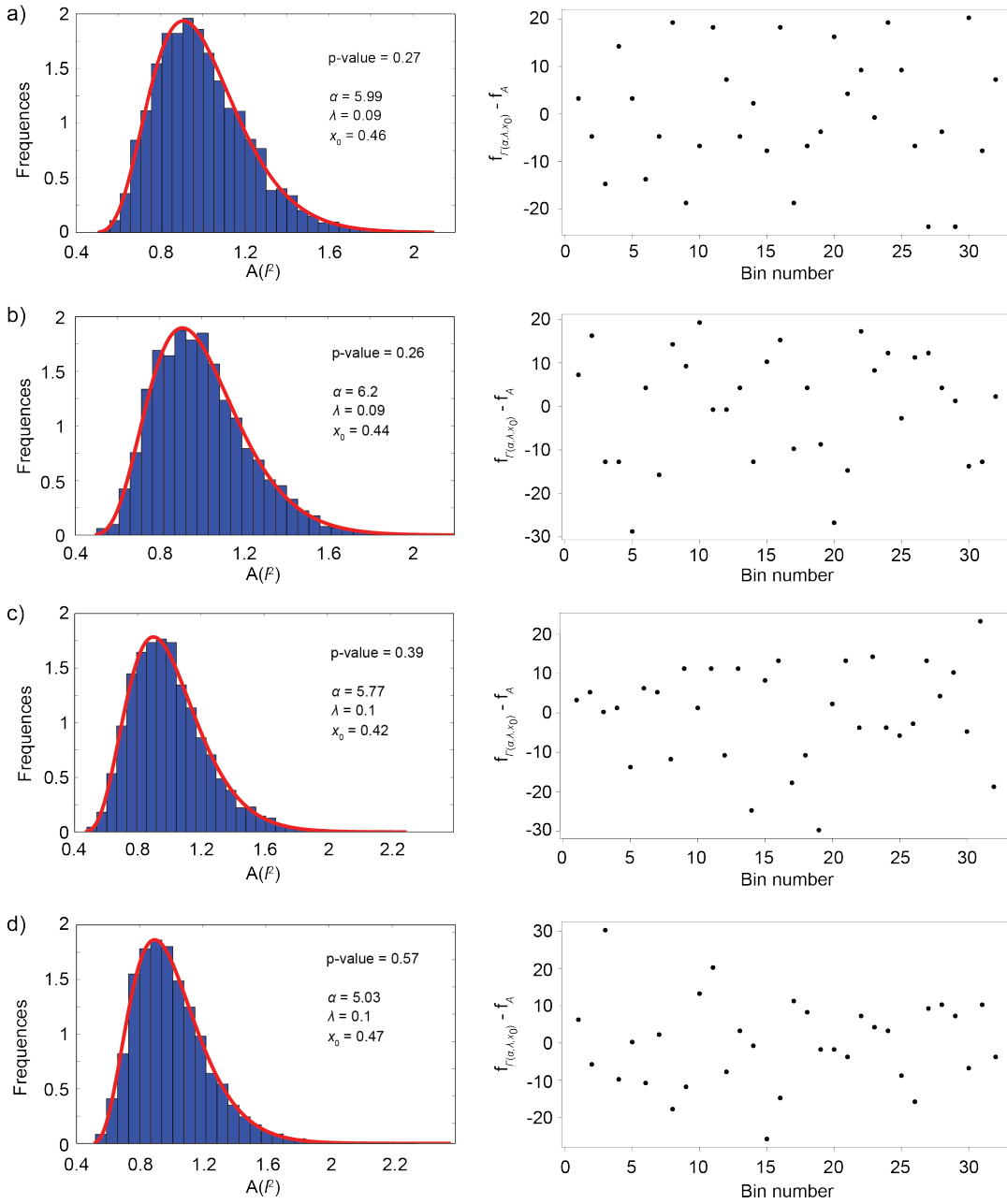


FIGURE A.7: Fits of gamma distribution to the cell area at packing fraction  $\phi_g = 0.35$ . Left figure shows fit together with p-value of  $\chi^2$  test and parameters of fitted distribution. Right figure shows difference between estimated frequencies and observed frequencies for each bin in  $\chi^2$  test. a)  $e = 3.33$  b)  $e = 2$ , c)  $e = 1.25$ , d)  $e = 1$ . This image was taken from reference [JL2].



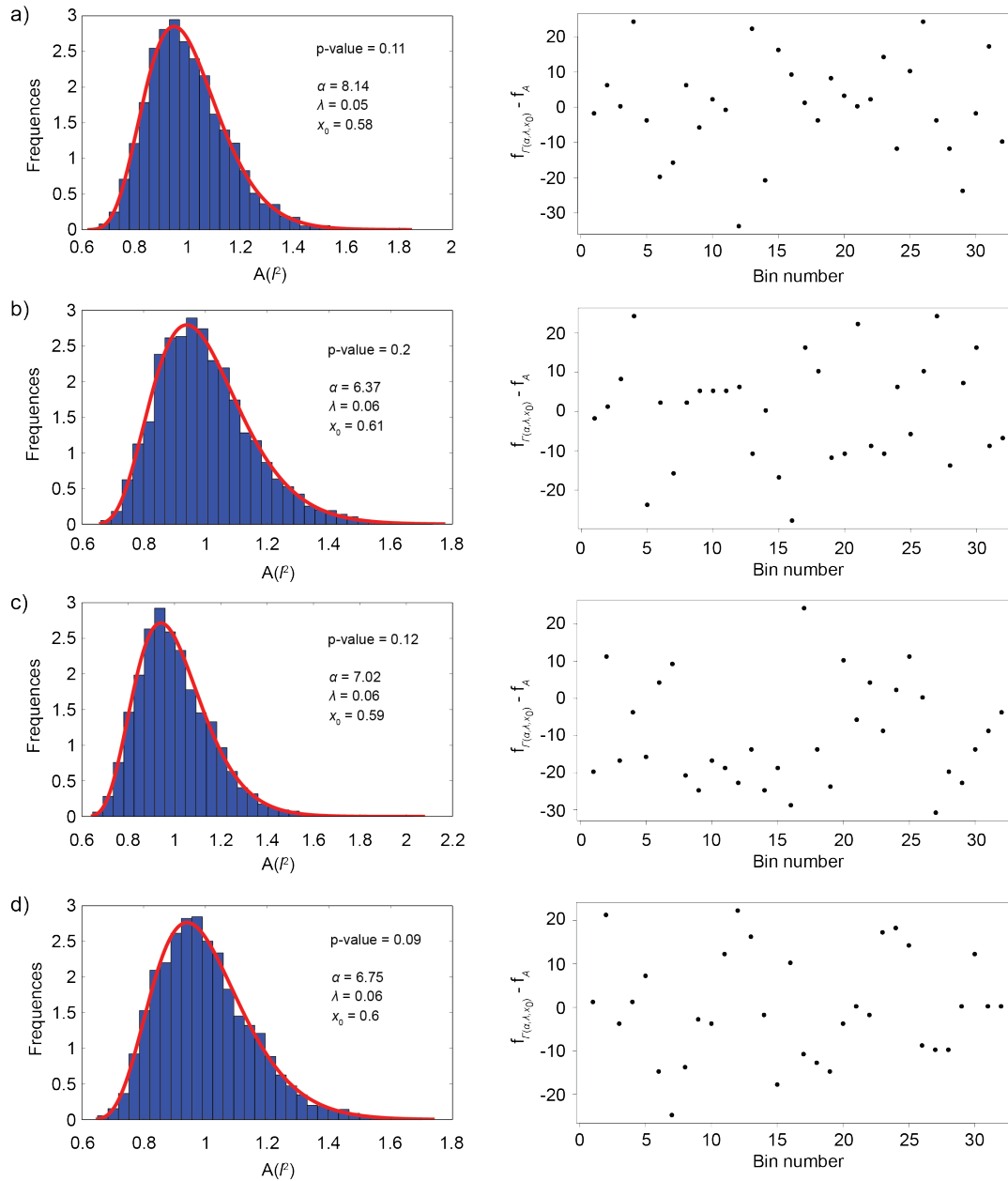


FIGURE A.8: Fits of gamma distribution to the cell area at packing fraction  $\phi_g = 0.5$ . Left figure shows fit together with p-value of  $\chi^2$  test and parameters of fitted distribution. Right figure shows difference between estimated frequencies and observed frequencies for each bin in  $\chi^2$  test. a)  $e = 3.33$  b)  $e = 2$ , c)  $e = 1.25$ , d)  $e = 1$ . This image was taken from reference [JL2].

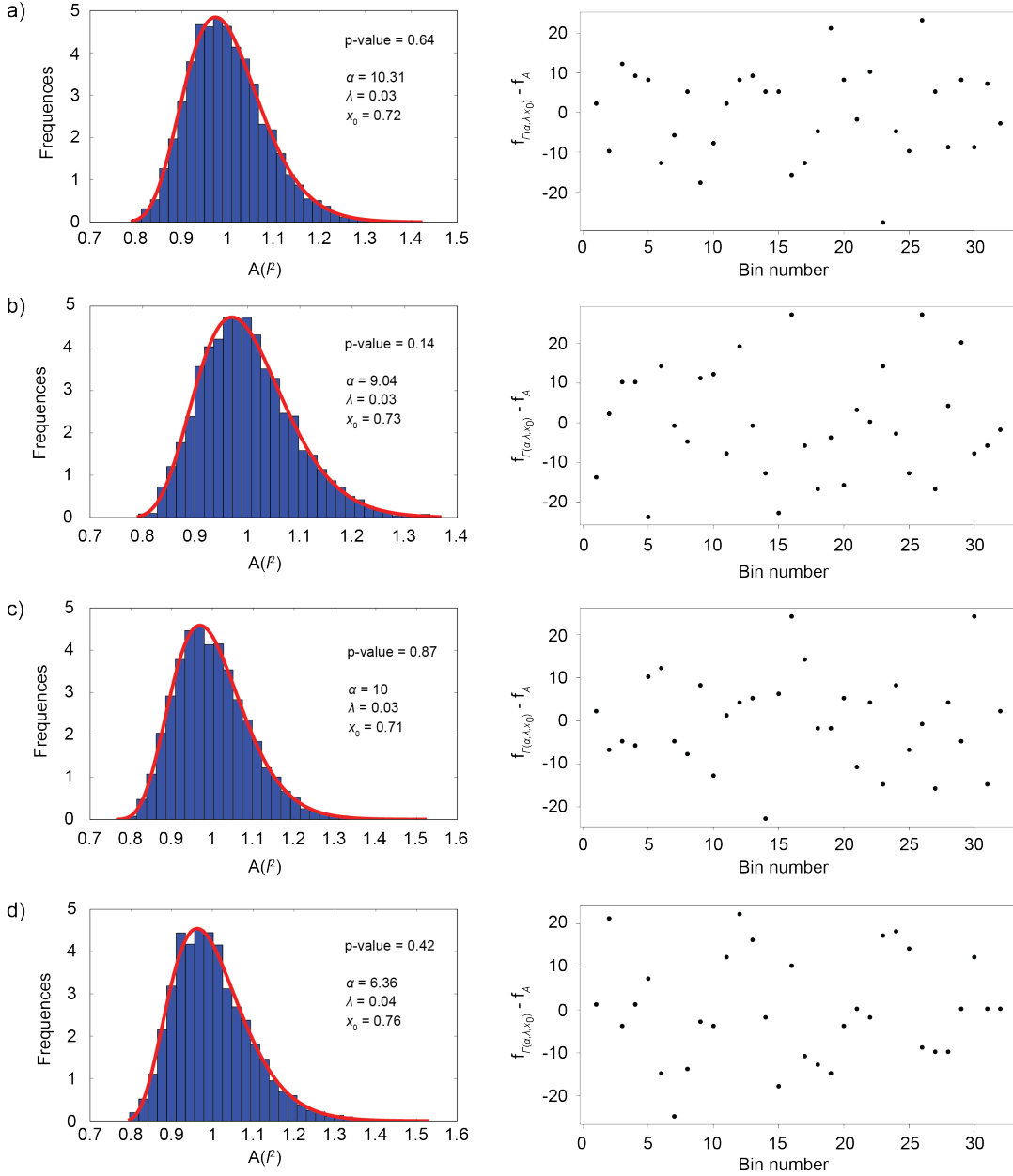


FIGURE A.9: Fits of gamma distribution to the cell area at packing fraction  $\phi_g = 0.65$ . Left figure shows fit together with p-value of  $\chi^2$  test and parameters of fitted distribution. Right figure shows difference between estimated frequencies and observed frequencies for each bin in  $\chi^2$  test. a)  $e = 3.33$  b)  $e = 2$ , c)  $e = 1.25$ , d)  $e = 1$ . This image was taken from reference [JL2].

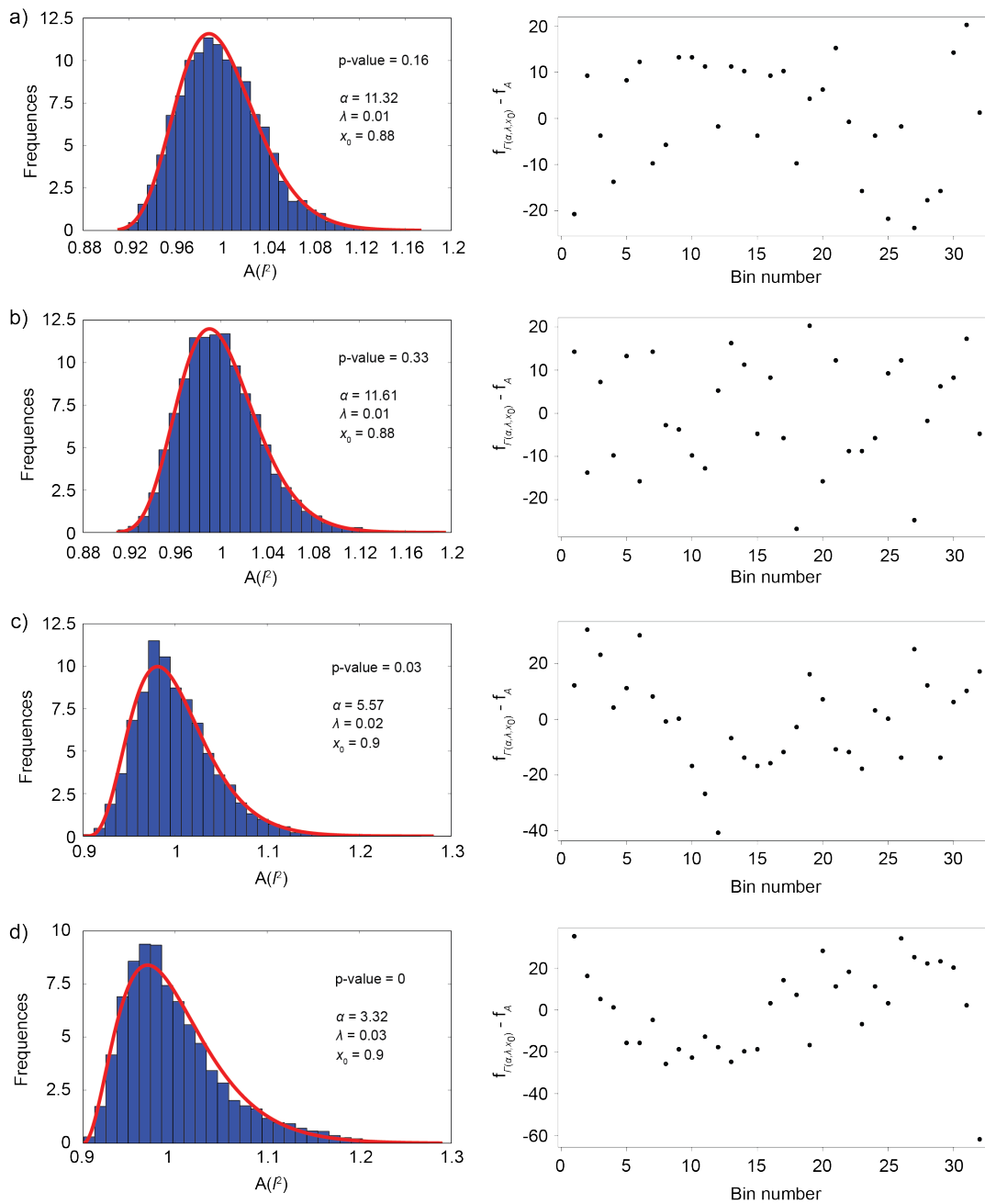


FIGURE A.10: Fits of gamma distribution to the cell area at packing fraction  $\phi_g = 0.8$ . Left figure shows fit together with  $p$ -value of  $\chi^2$  test and parameters of fitted distribution. Right figure shows difference between estimated frequencies and observed frequencies for each bin in  $\chi^2$  test. a)  $e = 3.33$  b)  $e = 2$ , c)  $e = 1.25$ , d)  $e = 1$ . This image was taken from reference [JL2].

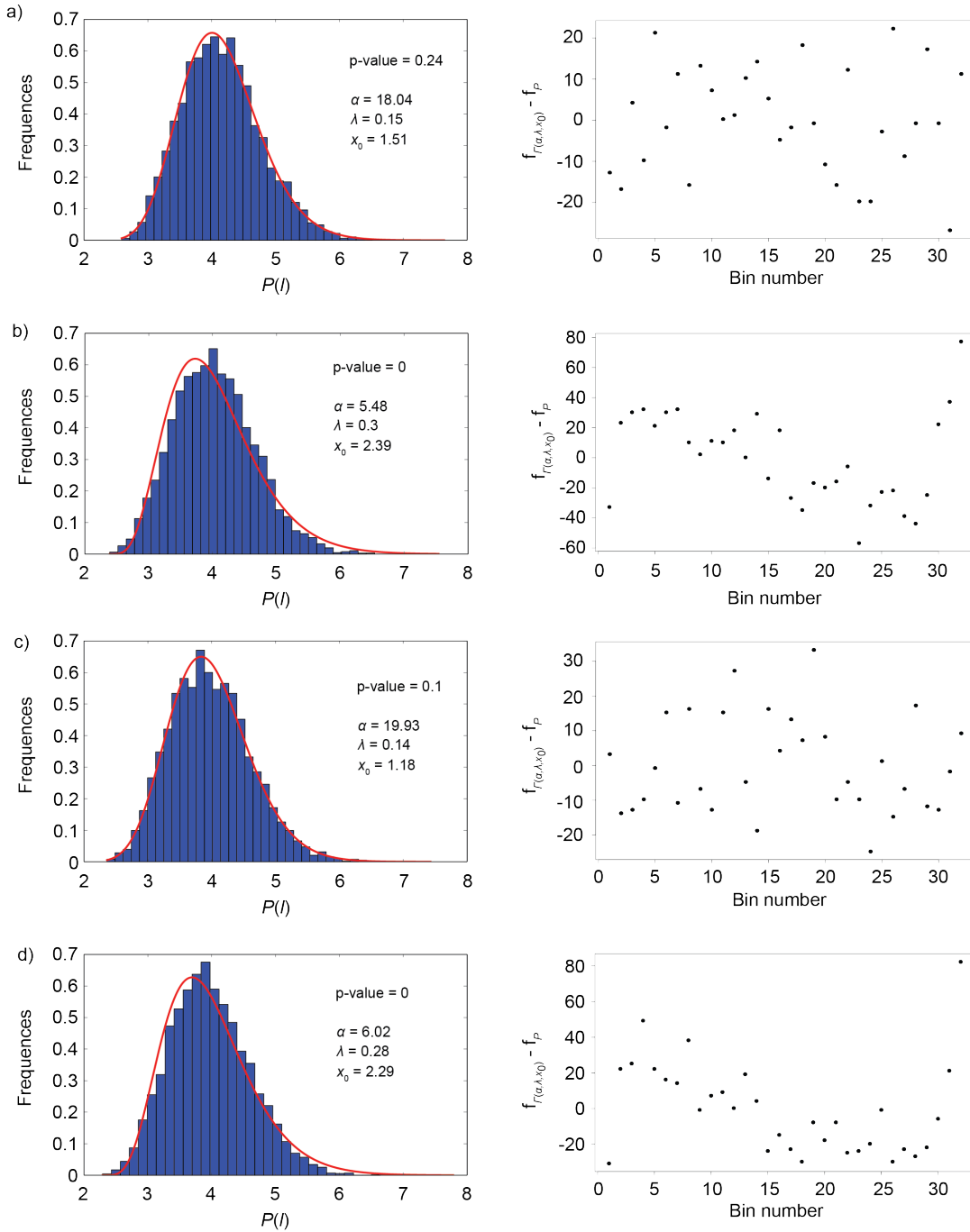


FIGURE A.11: Fits of gamma distribution to the cell perimeter at packing fraction  $\phi_g = 0.2$ . Left figure shows fit together with p-value of  $\chi^2$  test and parameters of fitted distribution. Right figure shows difference between estimated frequencies and observed frequencies for each bin in  $\chi^2$  test. a)  $e = 3.33$  b)  $e = 2$ , c)  $e = 1.25$ , d)  $e = 1$ . This image was taken from reference [JL2].

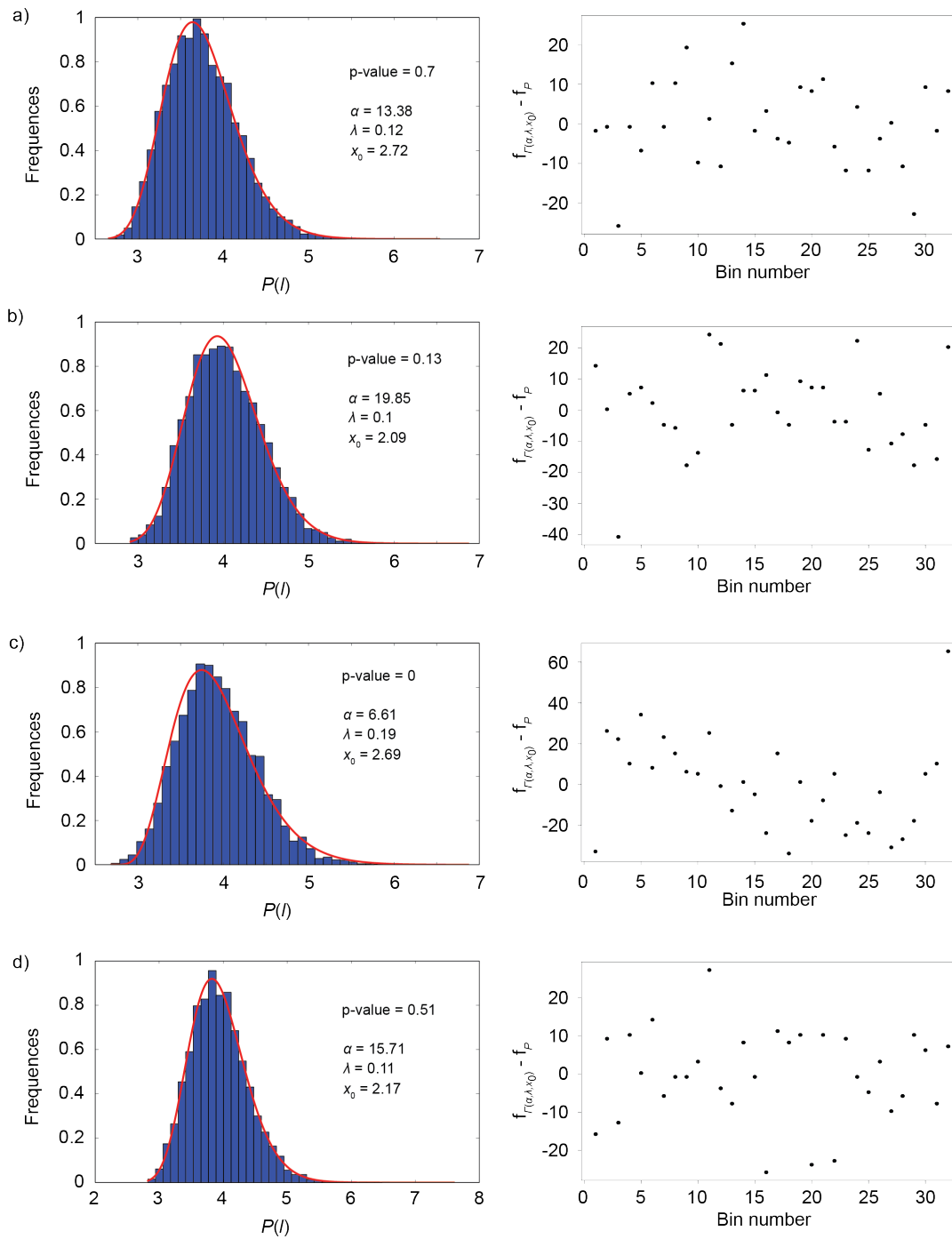


FIGURE A.12: Fits of gamma distribution to the cell perimeter at packing fraction  $\phi_g = 0.35$ . Left figure shows fit together with p-value of  $\chi^2$  test and parameters of fitted distribution. Right figure shows difference between estimated frequencies and observed frequencies for each bin in  $\chi^2$  test. a)  $e = 3.33$  b)  $e = 2$ , c)  $e = 1.25$ , d)  $e = 1$ . This image was taken from reference [JL2].

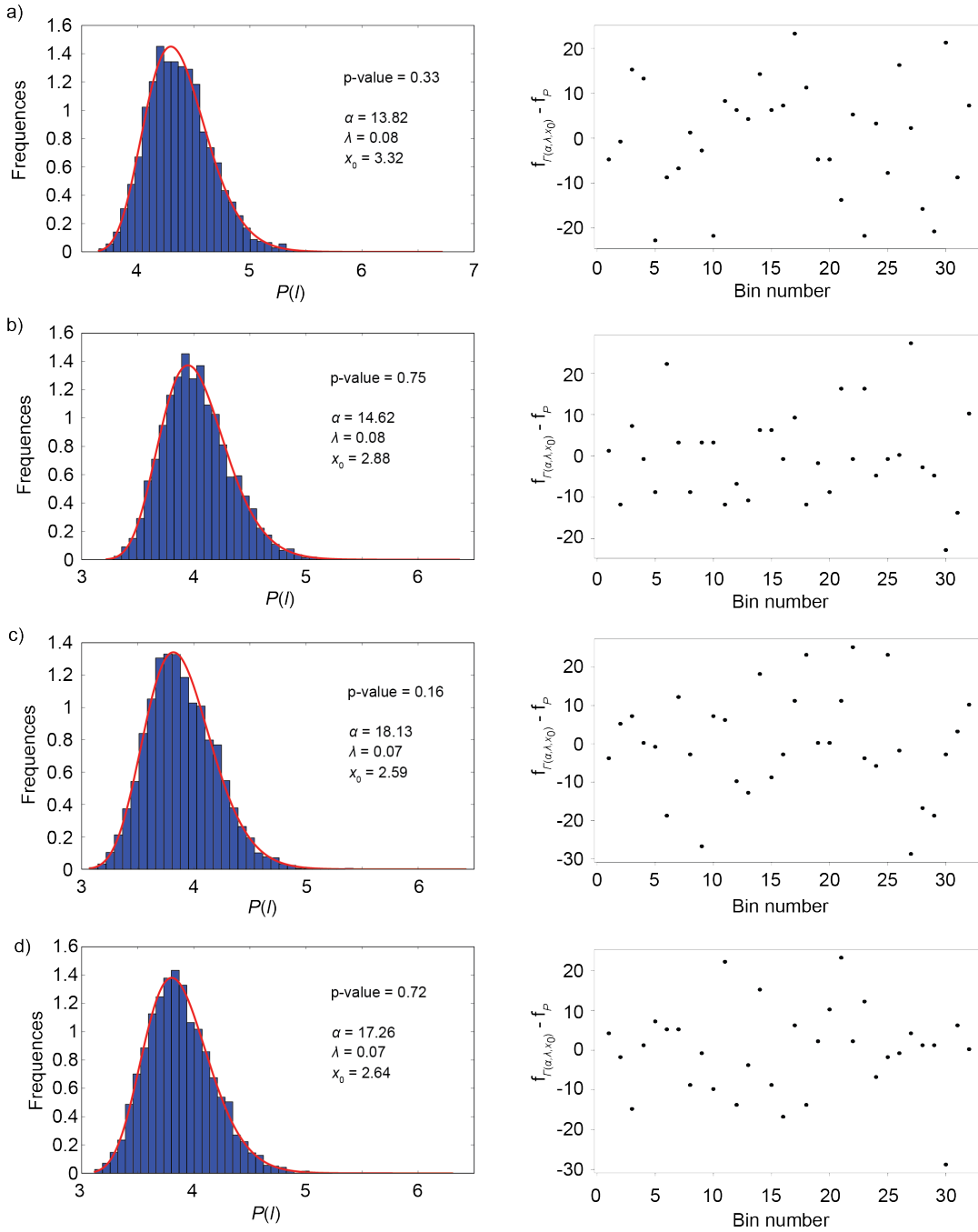


FIGURE A.13: Fits of gamma distribution to the cell perimeter at packing fraction  $\phi_g = 0.5$ . Left figure shows fit together with p-value of  $\chi^2$  test and parameters of fitted distribution. Right figure shows difference between estimated frequencies and observed frequencies for each bin in  $\chi^2$  test. a)  $e = 3.33$  b)  $e = 2$ , c)  $e = 1.25$ , d)  $e = 1$ . This image was taken from reference [JL2].

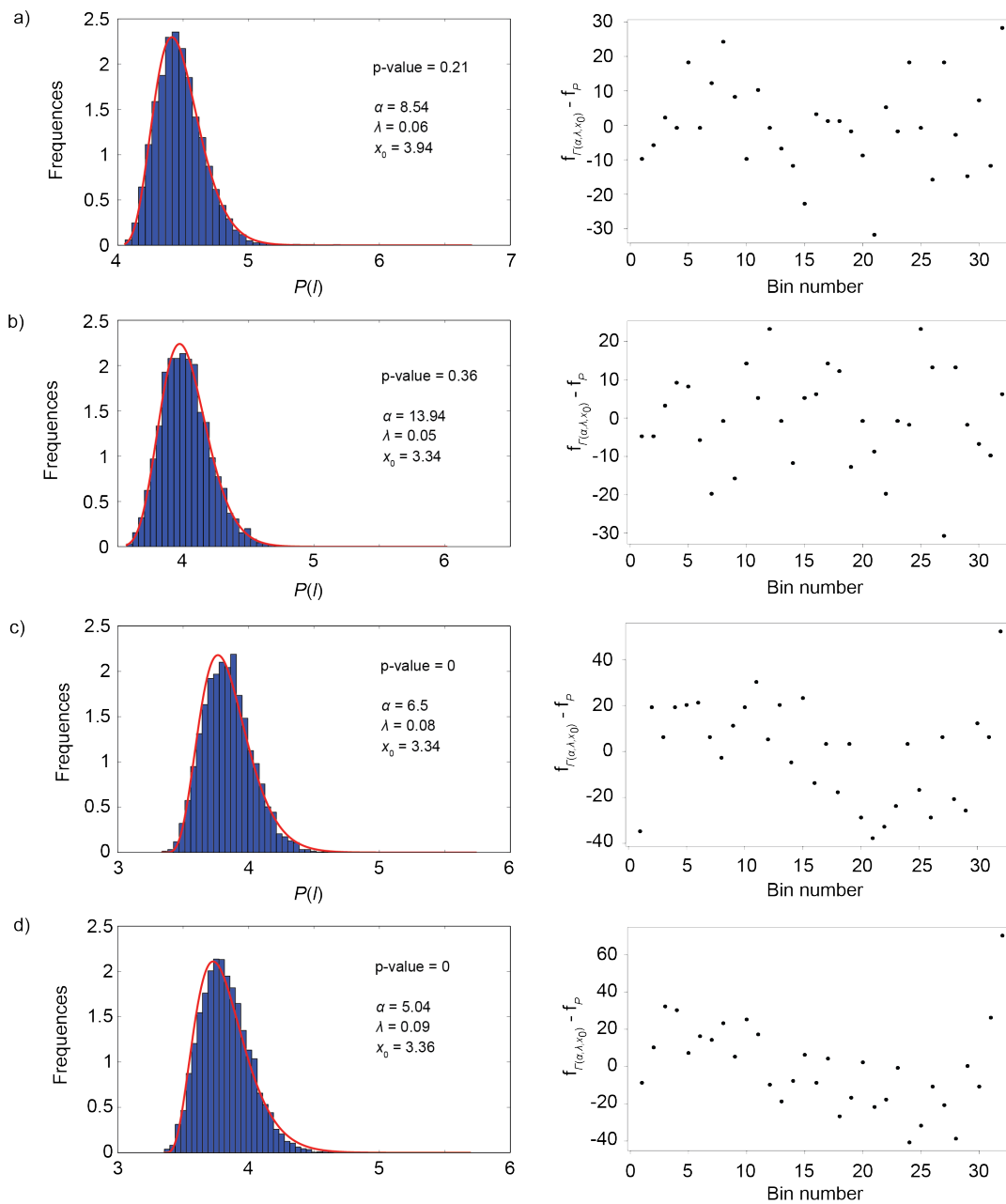


FIGURE A.14: Fits of gamma distribution to the cell perimeter at packing fraction  $\phi_g = 0.65$ . Left figure shows fit together with p-value of  $\chi^2$  test and parameters of fitted distribution. Right figure shows difference between estimated frequencies and observed frequencies for each bin in  $\chi^2$  test. a)  $e = 3.33$  b)  $e = 2$ , c)  $e = 1.25$ , d)  $e = 1$ . This image was taken from reference [JL2].

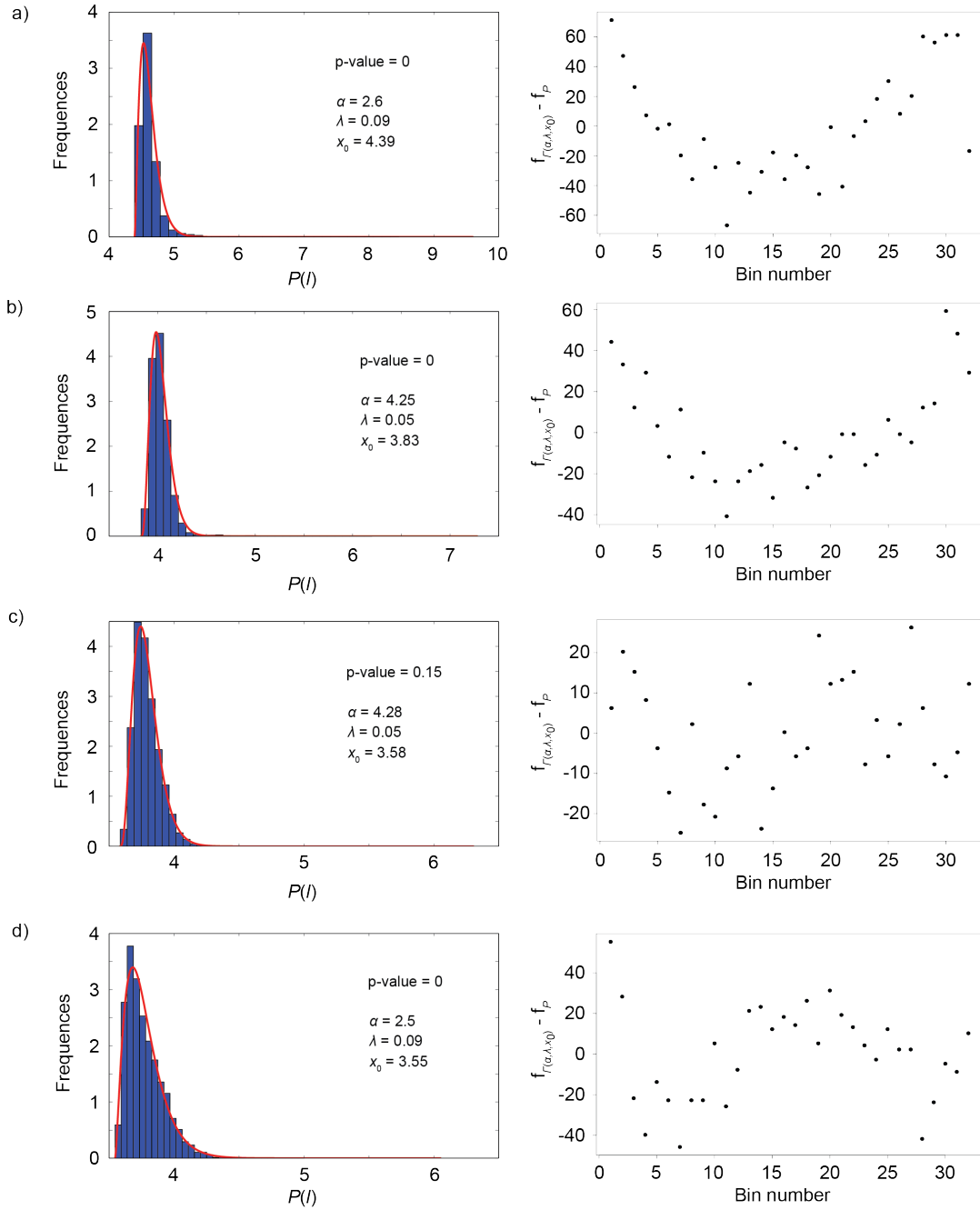


FIGURE A.15: Fits of gamma distribution to the cell perimeter at packing fraction  $\phi_g = 0.8$ . Left figure shows fit together with p-value of  $\chi^2$  test and parameters of fitted distribution. Right figure shows difference between estimated frequencies and observed frequencies for each bin in  $\chi^2$  test. a)  $e = 3.33$  b)  $e = 2$ , c)  $e = 1.25$ , d)  $e = 1$ . This image was taken from reference [JL2].



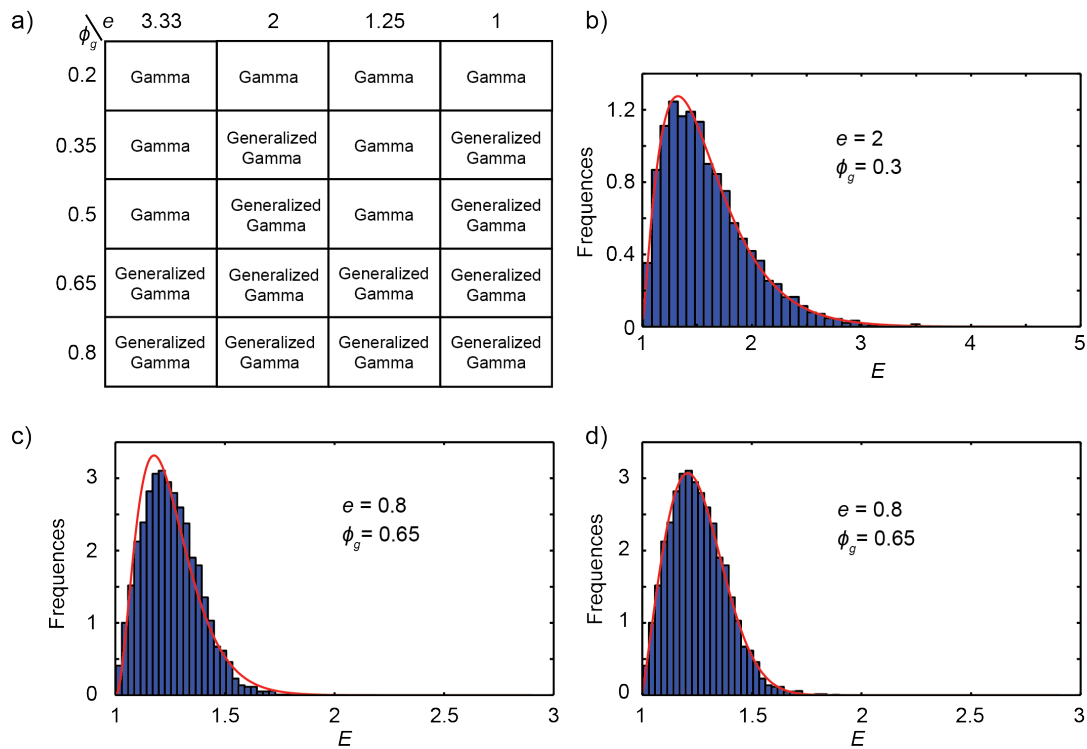


FIGURE A.16: Details of gamma distribution fits to the cell elongation data. a) Table shows where gamma distributed was successfully fitted across whole phase space of studied assemblies. b) Example of a good fit of gamma distribution to cell elongation measure. c) Example of a bad fit of gamma distribution to cell elongation measure. d) Example of a good fit of generalized gamma distribution to cell elongation measure. This image was taken from reference [JL2].

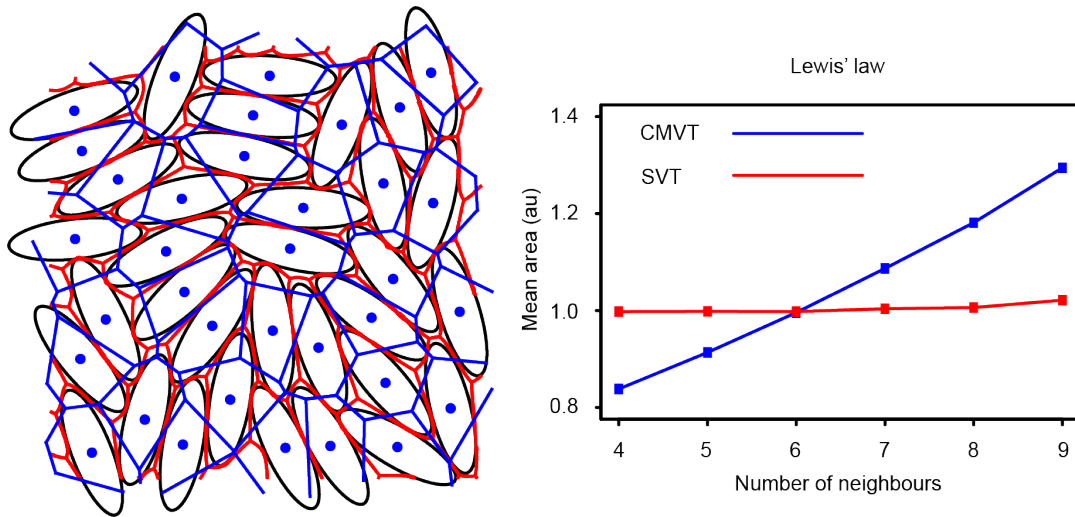


FIGURE A.17: Comparison between set Voronoi tessellation and standard Voronoi tessellations. Difference between two tessellations clearly emerge when Lewis' law is calculated. This image was taken from reference [JL2].

# Bibliography

- [1] D.A. Aboav. "The arrangement of cells in a net". In: *Metallography* 13.1 (1980), pp. 43–58. ISSN: 0026-0800. DOI: [https://doi.org/10.1016/0026-0800\(80\)90021-X](https://doi.org/10.1016/0026-0800(80)90021-X). URL: <http://www.sciencedirect.com/science/article/pii/002608008090021X>.
- [2] D.A. Aboav. "The arrangement of grains in a polycrystal". In: *Metallography* 3.4 (1970), pp. 383–390. ISSN: 0026-0800. DOI: [https://doi.org/10.1016/0026-0800\(70\)90038-8](https://doi.org/10.1016/0026-0800(70)90038-8). URL: <http://www.sciencedirect.com/science/article/pii/0026080070900388>.
- [3] L D Abreu et al. "The Weyl–Heisenberg ensemble: hyperuniformity and higher Landau levels". In: *Journal of Statistical Mechanics: Theory and Experiment* 2017.4 (2017), p. 043103. DOI: [10.1088/1742-5468/aa68a7](https://doi.org/10.1088/1742-5468/aa68a7). URL: <https://doi.org/10.1088/1742-5468/aa68a7>.
- [4] MARTIN D. ADICKES et al. "Optimization of indoor wireless communication network layouts". In: *IIE Transactions* 34.9 (2002), pp. 823–836. DOI: [10.1080/07408170208928915](https://doi.org/10.1080/07408170208928915). eprint: <https://doi.org/10.1080/07408170208928915>. URL: <https://doi.org/10.1080/07408170208928915>.
- [5] C. H. Arns, M. A. Knackstedt, and K. R. Mecke. "Characterisation of irregular spatial structures by parallel sets and integral geometric measures". In: *Colloids and Surfaces A: Physicochemical and Engineering Aspects* 241.1-3 (July 2004), pp. 351–372. DOI: [10.1016/j.colsurfa.2004.04.034](https://doi.org/10.1016/j.colsurfa.2004.04.034). URL: <http://www.sciencedirect.com/science/article/pii/S0927775704002274>.
- [6] T. Aste and T. Di Matteo. "Emergence of Gamma distributions in granular materials and packing models". In: *Phys. Rev. E* 77 (2 2008), p. 021309. DOI: [10.1103/PhysRevE.77.021309](https://doi.org/10.1103/PhysRevE.77.021309). URL: <http://link.aps.org/doi/10.1103/PhysRevE.77.021309>.
- [7] T. Aste and D. Weaire. *The pursuit of perfect packing*. 2nd ed. CRC Press, 2008. ISBN: 9781420068177. URL: <http://www.worldcat.org/isbn/9781420068177>.

- [8] L. Atia et al. “Author Correction: Geometric constraints during epithelial jamming”. In: *Nature Physics* 14.6 (2018), pp. 629–629. ISSN: 1745-2481. DOI: 10.1038/s41567-018-0168-y. URL: <https://doi.org/10.1038/s41567-018-0168-y>.
- [9] Steven Atkinson, Frank H. Stillinger, and Salvatore Torquato. “Detailed characterization of rattlers in exactly isostatic, strictly jammed sphere packings”. In: *Phys. Rev. E* 88 (6 2013), p. 062208. DOI: 10.1103/PhysRevE.88.062208. URL: <https://link.aps.org/doi/10.1103/PhysRevE.88.062208>.
- [10] Steven Atkinson et al. “Critical slowing down and hyperuniformity on approach to jamming”. In: *Phys. Rev. E* 94 (1 2016), p. 012902. DOI: 10.1103/PhysRevE.94.012902. URL: <https://link.aps.org/doi/10.1103/PhysRevE.94.012902>.
- [11] Adrian Baddeley, Ege Rubak, and Rolf Turner. *Spatial Point Patterns: Methodology and Applications with R*. London: Chapman and Hall/CRC Press, 2015. URL: <http://www.crcpress.com/Spatial-Point-Patterns-Methodology-and-Applications-with-R/Baddeley-Rubak-Turner/9781482210200/>.
- [12] Adrian Baddeley and Rolf Turner. “spatstat: An R Package for Analyzing Spatial Point Patterns”. In: *Journal of Statistical Software* 12.6 (2005), pp. 1–42. URL: <http://www.jstatsoft.org/v12/i06/>.
- [13] Adrian Baddeley et al. “Hybrids of Gibbs Point Process Models and Their Implementation”. In: *Journal of Statistical Software* 55.11 (2013), pp. 1–43. URL: <http://www.jstatsoft.org/v55/i11/>.
- [14] E. S. Barnes and N. J. A. Sloane. “The Optimal Lattice Quantizer in Three Dimensions”. In: *SIAM Journal on Algebraic Discrete Methods* 4.1 (1983), pp. 30–41. DOI: 10.1137/0604005. eprint: <https://doi.org/10.1137/0604005>. URL: <https://doi.org/10.1137/0604005>.
- [15] J. D. Bernal and J. Mason. “Packing of Spheres: Co-ordination of Randomly Packed Spheres”. In: *Nature* 188.4754 (1960), pp. 910–911. DOI: 10.1038/188910a0.
- [16] J. G. Berryman. “Random close packing of hard spheres and disks”. In: *Phys. Rev. A* 27 (2 1983), pp. 1053–1061. DOI: 10.1103/PhysRevA.27.1053. URL: <https://link.aps.org/doi/10.1103/PhysRevA.27.1053>.

- [17] Dapeng Bi et al. “A density-independent rigidity transition in biological tissues”. In: *Nature Physics* 11 (Dec. 2015), pp. 1074–1079. DOI: 10.1038/nphys3471. arXiv: 1409.0593 [physics.bio-ph].
- [18] R. Bose. *Information Theory, Coding and Cryptography*. Tata McGraw-Hill Publishing Company lim., 2008. ISBN: 9780070669017. URL: <https://books.google.hr/books?id=AizEjrRIEHC>.
- [19] M. Brehm et al. “TRAVIS—A free analyzer for trajectories from molecular simulation”. In: *The Journal of Chemical Physics* 152.16 (2020), p. 164105. DOI: 10.1063/5.0005078. eprint: <https://doi.org/10.1063/5.0005078>. URL: <https://doi.org/10.1063/5.0005078>.
- [20] J. B. Burns. “Centroidal Voronoi Tessellations”. In: *Centroidal Voronoi Tessellations* (2009). URL: <https://www.whitman.edu/Documents/Academics/Mathematics/burns.pdf>.
- [21] G. Le Caer and R. Delannay. “Correlations in topological models of 2D random cellular structures”. In: *Journal of Physics A: Mathematical and General* 26.16 (1993), p. 3931. URL: <http://stacks.iop.org/0305-4470/26/i=16/a=011>.
- [22] *Cannonball stack with FCC unit cell*. [https://commons.wikimedia.org/wiki/File:Cannonball\\_stack\\_with\\_FCC\\_unit\\_cell.jpg](https://commons.wikimedia.org/wiki/File:Cannonball_stack_with_FCC_unit_cell.jpg). Accessed: 2021-03-05.
- [23] M. Emre Celebi and Kemal Aydin, eds. *Unsupervised Learning Algorithms*. Springer International Publishing, 2016. DOI: 10.1007/978-3-319-24211-8. URL: <https://doi.org/10.1007%2F978-3-319-24211-8>.
- [24] Duyu Chen et al. “Structural Characterization and Statistical-Mechanical Model of Epidermal Patterns.” In: *Biophysical journal* 111 11 (2016), pp. 2534–2545.
- [25] *Chicken eyes*. <https://telescoper.wordpress.com/tag/chicken-eyes/>. Accessed: 2021-11-08.
- [26] S. N. Chiu. “Aboav-Weaire’s and Lewis’ laws — A review”. In: *Materials Characterization* 34.2 (1995), pp. 149–165. ISSN: 1044-5803. DOI: [http://dx.doi.org/10.1016/1044-5803\(94\)00081-U](http://dx.doi.org/10.1016/1044-5803(94)00081-U). URL: <http://www.sciencedirect.com/science/article/pii/104458039400081U>.
- [27] Sung Chiu et al. *Stochastic Geometry and Its Applications*. Sept. 2013. DOI: 10.1002/9781118658222.

- [28] L. Ciupinski, K. J. Kurzydłowski, and B. Ralph. *On the Application of Lewis's Law to Grain Sections of Polycrystalline Metallic Materials*. Vol. 40. Apr. 1998, pp. 215–219.
- [29] Andrew Clark and Ewa Paluch. “Mechanics and Regulation of Cell Shape During the Cell Cycle”. In: *Results and problems in cell differentiation* 53 (Apr. 2011), pp. 31–73. DOI: 10.1007/978-3-642-19065-0\_3.
- [30] J. H. Conway, N. J. A. Sloane, and E. Bannai. *Sphere-Packings, Lattices, and Groups*. Berlin, Heidelberg: Springer-Verlag, 1987. ISBN: 038796617X.
- [31] John Conway and N. Sloane. *Sphere Packings, Lattices and Groups*. Vol. 290. Jan. 1988. DOI: 10.1007/978-1-4757-2016-7.
- [32] A. Dasgupta et al. “Cell volume changes contribute to epithelial morphogenesis in zebrafish Kupffer's vesicle”. In: *eLife* 7 (2018). Ed. by Marianne Bronner, e30963. ISSN: 2050-084X. DOI: 10.7554/eLife.30963. URL: <https://doi.org/10.7554/eLife.30963>.
- [33] G. Delaney et al. “Random packing of elliptical disks”. In: *Philosophical Magazine Letters* 85.2 (2005), pp. 89–96. DOI: 10.1080/09500830500080763. eprint: <http://dx.doi.org/10.1080/09500830500080763>. URL: <http://dx.doi.org/10.1080/09500830500080763>.
- [34] N. Deng, W. Zhou, and M. Haenggi. “The Ginibre Point Process as a Model for Wireless Networks With Repulsion”. In: *IEEE Transactions on Wireless Communications* 14.1 (2015), pp. 107–121.
- [35] C. H. Desch. “The solidification of metals from the liquid state”. In: *J. Inst. Metals* 22.2 (1919), pp. 241–276.
- [36] A. Donev, S. Torquato, and F. H. Stillinger. “Neighbor list collision-driven molecular dynamics simulation for nonspherical hard particles. I. Algorithmic details”. In: *Journal of Computational Physics* 202.2 (2005), pp. 737–764. ISSN: 0021-9991. DOI: <http://dx.doi.org/10.1016/j.jcp.2004.08.014>. URL: [//www.sciencedirect.com/science/article/pii/S0021999104003146](http://www.sciencedirect.com/science/article/pii/S0021999104003146).
- [37] A. Donev, S. Torquato, and F. H. Stillinger. “Neighbor list collision-driven molecular dynamics simulation for nonspherical hard particles.: II. applications to ellipses and ellipsoids”. In: *Journal of Computational Physics* 202.2 (2005), pp. 765–793.
- [38] A. Donev et al. “Improving the density of jammed disordered packings using ellipsoids”. In: *Science* 303.5660 (2004), pp. 990–993.

- [39] A. Donev et al. "Underconstrained jammed packings of nonspherical hard particles: Ellipses and ellipsoids". In: *Phys. Rev. E* 75 (5 2007), p. 051304. DOI: 10.1103/PhysRevE.75.051304. URL: <http://link.aps.org/doi/10.1103/PhysRevE.75.051304>.
- [40] Aleksandar Donev, Frank H. Stillinger, and Salvatore Torquato. "Unexpected Density Fluctuations in Jammed Disordered Sphere Packings". In: *Phys. Rev. Lett.* 95 (9 2005), p. 090604. DOI: 10.1103/PhysRevLett.95.090604. URL: <https://link.aps.org/doi/10.1103/PhysRevLett.95.090604>.
- [41] K. A. Dowsland and W. B. Dowsland. "Packing problems". In: *European Journal of Operational Research* 56.1 (1992), pp. 2–14. ISSN: 0377-2217. DOI: [http://dx.doi.org/10.1016/0377-2217\(92\)90288-K](http://dx.doi.org/10.1016/0377-2217(92)90288-K). URL: <http://www.sciencedirect.com/science/article/pii/S037722179290288K>.
- [42] Q. Du, V. Faber, and M. Gunzburger. "Centroidal Voronoi Tessellations: Applications and Algorithms". In: *SIAM Review* 41.4 (1999), pp. 637–676. DOI: 10.1137/S0036144599352836. eprint: <https://doi.org/10.1137/S0036144599352836>. URL: <https://doi.org/10.1137/S0036144599352836>.
- [43] Qiang Du, Maria Emelianenko, and Lili Ju. "Convergence of the Lloyd Algorithm for Computing Centroidal Voronoi Tessellations". In: *SIAM Journal on Numerical Analysis* 44.1 (2006), pp. 102–119. DOI: 10.1137/040617364. eprint: <https://doi.org/10.1137/040617364>. URL: <https://doi.org/10.1137/040617364>.
- [44] Qiang Du and Desheng Wang. "The optimal centroidal Voronoi tessellations and the Gersho's conjecture in the three-dimensional space". In: *Computers & Mathematics with Applications* 49.9 (2005), pp. 1355–1373. ISSN: 0898-1221. DOI: <https://doi.org/10.1016/j.camwa.2004.12.008>. URL: <http://www.sciencedirect.com/science/article/pii/S0898122105001550>.
- [45] M. Durand et al. "Statistical mechanics of two-dimensional shuffled foams: Geometry-topology correlation in small or large disorder limits". In: *Phys. Rev. E* 89 (6 2014), p. 062309. DOI: 10.1103/PhysRevE.89.062309. URL: <https://link.aps.org/doi/10.1103/PhysRevE.89.062309>.

- [46] M. Durand et al. "Statistical Mechanics of Two-Dimensional Shuffled Foams: Prediction of the Correlation between Geometry and Topology". In: *Phys. Rev. Lett.* 107 (16 2011), p. 168304. DOI: 10.1103/PhysRevLett.107.168304. URL: <https://link.aps.org/doi/10.1103/PhysRevLett.107.168304>.
- [47] J. C. Earnshaw and D. J. Robinson. "Topological correlations in colloidal aggregation". In: *Phys. Rev. Lett.* 72 (23 1994), pp. 3682–3685. DOI: 10.1103/PhysRevLett.72.3682. URL: <https://link.aps.org/doi/10.1103/PhysRevLett.72.3682>.
- [48] Myfanwy E. Evans et al. "Networklike Propagation of Cell-Level Stress in Sheared Random Foams". In: *Phys. Rev. Lett.* 111 (13 2013), p. 138301. DOI: 10.1103/PhysRevLett.111.138301. URL: <https://link.aps.org/doi/10.1103/PhysRevLett.111.138301>.
- [49] S. Farhadi and R. P. Behringer. "Dynamics of sheared ellipses and circular disks: effects of particle shape". In: *Physical review letters* 112.14 (2014), p. 148301.
- [50] R. S. Farr and R. D. Groot. "Close packing density of polydisperse hard spheres". In: *The Journal of chemical physics* 131.24 (2009), p. 244104.
- [51] Alexander Fletcher et al. "Vertex Models of Epithelial Morphogenesis". In: *Biophysical journal* 106 (June 2014), pp. 2291–2304. DOI: 10.1016/j.bpj.2013.11.4498.
- [52] V. E. Fradkov et al. "Determinism and stochasticity in ideal two-dimensional soap froths". In: *Philosophical Magazine Letters* 67.3 (1993), pp. 203–211. DOI: 10.1080/09500839308240930. eprint: <https://doi.org/10.1080/09500839308240930>. URL: <https://doi.org/10.1080/09500839308240930>.
- [53] A. Gabrielli, M. Joyce, and S. Torquato. "Tilings of space and superhomogeneous point processes". In: *Phys. Rev. E* 77 (3 2008), p. 031125. DOI: 10.1103/PhysRevE.77.031125. URL: <https://link.aps.org/doi/10.1103/PhysRevE.77.031125>.
- [54] Andrea Gabrielli. "Point processes and stochastic displacement fields". In: *Phys. Rev. E* 70 (6 2004), p. 066131. DOI: 10.1103/PhysRevE.70.066131. URL: <https://link.aps.org/doi/10.1103/PhysRevE.70.066131>.



- [55] Andrea Gabrielli and Salvatore Torquato. “Voronoi and void statistics for superhomogeneous point processes”. In: *Phys. Rev. E* 70 (4 2004), p. 041105. DOI: 10.1103/PhysRevE.70.041105. URL: <https://link.aps.org/doi/10.1103/PhysRevE.70.041105>.
- [56] A. Gersho. “Asymptotically optimal block quantization”. In: *IEEE Transactions on Information Theory* 25.4 (1979), pp. 373–380. ISSN: 1557-9654. DOI: 10.1109/TIT.1979.1056067.
- [57] Giraffe. [https://quantdare.com/k-means-algorithm/giraffe-59009\\_1920](https://quantdare.com/k-means-algorithm/giraffe-59009_1920). Accessed: 2021-03-09.
- [58] J. A. Glazier, S. P. Gross, and J. Stavans. “Dynamics of two-dimensional soap froths”. In: *Phys. Rev. A* 36 (1 1987), pp. 306–312. DOI: 10.1103/PhysRevA.36.306. URL: <https://link.aps.org/doi/10.1103/PhysRevA.36.306>.
- [59] Daniel A. Goldston and Hugh L. Montgomery. “Pair Correlation of Zeros and Primes in Short Intervals”. In: *Analytic Number Theory and Diophantine Problems: Proceedings of a Conference at Oklahoma State University, 1984*. Boston, MA: Birkhäuser Boston, 1987, pp. 183–203. ISBN: 978-1-4612-4816-3. DOI: 10.1007/978-1-4612-4816-3\_10. URL: [https://doi.org/10.1007/978-1-4612-4816-3\\_10](https://doi.org/10.1007/978-1-4612-4816-3_10).
- [60] Charlene Guillot and Thomas Lecuit. “Mechanics of Epithelial Tissue Homeostasis and Morphogenesis”. In: *Science (New York, N.Y.)* 340 (June 2013), pp. 1185–9. DOI: 10.1126/science.1235249.
- [61] Thomas Hales. “A proof of the Kepler conjecture”. In: *Ann. Math.* 162 (2005), p. 1065.
- [62] Lothar Heinrich, Hendrik Schmidt, and Volker Schmidt. “Central limit theorems for Poisson hyperplane tessellations”. In: *Ann. Appl. Probab.* 16 (Aug. 2006). DOI: 10.1214/105051606000000033.
- [63] Daniel Hexner and Dov Levine. “Hyperuniformity of Critical Absorbing States”. In: *Phys. Rev. Lett.* 114 (11 2015), p. 110602. DOI: 10.1103/PhysRevLett.114.110602. URL: <https://link.aps.org/doi/10.1103/PhysRevLett.114.110602>.
- [64] H. J. Hilhorst. “Planar Voronoi cells: the violation of Aboav’s law explained”. In: *Journal of Physics A: Mathematical and General* 39.23 (2006), p. 7227. URL: <http://stacks.iop.org/0305-4470/39/i=23/a=004>.

- [65] A. L. Hinde and R. E. Miles. "Monte carlo estimates of the distributions of the random polygons of the voronoi tessellation with respect to a poisson process". In: *Journal of Statistical Computation and Simulation* 10.3-4 (1980), pp. 205–223. DOI: 10.1080/00949658008810370. eprint: <http://dx.doi.org/10.1080/00949658008810370>. URL: <http://dx.doi.org/10.1080/00949658008810370>.
- [66] M. Jaber Hossain et al. "Establishment and Characterization of a Madin-Darby Canine Kidney Reporter Cell Line for Influenza A Virus Assays". In: *Journal of Clinical Microbiology* 48.7 (2010), pp. 2515–2523. ISSN: 0095-1137. DOI: 10.1128/JCM.02286-09. eprint: <https://jcm.asm.org/content/48/7/2515.full.pdf>. URL: <https://jcm.asm.org/content/48/7/2515>.
- [67] B. Jancovici. "Exact Results for the Two-Dimensional One-Component Plasma". In: *Phys. Rev. Lett.* 46 (6 1981), pp. 386–388. DOI: 10.1103/PhysRevLett.46.386. URL: <https://link.aps.org/doi/10.1103/PhysRevLett.46.386>.
- [68] X. Jia and R.A Williams. "A packing algorithm for particles of arbitrary shapes". In: *Powder Technology* 120.3 (2001), pp. 175–186. ISSN: 0032-5910. DOI: [http://dx.doi.org/10.1016/S0032-5910\(01\)00268-6](http://dx.doi.org/10.1016/S0032-5910(01)00268-6). URL: <http://www.sciencedirect.com/science/article/pii/S0032591001002686>.
- [69] Yang Jiao and Salvatore Torquato. "Maximally random jammed packings of Platonic solids: Hyperuniform long-range correlations and isotaticity". In: *Phys. Rev. E* 84 (4 2011), p. 041309. DOI: 10.1103/PhysRevE.84.041309. URL: <https://link.aps.org/doi/10.1103/PhysRevE.84.041309>.
- [70] Y. Jin, J. G. Puckett, and H. A. Makse. "Statistical theory of correlations in random packings of hard particles". In: *Physical Review E* 89.5 (2014), p. 052207.
- [71] *Jmol*. 2019. URL: <https://matin.gatech.edu/resources/jmol>.
- [72] I. Jorjadze et al. "Jamming phase diagram of athermal emulsions with short-range attraction". In: *arXiv preprint arXiv:1104.1394* - (2011), pp. –.
- [73] Lili Ju, Qiang Du, and Max Gunzburger. "Probabilistic methods for centroidal Voronoi tessellations and their parallel implementations". In: *Parallel Computing* 28.10 (2002), pp. 1477–1500. ISSN: 0167-8191.

- DOI: [https://doi.org/10.1016/S0167-8191\(02\)00151-5](https://doi.org/10.1016/S0167-8191(02)00151-5). URL: <http://www.sciencedirect.com/science/article/pii/S0167819102001515>.
- [74] S. Kaliman et al. "Limits of Applicability of the Voronoi Tessellation Determined by Centers of Cell Nuclei to Epithelium Morphology". In: *Frontiers in Physiology* 7 (2016), p. 551. ISSN: 1664-042X. DOI: 10.3389/fphys.2016.00551. URL: <http://journal.frontiersin.org/article/10.3389/fphys.2016.00551>.
- [75] Sara Kaliman. "Morphological analysis of epithelial cells". doctoralthesis. Friedrich-Alexander-Universität Erlangen-Nürnberg (FAU), 2018.
- [76] Sara Kaliman et al. "Mechanical Regulation of Epithelial Tissue Homeostasis". In: *Phys. Rev. X* 11 (3 2021), p. 031029. DOI: 10.1103/PhysRevX.11.031029. URL: <https://link.aps.org/doi/10.1103/PhysRevX.11.031029>.
- [77] Sara Kaliman et al. "Novel growth regime of MDCK II model tissues on soft substrates". In: *Biophysical journal* 106 (Apr. 2014), pp. L25–8. DOI: 10.1016/j.bpj.2013.12.056.
- [78] S. C. Kapfer et al. "Jammed spheres: Minkowski tensors reveal onset of local crystallinity". In: *Phys. Rev. E* 85 (3 2012), p. 030301. DOI: 10.1103/PhysRevE.85.030301. URL: <https://link.aps.org/doi/10.1103/PhysRevE.85.030301>.
- [79] Jaeuk Kim and Salvatore Torquato. "Effect of imperfections on the hyperuniformity of many-body systems". In: *Phys. Rev. B* 97 (5 2018), p. 054105. DOI: 10.1103/PhysRevB.97.054105. URL: <https://link.aps.org/doi/10.1103/PhysRevB.97.054105>.
- [80] S. Kim, M. Cai, and S. Hilgenfeldt. "Lewis' law revisited: the role of anisotropy in size–topology correlations". In: *New Journal of Physics* 16.1 (2014), p. 015024. URL: <http://stacks.iop.org/1367-2630/16/i=1/a=015024>.
- [81] S. Kim and S. Hilgenfeldt. "A simple landscape of metastable state energies for two-dimensional cellular matter". In: *Soft Matter* 15 (2 2019), pp. 237–242. DOI: 10.1039/C8SM01921E. URL: <http://dx.doi.org/10.1039/C8SM01921E>.
- [82] S. Kim and S. Hilgenfeldt. "Cell shapes and patterns as quantitative indicators of tissue stress in the plant epidermis". In: *Soft Matter* 11 (37 2015), pp. 7270–7275. DOI: 10.1039/C5SM01563D. URL: <http://dx.doi.org/10.1039/C5SM01563D>.

- [83] S. Kim, Y. Wang, and S. Hilgenfeldt. "Universal Features of Metastable State Energies in Cellular Matter". In: *Phys. Rev. Lett.* 120 (24 2018), p. 248001. DOI: 10.1103/PhysRevLett.120.248001. URL: <https://link.aps.org/doi/10.1103/PhysRevLett.120.248001>.
- [84] M. A. Klatt and S. Torquato. "Characterization of maximally random jammed sphere packings: Voronoi correlation functions". In: *Physical Review E* 90.5 (2014), p. 052120.
- [85] M. A. Klatt et al. "Universal hidden order in amorphous cellular geometries". In: *Nature Communications* 10.1 (Feb. 2019), p. 811. DOI: 10.1038/s41467-019-08360-5. URL: <https://doi.org/10.1038/s41467-019-08360-5>.
- [86] Michael Klatt et al. "Cell Shape Analysis of Random Tessellations Based on Minkowski Tensors". In: vol. 2177. June 2017, pp. 385–421. ISBN: 978-3-319-51950-0. DOI: 10.1007/978-3-319-51951-7\_13.
- [87] Michael A. Klatt and Salvatore Torquato. "Characterization of maximally random jammed sphere packings. II. Correlation functions and density fluctuations". In: *Phys. Rev. E* 94 (2 2016), p. 022152. DOI: 10.1103/PhysRevE.94.022152. URL: <https://link.aps.org/doi/10.1103/PhysRevE.94.022152>.
- [88] S. Kumar et al. "Properties of a three-dimensional Poisson-Voronoi tessellation: A Monte Carlo study". In: *Journal of Statistical Physics* 67.3 (1992), pp. 523–551. ISSN: 1572-9613. DOI: 10.1007/BF01049719. URL: <http://dx.doi.org/10.1007/BF01049719>.
- [89] V. Senthil Kumar and V. Kumaran. "Voronoi neighbor statistics of hard-disks and hard-spheres". In: *The Journal of Chemical Physics* 123.7 (2005), p. 074502. DOI: 10.1063/1.2000233. eprint: <http://dx.doi.org/10.1063/1.2000233>. URL: <http://dx.doi.org/10.1063/1.2000233>.
- [90] Frédéric Lavancier, Jesper Møller, and Ege Rubak. "Determinantal point process models and statistical inference : Extended version". In: *Journal of the Royal Statistical Society: Series B (Statistical Methodology)* 77 (May 2012). DOI: 10.1111/rssb.12096.
- [91] E. A. Lazar et al. "Statistical topology of three-dimensional Poisson-Voronoi cells and cell boundary networks". In: *Phys. Rev. E* 88 (6 2013), p. 063309. DOI: 10.1103/PhysRevE.88.063309. URL: <https://link.aps.org/doi/10.1103/PhysRevE.88.063309>.

- [92] F. T. Lewis. "The correlation between cell division and the shapes and sizes of prismatic cells in the epidermis of Cucumis". In: *The Anatomical Record* 38.3 (1928), pp. 341–376.
- [93] L. T. Lewis. "A comparison between the mosaic of polygons in a film of artificial emulsion and the pattern of simple epithelium in surface view (cucumber epidermis and human amnion)". In: *The Anatomical Record* 50.3 (1931), pp. 235–265. ISSN: 1097-0185. DOI: 10.1002/ar.1090500303. URL: <http://dx.doi.org/10.1002/ar.1090500303>.
- [94] Leo Liberti, Nelson Maculan, and Yue Zhang. "Optimal configuration of gamma ray machine radiosurgery units: The sphere covering subproblem". In: *Optimization Letters* 3 (Aug. 2009), pp. 109–121. DOI: 10.1007/s11590-008-0095-4.
- [95] Enrique Lomba, Jean-Jacques Weis, and Salvatore Torquato. "Disordered hyperuniformity in two-component nonadditive hard-disk plasmas". In: *Phys. Rev. E* 96 (6 2017), p. 062126. DOI: 10.1103/PhysRevE.96.062126. URL: <https://link.aps.org/doi/10.1103/PhysRevE.96.062126>.
- [96] Enrique Lomba, Jean-Jacques Weis, and Salvatore Torquato. "Disordered multihyperuniformity derived from binary plasmas". In: *Phys. Rev. E* 97 (1 2018), p. 010102. DOI: 10.1103/PhysRevE.97.010102. URL: <https://link.aps.org/doi/10.1103/PhysRevE.97.010102>.
- [97] Jakov Lovrić. "Statistical analysis of structure of Voronoi cells generated by randomly packed ellipses and application on the cell tissue". MA thesis. 2016, p. 65.
- [98] B. D. Lubachevsky and F. H. Stillinger. "Geometric properties of random disk packings". In: *Journal of statistical physics* 60 (1990), pp. 561–583. ISSN: 0022-4715. URL: <http://cat.inist.fr/?aModele=afficheN&csid=19573310>.
- [99] Vladimir Lugovtsev, Darya Melnyk, and Jerry Weir. "Heterogeneity of the MDCK Cell Line and Its Applicability for Influenza Virus Research". In: *PloS one* 8 (Sept. 2013), e75014. DOI: 10.1371/journal.pone.0075014.
- [100] Fausto Martelli et al. "Large-Scale Structure and Hyperuniformity of Amorphous Ices". In: *Phys. Rev. Lett.* 119 (13 2017), p. 136002. DOI: 10.1103/PhysRevLett.119.136002. URL: <https://link.aps.org/doi/10.1103/PhysRevLett.119.136002>.

- [101] Ira Mellman and W Nelson. “Mellman I, Nelson WJ Coordinated protein sorting, targeting and distribution in polarized cells. *Nat Rev Mol Cell Biol* 9(11): 833-845”. In: *Nature reviews. Molecular cell biology* 9 (Dec. 2008), pp. 833–45. DOI: 10.1038/nrm2525.
- [102] M. Merkel and M. L. Manning. “A geometrically controlled rigidity transition in a model for confluent 3D tissues”. In: *New Journal of Physics* 20.2 (2018), p. 022002. DOI: 10.1088/1367-2630/aaaa13. URL: <https://doi.org/10.1088/1367-2630/aaaa13>.
- [103] M. Merkel et al. “A minimal-length approach unifies rigidity in underconstrained materials”. In: *Proceedings of the National Academy of Sciences* 116.14 (2019), pp. 6560–6568. ISSN: 0027-8424. DOI: 10.1073/pnas.1815436116. eprint: <https://www.pnas.org/content/116/14/6560.full.pdf>. URL: <https://www.pnas.org/content/116/14/6560>.
- [104] Madan Lal Metha. “Random matrices and matrix models: The JNU lectures”. In: *Mathematical Aspects Of Dynamical Systems* 48 (1997), pp. 7–48. DOI: 10.1007/BF02845621. URL: <https://link.springer.com/article/10.1007/BF02845621#citeas>.
- [105] Walter Mickel et al. “Robust Pore Size Analysis of Filamentous Networks from Three-Dimensional Confocal Microscopy”. In: *Biophysical Journal* 95.12 (2008), pp. 6072–6080. ISSN: 0006-3495. DOI: <https://doi.org/10.1529/biophysj.108.135939>. URL: <http://www.sciencedirect.com/science/article/pii/S0006349508820218>.
- [106] M. P. Miklius and S. Hilgenfeldt. “Analytical results for size-topology correlations in 2D disk and cellular packings”. In: *Physical review letters* 108.1 (2012), p. 015502.
- [107] J. C. M. Mombach, R. M. C. de Almeida, and J. R. Iglesias. “Two-cell correlations in biological tissues”. In: *Phys. Rev. E* 47 (5 1993), pp. 3712–3716. DOI: 10.1103/PhysRevE.47.3712. URL: <https://link.aps.org/doi/10.1103/PhysRevE.47.3712>.
- [108] J. C. M. Mombach, M. A. Z. Vasconcellos, and R. M. C. de Almeida. “Arrangement of cells in vegetable tissues”. In: *Journal of Physics D: Applied Physics* 23.5 (1990), p. 600. URL: <http://stacks.iop.org/0022-3727/23/i=5/a=021>.

- [109] P. K. Morse and E. I. Corwin. “Geometric order parameters derived from the Voronoi tessellation show signatures of the jamming transition”. In: *Soft Matter* 12 (4 2016), pp. 1248–1255. DOI: 10.1039/C5SM02575C. URL: <http://dx.doi.org/10.1039/C5SM02575C>.
- [110] Tatsuzo Nagai and Hisao Honda. “A dynamic cell model for the formation of epithelial tissue”. In: *Philosophical Magazine B* 81 (July 2001), pp. 699–719. DOI: 10.1080/13642810108205772.
- [111] Carl Nassar. “Chapter 4 - Source Coding and Decoding: Making it Digital”. In: *Telecommunications Demystified*. Ed. by Carl Nassar. Boston: Newnes, 2001, pp. 61–114. ISBN: 978-0-08-051867-1. DOI: <https://doi.org/10.1016/B978-0-08-051867-1.50010-X>. URL: <https://www.sciencedirect.com/science/article/pii/B978008051867150010X>.
- [112] C. B. O’Donovan, E. I. Corwin, and M. E. Möbius. “Mean-field granocentric approach in 2D & 3D polydisperse, frictionless packings”. In: *Philosophical Magazine* 93.31-33 (2013), pp. 4030–4056.
- [113] L. Oger et al. “Voronoi tessellation of packings of spheres: Topological correlation and statistics”. In: *Philosophical Magazine Part B* 74.2 (1996), pp. 177–197. DOI: 10.1080/01418639608240335. URL: <http://dx.doi.org/10.1080/01418639608240335>.
- [114] Erdal C. Oğuz et al. “Hyperuniformity and anti-hyperuniformity in one-dimensional substitution tilings”. In: *Acta Crystallographica Section A* 75.1 (2019), pp. 3–13. DOI: 10.1107/S2053273318015528. URL: <https://doi.org/10.1107/S2053273318015528>.
- [115] Atsuyuki Okabe et al. *Spatial Tessellations: Concepts and Applications of Voronoi Diagrams*. 2nd ed. Series in Probability and Statistics. John Wiley and Sons, Inc., 2000.
- [116] Romelda Omeir et al. “Heterogeneity of the Tumorigenic Phenotype Expressed by Madin-Darby Canine Kidney Cells”. In: *Comparative medicine* 61 (June 2011), pp. 243–50.
- [117] Phillip James Edwin Peebles. *Principles of physical cosmology*. Princeton University Press, 1993.
- [118] P. Pina and M. A. Fortes. “Characterization of cells in cork”. In: *Journal of Physics D: Applied Physics* 29.9 (1996), p. 2507. URL: <http://stacks.iop.org/0022-3727/29/i=9/a=041>.

- [119] M. Poujade et al. "Collective migration of an epithelial monolayer in response to a model wound". In: *Proceedings of the National Academy of Sciences* 104.41 (2007), pp. 15988–15993. DOI: 10.1073/pnas.0705062104. eprint: <https://www.pnas.org/content/104/41/15988.full.pdf>. URL: <https://www.pnas.org/content/104/41/15988>.
- [120] Reinhard Prix. "Template-based searches for gravitational waves: efficient lattice covering of flat parameter spaces". In: *Classical and Quantum Gravity* 24.19 (2007), S481–S490. ISSN: 1361-6382. DOI: 10.1088/0264-9381/24/19/s11. URL: <http://dx.doi.org/10.1088/0264-9381/24/19/S11>.
- [121] Alberto Puliafito et al. "Collective and single cell behavior in epithelial contact inhibition". In: *Proceedings of the National Academy of Sciences* 109.3 (2012), pp. 739–744. ISSN: 0027-8424. DOI: 10.1073/pnas.1007809109. eprint: <https://www.pnas.org/content/109/3/739.full.pdf>. URL: <https://www.pnas.org/content/109/3/739>.
- [122] R Core Team. *R: A Language and Environment for Statistical Computing*. R Foundation for Statistical Computing. Vienna, Austria, 2013. URL: <http://www.R-project.org/>.
- [123] N. Rivier. "Statistical crystallography Structure of random cellular networks". In: *Philosophical Magazine B* 52.3 (1985), pp. 795–819. DOI: 10.1080/13642818508240637. eprint: <https://doi.org/10.1080/13642818508240637>. URL: <https://doi.org/10.1080/13642818508240637>.
- [124] Enrique Rodriguez-Boulan and Ian Macara. "Organization and execution of the epithelial polarity programme". In: *Nature reviews. Molecular cell biology* 15 (Mar. 2014), pp. 225–42. DOI: 10.1038/nrm3775.
- [125] M. E. Rosa. "An introduction to solid foams". In: *Philosophical Magazine Letters* 88.9-10 (2008), pp. 637–645. DOI: 10.1080/09500830802302014.
- [126] R. Rutgers. "Packing of Spheres". In: *Nature* 193 (4814 1962), pp. 465–466. DOI: 10.1038/193465a0. URL: <http://dx.doi.org/10.1038/193465a0>.
- [127] J. Saraiva et al. "Polygonal networks on the surface of Mars; applicability of Lewis, Desch and Aboav – Weaire laws". In: *Philosophical Magazine Letters* 89.3 (2009), pp. 185–193. DOI: 10.1080/09500830902720925. eprint: <https://doi.org/10.1080/09500830902720925>. URL: <https://doi.org/10.1080/09500830902720925>.



- [128] F. Schaller, R. Weigel, and S. Kapfer. “Densest Local Structures of Uniaxial Ellipsoids”. In: *Phys. Rev. X* 6 (4 2016), p. 041032. DOI: 10.1103/PhysRevX.6.041032. URL: <http://link.aps.org/doi/10.1103/PhysRevX.6.041032>.
- [129] F. M. Schaller et al. “Local Origin of Global Contact Numbers in Frictional Ellipsoid Packings”. In: *Phys. Rev. Lett.* 114 (15 2015), p. 158001. DOI: 10.1103/PhysRevLett.114.158001. URL: <http://link.aps.org/doi/10.1103/PhysRevLett.114.158001>.
- [130] F. M. Schaller et al. “Non-universal Voronoi cell shapes in amorphous ellipsoid packs”. In: *EPL (Europhysics Letters)* 111.2 (2015), p. 24002. URL: <http://stacks.iop.org/0295-5075/111/i=2/a=24002>.
- [131] F. M. Schaller et al. “Set Voronoi diagrams of 3D assemblies of aspherical particles”. In: *Philosophical Magazine* 93.31-33 (2013), pp. 3993–4017. DOI: 10.1080/14786435.2013.834389. eprint: <https://doi.org/10.1080/14786435.2013.834389>. URL: <https://doi.org/10.1080/14786435.2013.834389>.
- [132] G E Schröder-Turk et al. “Minkowski tensors of anisotropic spatial structure”. In: *New Journal of Physics* 15.8 (2013), p. 083028. DOI: 10.1088/1367-2630/15/8/083028. URL: <https://doi.org/10.1088/1367-2630/15/8/083028>.
- [133] C. F. Schreck, N. Xu, and C. S. O’Hern. “A comparison of jamming behavior in systems composed of dimer-and ellipse-shaped particles”. In: *Soft Matter* 6.13 (2010), pp. 2960–2969.
- [134] G. E. Schröder-Turk et al. “Tensorial Minkowski functionals and anisotropy measures for planar patterns”. In: *Journal of Microscopy* 238.1 (2010), pp. 57–74. ISSN: 1365-2818. DOI: 10.1111/j.1365-2818.2009.03331.x. URL: <http://dx.doi.org/10.1111/j.1365-2818.2009.03331.x>.
- [135] G. D. Scott. “Packing of Spheres: Packing of Equal Spheres”. In: *Nature* 188 (4754 1960), pp. 908–909. DOI: 10.1038/188908a0. URL: <http://dx.doi.org/10.1038/188908a0>.
- [136] T. A. Sharp et al. “Inferring statistical properties of 3D cell geometry from 2D slices”. In: *PLOS ONE* 14.2 (Feb. 2019), pp. 1–18. DOI: 10.1371/journal.pone.0209892. URL: <https://doi.org/10.1371/journal.pone.0209892>.
- [137] Jakob Sheridan. “Physical Origin of Hyperuniformity in Epithelial Tissue”. bachelorthesis. University of Michigan, 2021.

- [138] Leonardo E. Silbert. “Jamming of frictional spheres and random loose packing”. In: *Soft Matter* 6 (13 2010), pp. 2918–2924. DOI: 10.1039/C001973A. URL: <http://dx.doi.org/10.1039/C001973A>.
- [139] Monica Skoge et al. “Packing hyperspheres in high-dimensional Euclidean spaces”. In: *Phys. Rev. E* 74 (4 2006), p. 041127. DOI: 10.1103/PhysRevE.74.041127. URL: <https://link.aps.org/doi/10.1103/PhysRevE.74.041127>.
- [140] C. Stiles et al. “Growth control of heterologous tissue culture cells in the congenitally athymic nude mouse.” In: *Cancer research* 36 4 (1976), pp. 1353–60.
- [141] Sebastian J. Streichan et al. “Spatial constraints control cell proliferation in tissues”. In: *Proceedings of the National Academy of Sciences* 111.15 (2014), pp. 5586–5591. ISSN: 0027-8424. DOI: 10.1073/pnas.1323016111. eprint: <https://www.pnas.org/content/111/15/5586.full.pdf>. URL: <https://www.pnas.org/content/111/15/5586>.
- [142] *The Wings of a Dragonfly*. <https://neoarchbeta.wordpress.com/tag/generative-architecture-2>. Accessed: 2021-03-09.
- [143] S. Torquato. “Reformulation of the covering and quantizer problems as ground states of interacting particles”. In: *Phys. Rev. E* 82 (5 2010), p. 056109. DOI: 10.1103/PhysRevE.82.056109. URL: <https://link.aps.org/doi/10.1103/PhysRevE.82.056109>.
- [144] S. Torquato and Y. Jiao. “Robust algorithm to generate a diverse class of dense disordered and ordered sphere packings via linear programming”. In: *Phys. Rev. E* 82 (6 2010), p. 061302. DOI: 10.1103/PhysRevE.82.061302. URL: <https://link.aps.org/doi/10.1103/PhysRevE.82.061302>.
- [145] S. Torquato, T. M. Truskett, and P. G. Debenedetti. “Is Random Close Packing of Spheres Well Defined?” In: *Phys. Rev. Lett.* 84 (10 2000), pp. 2064–2067. DOI: 10.1103/PhysRevLett.84.2064. URL: <https://link.aps.org/doi/10.1103/PhysRevLett.84.2064>.
- [146] S. Torquato, G. Zhang, and F. H. Stillinger. “Ensemble Theory for Stealthy Hyperuniform Disordered Ground States”. In: *Phys. Rev. X* 5 (2 2015), p. 021020. DOI: 10.1103/PhysRevX.5.021020. URL: <https://link.aps.org/doi/10.1103/PhysRevX.5.021020>.
- [147] Salvatore Torquato. “Hyperuniform states of matter”. In: *Physics Reports* 745 (June 2018). DOI: 10.1016/j.physrep.2018.03.001.

- [148] Salvatore Torquato, A Scardicchio, and Chase E Zachary. “Point processes in arbitrary dimension from fermionic gases, random matrix theory, and number theory”. In: *Journal of Statistical Mechanics: Theory and Experiment* 2008.11 (2008), P11019. DOI: 10.1088/1742-5468/2008/11/p11019. URL: <https://doi.org/10.1088/1742-5468/2008/11/p11019>.
- [149] Salvatore Torquato and Frank H. Stillinger. “Local density fluctuations, hyperuniformity, and order metrics”. In: *Phys. Rev. E* 68 (4 2003), p. 041113. DOI: 10.1103/PhysRevE.68.041113. URL: <https://link.aps.org/doi/10.1103/PhysRevE.68.041113>.
- [150] Xavier Trepas et al. “Physical forces during collective cell migration”. In: *Nature Physics* 5 (2009). Times Cited: 162, pp. 426–430.
- [151] Guido Van Rossum and Fred L Drake Jr. *Python reference manual*. Centrum voor Wiskunde en Informatica Amsterdam, 1995.
- [152] M. F. Vaz. “Liquid foams: an introduction”. In: *Philosophical Magazine Letters* 88.9-10 (2008), pp. 627–636. DOI: 10.1080/09500830802251427.
- [153] G. Vincze, I. Zsoldos, and A. Szasz. “On the Aboav–Weaire law”. In: *Journal of Geometry and Physics* 51.1 (2004), pp. 1–12. ISSN: 0393-0440. DOI: <https://doi.org/10.1016/j.geomphys.2003.08.003>. URL: <http://www.sciencedirect.com/science/article/pii/S0393044003001335>.
- [154] Chun-Chao Wang, Leen Schafer, and Kevin Janes. “Normal morphogenesis of epithelial tissues and progression of epithelial tumors”. In: *Wiley interdisciplinary reviews. Systems biology and medicine* 4 (Jan. 2012), pp. 51–78. DOI: 10.1002/wsbm.159.
- [155] S Warr and J.-P Hansen. “Relaxation of local density fluctuations in a fluidized granular medium”. In: *Europhysics Letters (EPL)* 36.8 (1996), pp. 589–594. DOI: 10.1209/epl/i1996-00273-1. URL: <https://doi.org/10.1209/ep1/i1996-00273-1>.
- [156] D. Weaire. “Some remarks on the arrangement of grains in a polycrystal”. In: *Metallography* 7.2 (1974), pp. 157–160. ISSN: 0026-0800. DOI: [https://doi.org/10.1016/0026-0800\(74\)90004-4](https://doi.org/10.1016/0026-0800(74)90004-4). URL: <http://www.sciencedirect.com/science/article/pii/0026080074900044>.
- [157] D. Weaire and R. Phelan. “A counter-example to Kelvin’s conjecture on minimal surfaces”. In: *Philosophical Magazine Letters* 69.2 (1994), pp. 107–110. DOI: 10.1080/09500839408241577. eprint: <https://doi.org/10.1080/09500839408241577>.

- org/10.1080/09500839408241577. URL: <https://doi.org/10.1080/09500839408241577>.
- [158] D. Weaire and N. Rivier. "Soap, cells and statistics—random patterns in two dimensions". In: *Contemporary Physics* 25.1 (1984), pp. 59–99. DOI: 10.1080/00107518408210979. eprint: <https://doi.org/10.1080/00107518408210979>. URL: <https://doi.org/10.1080/00107518408210979>.
- [159] *Weaire-Phelan Structure*. <https://www.designcoding.net/weaire-phelan-structure>. Accessed: 2021-03-05.
- [160] Weis, S. et al. "Pomelo, a tool for computing Generic Set Voronoi Diagrams of Aspherical Particles of Arbitrary Shape". In: *EPJ Web Conf.* 140 (2017), p. 06007. DOI: 10.1051/epjconf/201714006007. URL: <https://doi.org/10.1051/epjconf/201714006007>.
- [161] W. Xu, H. Chen, and Z. Lv. "A 2D elliptical model of random packing for aggregates in concrete". In: *Journal of Wuhan University of Technology-Mater. Sci. Ed.* 25.4 (2010), pp. 717–720. DOI: 10.1007/s11595-010-0078-z. URL: <http://dx.doi.org/10.1007/s11595-010-0078-z>.
- [162] X. Yang et al. "Correlating cell shape and cellular stress in motile confluent tissues". In: *Proceedings of the National Academy of Sciences* 114.48 (2017), pp. 12663–12668. ISSN: 0027-8424. DOI: 10.1073/pnas.1705921114. eprint: <https://www.pnas.org/content/114/48/12663.full.pdf>. URL: <https://www.pnas.org/content/114/48/12663>.
- [163] X. Ye et al. "Competition of shape and interaction patchiness for self-assembling nanoplates". In: *Nature Chemistry* 5.6 (June 2013), pp. 466–473. ISSN: 1755-4330. DOI: 10.1038/nchem.1651.
- [164] Chase Zachary and Salvatore Torquato. "Hyperuniformity in point patterns and two-phase random heterogeneous media". In: *Journal of Statistical Mechanics Theory and Experiment* 2009 (Oct. 2009). DOI: 10.1088/1742-5468/2009/12/P12015.
- [165] F. Zamponi. "Mathematical physics: Packings close and loose". In: *Nature* 453 (2008), pp. 606–607.
- [166] Steven Zehnder et al. "Cell Volume Fluctuations in MDCK Monolayers". In: *Biophysical Journal* 108 (Jan. 2015). DOI: 10.1016/j.bpj.2014.11.1856.

- 
- [167] G. Zhang, F. H. Stillinger, and S. Torquato. “Ground states of stealthy hyperuniform potentials: I. Entropically favored configurations”. In: *Phys. Rev. E* 92 (2 2015), p. 022119. DOI: 10.1103/PhysRevE.92.022119. URL: <https://link.aps.org/doi/10.1103/PhysRevE.92.022119>.
- [168] H. X. Zhu, S. M. Thorpe, and A. H. Windle. “The geometrical properties of irregular two-dimensional Voronoi tessellations”. In: *Philosophical Magazine A* 81.12 (2001), pp. 2765–2783.
- [169] C. Zong. “A Mathematical Theory for Random Solid Packings”. In: arXiv:1410.1102v1, 2014, p. 1. URL: <https://arxiv.org/abs/1410.1102v1>.
- [170] Matthias Zorn et al. “Phenomenological Approaches to Collective Behavior in Epithelial Cell Migration.” In: *Biochimica et biophysica acta* 1853 (May 2015). DOI: 10.1016/j.bbamcr.2015.05.021.



# List of publications

- [JL1] Michael A. Klatt\*; **Jakov Lovrić\***; Duyu Chen; Sebastian C. Kapfer; Fabian M. Schaller; Philipp W. A. Schönhöfer; Bruce S. Gardiner; Ana-Sunčana Smith; Gerd E. Schröder-Turk; Salvatore Torquato. Universal hidden order in amorphous cellular geometries. *Nature Communications*. **2019**, 10, 811
- [JL2] **Jakov Lovrić**; Sara Kaliman; Wolfram Barfuss; Gerd E. Schröder-Turk; Ana-Sunčana Smith. Geometric effects in random assemblies of ellipses. *Soft Matter*. **2019**, 15, 8566-8577
- [JL3] Sara Kaliman; Maxime Hubert; Carina Wollnik; Lovro Nuić; Damir Vurnek; Simone Gehler; **Jakov Lovrić**; Diana Dudziak; Florian Rehfeldt; Ana-Sunčana Smith. Mechanical Regulation of Epithelial Tissue Homeostasis. *Physical Review X*. **2021**, 11, 031029





# Curriculum Vitae

## Personal information

- Name and surname: Jakov Lovrić
- Date of birth: 16/09/1992
- Place of birth: Cambridge, UK

## Education

- (2016 - ) PhD in Physics, Friedrich-Alexander-Universität Erlangen-Nürnberg, Faculty of Sciences, Department of Physics
- (2014 - 2016) Masters degree in Mathematic, University of Zagreb, Faculty of Science, Department of Mathematics
- (2011 - 2014) Bachelor degree in Mathematics, University of Zagreb, Faculty of Science, Department of Mathematics

## Work experience

- (12/2021 - ) Velebit AI, Zagreb, Croatia
- (12/2016 - 12/2021) Ruđer Bošković Institute, Zagreb, Croatia
- (9/2016 - 11/2016) Murdoch University, Perth, WA, Australia
- (12/2014 - 9/2016) Ruđer Bošković Institute, Zagreb, Croatia

## Talks and poster presentations

- 2015 Particle Simulations, Erlangen, Germany, Poster title: Morphological measures of randomly packed ellipses in 2D
- 2016 Imaging Particles, Erlangen, Germany, Poster title: Morphological measures of randomly packed ellipses in 2D
- 2016 Workshop on Innovative Surfaces and Materials, Primošten, Croatia, Poster title: Morphological properties of the epithelial tissue
- 2016 Animal, Vegetal, Mineral?, Yallingup, WA, Australia, Poster title: Morphological properties of the epithelial tissue
- 2017 DPG Spring Meeting, Dresden, Germany, Poster title: Morphological properties of the epithelial tissue

- 2017 International Congress Engineering of Advanced Materials, Erlangen, Germany, Talk title: Morphological properties of the epithelial tissue
- 2018 Measuring and Modelling Cell Migration, Vienna, Austria, Poster title: Structure of the epithelial tissue
- 2018 DPG Spring Meeting, Berlin, Germany, Talk title: Structure of the epithelial tissue
- 2018 Physics of Cells, From Biochemical to Mechanical (PhysCell 2018), Harrogate, UK, Poster title: Structure of the epithelial tissue
- 2018 11. znanstveni sastanak Hrvatskog fizikalnog društva, Beli Manastir, Croatia, Talk title: Struktura epitelnog tkiva
- 2019 4th Grandmaster Early-Career Workshop in Physics, Split, Croatia, Poster title: Structure of the epithelial tissue
- 2021 DPG Spring Meeting, Online Conference, Germany, Poster title: Structure of the epithelial tissue

### **Awards**

- 2020 Yearly Award of Ruđer Bošković Institute for Scientific Paper

# Statutory Declaration

Full name of the candidate:

Jakov Lovrić

Faculty:

Faculty of Sciences, Friedrich-Alexander-Universität Erlangen-Nürnberg

Thesis title:

Structural properties of Quantizer problem solutions

Statutory declaration:

I hereby solemnly declare that I am the author of the enclosed thesis and that I have not used materials and sources without corresponding declaration or citation in the text. All thoughts or quotations which were inferred from the sources are marked as such. I formally declare that this thesis was not submitted to any other authority to achieve an academic degree.

Date and signature:

Erlangen, 1 December 2021.



Jakov Lovrić